AD-A215 518 (4)

GL-TR-89-0163

INTEGRATED ANALYTICAL EVALUATION
AND OPTIMIZATION OF MODEL PARAMETERS
AGAINST PREPROCESSED MEASUREMENT DATA

J.	N.	Bass	K.	H.	Bhavnani
N.	A.	Bonito	K.		Bounar
C.	A.	Hein	C.	J.	Jordan
W.	J.	McNeil	M.	M.	Pratt
D.	S.	Reynolds	F.	R.	Roberts
C.	I.	Roth	D.	A.	Sannerud
M.	F.	Tautz	R.	P.	Vancour

RADEX, Inc.
3 Preston Court
Bedford, Massachusetts 01730

23 June 1989

Final Report
March 1987 - May 1989

GEOPHYSICS LABORATORY
AIR FORCE SYSTEMS COMMAND
UNITED STATES AIR FORCE
HANSCOM AFB, MASSACHUSETTS 01731-5000

89 12 06 095

"This technical report has been reviewed and is approved for publication"

EDWARD C. ROBINSON
Contract Manager
Data Systems Branch
Aerospace Engineering Division

ROBERT E. McINERNEY
Branch Chief
Data Systems Branch
Aerospace Engineering Division

FOR THE COMMANDER

C. NEALON STARK
Director
Aerospace Engineering Division

This report has been reviewed by the ESD Public Affairs Office (PA) and is releasable to the National Technical Information Service (NTIS).

Qualified requestors may obtain additional copies from the Defense Technical Information Center. All others should apply to the National Technical Information Service.

If your address has changed, or if you wish to be removed from the mailing list, or if the addressee is no longer employed by your organization, please notify GL/IMA, Hanscom AFB, MA 01731. This will assist us in maintaing a current mailing list.

Do not return copies of this report unless contractual obligations or notices on a specific document requires that it be returned.

Unclassified
SECURITY CLASSIFICATION OF THIS PAGE

REPORT DOCUMENTATION PAGE

1a. REPORT SECURITY CLASSIFICATION	1b. RESTRICTIVE MARKINGS
Unclassified	

2a. SECURITY CLASSIFICATION AUTHORITY	3. DISTRIBUTION/AVAILABILITY OF REPORT
	Approved for public release;
2b. DECLASSIFICATION/DOWNGRADING SCHEDULE	distribution unlimited

4. PERFORMING ORGANIZATION REPORT NUMBER(S)	5. MONITORING ORGANIZATION REPORT NUMBER(S)
RXR-89X623	GL-TR-89-0163

6a. NAME OF PERFORMING ORGANIZATION	6b. OFFICE SYMBOL (If applicable)	7a. NAME OF MONITORING ORGANIZATION
Radex, Inc.		Geophysics Laboratory

6c. ADDRESS (City, State, and ZIP Code)	7b. ADDRESS (City, State, and ZIP Code)
Three Preston Court Bedford, MA 01730	Hanscom AFB Bedford, MA 01731

8a. NAME OF FUNDING/SPONSORING ORGANIZATION	8b. OFFICE SYMBOL (If applicable)	9. PROCUREMENT INSTRUMENT IDENTIFICATION NUMBER
Aerospace Engineering Div	LCY	Contract F19628-87-C-0084

8c. ADDRESS (City, State, and ZIP Code)	10. SOURCE OF FUNDING NUMBERS			
	PROGRAM ELEMENT NO.	PROJECT NO.	TASK NO.	WORK UNIT ACCESSION NO.
GL/Hanscom AFB, MA 01731	62101F	9993	XX	YG

11. TITLE (Include Security Classification)

Integrated Analytical Evaluation and Optimization of Model Parameters against Preprocessed Measurement Data

12. PERSONAL AUTHOR(S) N.Bass, N.A.Bonito, C.A.Hein, W.J.McNeil, M.M.Pratt, C.J.Roth, M.F.Tautz, K.H.Bhavnani, K.Bounar, C.J.Jordan, D.S.Reynolds, F.R.Roberts*, D.A.Sannerud, R.P.Vancour

13a. TYPE OF REPORT	13b. TIME COVERED	14. DATE OF REPORT (Year, Month, Day)	15. PAGE COUNT
FINAL	FROM 3/87 TO 5/89	1989 JUN 23	284

16. SUPPLEMENTARY NOTATION

* Logicon, Inc., Bedford, MA

17. COSATI CODES			18. SUBJECT TERMS (Continue on reverse if necessary and identify by block number)
FIELD	GROUP	SUB-GROUP	Ephemerides; Atmospheric Density; Spacecraft Interactions; Contamination; CIV; Auroral Models; CRRES; Magnetic Fields; Magnetometers; Spectrograms; Shuttle Simulation; POLAR-BEAR; Attitude Determination; Ionosphere; Lightning; Graphics. (EDC)
	(Group Excluded)		

19. ABSTRACT (Continue on reverse if necessary and identify by block number)

This contract supported investigations for integrated applications on of ephemerides, physics, and mathematics of the atmosphere and near space. Projects undertaken and reported here included satellite, rocket, and astronomical circumstances; data based studies of atmospheric density and structure; spacecraft interactions leading to charging and contamination; auroral ion and electric field modeling; trapped particle, magnetic field, and instrumentation studies for CRRES; shuttle simulation and mission support; POLAR BEAR imaging and attitude determination; scintillation and spaced receivers; GEOTHB Radar processing system; lightning detection; file generating systems for ephemeris and attitude; study of common data formats; and software for interactive graphics. Keywords: Remote detectors; CRRES (Combined Release and Radiation Effects Satellite), Polar Bear Project, Aurorae. Array detinagers; POLAR computer program; Atmospheric physics, Spacecraft charging; Over-the-horizon backscatter radar. Scientific satellite orbits; Satellite attitude, CIV (Critical) Ionization Velocity;

20. DISTRIBUTION/AVAILABILITY OF ABSTRACT	21. ABSTRACT SECURITY CLASSIFICATION
☒ UNCLASSIFIED/UNLIMITED ☐ SAME AS RPT. ☐ DTIC USERS	Unclassified

22a. NAME OF RESPONSIBLE INDIVIDUAL	22b. TELEPHONE (Include Area Code)	22c. OFFICE SYMBOL
Edward C. Robinson	(617) 377-3840	GL/CY

DD FORM 1473, 84 MAR 83 APR edition may be used until exhausted. SECURITY CLASSIFICATION OF THIS PAGE
All other editions are obsolete.

REPORT DOCUMENTATION PAGE

1a. REPORT SECURITY CLASSIFICATION Unclassified	1b. RESTRICTIVE MARKINGS

2a. SECURITY CLASSIFICATION AUTHORITY	3. DISTRIBUTION / AVAILABILITY OF REPORT Approved for public release;
2b. DECLASSIFICATION / DOWNGRADING SCHEDULE	distribution unlimited

4. PERFORMING ORGANIZATION REPORT NUMBER(S) RXR-890623	5. MONITORING ORGANIZATION REPORT NUMBER(S) GL-TR-89-0163

6a. NAME OF PERFORMING ORGANIZATION Radex, Inc.	6b. OFFICE SYMBOL (If applicable)	7a. NAME OF MONITORING ORGANIZATION Geophysics Laboratory

6c. ADDRESS (City, State, and ZIP Code) Three Preston Court Bedford, MA 01730	7b. ADDRESS (City, State, and ZIP Code) Hanscom AFB Bedford, MA 01731

8a. NAME OF FUNDING / SPONSORING ORGANIZATION Aerospace Engineering Div	8b. OFFICE SYMBOL (If applicable) LCY	9. PROCUREMENT INSTRUMENT IDENTIFICATION NUMBER Contract F19628-87-C-0084

8c. ADDRESS (City, State, and ZIP Code) GL/Hanscom AFB, MA 01731	10. SOURCE OF FUNDING NUMBERS			
	PROGRAM ELEMENT NO. 62101F	PROJECT NO. 9993	TASK NO. XX	WORK UNIT ACCESSION NO. YG

11. TITLE (Include Security Classification)

Integrated Analytical Evaluation and Optimization of Model Parameters against Preprocessed Measurement Data

12. PERSONAL AUTHOR(S) N.Bass, N.A.Bonito, C.A.Hein, W.J.McNeil, M.M.Pratt, C.J.Roth, M.F.Tautz, K.H.Bhavnani, K.Bounar, C.J.Jordan, D.S.Reynolds, F.R.Roberts*, D.A.Sannerud, R.P.Vancour

13a. TYPE OF REPORT FINAL	13b. TIME COVERED FROM 3/87 TO 5/89	14. DATE OF REPORT (Year, Month, Day) 1989 JUN 23	15. PAGE COUNT 284

16. SUPPLEMENTARY NOTATION

* Logicon, Inc., Bedford, MA

17.	COSATI CODES		18. SUBJECT TERMS (Continue on reverse if necessary and identify by block number)
FIELD	GROUP	SUB-GROUP	Ephemerides, Atmospheric Density; Spacecraft Interactions, Contamination; CIV, Auroral Models, CRRES, Magnetic Fields, Magnetometers, Spectrograms; Shuttle Simulation; POLAR BEAR, Attitude Determination, Ionosphere; Lightning; Graphics.

19. ABSTRACT (Continue on reverse if necessary and identify by block number)

This contract supported investigations for integrated applications of ephemerides, physics, and mathematics of the atmosphere and near space. Projects undertaken and reported here included satellite, rocket, and astronomical circumstances; data based studies of atmospheric density and structure; spacecraft interactions leading to charging and contamination; auroral ion and electric field modeling; trapped particle, magnetic field, and instrumentation studies for CRRES; shuttle simulation and mission support; POLAR BEAR imaging and attitude determination; scintillation and spaced receivers; GE.OTHB Radar processing system; lightning detection; file generating systems for ephemeris and attitude; study of common data formats; and software for interactive graphics.

20. DISTRIBUTION / AVAILABILITY OF ABSTRACT ☒ UNCLASSIFIED/UNLIMITED ☐ SAME AS RPT. ☐ DTIC USERS	21. ABSTRACT SECURITY CLASSIFICATION Unclassified
22a. NAME OF RESPONSIBLE INDIVIDUAL Edward C. Robinson	22b. TELEPHONE (Include Area Code) (617) 377-3840 — 22c. OFFICE SYMBOL GL/LCY

DD FORM 1473, 84 MAR — 83 APR edition may be used until exhausted. All other editions are obsolete.

ACKNOWLEDGEMENTS

TABLE OF CONTENTS

TABLE OF CONTENTS (cont'd)

TABLE OF CONTENTS (cont'd)

LIST OF FIGURES

LIST OF TABLES

1. EPHEMERIS

Various requirements for spacecraft and astronomical ephemerides continued to arise at Geophysics Laboratory (GL). Applications consisted of adaptations to established programs already in operational use, investigations for operational and accuracy improvement, and greater use of graphics output - in particular using laser printers. Some special studies and new software products were also completed.

1.1 SPACECRAFT EPHEMERIS

Satellite and rocket ephemerides are covered in this section. LOKANGL continued to be the basic program for satellite orbit generation. Speed improvement, a compact viewing chart, a prediction accuracy study, and the adaptation of LOKANGL for CRRES are described. Prospects for application of the Tracking and Data Relay Satellite System (TDRSS) at GL were evaluated. Finally, some improvements were made to the rocket trajectory system for application to flights with separating modules.

1.1.1 LOKANGL Modifications

Many orbital prediction packages, including WRSTP in LOKANGL, make use of "stepping" to compute the satellite/spacecraft position at equally spaced intervals, and determine whether it is visible from a given sensor at each interval. The HISTEP option and the newer RISETM option use orbital element information and sensor coordinates to predict times at which the satellite/spacecraft will be visible, revert to stepping only during these passes. For low altitude satellites this reduces CPU usage to about 25% of that required for stepping.

In the present implementation, both the HISTEP and RISETM algorithms predict the rise time or visibility of a satellite as viewed from a single sensor only. HISTEP predicts the time of latitude crossings (using the latitude of the sensor) and, if the satellite may be visible during the next pass, estimates the rise time. Since the latitude for viewing is used, additional checking is required since visibility is possible at sensor latitudes higher than orbit inclination.

The new algorithm RISETM is based on an analytic method described in Escobal [1965] (5.4.2-5.4.5). The algorithm has been implemented so as to be easily incorporated into other orbit prediction packages. RISETM predicts the next rise time (if one occurs before the next perigee) of a satellite. If no rise time is predicted before the next perigee, the subroutine returns the time of next perigee. A flag is used to indicate whether the time returned is a predicted rise time or the next perigee time. If the flag is set, control is returned to LOKANGL to continue stepping at the predicted time, otherwise a single step is performed and then the next orbit is searched for a possible rise time. RISETM has been successfully integrated within LOKANGL.

Preliminary tests indicate that the RISETM subroutine is working correctly. Comparisons have been made with LOKANGL output using both the HISTEP and stepping options. The performance of RISETM appears to be more consistent than HISTEP. The only disadvantage noticed so far is that some low elevation passes (< 5 degrees) have been missed by RISETM. A version of LOKANGL using the RISETM routines is now in regular use. Further tests are warranted before it is integrated into the LOKANGL production version.

1.1.2 Viewing Diagrams for Low Earth Satellites (Hussey Charts)

LOKANGL output provides detailed satellite tracking information over an extended period at regular time intervals, such as one minute steps. However, as an adjunct to routine WRSTP that was provided by Isabel Hussey of GL, a convenient means of viewing the data in compact format is implemented in routine VIEWSAT which generates **Hussey** charts (Figure 1.1).

All opportunities for viewing a low earth satellite during a calendar month or an arbitrary 30 day interval are presented on a single sheet plot. The day of the month and the day number for the year are displayed on the left and right sides of the plot, respectively. Time of the day (UT) is displayed on the top and bottom of the plot. Each viewable pass is displayed as a circle, centered in time at the maximum elevation. The time in minutes at which maximum elevation occurs is printed within the circle. Dots or crosses within the circle depict the predicted azimuth and elevation on a uniform time step basis, such as every minute on each pass. Elevations less than a user specified value are dispensed with.

The observer is considered to be at the center of the circle, with the circumference at the horizon (0° elevation). Elevations from zero to directly overhead can be deduced. Azimuth is also implicit, with North at the top and East to the right. A large dot near the horizon shows where the observations would commence, and therefore also indicates the direction of motion. The position of maximum elevation is indicated by a large open dot.

Solar conditions on the ground and on the satellite appear as follows:

Two pairs of dashed lines show the daily ground sunrise and sunset times at the horizon and at an elevation of -10°.

Dark circles show the cases when the satellite is in darkness at maximum elevation.

Light circles show when the observer and the satellite are in sunlight at maximum elevation.

Dashed circles show when the observer is in darkness and the satellite is illuminated by the sun at maximum elevation. These are the best conditions for visual sighting of the satellite. If the satellite is in the earth's shadow during part of the pass, the corresponding points are marked with an "X".
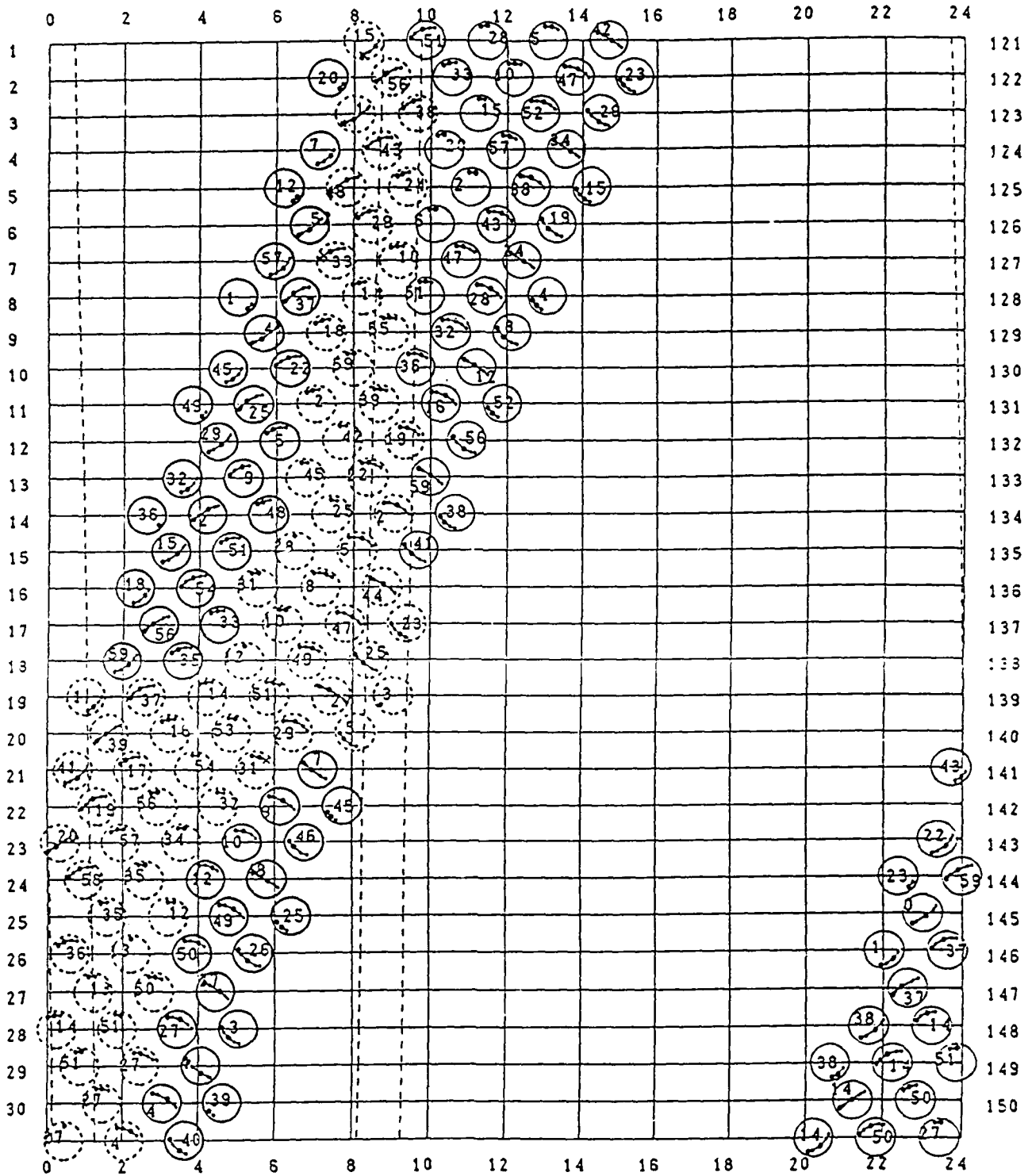
Figure 1.1. VIEWSAT

1.1.3 Prediction Study on D MSP F7 Orbital Elements

LOKANGL was used to perform a prediction study on the orbital elements provided by SPACECOM for the DMSP F7 satellite. The data used for the study spanned the interval from June 5, 1988 to March 22, 1989.

Data from the orbital elements are displayed in graphical form in Figures 1.2-1.5. Additional related data is provided in Figures 1.6-1.8. The time displayed on the horizontal scale is the number of days elapsed from 0 hr UT on 0 January 1988 (December 31, 1987). The data provided in Figures 1.2-1.10 are as follows:

Figure	Data	Units
1.2	Eccentricity	
1.3	Argument of Perigee	degrees
1.4	Mean Motion	rev/day
1.5	Ndot/2 (derivative of mean motion)	
1.6	Actual - Predicted Mean Motion	rev/day
1.7	Semi-Major axis	km
1.8	Perigee Height	km
1.9	Solar Activity	
1.10	Time Difference Actual - Predicted for Nodal Crossings	seconds

Figure 1.4 displays the actual mean motion (data symbol is a small square), and the predicted mean motion. The latter, identified with a +, is obtained from the previous value of the mean motion and Ndot/2 by linear extrapolation. The difference between these values is displayed in Figure 1.6.

In Figure 1.5 Ndot/2 is increasing (on average) with time and exhibits large fluctuations. The variation in Ndot/2 is also reflected in the increase in the mean motion displayed in Figure 1.8 and the decrease in the semi-major axis (computed from the mean motion) displayed in Figure 1.7.

Figure 1.8 displays the perigee height (the altitude of the satellite at perigee). The perigee height depends upon the inclination and the argument of perigee and reflects the deviation of the earth's surface from a sphere. The periodic behavior of perigee height reflects the fact that the argument of perigee for F7 precesses 360 degrees in about 140 days. The perigee height is maximum when the perigee point is near the south pole; it is at a smaller maximum when the perigee is near the north pole. It is at a minimum when the perigee point is near the equator. The amount of drag experienced by a high inclination satellite should be maximal when the perigee point is at or near the equator. Thus, at times of low solar activity, Ndot/2 should exhibit some periodic behavior with a period of 140 days. If present, in Figure 1.5, this behavior is masked by solar activity (see below).

4
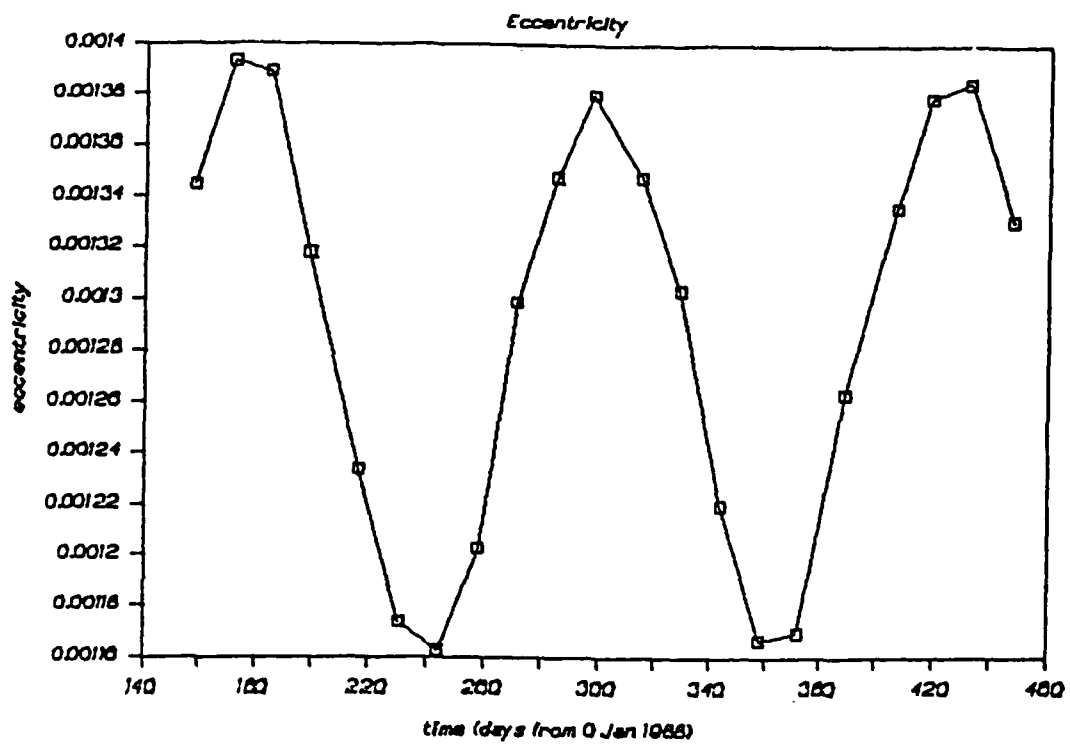
Figure 1.2. Eccentricity vs. time (days)
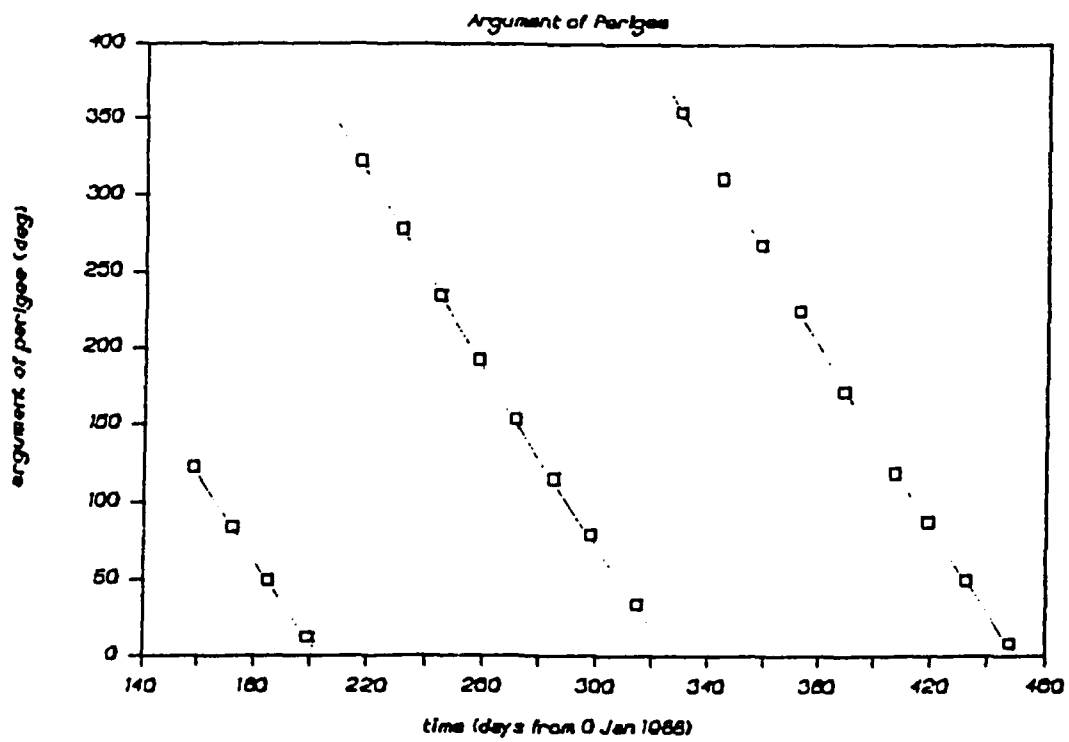
Figure 1.3. Argument of perigee
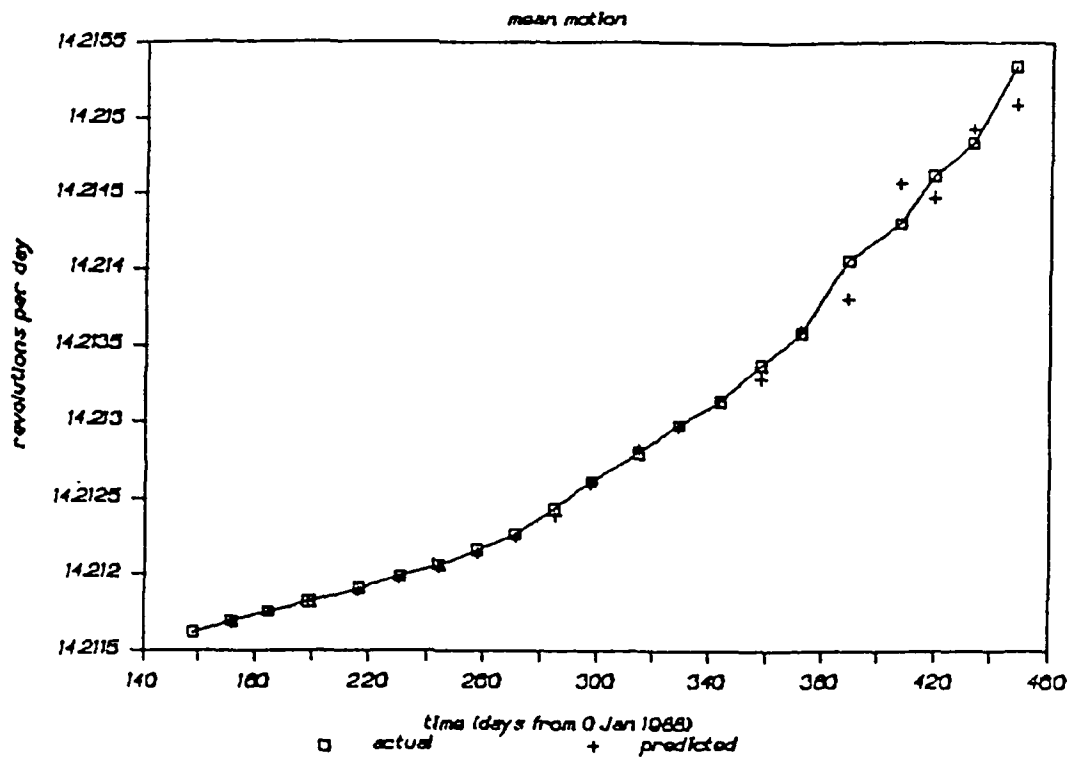
Figure 1.4. Mean motion
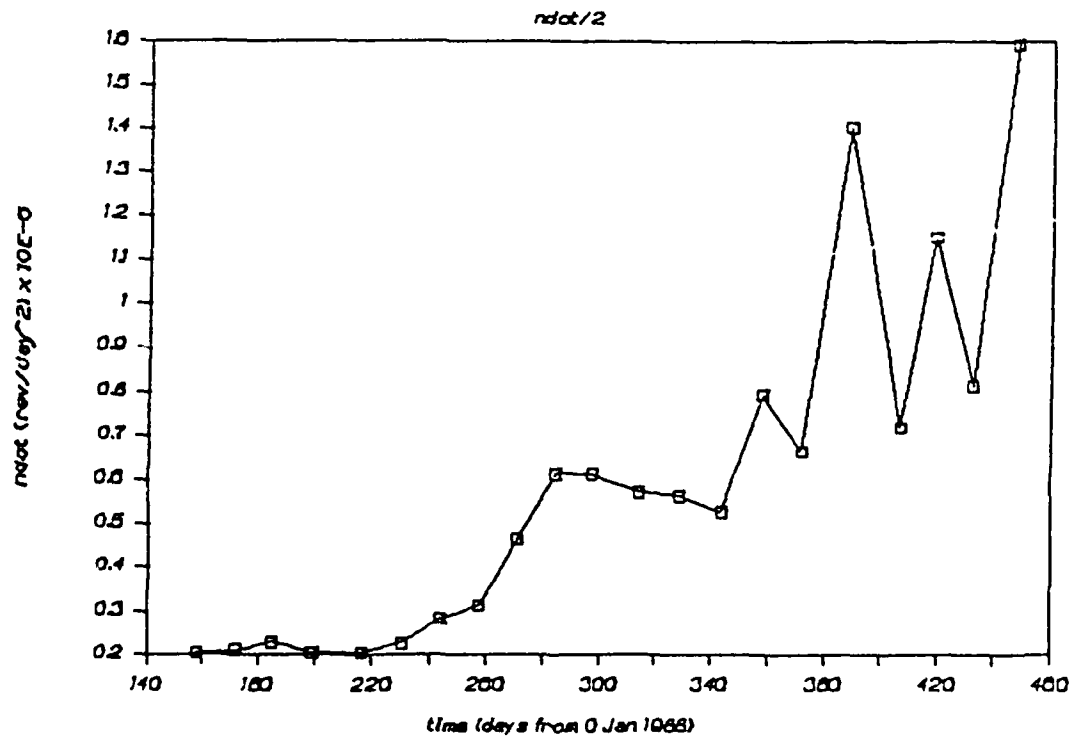
Figure 1.5. Derivative of mean motion

6
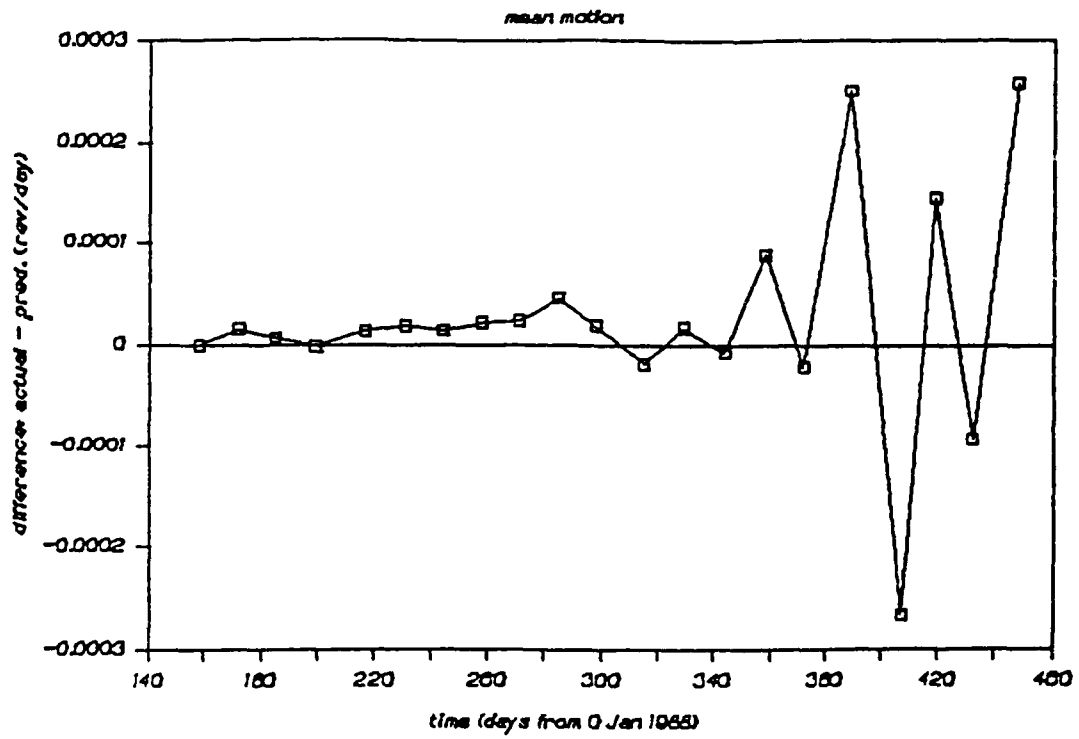
Figure 1.6. Actual-predicted mean motion
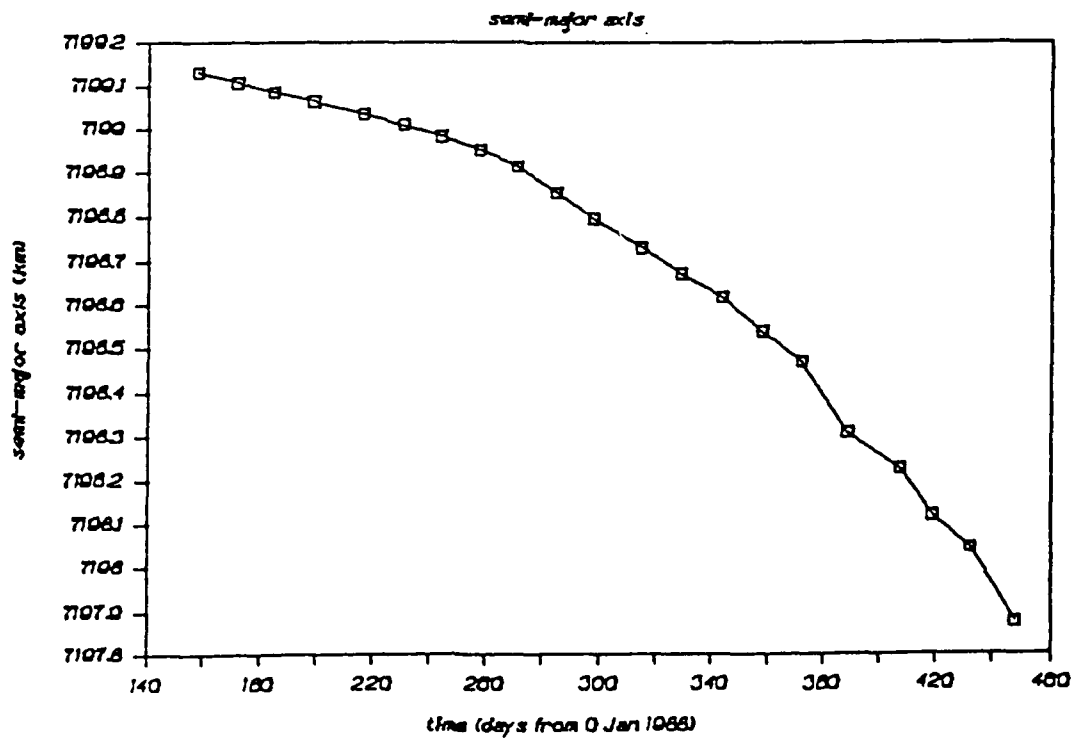
Figure 1.7. Semi-major axis
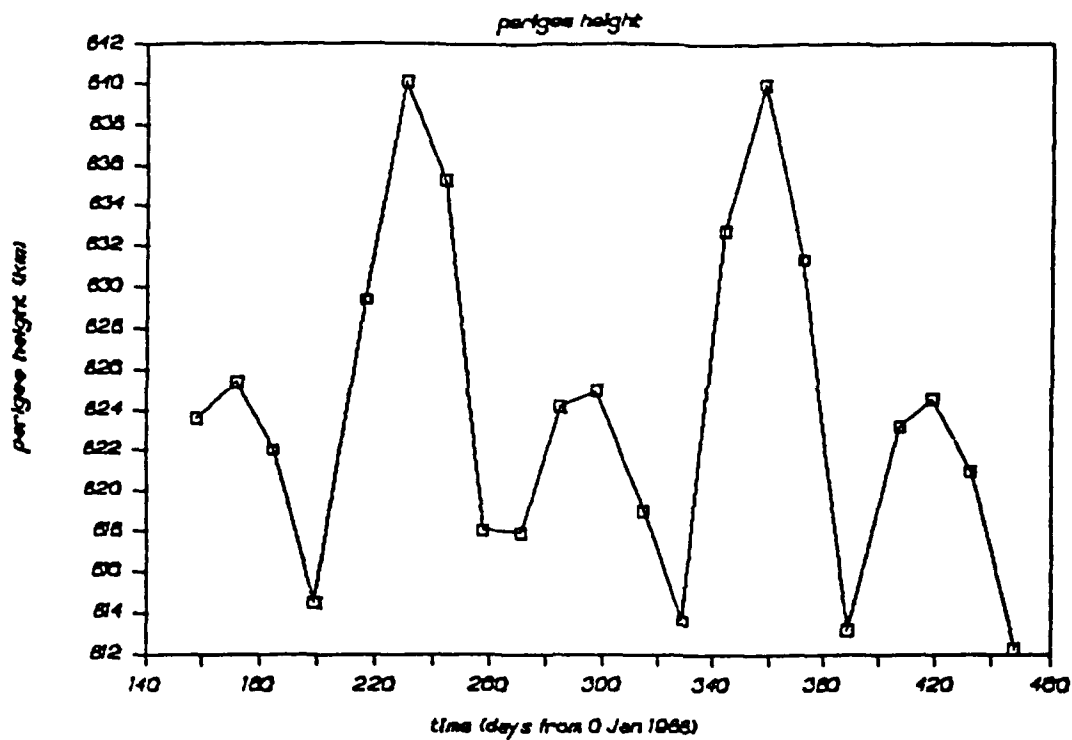
Figure 1.8. Perigee height
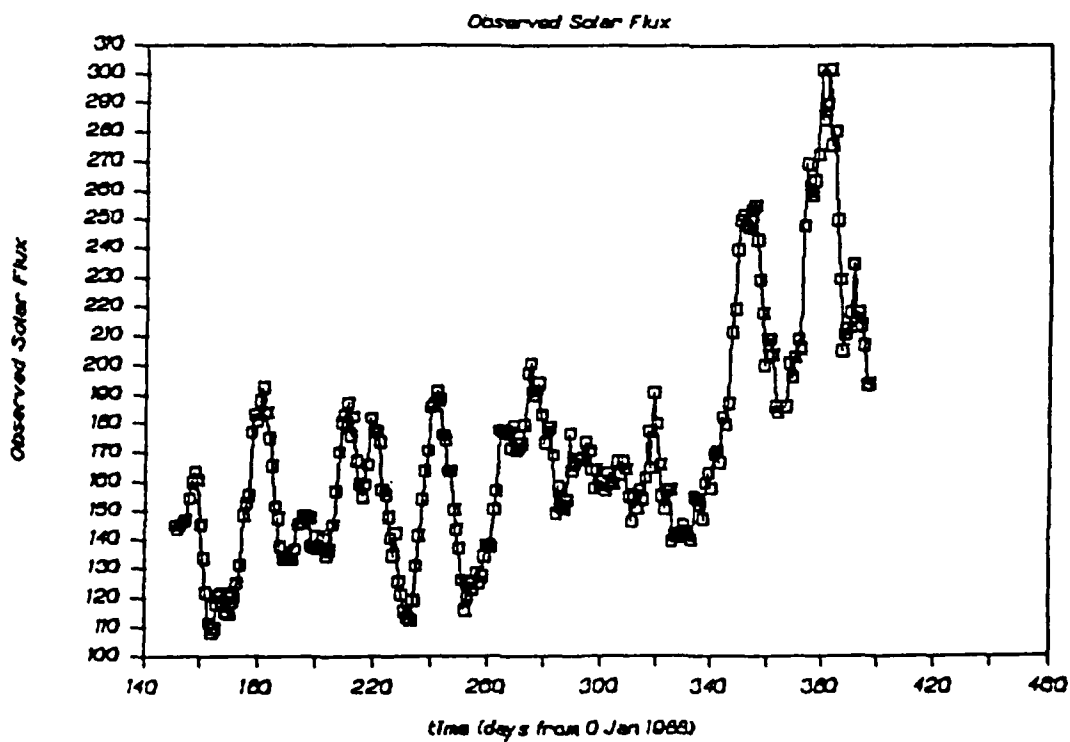
Figure 1.9. Observed solar flux

8

The value of the second derivative of mean motion (N2dot) provided in the data was zero. Values of a drag parameter were also provided in the data. This drag parameter is not used by LOKANGL.

Figure 1.9 displays the daily solar flux values (Ottawa), from June 1, 1988 to January 31, 1989, taken from the Daily Solar Indices. The data is displayed on the same time scale as the orbital data. There is a strong correlation between the solar flux data and the values of Ndot/2 displayed in Figure 1.5, indicating that the variability of NDot/2 in Figure 1.4 is largely due to high altitude drag related to solar activity. Since solar activity is often due to sunspot and solar flare activity on small areas of the sun, the solar flux data exhibits periodic behavior at the solar rotation period.

The orbital prediction capability of LOKANGL was used to compute mean elements at the epoch times of each subsequent element set. For the DMSP satellites, the argument of latitude (the sum of the argument of perigee W and the true anomaly V) at the times at which element sets are issued is close to 360 degrees. This means that the orbital elements are provided at nodal crossings. For small eccentricity the true anomaly V is nearly equal to the mean anomaly M. This means that it is possible to accurately estimate the time delay between the actual and predicted nodal crossing by computing the difference between the actual and predicted (using LOKANGL) values of W + M and dividing by the mean motion n.

Figure 1.10 displays the result of this procedure. The first 12 element sets (epochs between 157 and 315 days) are propagated to the times of the following nine element sets - a time interval of about 140 days. The difference between the actual (= epoch element set) value of (W + M)/n and the predicted (= propagated) value is plotted vs time. Each curve begins at the epoch time of one of the element sets with a zero vertical displacement. The vertical displacement of subsequent data points on the curve represents the time delay of the predicted nodal crossing of the original element set relative to the element set corresponding to the propagated time (the actual nodal crossing). In most cases, the actual nodal crossings are earlier than those predicted from previous element sets. A few of the values from later element sets (day 329 and beyond) not included on Figure 1.9 exhibit negative values.

The qualitative behavior of the individual curves on Figure 1.9 can be explained, in part, by the fact that the mean motion of the satellite F7 is increasing with time due to atmospheric drag. In order to model the effect of drag, an estimate of the value of the first derivative of the mean motion (ndot/2) is provided with each F7 element set. If the drag environment does not vary appreciably over time and the estimate of (ndot/2) is reasonably accurate, then the LOKANGL predictions for F7 will be good for a few months. Where the mean motion (Figure 1.4) is linear, this appears to be the case. With few exceptions, the values of Ndot/2 provided by the orbital element sets systematically underestimate the actual orbital decay of the satellite.

It may be possible to improve the prediction accuracy of LOKANGL by obtaining better estimates of Ndot/2 from the use of perigee height and recent solar activity data.

9
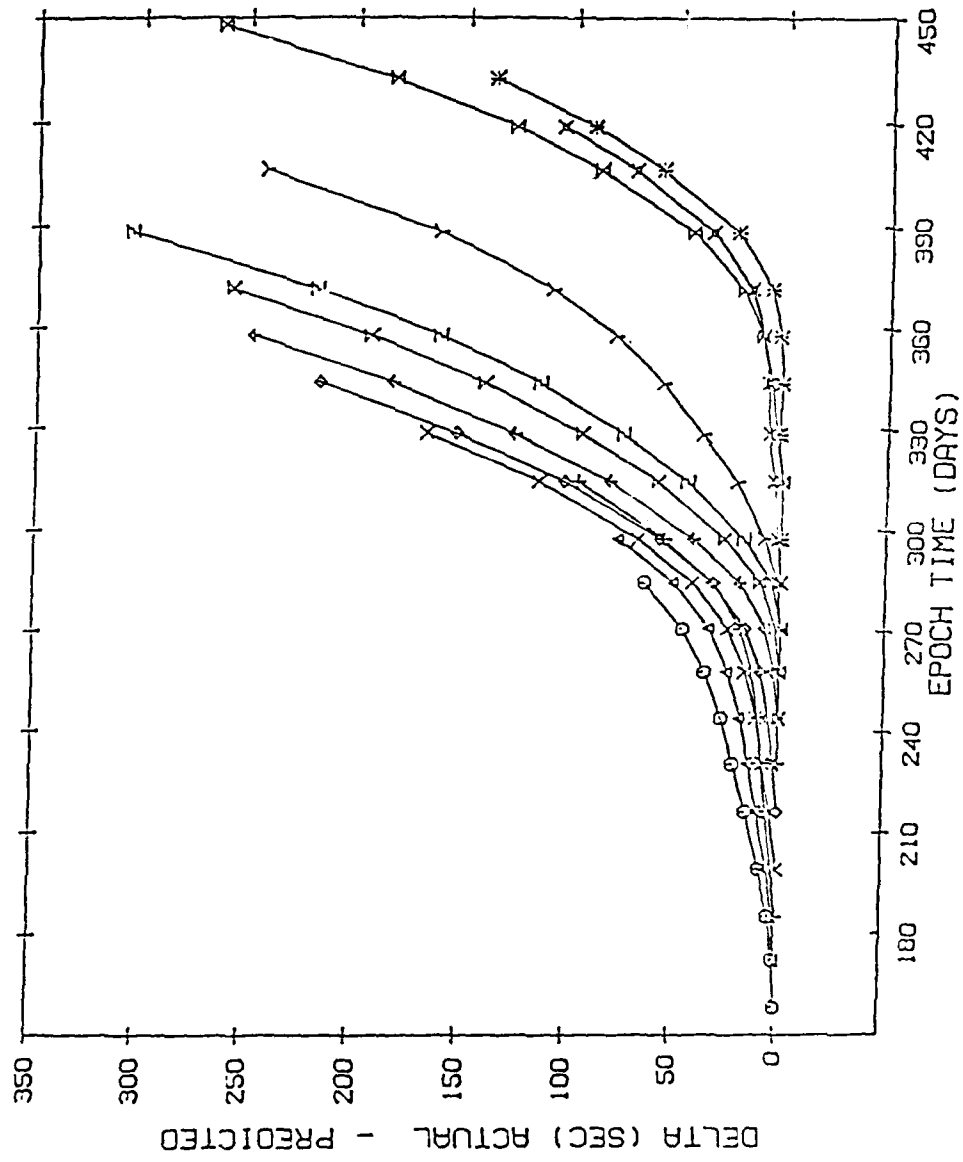
Figure 1.10. Time difference, actual-predicted for nodal crossings

10

1.1.4 CRRES Orbit Generation Accuracy Study

During the course of the development of the CRRES Ephemeris Generating system [Bhavnani, et al., 1987], various one-day reference orbits provided by Geodynamics Corp. were employed in conjunction with GL's satellite orbit generation program, LOKANGL, to evaluate the accuracy of the latter system. The results of this study have been reported [Robinson, et al., 1988] and have suggested that the range of unmodeled deviations that are inherent in the LOKANGL approach may amount to 5 km when spanning elements one day or less apart. The question of the uncertainty when elements had to span a week or so required the availability of reference orbits covering longer periods than one day.

Geodynamics Corp. was requested to provide four CRRES type reference orbits using their MVS/TRACE precision orbit determination system. Fifteen days of model ephemerides with and without full geopotentials and perturbations were desired at 10 minute intervals, and were delivered to GL on floppies. Each orbit started at 0 UT on day 90, 1990, and had common characteristics as follows:

$$i = 18^0 \qquad n = 2.559 \qquad e = 0.7$$
$$\Omega = 60^0 \qquad M = 0^0$$

Specific features requested for each case were:

1. $\omega = 0^0$ with all perturbations present so as to limit modeling inaccuracies to a few meters.
2. Repeat (1) above with moon, drag, radiation pressure, and all geopotentials except μ, J_2 and J_3 turned off.
3. $\omega = 90^0$ with all perturbations present so as to limit modeling inaccuracies to a few meters.
4. Repeat (3) above with moon, drag, radiation pressure, and all geopotentials except μ, J_2 and J_3 turned off.

Cases (1) and (3) introduced deliberate variabilities in the study through different arguments of perigee, while (2) and (4) represented the analytical LOKANGL model situation, even though obtained by numerical integration   Extensive testing was conducted, simulating CRRES operational conditions using "position-velocity vectors" spanning one orbit to days apart. These vectors were in fact available in the reference orbits, so that deviations at other times, between LOKANGL and the reference orbits, could be ascribed to modeling inadequacy.

Table 1.1 presents selected results for all four orbits, in particular the best and the worst cases for spanning single orbits, 1 to 7 days, and 15 days. These results show that in cases (2) and (4) where higher order perturbations are turned off, the one orbit and 7 day deviations are similar and rarely greater than 1 km in-track. The variations are probably accounted for by differences in J_2 and J_3 between the two generating progr ... Cases (1) and (3) are more realistic, and deviate starting with a single orbit (as seen in our previous studies), with some further deterioration in LOKANGL's ability to reproduce orbits as the tie-down span increases. Even when spanning a single orbit, the maximum in-track error approaches 3 km in the worst case. When spanning 7 days, the maximum in-track error ranged between 10 km in the best case and 20 km in the worst case. Figures 1.11(a) and 1.11(b) show worst case results for cases (1) and (2) respectively, which are also listed in Table 1.1. Figures 1.11(c) and 1.11(d) similarly show results of some relatively poor cases for (3) and (4).

11

Table 1.1 Selected Results Comparing LOKANGL Orbits Generated based on Four Accurate Reference Orbits provided by Geodynamics Corp.

Greatest Deviations are Determined for Typical Vector Spans.
(Initial and Final Position Tie-Down is employed by LOKANGL)

VECTOR SET		STARTING D T (SEC)		SPANNING D T (SEC)	INTRACK MIN	INTRACK MAX	RADIAL MIN	RADIAL MAX	CROSSTRACK MIN	CROSSTRACK MAX
GDVEC1X	94	24600.0	0	33600.0	-.890	.520	.000	.960	-.150	.030
GDVEC1X	98	15000.0	0	33600.0	-2.180	1.140	.000	2.450	-.190	.050
GDVEC1X	90	15000.0	5	0.0	-13.200	2.410	-2.400	2.540	-.980	.910
GDVEC1X	95	72000.0	5	5400.0	-2.260	10.090	-.920	3.230	-.900	.950
GDVEC1X	90	.0	7	.0	-21.140	3.890	-2.590	5.520	-1.300	1.270
GDVEC1X	94	.0	7	.0	-4.570	13.750	-3.270	4.420	-1.190	1.490
GDVEC1X	90	.0	15	.0	-15.550	32.510	-6.910	10.170	-3.310	3.000
GDVEC2X	97	67800.0	0	33600.0	-1.110	1.160	.000	1.570	-.030	.000
GDVEC2X	92	.0	7	.0	-.440	.510	.000	.300	-.020	.010
GDVEC2X	93	.0	7	.0	-.050	1.260	.000	.110	-.030	.000
GDVEC2X	90	.0	15	.0	-1.130	4.360	.000	1.670	-.030	.000
GDVEC3X	90	4200.0	0	33600.0	-.160	.100	.000	.190	-.170	.010
GDVEC3X	94	24600.0	0	33600.0	-3.020	2.710	.000	5.910	-.050	.170
GDVEC3X	97	600.0	0	33600.0	-1.110	2.280	-.010	2.160	-.110	.100
GDVEC3X	97	.0	1	.0	-1.350	1.540	-.160	1.720	-.100	.140
GDVEC3X	91	.0	7	.0	-5.180	11.330	-4.350	3.270	-1.690	1.330
GDVEC3X	95	.0	7	.0	-20.610	3.830	-4.290	3.700	-.260	1.090
GDVEC3X	90	.0	15	.0	-44.960	10.130	-10.520	8.970	-2.570	3.000
GDVEC4X	94	56400.0	0	33600.0	-.630	.610	.000	.840	-.030	.000
GDVEC4X	98	15000.0	0	33600.0	-1.260	1.220	.000	1.720	-.030	.000
GDVEC4X	90	15600.0	1	15000.0	-.070	.060	.000	.060	-.010	.000
GDVEC4X	92	.0	7	.0	-.480	.430	.000	.380	-.030	.000
GDVEC4X	90	.0	15	.0	-1.150	4.370	.000	1.710	-.030	.000

COVEC1. DAY 90 TO DAY 97   DATA - TAPE3
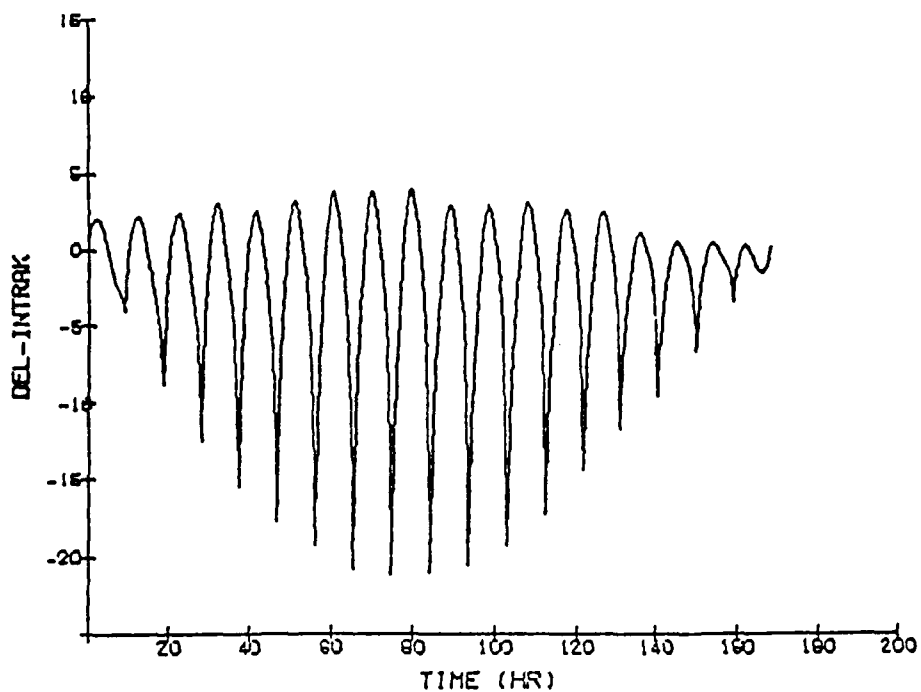
Figure 1.11a.

COVEC2 93/0 - 100/0   DATA - TAPE3
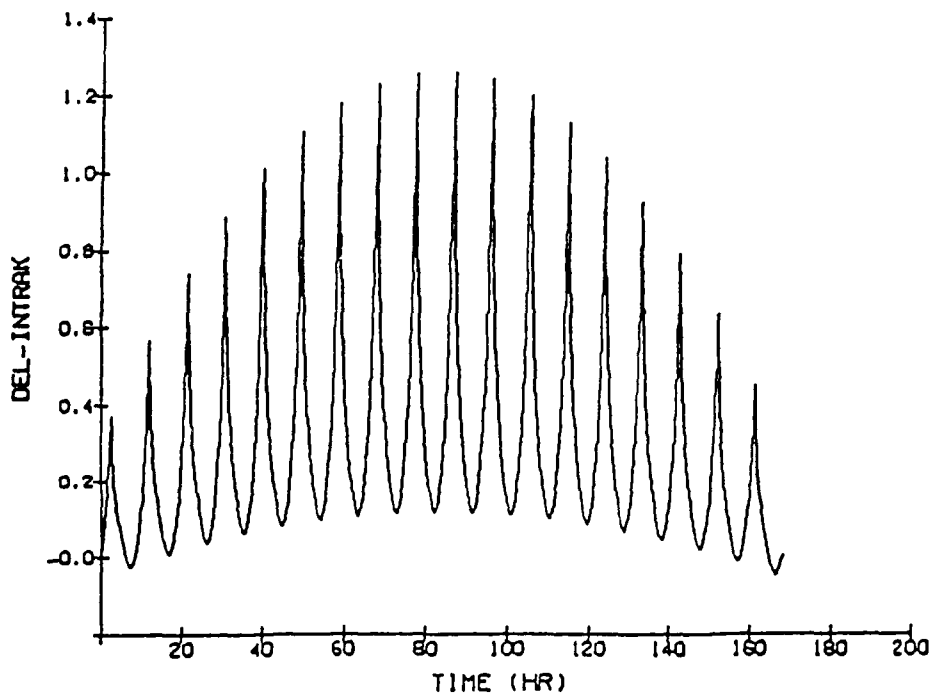
Figure 1.11b.

Figures 1.11a. and 1.11b. show worst case results for cases (1) and (2), respectively

13
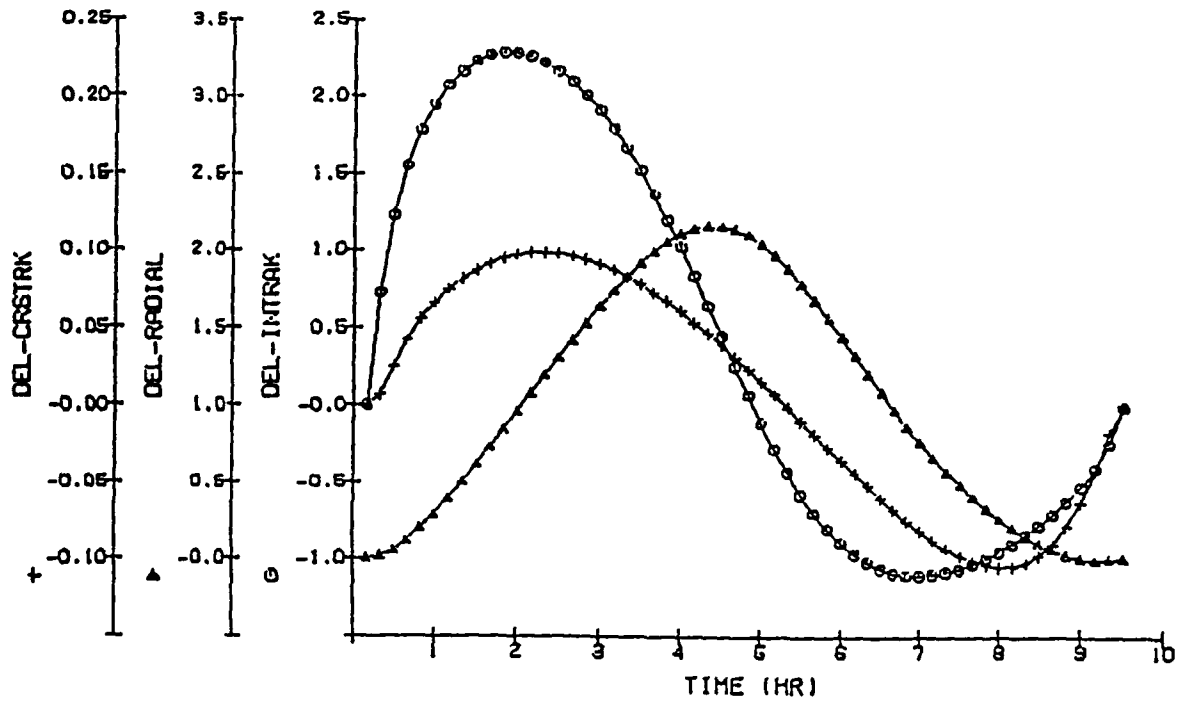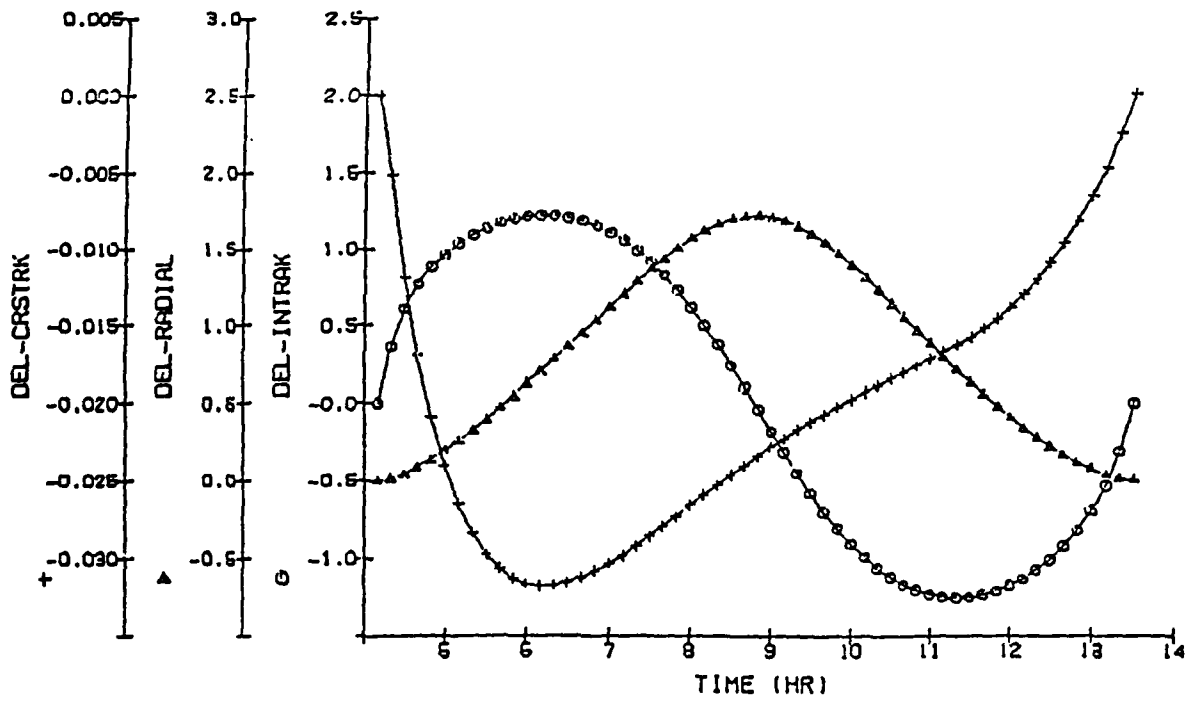
Figure 1.11c.

Figure 1.11d.

Figures 1.11c. and 1.11d. show results of relatively poor cases for (3) and (4), respectively

1.1.5 TDRSS Report

A study of NASA's Tracking and Data Relay Satellite System (TDRSS) system was performed in order to determine whether it is possible to make inexpensive use of TDRSS data for orbit determination studies at GL. The study included a literature search and communications with individuals currently involved with TDRSS activities. Potential uses of TDRSS data at GL are high accuracy orbital studies and/or more timely orbit determination. Tracking data for satellites using the TDRSS system are collected by NASA GSFC and are made available to government agencies and contractors. The TDRSS tracking data are also incorporated into the orbital elements information released by NASA GSFC and other agencies.

The primary advantage to the use of TDRSS over conventional ground based communication and tracking is the extensive coverage provided, particularly for Shuttle missions and low altitude satellites. Communications with a user satellite or spacecraft can be maintained over a large part of an orbit, as compared with a single pass for a single ground station. The tracking accuracy of the TDRSS system is comparable or better than the accuracy attainable with NASA's ground station network. Current NASA plans are to phase out the ground station network.

The TDRSS system consists of a pair of geostationary Tracking and Data Relay Satellites (TDRS) satellites and a ground station. The TDRS satellites are parked at 41° and 171° west longitude respectively. The ground station is located at White Sands, New Mexico (106° west longitude). A spare TDRS satellite is stationed at 106° west longitude. Although primarily intended as a replacement for one of the other satellites, the spare is also available for regular use when needed.

The TDRS geostationary satellites provide high capacity data communication links between the ground station and spacecraft or satellites equipped with a TDRSS transponder. The TDRSS tracking function is an integral part of the communications link and makes use of time delay and doppler offset information obtained from the communications link to estimate the orbital elements for a spacecraft or satellite.

TDRSS tracking data is reduced by performing a backwards signal trace in an inertial coordinate system. From the tracking configuration in use (using either one or two TDRS satellites) it is possible to obtain precise range and range rate data along the various "legs" of the signal path. Using the less accurate angle data (from the pointing of the TDRS antenna) it is possible to obtain precise estimates of the satellite's ECI position and velocity vectors.

Note that the data obtained would be substantially different from the usual radar or optical data normally used in orbit determination and estimation programs. Proper use and interpretation of the data would require a detailed understanding of the description of TDRSS observation measurement and modeling presented in a NASA publication [Pfung, et al., 1980].

In order for GL to use TDRSS data, it is necessary to either (1) obtain an existing orbit determination/estimation program which accepts TDRSS data, (2) modify an existing orbit determination program to accept TDRSS data, or (3) write a program to convert the TDRSS data to equivalent radar range and range rate data for sensors located at the position of the TDRS satellites for input into a standard orbit determination/estimation program.

In addition, the processing and archival aspects appear comparable to these services which are now performed by orbit determining agencies, and the possibility of making inexpensive use of actual TDRSS data is presently limited.

1.1.6 Rocket Trajectory Models for Module Separations

The dynamics of the upper atmosphere is sometimes probed by rocket launches of experimental payloads to high altitudes. Sometimes these payloads remain attached to the launching vehicle (rocket) throughout the flight. However, recently it has become more common for the payload to be separated from the rocket shortly after completion of the burn sequence, and/or for various modules within the payload to be separated from the rest of the package at various times during the flight. In each of these separations, each module involved receives an impulse which must be estimated accurately if we are to obtain an accurate estimate of its subsequent trajectory. The rocket trajectory system handles explicitly only the simple launches, involving no separations. To handle the more complex (separation) cases, we have provided specially-tailored versions containing hand-calculated short-term thrusts to simulate the impulse received by each separating vehicle.

Recently we have developed, for the ECHO-7 launch, a version of subroutine THRUST [Logicon F.R., 1976, Bhavnani et al., 1979] which performs these calculations automatically for a given sequence of separations events, for each of which is specified the time, relative separation velocity (including direction), masses of the two separation portions, and identification of the individual modules carried within each separating portion. To track an individual module, subroutine THRUST, in its initialization call, constructs the operating thrust table from the appropriate stored rocket model, which does not include separations, and then adds to this table subsequent time lines to handle the separations. Each separation is handled as a thrust of duration Δt, currently set at 0.5 sec. The thrust T_i imparted to each separating portion is ($i = 1$ or 2):

$$T_i = I_i/\Delta t, \tag{1.1}$$

where I_i is the impulse imparted to portion i. In the center of mass system, the velocity of each portion is 0 before the separation and v_i after the separation. Thus the impulse imparted is:

$$I_i = m_i v_i. \tag{1.2}$$

By conservation of momentum:

$$m_1 v_1 + m_2 v_2 = 0. \tag{1.3}$$

For relative separation velocity v_r,

$$v_1 - v_2 = v_r \tag{1.4}$$

Solving Equations (1.3) and (1.4) for the v_i's, and then substituting back into equations (1.1) and (1.2), we obtain:

$$T_1 = -T_2 = \mu v_r/\Delta t, \tag{1.5}$$

where μ, commonly called the reduced mass, is given by:

$$\mu = m_1 m_2/(m_1 + m_2). \tag{1.6}$$

16

Subroutine THRUST assumes that the masses are in pounds, and that v_r is given in m/sec. Thus the form of equation (1.6) used in THRUST contains conversion factors necessary to provide the thrust in pounds:

$$T_1 = -T_2 = 3.28\mu v_r/(32.1\Delta t). \qquad (1.6')$$

The factor 3.28 is necessary to convert m/sec to ft/sec, and the 32.1 converts the masses from pounds to slugs, the formal English units.

The operating thrust tables set up in this way accommodate 21 time lines. Two lines are required for each separation, one at the start of the separation, in which the thrust is given by equation (1.6'), and one at the end of the separation (Δt sec later), in which the thrust is zero. Thus the number of separations we can accommodate with the present allocations is

$$\text{NSEPMAX} = (21-\text{NTHR})/2, \qquad (1.7)$$

where NTHR is the number of time lines in the rocket thrusting model.

Unlike the rocket burns, the direction of a separation, and therefore the simulating thrust, may be different from the instantaneous velocity direction immediately before the separation. Therefore THRUST maintains stored tables containing the azimuth and elevation of each separation, defining the direction of v_1 (v_2 is in the opposite direction). For each thrust time line after completion of the main rocket burns (i.e., each separation), THRUST redefines, during the main integration of the trajectory, the direction of the thrust from these tables.

1.1.6.1 Improvements to Subroutine THRUST

In conjunction with the refinements for modeling of several module trajectories, the subroutine THRUST in DRIVEB was improved to eliminate limitations due to fixed data array sizes in THRUST. The thrust and mass loss history, which is used in THRUST, is contained in an auxiliary file called THRTAB. This file is standardized so that models for payloads with or without separating modules can be analyzed.

A sample of two models for different rocket trajectories from THRTAB are shown in Table 1.2 below. They represent thrust and mass loss history for payloads with and without separating modules. THREAD is a routine that reads the information in the auxiliary file. To differentiate between the two cases (with and without separations), it looks for the word END in any line after thrust and mass loss information is read to return control to the THRUST routine. The word END must be separated by spaces; (END), for instance, is not acceptable.

In Table 1.2, the rocket ID number marks the beginning of information on the desired rocket. Next, the rocket name is given. The number of data points is also provided. For example, the rocket ID number 53 in Table 1 has 21 data points, of which 9 occured after the first module separation took place. There are four separations in this case, with the azimuth and elevation angles providing the direction of the module after its separation. For rocket ID number 02 in Table 1.2, there were no separations, so the word END appears in the line just after the thrust and mass information.

1.1.6.2 Generation of ECHO-7 Module Trajectories

Trajectories were generated for all the separating modules for the ECHO-7 experiment [Malcolm, 1988]. The critical element for the investigators was the relative separation of the various sections. An initial run was available for the ACS module using the above models and the standard radar data filtering process of the Rocket Trajectory program. Pure integration runs were then performed for each of the modules, viz. ACS, Nose Cone, PDP, EPP, and the rocket body. The differenced results (relative to the ACS) were then added to the ACS trajectory to provide best estimate trajectories for each separating module. Complete files for position and velocity, and supporting plots for actual as well as relative position and velocity, were generated. Figure 1.12a shows a typical velocity profile for the nose cone. Figure 1.12b shows the relative velocity vector (in elevation, azimuth, and range) for the nose cone relative to the ACS module.

Table 1.2 Sample of thrust and mass loss values for rocket ID values 53 and 02.
Note that there is no separation for rocket ID 02.

```
53
ROCKET NAME :
BLACK BRANT IX. ACS
NUMBER OF DATA POINTS :
21
DATA TABLE FOR 53
TIME      THRUST   & RATE       WEIGHT &  RATE      AREA     COEF     STAGE
0.0,      4000.,    465000.,    5279.,    276.,     1.625,   1.20,    1.0,
0.1,      50500.,   5395.,      5252.,    276.,     1.625,   1.20,    1.0,
3.9,      71000.,   -142000.,   4203.,    276.,     1.625,   1.20,    1.0,
4.4,      0.,       0.,         3334.,    0.,       1.625,   0.45,    2.0,
11.1,     0.,       20048.,     3334.,    72.,      1.625,   0.36,    2.0,
12.2,     22253.,   -5104.,     3254.,    72.,      1.625,   0.36,    2.0,
12.9,     18680.,   73.,        3204.,    72.,      1.625,   0.36,    2.0,
23.9,     19490.,   -142.,      2412.,    72.,      1.625,   0.36,    2.0,
34.4,     18004.,   -205.,      1656.,    72.,      1.625,   0.36,    2.0,
38.9,     17081.,   -1875.,     1332.,    50.,      1.625,   0.36,    2.0,
42.9,     9582.,    -6844.,     1132.,    29.,      1.625,   0.36,    2.0,
44.3,     0.,       0.,         1091.,    0.,       1.625,   0.45,    2.0,
65.0,     96.6,     0.,         834.3,    0.,       1.625,   0.45,    3.0,
65.5,     0.,       C.,         834.3,    0.,       1.625,   0.45,    3.0,
67.0,     0.,       0.,         786.8,    0.,       1.625,   0.45,    3.0,
87.33,    -80.7,    0.,         676.99,   0.,       1.625,   0.45,    4.0,
87.83,    0.,       0.,         676.99,   0.,       1.625,   0.45,    4.0,
95.87,    -40.7,    0.,         534.34,   0.,       1.625,   0.45,    5.0,
96.37,    0.,       0.,         534.34,   0.,       1.625,   0.45,    5.0,
109.99,   -36.5,    0.,         421.59,   0.,       1.625,   0.45,    6.0,
110.49,   0.,       0.,         421.59,   0.,       1.625,   0.45,    6.0
SEPARATION PARAMETERS
# OF SEPARATION RECORDS, & # OF SEPARATIONS
9, 4
TIME      AZIMUTH*  ELEVATION*
65.0,     1000.,    1000.
87.33,    209.,     78.
95.87,    209.,     68.
109.99,   299.,     62.
* 1000 MEANS SAME AS VELOCITY DIRECTION

          -- END OF 53 --


02
ROCKET NAME :
SERGEANT  HYDAC
NUMBER OF DATA POINTS :
13
DATA TABLE FOR 02
TIME      THRUST   & RATE       WEIGHT &  RATE      AREA     COEF     STAGE
0.,       43100.,   -608.,      8400.,    224.,     5.241,   0.25,    1.0,
5.,       39700.,   573.3,      7280.,    224.,     5.241,   0.34,    1.0,
20.,      48300.,   -5080.,     3920.,    224.,     5.241,   0.37,    1.0,
25.,      22900.,   -3660.,     2800.,    48.,      5.241,   0.38,    1.0,
30.,      4600.,    -767.,      2560.,    10.,      5.241,   0.38,    1.0,
36.,      0.,       0.,         2500.,    0.,       5.241,   0.38,    1.0,
40.,      4000.,    5393.,      1055.,    34.5,     0.785,   0.58,    2.0,
42.,      10785.,   1650.,      986.,     47.,      0.785,   0.58,    2.0,
44.,      14085.,   1500.,      892.,     58.5,     0.785,   0.58,    2.0,
46.,      17085.,   0.,         775.,     63.5,     0.785,   0.58,    2.0,
48.,      8385.,    -15982.,    648.,     16.,      0.785,   0.58,    2.0,
48.5,     0.,       0.,         640.,     0.,       0.785,   0.71,    2.0,
60.,      0.,       0.,         604.,     0.,       0.785,   0.71,    3.0
          -- END OF 02 --
```
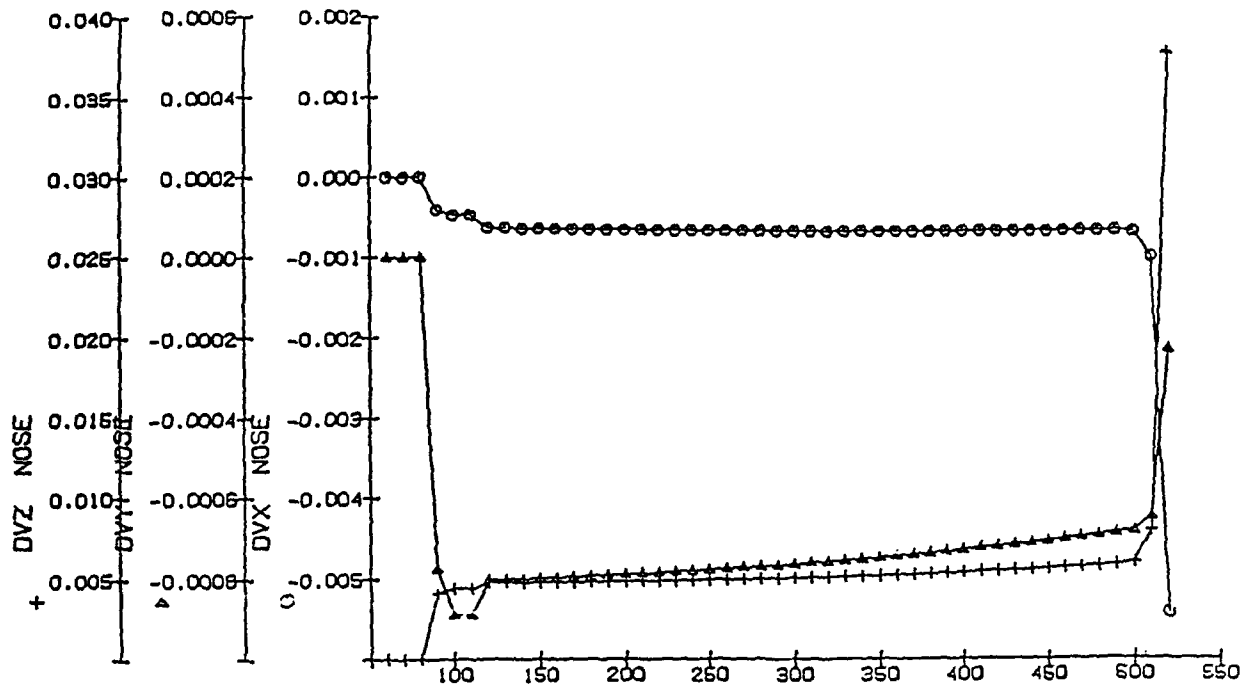
Figure 1.12a. Typical velocity profile for the nose cone

NOSE   REL. TO   ACS

TIFL
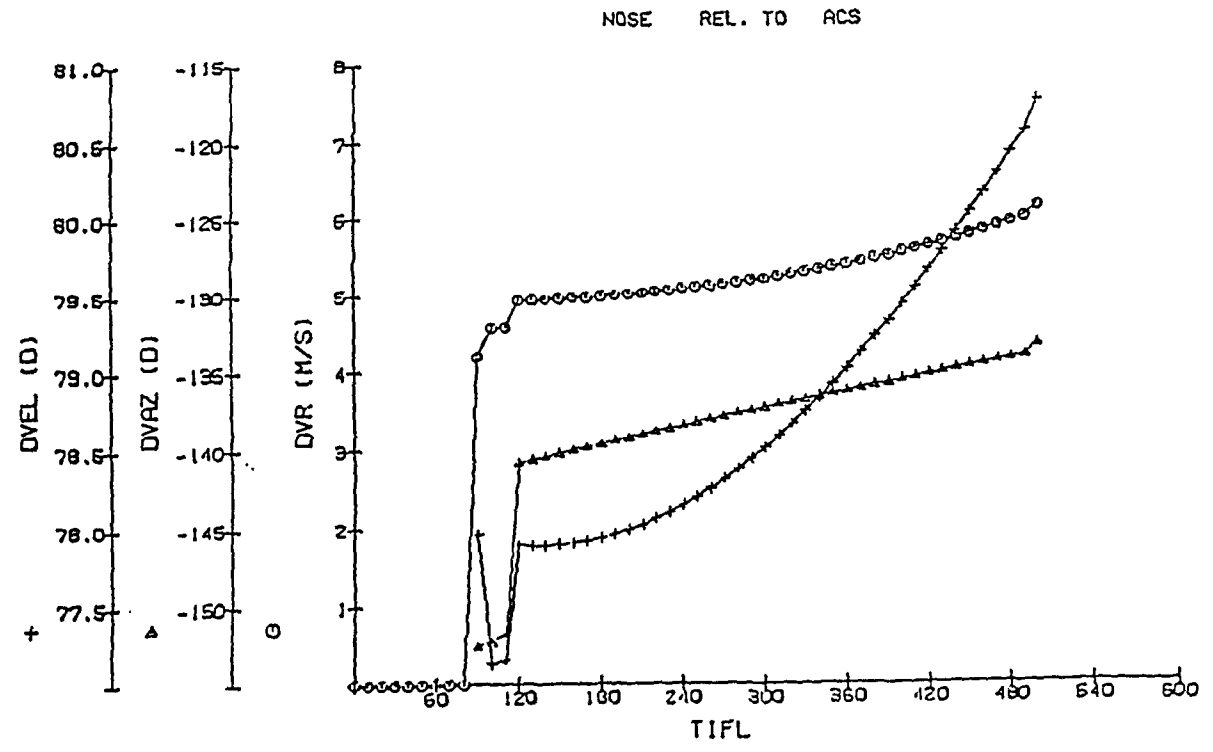
Figure 1.12b. Relative velocity vector for the nose cone relative to the ACS module

20

1.2 ASTRONOMICAL EPHEMERIS

1.2.1 Shaded Sun - Moon Plots

Sun and moon rise-set plots for extreme northern latitudes are difficult to interpret due to the unusual behavior of the moon at these locations. When no solar or lunar events occur over a span of several days, the status of the particular body is not clear in that interval. Presentations have been developed on PCs that improve over the traditional SOUPLT / SOLPLT line plots by utilizing coloring and shading. High quality hard copies are available in an eight by eleven format on our Canon laser printers (Figure 1.13). Color prints may also be made using a Tektronix 4696 color printer.

As many as two elevation angles may be treated for each body. Instances when a body is between the two elevation angles are essentially "twilight" regions.

Each plot provides data for 46 twenty-four hour periods: 45 complete days, and fractions of two other days. Thus, two plots may provide 92 days of coverage, or enough to show information for any three month period. The vertical axis covers 32 hours so that a region near either the top or bottom border is repeated elsewhere for more convenient viewing. Since researchers tend to be interested in periods of darkness for observational purposes, the plots are centered around local midnight; centering on local noon is also available, if desired.

In order to maintain a strong association with the axis labels, all points for a given day have the same x coordinate (i.e., the x axis is discrete, rather than continuous). This approach introduces a discontinuity at the junction of 0 UT and 24 UT. As a means of avoiding this problem, points below the junction are shifted one day to the right, and two sets of day labels are written along the borders. All information above the transition point is for the day indicated by the top label, while hours below this point correspond to the day given by the bottom label. Thus, the largest day number along the bottom gives the last day for which complete information is provided, while the smallest day number along the top indicates the first day with complete information.

The inset in the lower right corner indicates the correspondence between the shades and the solar/lunar conditions. Note that solid black indicates that both bodies are in total darkness; the pattern of the conditions for the sun and moon suggests the other relations. The rise/set data file is also saved in a tabulated format and remains available if more specific information is required.

Figure 1.13. Sun and Moon rise-set plot
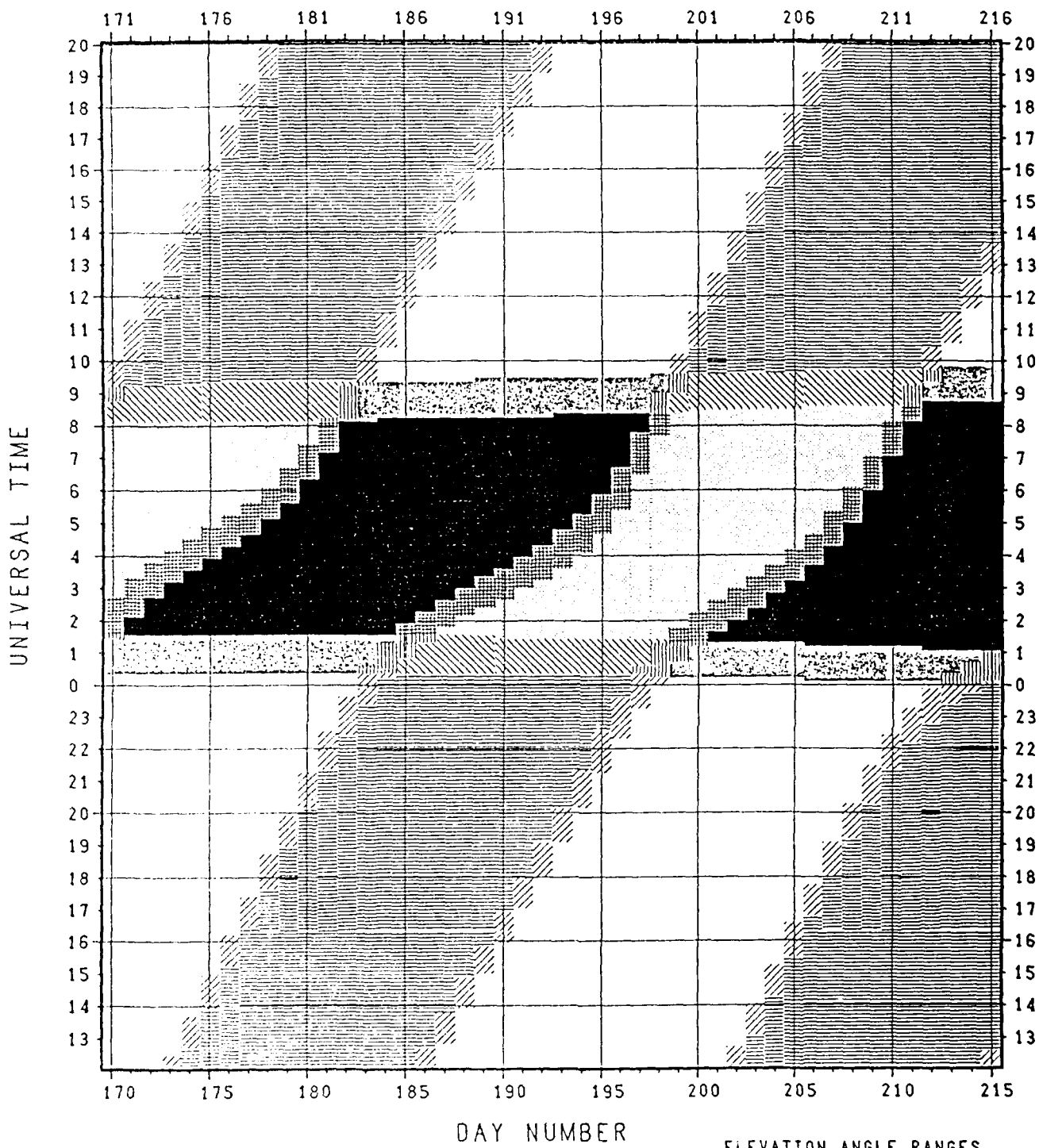
AFGL 1989
Lat = 42.45
Long(E) = -71.27
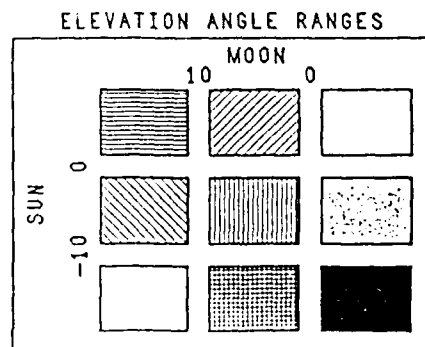
1.2.2 Sun - Moon Rise/Set Tables

SOLUNTIM is a FORTRAN program for use on IBM PC's that provides rise and set data for the sun and moon in tabulated format. The ground station is either selected from a stored list, or input by the user. One elevation angle is specified for each body. Any range of days may be selected within a given calendar year.

All events are indicated in universal time. It is possible that a particular event might not occur during a given day; since time is measured in UT rather than in local time, this can happen even at a station that is not near the poles. When an event does not occur during a given day, an entry of -99.0000 is placed in the table. A typical output file follows (note that there is no moonrise on day 6):

GL			1988.	
SOLAR ELEVATION ANGLE:			-10.00	
LUNAR ELEVATION ANGLE:			10.00	
DAY	SUNRISE	SUNSET	MOONRISE	MOONSET
1	11.3168	22.3010	20.1279	9.3147
2	11.3193	22.3144	20.9581	10.3161
3	11.3213	22.3282	21.8912	11.2091
4	11.3226	22.3425	22.8913	11.9732
5	11.3233	22.3570	23.9197	12.6085
6	11.3234	22.3720	-99.0000	13.1310
7	11.3230	22.3872	.9482	13.5626
8	11.3219	22.4029	1.9656	13.9262
9	11.3202	22.4187	2.9762	14.2422
10	11.3180	22.4350	3.9955	14.5298

The possibility also exists for three solar events in one day of universal time. This occurs due to the shortening of days in the fall (in the spring in the southern hemisphere). When such a case arises, the third event is chronologically placed in the table as a separate entry, as in the following example:

GL			1988.	
SOLAR ELEVATION ANGLE:			-10.00	
LUNAR ELEVATION ANGLE:			10.00	
249	9.3874	.0812	5.4761	19.6312
250	9.4070	.0504	6.4880	20.2868
251	9.4265	.0197	7.5266	20.8210
DAY 251: SUN SET AT 23.9889				
252	9.4459	23.9581	8.5646	21.2607
253	9.4653	23.9272	9.5905	21.6307
254	9.4846	23.8963	10.6067	21.9512

Tests of the solar/lunar algorithms against the SOLLUN software package and tabulated data in The 1985 Astronomical Almanac indicate an accuracy similar to that of SOLLUN.

1.2.3 Planetary Ephemeris

PLANEPH generates planetary ephemerides in azimuth and elevation. It was combined from a set of routines used to calculate planetary positions in right ascension and declination from orbital elements, and a program used to generate solar and lunar ephemeris data in azimuth and elevation. In this particular case, azimuth and elevation for Aries, Mars, Jupiter, and Saturn were desired for the White Sands station for April, May, and June of 1989.

First, the routines for RA and Dec were run using 1984 orbital elements to obtain 1984 ephemeris data. Comparing the results with the 1984 Nautical Almanac (Table 1.3), the errors in right ascension and declination for the three planets of interest were all less than one-tenth degree. Running the program again with 1984 orbital data, this time to generate 1986 ephemerides, the errors were all less than five-hundredths of a degree (except for the right ascension of Mars which was somewhat worse, but still all less than three-tenths of a degree). Next, the 1987 orbital elements were used and the results compared to the 1987 almanac. This time all errors were less than six-hundredths of a degree. See Table 1 for a further breakdown. These results indicate that using the 1987 elements to obtain data for 1989 should give reasonable results. The software which just provides RA and Dec is PLAN89. This program writes a file containing RA and Dec for Mars, Jupiter, and Saturn from April to June of 1989.

Second, the solar-lunar ephemeris program (SOLLUN) was translated to Fortran 5 and rewritten for use with these planets, thus eliminating calculations particular to the sun and moon. Using the file written by PLAN89 as input (PRADEC), the program WHSNDS writes a file (PAZELS) containing the azimuth and elevation data for Aries and the three planets considered in this case.

Third, to simplify this two step procedure, the two programs were combined, eliminating the need for PRADEC entirely. PLANEPH is the result of this. It is worth noting that PLAN89 uses epoch 1950 data, while WHSNDS uses epoch 1900. Rather than eliminate the redundancy in the time calculations in PLANEPH, it was simpler and more efficient to retain both systems.

Finally, PLANEPH is fairly easily modified (see comments in the software) for other time periods, stations, and planets. Note, the third of these requires changes in the output format, whereas the first two do not.

Table 1.3 Errors between calculations and the Nautical Almanac (degrees)

Orb. Els.	Eph. Data	Mars		Jupiter		Saturn	
		RA	Dec	RA	Dec	RA	Dec
1984	1984	<.1	<.05	<.1	<.005	<.05	<.02
1984	1986	<.3	<.03	<.04	<.02	<.05	<.01
1987	1987	<.05	<.01	<.06	<.03	<.04	<.005

1.2.4 Oblate Earth Model

1.2.4.1 Elevation Angle

The elevation angle of an object is defined as the angle measured perpendicularly from the planet surface to the object as seen by the observer. In the following discussion, in terms of Earth centered vectors, let O be the position of the observer and P be the point observed. An approximate elevation angle can be computed by modeling the planet as a sphere with radius r. This simplification gives.

$$\eta = \frac{\pi}{2} - \angle OP + \cos^{-1}\left(\frac{r}{|O|}\right)$$

This solution will be referred to as spherical or zero-th order approximation.

The zero-th order approximation can be improved by adding first order terms in a perturbation expansion, or by solving the full set of nonlinear equations iteratively.

All three elevation angle methods, zero-th order, first order, and iterative, were applied to a test case and the results are shown in Figures 1.14 and 1.15. In Figure 1.14, the elevation angle of the Sun as seen throughout a nearly circular 6500 Km orbit is plotted. The date of the orbit was chosen to be near the vernal equinox. The orbit inclination was 60^0 and the right ascension was 80^0. The three curves in Figure 1.15 are almost indistinguishable. In Figure 1.15, the spherical approximation minus the iterated solution and the first order approximation minus the iterated solution are plotted. It can be seen that the spherical approximation is good to approximately 1^0 and the first order solution to 0.1^0. One motivation for using the first order approximation rather than the iterative solution is execution time. Sample runs, performed double precision on a VAX 8650, showed that the spherical approximation required 0.5 ms, the first order solution 1.0 ms and the iterative solution about 1.3 ms. The first order and iterative methods are close in CPU requirements, since the first order method must do a 3 x 3 matrix inverse and the iterative method converges rapidly, usually in three or four iterations.

1.2.4.2 Geodetic Coordinates

The geodetic latitude and altitude of an object are determined by finding the surface normal which passes through the object. The angle between this line and the equatorial plane is the geodetic latitude. The geodetic altitude is the distance between the intersection of the line with the surface and the object.

The nonlinear equations which describe this problem can be reduced to a sequence of linear perturbation equations by expanding the intersection point as a power series in the eccentricity. Figure 1.16 shows the differences between the zero-th first, second and third order approximations to the geodetic latitude and the "exact" iterated solution. The curves were generated for an object at $1.025*a(6537.5$ Km) using a planet with the figure of Earth. It should be noted that the zero-th order approximation is, in fact, the geocentric latitude. It can be seen that each increase in the order reduces the error by two orders of magnitude. The first order solution has an absolute error of approximately 2×10^{-2} degrees, the second order about 2×10^{-4} degrees and the third 2×10^{-6} degrees.

25
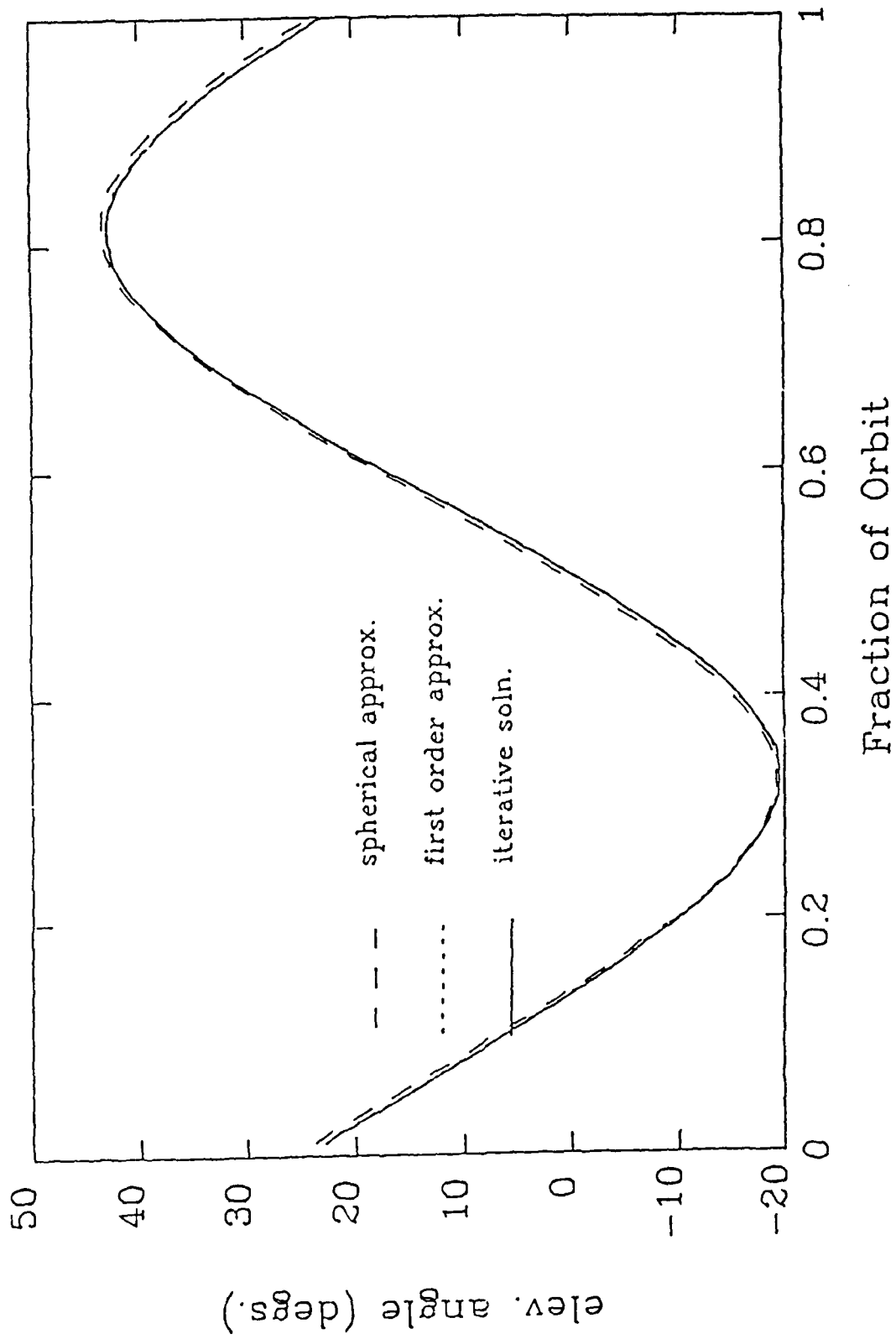
Figure 1.14. Elevation angle of Sun above Earth

spherical approx.

first order approx.

iterative soln.

Fraction of Orbit

elev. angle (degs.)
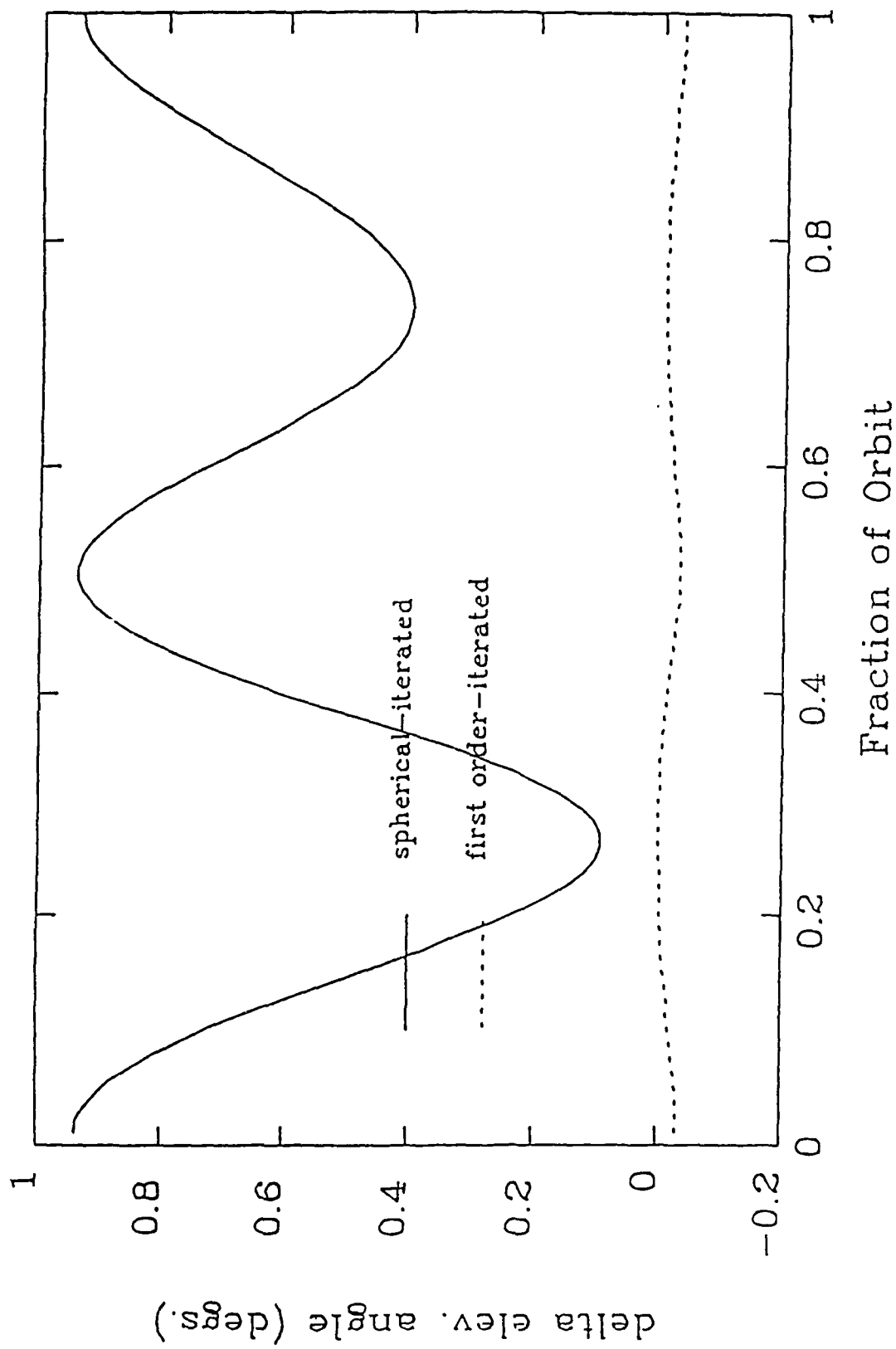
Figure 1.15. Error in elevation angle
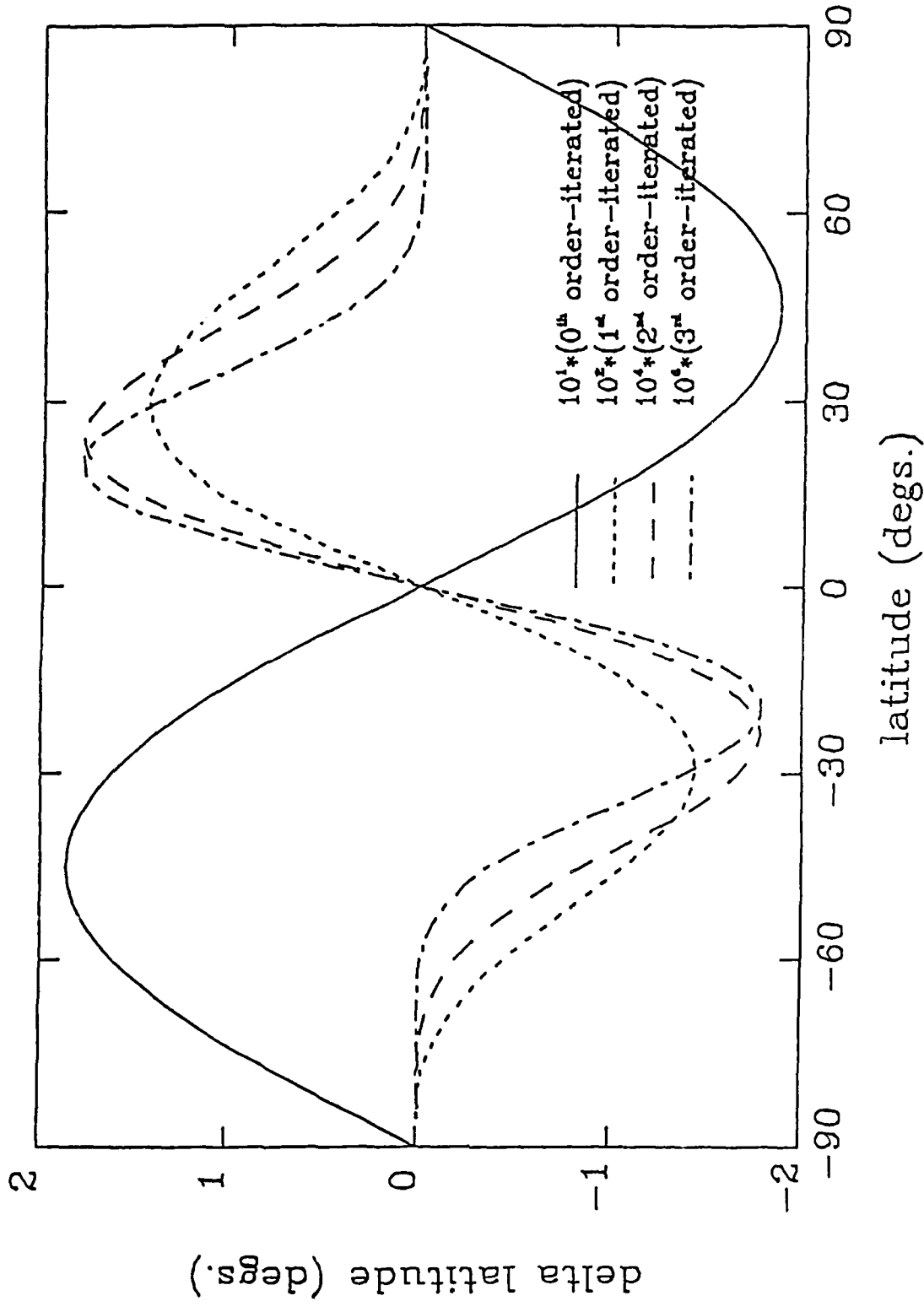
Figure 1.16. Error in geodetic latitude

1.2.5 Precession and Nutation Effects On Satellite Elements

The smooth motion of the Earth's axis of rotation around the ecliptic normal is termed precession. The periodic fluctuations in this motion are termed the nutation. A coordinate system which accounts for both precession and nutation is called "true of date", while one which includes only precession is called "mean". It is common to use coordinates relative to mean axis of a particular epoch, for example mean of 1950 or mean of 2000. The difference between true of the current epoch and say mean of 1950 is given by adding the effects of precession between 1950 and the current epoch to the current nutation. The precessional motion is very slow, having a period of approximately 25,800 years and has no effect on the obliquity, the angle between the equatorial and ecliptic planes. The astronomical nutation has a period of 18.6 years and causes changes in obliquity up to 9" and in longitude up to 17", or only about 0.5 km in-track error for low Earth satellites. Plots are given showing the magnitude and period of the most important modes.

The calculations in this study were based on transformations given in the "Explanatory Supplement to the Astronomical Ephemeris" [ESE, 1961], and two programs PRECESS and NUTATE were written for this purpose. The equations for nutation are in turn based on a paper by Woolard [1953], prepared for the use of the American Ephemeris and Nautical Almanac. It should be noted that new models for nutation continue to be considered [Wilkins, 1980].

The transformation matrix which maps mean coordinates of one epoch to true coordinates of another epoch is given by the product of the nutation R_n and precession R_p transformations,

$$R = R_n R_p$$

Some results of this transformation are shown in Figures 1.17 and 1.18 which present the effects of precession and nutation respectively, over a span of 50 years (1950-2000), the time span of interest. The amplitude of the nutation is approximately 17" (0.0048°) in longitude and 9.2" (0.0026°) in latitude. The amplitude of the precession in latitude is about 23°. For reference, an error of 0.01° in the location of a 6600 km satellite represents about a 1.15 km along-path error. It follows that nutational effects are unimportant when a satellite's positional uncertainty exceeds .5 km.

29
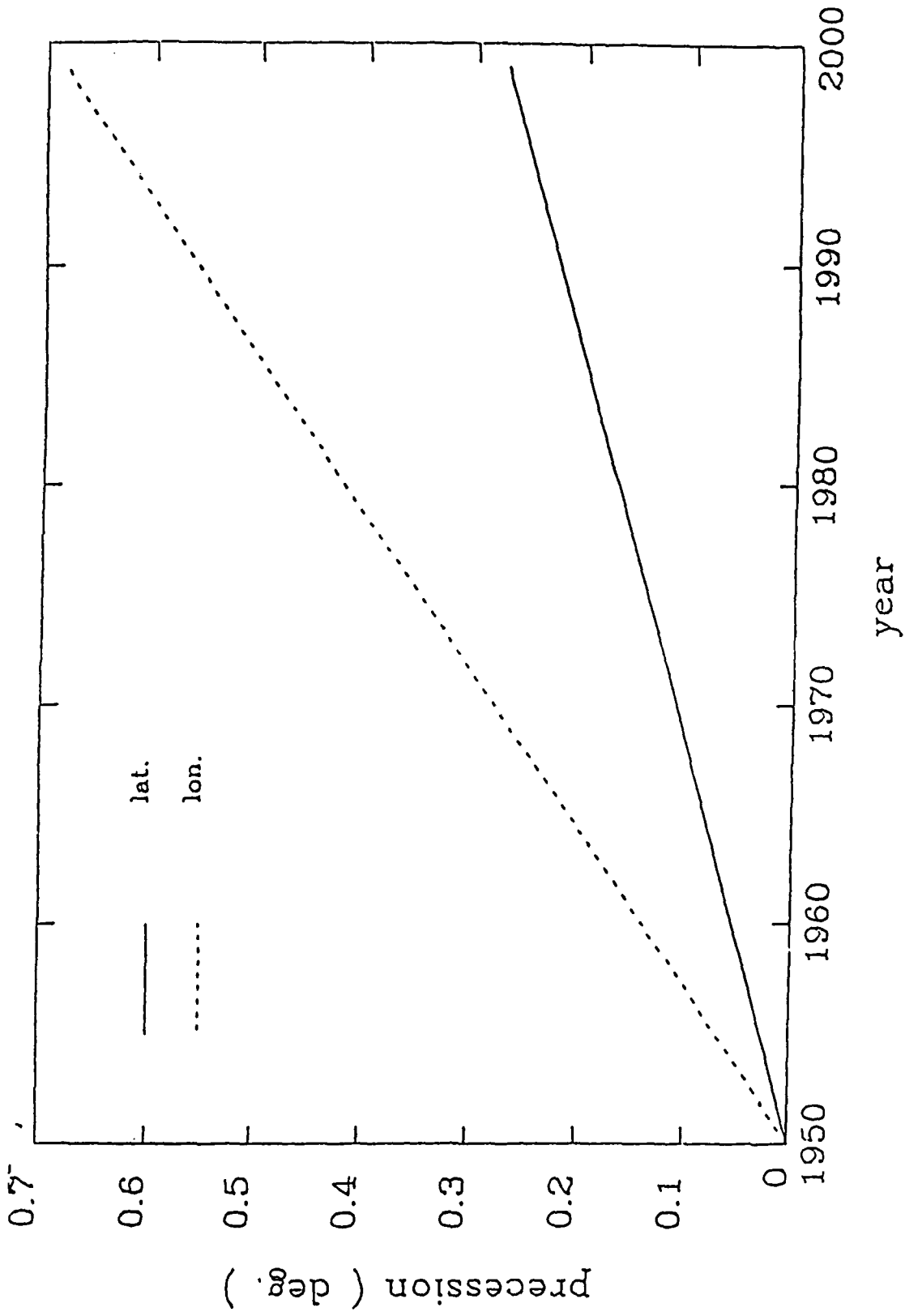
Figure 1.17. 50 year variation in latitude/longitude due to precession
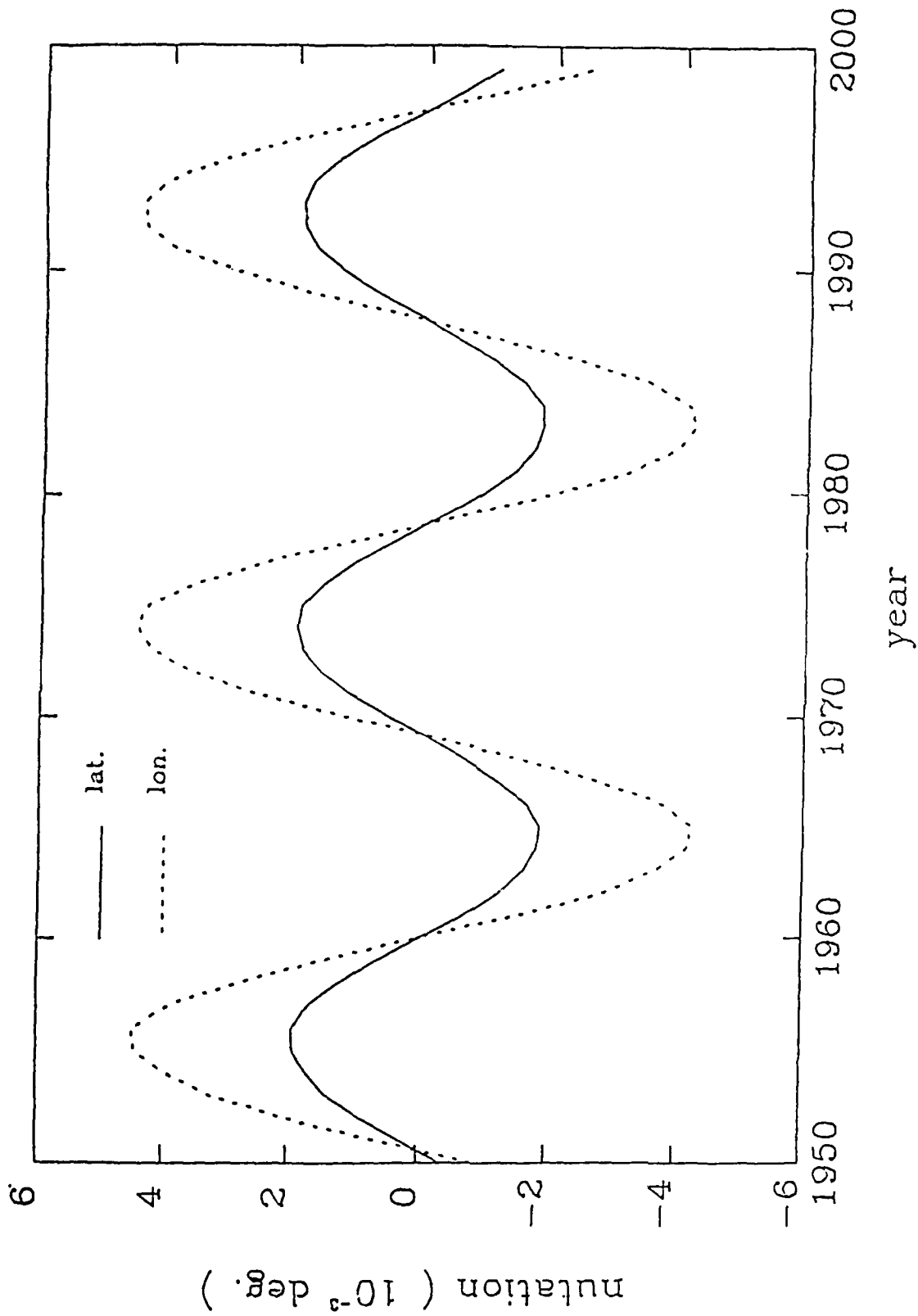
Figure 1.18. 50 year variation in latitude/longitude due to nutation

1.2.6 Coordinate Systems and Transformations

Many different coordinate systems are used to represent vehicle orbit and magnetic field parameters in the analysis, processing, and display of satellite data because physical processes may be better understood if the experimental data are more ordered, or if calculations are more easily performed in one coordinate system rather than another. An extensive repertoire of coordinate systems, particularly astronomical, geomagnetic and spacecraft ephemeris/attitude related systems are pertinent to the GL research activities.

Though these systems are often depicted in various ways, including rectangular and spherical coordinates after the origin is defined, a primary axis direction and a secondary direction (or reference plane) suffices to define coordinates uniquely. This approach reduces to a right-handed Cartesian system, as may be seen from Table 1.4, and is advantageous because:

1) The fundamental origins and directions are identified.
2) Semantics of different names for any system is clarified.
3) Coordinate conversion between systems reduces to matrix
   rotation as implied by their fundamental directions.

The table shows many of the commonly encountered coordinate systems used at GL. Vehicle dynamics and ephemerides are most conveniently generated in a fixed or inertial coordinate system. For this, the rectangular Earth Centered Inertial (ECI) System is particularly useful. Latitude/longitude or Geographic coordinates, and Geomagnetic coordinate systems are non-inertial systems which, being earth-fixed, rotate with the earth. The Geocentric Solar Magnetospheric System is an earth-centered frame that is particularly useful in ordering data associated with solar-terrestrial interactions.

A revision of "Coordinate Systems for Space and Geophysical Applications," [Cottrell et al., 1985] was prepared for publication. In addition to the description and figures, a complete form of the table was included listing applications of the various coordinate systems and, with other tables, presents a general overview of all systems.

Oftentimes it is necessary to convert between coordinate systems using transformation matrices. If the two systems are not concentric, a vector translation is first applied. If the relative orientation of the two coordinate systems is constant with respect to time, positions and velocities transform as $Y = M \cdot X$ where X is the original, and Y the final vector. If the coordinate systems are not fixed relative to each other, the time-dependent transformation matrix M_t and its derivative M_t' are required.

Positions transform as before $Y = M_t \cdot X$
but Velocities transform as $Y' = M_t \cdot X' + M_t' \cdot X$

TABLE 1.4 SPACE COORDINATE SYSTEMS (RECTANGULAR)

	ORIG	ROT AXIS	ECL AXIS	VERN EQUS	SUN	GRWH MERI	GEOM NORTH	GEOM AXIS	SOL WIND	PERP RAD VEC	ZEN	GEOC	VEL VEC	PRIM BODY AXIS	SEC BODY AXIS
EARTH-FIXED															
GEOCENTRIC	EC	(Z)				X									
GEODETIC (1)	EC	(Z)				X									
TOPOCEN EQUAT	PI					X*									
TOPOCEN HORIZ	PI						X*				(Z)				
INERTIAL/QUASI-INERTIAL															
ARIES-MEAN-OF 1950 (2)	EC	Z		(X)*											
ATS-1 (8)	EC	(Z)			X										
EARTH CENT INERT (3)	EC	Z		(X)											
ECLIPTIC (4)	EC		Z		(X)										
GEOCEN SOL EQUAT (9)	EC	Z*			(X)										
MAGNETIC															
DIPOLE (10)	EC	X*						(Z)							
DIPOLE MERIDIAN	EC							(Z)		Y					
GEOC SOL MAGSPH (5,11)	MC/EC				(X)		Z*								
MAGNETIC (12)	MC	X*						(Z)*							
MAGNETIC FIELD (13)	PI						(X)			-Z*					
SOLAR GEOMAG (6,14)	MC/EC				X*			(Z)							
SOL WIND MAGSPH (11)	EC						Z*		(X)						
OTHER SYSTEMS															
BODY AXIS	CG													(X)*	Y*
LOCAL VERTICAL (7)	CG											(Z)*	X		

LEGEND
X: X-AXIS; Y: Y-AXIS; Z: Z-AXIS
( ): PRIMARY DIRECTION
UNMARKED: SECONDARY DIRECTION
EC: EARTH CENTERED
PI: POINT OF INTEREST
NEC: NEAR CENTER OF EARTH
MC: MAGNETIC CENTER (can be either EC or NEC for CRRES Program)
*: MORE PRECISE REFERENCE REQUIRED TO CLARIFY
ROT AXIS: COINCIDENT OR PARALLEL TO ROTATIONAL AXIS
ECL AXIS: COINCIDENT OR PARALLEL TO ECLIPTIC AXIS
GEOM AXIS: COINCIDENT OR PARALLEL TO GEOMAGNETIC AXIS
GEOC: POINTS TO CENTER OF EARTH
(1): Same as GEOGRAPHIC System
(2): Similar to ARIES-TRUE-OF-DATE System
(3): Same as GEOCENTRIC CELESTIAL INERTIAL and GEOCENTRIC EQUATORIAL INERTIAL Systems
(4): Same as GEOCENTRIC SOLAR ECLIPTIC and SOLAR ECLIPTIC Systems
(5): Same as SOLAR MAGNETOSPHERIC Systems
(6): Same as SOLAR MAGNETIC System
(7): Same as LOCAL ORBITAL System
(8): X-Axis points to Local Noon Meridian and lies in Equatorial Plane
(9): Z-Axis lies in plane containing X-Axis and Rotational Axis
(10): X-Axis lies in plane containing North Dipole Axis and Rotational Axis.
      Sometimes called the GEOMAGNETIC System.
(11): Z-Axis lies in plane containing X-Axis and North Dipole Axis;
      is perpendicular to the X-Axis and is positive towards North
(12): Z-Axis is parallel to Magnetic Dipole Axis but is magnetic centered
      X-Axis lies is in plane containing Z or Dip Pole Axis and South Geographic Pole
(13): (-Z)-Axis is perpendicular to the magnetic meridian (horiz component of B field)
(14): X-Axis lies in plane containing Z-Axis and the Sun (but not necessarily
      pointing to the Sun); lies in Geomagnetic Equatorial Plane.

References

Bhavnani, K.H., Bonito, N.A. and McNeil, W.J., "CRRES Data Processing Ephemeris File Generating System, Product Development Specification and Test Plan", Radex Report RXR87011, January 1987.

Bhavnani, K.H. and Robinson, E.C., "Functional and Operational Advances in the AFGL Rocket Trajectory System - I", AFGL-TR-79-0183, July 1979, ADA 081447.

Escobal, P.R., Methods of Orbit Determination, John Wiley & Sons, Inc., New York (1965).

Gurnette, B. L and R. v. d. R. Wodley, Explanatory Supplement to the Astronomical Ephemeris, (1961) H. M. Stationery Office, pp 24-45.

Logicon, Inc., "Analysis and Programming for Research in Physics of the Upper Atmosphere", Final Report AFGL-TR-76-0231, September 1976, ADA 034066.

Malcolm, P.R., "Rocket Trajectory Request, NASA 36.015UE", Analysis and Simulation Section, AFGL, April 1988.

Roberts, C. K. and A. Boksenberg, The Astronomical Ephemeris, (1986).

Robinson, E.C., Bhavnani, K.H. and Vancour, R.P., Private Communication, June 1988.

Wilkins, G. A., "The Specification of Nutation in the IAU System of Astronomical Constants", Nutation and the Earth's Rotation, IAU (1980).

Woolard, E. W., "Theory of the Rotation of the Earth around its Center of Mass", Astronomical Papers, Vol. XV, 1953.

2. ATMOSPHERIC DENSITY AND STRUCTURE

2.1 ATMOSPHERIC DENSITY

2.1.1 Data Bases and Processing System

2.1.1.1 MDRIVER

The MDRIVER program is designed to be a user-friendly program which produces tables and SUATEK-formatted files, if desired, of either latitude or altitude profiles of atmospheric model values for one of the seven available models. Currently, these seven models are : US 1976 [COESA, 1976], MSIS 83 [Hedin, 1983], MSIS 86 [Hedin, 1986], JACCHIA 71 [Jacchia, 1971], JACCHIA 77 [Jacchia, 1977], AFRA 86 and GROVES/MSIS. These last two models are described below. To impliment the MDRIVER program, enter the commands:

"GET,MRUN/UN=ROTHC", and then "MRUN".

The program will then prompt the user for the model to be run. According to the model chosen, the user is presented with one or more lists of available model values to choose from. When all model values to be tabulated have been chosen, the program prompts the user for all parameters required for the model, such as the date, time, position, and geophysical values. The US 1976 model requires only the altitude. If a SUATEK-formatted file is also being created, the program prompts the user for plot titles. The requested model is then run, and a text file tabulating all specified model values is created, along with a SUATEK-formatted file if needed.

2.1.1.1.1 AFRA-86 Atmospheric Model

The AFRA-86 (Air Force Reference Atmosphere - 1986 Supplements) is a reference atmosphere specifying temperature, pressure, and total mass density between 80 km and 200 km. It is derived by merging the MSIS-83 model with a model of Forbes [1985] based an low altitude rocket and incoherent scatter measurements of temperature. The Forbes model specifies monthly mean profiles of total mass density, temperature, and pressure between 65 and 120 km in strictly tabular form. Temperature profiles were generated first by least squares fits to the data. The pressure profiles are solutions to the barometric equation, using the pressure at 68 km given by the AFRA-78 [Cole and Kantor, 1968] as a lower boundary condition. The density is then derived from the perfect gas law.

The currently used version has been developed by Bass et al. [1987]. In this version, the Forbes model is used, by spline interpolation of the tables, up to 104 km. Four-point spline fits through Forbes model values at 102 km and 104 km, and the MSIS-83 values at 120 km and 122 km, are employed between 104 and 120 km. Above 120 km the MSIS-83 model is used.

2.1.1.1.2 Groves/MSIS Atmospheric Model

The Groves/MSIS model is a hybrid similar to the AFRA model. For the altitudes 18 to 70 km, the model is defined by a Global Reference Atmosphere [Groves, 1985], and from 130 upwards, the model is defined by the MSIS 83 thermospheric model. Between the two regions, a transition zone is used.

35

The Global Reference Atmosphere is derived from monthly means of zonal mean temperature, pressure, density, number density, and pressure scale height which have been tabulated at heights from 18 to 80 km and latitudes from 80° S to 80° N with a latitude interval of 10°. These tabulated values have been formulated for the model algorithm. Monthly mean longitudinal variations of temperature, pressure and density have also been tabulated for specific months in each hemisphere, and similarly formulated. The zonal means are derived from tabulations of temperature and geopotential height based on Nimbus 5 SCR and Nimbus 6 PMR and a Southern hemisphere reference atmosphere based on rocketsonde data that were both prepared for the COSPAR Meeting, [Graz 1984] and two earlier Northern Hemisphere rocket-based reference atmospheres, CIRA 72 and Air Force Reference Atmospheres [1978]. The longitudinal variations are derived solely from satellite-based tabulations.

The transition zone was formulated to maintain continuity in the second derivative of temperature, pressure, density and constituent gas concentrations with respect to height between the Global Reference Atmosphere model and the MSIS 83 Thermospheric model [Groves, 1987]. This formulation used temperature as the prime parameter requiring simultaneously a best fit to available temperature data and hydrostatic consistency between the nitrogen partial pressures at 70 and 130 km. The MSIS 83 model is used above 120 km.

2.1.1.2 Satellite Database Format Conversion

In the advent of future models, the satellite database library needs to be as compact and uniform as possible to avoid future problems due to a wide range of inconsistancies between the tapes. Inventory of the tape library was taken in the spring of 1988. At that time, the library consisted of 54 tapes, each of which contained at most four of the nineteen available models. Most of the satellites each had several tapes which contained the same model, but in different combinations with other models, to allow many of the numerous model combinations that might be required. Because of this small model capacity and numerous models, much of this library was redundant.

In order to reduce this greatly oversized tape library, the model capacity of the tapes has been increased from four models to eight. With this new format, only three tapes are needed per satellite to accomodate the 19 models. The first of these model tapes contains the more commonly used models, and the other models, which are older and/or infrequently used, on the other two model tapes. A master tape for each satellite has been created, which is a backup for the non-model values, such as orbit number, time, latitude, longitude, etc. For each satellite, there are the three model tapes (S85-1 has only six models available, and therefore requires only one model tape) plus the master and a backup for the third model tape, which makes a total of twenty-seven tapes required. In this current format, up to five models may be added to the database library without increasing the number of tapes required (with the exception of the S85-1 satellite database).

2.1.1.2.1 General Procedure for Tape Conversion

In order to confirm the existence of all models on the tapes as documented in the database library list, and the integrity of all the tapes, a program to audit the contents of the tapes was written. This program reads in the database tapes and produces printed output of all the header records and a sample data record, and a summary at the end, which consists of the total number of points, records, and files, the min-max ranges of the date, time, altitude, and latitude. Similar statistics are also given for each file. Using the overall statistics, the statistics for each satellite have been corrected where necessary.

From this survey of the tapes, several tapes were found to have data which was absent, unreliable, or incomplete. These tapes were not used in creating the new database tapes. Several of the S3-4 satellite tapes were found to have differing numbers of points. This discrepancy was found to be due to several duplicate datapoints, which were removed when the tape was converted to the new format. The A_p values were found to be overwritten on some of the unpacked tapes, but still available on other tapes of the same satellite. With this information, all the valid tapes were compared to each other, identifying all inconsistencies between formats, existing A_p values, and models available. From this, the new header and data record formats were created (See Tables 2.1 and 2.2).

The tapes for each satellite were set up so that the more commonly used models, such as the J71, MSIS86, US76, etc, were placed on the first tape, and the lesser used models were placed on the second and third tapes. A Master tape has also been created, which has unspecified models, but contains all the other important data, such as the time, latitude, longitude, altitude, A_p, K_p, and $F_{10.7}$ values, and other non-model values.

To create the new tapes, a tape processing program was written to convert the valid tapes to the new format. This conversion consisted of rearranging the header record and redefining the model value locations, and moving the model values to their correct positions. For most satellites, the US76 model did not exist on tape, and therefore was computed "on the fly" when required. To ensure the accuracy of the conversion, a slightly modified version of the tape auditing program was run to give the same type of survey done on the original tapes, except using the new format, for confirming the correctness of the conversion. This comparison examined the header records for the correct format and values, and the data record for the proper A_p and model values in the correct locations.

These new converted tapes were then merged with other tapes to generate the final version of the new tape, for which a second tape processing program was written. This merging process consisted of identifying the values to be used from each tape, and changing the header record to reflect the new models. When intermediate and final tapes were produced, the modified tape auditing program was run again, in order to verify the accuracy of the merge and/or final tape against the data of the original tapes.

2.1.1.2.2 Data Format Changes

1. Header Record: (packed and unpacked databases) The filter date and filter data for the SETA-2, SETA-3 and S85-1 satellites have been retained, and have been moved up in the header record. The previously undocumented model identification and word location format has been changed, due to lack of space for all eight models. The new format is as follows: the number after each model name is the sum of 100 times the word number of the density word number, and the ratio word number.

2. Header Record 2: (packed databases) Only the scales have been modified to accomodate the four additional model values.

3. Data Record: (unpacked databases) The data formats remain basically the same, with a few minor changes. The A_p values have been recovered for the unpacked tapes, where available. The values of UT(HR) and LT(HR) have been changed to UT(HR.FRAC) and LT(HR.FRAC), respectively. UT(MIN OF HR), LT(MIN OF HR), UT(SEC OF MIN), LT(SEC OF MIN) have been replaced by model values. Infrequently used data, such as the wind data for the SETA-1 satellite and the empirical model values for the AE/S3-1 satellites, have been retained.

Table 2.1. *New Unpacked Database Format*

HEADER RECORD:

WORD#	CONTENTS
0.1	WORD COUNT (40)
0.2	GROUP COUNT (1)
1	SATELLITE ID
2	EXPERIMENT NAME
3	ALTITUDE (KM) (AE/S3-1 ONLY)
4	100*(NUMBER OF FILES) + (NUMBER FOR THIS FILE)
5	DATA BASE CREATION DATE (YYDDD)
6	SATELLITE NAME (AE/S3-1 ONLY)
7	SATELLITE NAME (AE/S3-1 ONLY)
8	SATELLITE NAME (AE/S3-1 ONLY)
9	SATELLITE NAME (AE/S3-1 ONLY)
10	JDATE OF FILTER RUN FOR SETA-2, SETA-3, S85-1
11	FILTER DATA FOR SETA-2, SETA-3, S85-1
12	FILTER DATA FOR SETA-2, SETA-3, S85-1
13	FILTER DATA FOR SETA-2, SETA-3, S85-1
14	FILTER DATA FOR SETA-2, SETA-3, S85-1
15	FILTER DATA FOR SETA-2, SETA-3, S85-1
16	FILTER DATA FOR SETA-2, SETA-3, S85-1
17	FILTER DATA FOR SETA-2, SETA-3
18	FILTER DATA FOR SETA-2, SETA-3
19	FILTER DATA FOR SETA-2, SETA-3
20	FILTER DATA FOR SETA-2, SETA-3
21	FILTER DATA FOR SETA-2, SETA-3
22	FILTER DATA FOR SETA-2, SETA-3
23	FILTER DATA FOR SETA-2, SETA-3
24	NUMBER OF MODELS
25	NAME OF MODEL #1
26	WORD # OF MODEL #1: DENSITY*100 + RATIO
27	NAME OF MODEL #2
28	WORD # OF MODEL #2: DENSITY*100 + RATIO
29	NAME OF MODEL #3
30	WORD # OF MODEL #3: DENSITY*100 + RATIO
31	NAME OF MODEL #4
32	WORD # OF MODEL #4: DENSITY*100 + RATIO
33	NAME OF MODEL #5
34	WORD # OF MODEL #5: DENSITY*100 + RATIO
35	NAME OF MODEL #6
36	WORD # OF MODEL #6: DENSITY*100 + RATIO
37	NAME OF MODEL #7
38	WORD # OF MODEL #7: DENSITY*100 + RATIO
39	NAME OF MODEL #8
40	WORD # OF MODEL #8: DENSITY*100 + RATIO

DATA RECORD:

WORD#	CONTENTS
0.1	WORD COUNT (40)
0.2	GROUP COUNT (12)
1	ORBIT NUMBER
2	JULIAN DATE (YYDDD)
3	U.T. (SECONDS)
4	U.T. (HOUR.FRAC)
5	MODEL #1 DENSITY (g/cm^3)
6	MODEL #1 RATIO
7	L.T. (HOUR.FRAC)
8	MODEL #2 DENSITY (g/cm^3)
9	MODEL #2 RATIO
10	UPLEG/DOWNLEG (AE/S3-1 ONLY)
11	DAY/NIGHT (AE/S3-1 ONLY)
12	SPUN/DESPUN (AE/S3-1 ONLY)
13	GEOGRAPHIC LATITUDE (° N)
14	GEOGRAPHIC LONGITUDE (° E)
15	GEOMAGNETIC LATITUDE (° N)
16	GEOMAGNETIC LONGITUDE (° E)
17	GEOMAGNETIC LOCAL TIME
18	MEASURED DENSITY (g/cm^3)
19	MODEL #3 DENSITY (g/cm^3)
20	MODEL #3 RATIO
21	MODEL #4 DENSITY (g/cm^3)
22	MODEL #4 RATIO
23	MODEL #5 DENSITY (g/cm^3)
24	MODEL #5 RATIO
25	A_p (DAILY AVERAGE) <N/A FOR PACKED DATABASES>
26	A_p (6.7 HOUR LAG) <N/A FOR PACKED DATABASES>
27	K_p (6.7 HOUR LAG)
28	$F_{10.7}$ (1 DAY LAG)
29	$F_{10.7}$ (81 DAY AVERAGE)
30	ALTITUDE (KM)
31	X DIR (SETA-1)
32	X WIND (SETA-1)
33	Y WIND (SETA-1)
34	Z WIND (SETA-1)
35	MODEL #6 DENSITY (g/cm^3) EMPIRICAL MD (AE/S3-1)
36	MODEL #6 RATIO EMPIRICAL MR (AE/S3-1)
37	MODEL #7 DENSITY (g/cm^3)
38	MODEL #7 RATIO
39	MODEL #8 DENSITY (g/cm^3)
40	MODEL #8 RATIO

Table 2.2. New Packed Database Formats

HEADER RECORD 1:   Same as unpacked database header.

HEADER RECORD 2:   Unpacked offsets and scale values to be
used to convert the packed data words to
the equivalent 60-bit unpacked values.

DATA RECORD: 60-bit word containing time in the form YYDDD.FFFF

where   YY = the last two digits of the year
DDD = the day number of the year
FFFF = the fraction of the day from UT midnight
followed by:
sixteen 15-bit data words, packed four per 60-bit word,
which are described as follows:

WORD #	DATA DESCRIPTION
1	Orbit Number
2	Latitude ($^\circ$ N)
3	Longitude ($^\circ$ E)
4	Altitude (Km)
5	$F_{10.7}$
6	$F_{10.7}$ Smoothed
7	K_p
8	Measured Density (g/cm^3)
9-16	Measured/Model density ratios for each of the eight models

4. Data Record: (packed databases) The number of words for each data record have been increased from twelve to sixteen to accomodate the additional four model values.

2.1.1.2.3 General Tape Setup

To maximize the efficiency of the tape library, all satellites have the same format as to the model locations. The table below shows the current model location format.

WORD#	LOCATIONS:							
DENSITY:	5	8	19	21	23	35	37	39
RATIO:	6	9	20	22	24	36	38	40
TAPE								
1	J71	J70T	MSIS86B	MSIS83B	US76			
2	MSIS77	MSIS78	MSIS83A	US62	US66	J71KP=1*		
3	J64	J70	J73	J77	L/N	USSR	DENSEL	JWB

*J71KP=1 IS AVAILABLE ONLY FOR SETA-1 AND SETA-2

2.1.1.2.4 PACKLIB Modifications

The PACKLIB library of tape reading and writing routines was modified to reflect these changes in the data format. All calls to these subroutines remain unchanged in format, but now up to eight models can be specified, and therefore the arrays related to the model names and word numbers are indexed to eight. The file DBINDEX, which is a listing of all database tapes and the models contained on them, has a slightly different format, as it now has up to eight models listed for each tape and the "H" column has been eliminated. It is possible to read the four model tape format from the new version of PACKLIB, provided the tapes are listed in DBINDEX if the DBTAPE routine is used, and the model locations are known when working with the data.

2.1.1.2.5 STAT Program Modifications

The STAT program [Bass, et al, 1987], which is an analysis tool for use with the atmospheric density database, has been modified slightly in order to accomodate the revised tape format.

2.1.1.2.6 New Packed Database Format

Within the PACKLIB routine DATAIN, the packed database data is modified by the scales and offsets contained in the second header record to calculate the actual values. The rest of the unpacked data record values are calculated from these values where possible. The A_p values are not available from packed databases, and are left blank.

2.1.1.3 Supporting Plotting Routines for the STAT Program

The program KL4 is a user-friendly program which generates K_p/latitude/local time plots from SUATEK format files produced by the STAT program [Bass, et al, 1987]. It generates plots of data corresponding to the binning chosen in the STAT run. This flexibility allows the program to produce plots for the various combinations of binning by time (all, seasons or months), latitude (2 or 5 degrees), and K_p bins (3 sets) for model mean ratio or standard deviation values. These plots separate the day and night data values by using a double latitude scale, begining at -90 latitude, increasing to +90 on the dayside, then decreasing to -90 on the nightside. The program prompts the user for the input file, presents a description of the types of binning present in the

file, and gives the user options for setting the latitude and data scale limits. The plots may be drawn on the terminal screen or sent to an off-line pen plotter. Sample plots are shown in figures 2.1a and 2.1b.

2.1.2 Statistical Parameters for Describing Model Accuracy

Methods of probability theory have been applied to determine parameters for describing the accuracy of a model, given a data base of measurements with which the predictions of the model are compared. From such comparisons, it is customary to determine the mean and standard deviation of the measured model difference or ratio. In the idealized case that the error distribution is Gaussian, we have shown that a single parameter, the root mean square (rms) of the mean and the standard deviation, approximately characterizes the accuracy of the model, since the width of the confidence interval whose center is at zero error can be represented as the product of the rms and the factor which is approximately independent of both the mean and the standard deviation. Using a modified version of Chebyshev's inequality, a similar result was obtained for the upper bound of the confidence interval width for any distribution of specified mean and standard deviation.

Empirical models, such as the MSIS 86 thermospheric model [Hedin, 1986], are used to obtain rapid, yet hopefully sufficiently accurate, estimates of key parameters which affect the design and/or operation of a man-made or natural system. These parameters may be environmental, primarily describing a system which interacts with the man-made system, or they may relate to the system itself.

For some such parameters a copious amount of data is available. Empirical models constructed by least squares fits to the data may incorporate the dynamics of the system, but often in some grossly simplified form, to permit ease of everyday computational use. We then become concerned with the accuracy of these models in predicting the behavior they describe.

2.1.2.1 Definition of Accuracy

Here we specify accuracy is through the use of confidence limits. Given a probability density function, f(x), of the model error x, we define the total probability, the integral of the probability density function, that the error lies between two values:

$$P(a,b) = \int_a^b f(x)dx \qquad (2.1)$$

Often we wish to find the bounds a and b of an interval whose center is at the mean of the distribution. Here in this report, however, we show how to define the confidence limits $\mp\Delta$ of an interval, whose center is at zero error, such that the probability $P(-\Delta,+\Delta)$ that the error lies within this interval is at least equal to some desired value. This specification has the advantage that it gives the user the desired "confidence" that the error magnitude is less than the half-width Δ of the interval.

We desire some simple parametric specification, accompanied by a table or simple computational algorithm, which would allow the user to easily derive confidence limits for any specified probability. This specification must be applicable in the presence of uncertain systematic error and non-zero mean error. We will show that if the probability density function is Gaussian, with zero or non-zero mean, then a single parameter nevertheless often suffices to derive desired

41

Figure 2.1b. SETA-3 satellite accelerometer data

Figure 2.1a. SETA-1 satellite accelerometer data

confidence limits. For non-Gaussian probability density functions, a modification of Chebyshev's inequality [Brunk, 1975] will allow us to derive from the same parameter an upper bound to the confidence interval width.

2.1.2.2 Probabilities for a Biased Gaussian

Assume that a data point is taken from Gaussian probability density (pd) with standard deviation σ and mean (bias) $B\sigma$. Then Table 2.3 gives the probability for the occurrence of the value (y) within the interval

$$-\sigma\Delta x \le y \le \sigma\Delta x,$$

where Δx is the value indicated first column, and B is the value indicated in the top line. For example, if $\Delta x = .5$, and $B = .4$, then the probability of occurrence within the interval $\pm\sigma\Delta x$ is 35.58%. If $\Delta x = 1$, and $B = 0$, then the probability is 68.27%.

Assume that a data point is taken from a Gaussian pd with standard deviation σ and bias $B\sigma$. Then Table 2.4 gives the probability of occurrence of the value (y) within the interval

$$-[\sigma^2 + B^2\sigma^2]^{1/2}\Delta x_N \le y \le [\sigma^2 + \sigma^2 B^2]^{1/2}\Delta x_N,$$

where Δx_N is the value indicated in the first column, and B is the value indicated in the top line.

Table 2.4 shows that by modifying σ to

$$rms = [\sigma^2 + \sigma^2 B^2]^{1/2} \tag{2.2}$$

the probability of occurrence within symmetric intervals is approximately independent of the bias (B) when B is "small". For example the probability of occurrence of y within the interval $\pm.5rms$ is 38.29% when the bias is zero, and 38.11% when the bias is $.4\sigma$.

2.1.2.3 Probabilities for Non-Gaussian Distributions

Chebyshev's inequality states an upper bound for the probability that the value of a random variable deviates from its mean by more than a certain amount:

$$P\{ |x - \mu| \ge \Delta \} \le \sigma^2/\Delta^2$$

where μ and σ are the mean and standard deviation of the value of the random variable x, and Δ is a positive number. Brunk [1975] points out that the proof of Chebyshev's inequality applies equally well to deviations of the random variable from any value, if the standard deviation σ is replaced by the square root of the mean square deviation of the variable from that value.

For our application to the deviation of errors about zero, the mean square deviation is simply the rms defined in Eq. (2.2), with $\mu = B\sigma$, since

43

Table 2.3. Probabilities for a Biased Gaussian vs. Fraction of Standard Deviation

TABLE SHOWING PER-CENT OF READINGS TAKEN FROM A GAUSSIAN DISTRIBUTION WITH SIGMA=1 AND THE INDICATED BIASES

ERROR-BAR -TO+ / BIAS=	.00	.20	.40	.60	.80	1.00	1.20	1.40	1.60	1.80	2.00
.00	.00	.00	.00	.00	.00	.00	.00	.00	.00	.00	.00
.10	7.97	7.81	7.36	6.66	5.79	4.84	3.89	3.00	2.22	1.59	1.09
.20	15.85	15.54	14.65	13.27	11.56	9.68	7.79	6.03	4.48	3.20	2.20
.30	23.58	23.13	21.82	19.80	17.29	14.52	11.73	9.11	6.81	4.89	3.39
.40	31.08	30.50	28.81	26.21	22.95	19.35	15.71	12.27	9.23	6.69	4.66
.50	38.29	37.59	35.58	32.45	28.53	24.17	19.74	15.53	11.78	8.61	6.06
.60	45.15	44.36	42.06	38.49	34.00	28.98	23.83	18.91	14.48	10.69	7.61
.70	51.61	50.74	48.22	44.30	39.34	33.75	27.98	22.41	17.33	12.95	9.33
.80	57.63	56.71	54.04	49.85	44.52	38.48	32.18	26.03	20.37	15.40	11.25
.90	63.19	62.24	59.47	55.11	49.53	43.15	36.42	29.78	23.58	18.06	13.38
1.00	68.27	67.31	64.50	60.06	54.33	47.72	40.68	33.64	26.96	20.93	15.73
1.10	72.87	71.91	69.12	64.69	58.92	52.20	44.94	37.59	30.51	24.01	18.31
1.20	76.99	76.06	73.33	68.98	63.27	56.54	49.18	41.61	34.20	27.29	21.12
1.30	80.64	79.75	77.14	72.93	67.36	60.72	53.36	45.67	38.02	30.76	24.15
1.40	83.85	83.01	80.54	76.54	71.18	64.72	57.46	49.74	41.94	34.39	27.39
1.50	86.64	85.86	83.56	79.81	74.73	68.53	61.44	53.80	45.92	38.16	30.83
1.60	89.04	88.33	86.22	82.74	77.99	72.11	65.29	57.79	49.93	42.04	34.44
1.70	91.09	90.45	88.53	85.36	80.97	75.46	68.96	61.69	53.93	45.99	38.20
1.80	92.81	92.25	90.53	87.67	83.67	78.56	72.44	65.47	57.89	49.98	42.07
1.90	94.26	93.76	92.25	89.70	86.09	81.41	75.71	69.10	61.77	53.97	46.01
2.00	95.45	95.02	93.70	91.46	88.24	84.00	78.75	72.54	65.53	57.92	50.00
2.10	96.43	96.06	94.92	92.97	90.13	86.34	81.55	75.78	69.14	61.79	53.98
2.20	97.22	96.91	95.94	94.26	91.79	88.42	84.10	78.80	72.57	65.54	57.92
2.30	97.86	97.59	96.78	95.36	93.22	90.27	86.41	81.58	75.80	69.14	61.79
2.40	98.36	98.14	97.47	96.27	94.45	91.89	88.48	84.13	78.81	72.57	65.54
2.50	98.76	98.58	98.03	97.03	95.50	93.30	90.31	86.43	81.59	75.80	69.15
2.60	99.07	98.92	98.48	97.66	96.37	94.50	91.92	88.49	84.13	78.81	72.57
2.70	99.31	99.19	98.83	98.17	97.11	95.53	93.31	90.32	86.43	81.59	75.80
2.80	99.49	99.40	99.11	98.58	97.71	96.40	94.52	91.92	88.49	84.13	78.81
2.90	99.63	99.56	99.33	98.90	98.20	97.12	95.54	93.32	90.32	86.43	81.59
3.00	99.73	99.68	99.50	99.16	98.60	97.72	96.41	94.52	91.92	88.49	84.13
3.10	99.81	99.77	99.63	99.37	98.92	98.21	97.13	95.54	93.32	90.32	86.43
3.20	99.86	99.83	99.73	99.53	99.18	98.61	97.72	96.41	94.52	91.92	88.49
3.30	99.90	99.88	99.80	99.65	99.38	98.93	98.21	97.13	95.54	93.32	90.32
3.40	99.93	99.92	99.86	99.74	99.53	99.18	98.61	97.72	96.41	94.52	91.92
3.50	99.95	99.94	99.90	99.81	99.65	99.38	98.93	98.21	97.13	95.54	93.32
3.60	99.97	99.96	99.93	99.86	99.74	99.53	99.18	98.61	97.72	96.41	94.52
3.70	99.98	99.97	99.95	99.90	99.81	99.65	99.38	98.93	98.21	97.13	95.54
3.80	99.99	99.98	99.97	99.93	99.87	99.74	99.53	99.18	98.61	97.72	96.41
3.90	99.99	99.99	99.98	99.95	99.90	99.81	99.65	99.38	98.93	98.21	97.13
4.00	99.99	99.99	99.98	99.97	99.93	99.87	99.74	99.53	99.18	98.61	97.72
4.10	100.00	100.00	99.99	99.98	99.95	99.90	99.81	99.65	99.38	98.93	98.21
4.20	100.00	100.00	99.99	99.98	99.97	99.93	99.87	99.74	99.53	99.18	98.61
4.30	100.00	100.00	100.00	99.99	99.98	99.95	99.90	99.81	99.65	99.38	98.93
4.40	100.00	100.00	100.00	99.99	99.98	99.97	99.93	99.87	99.74	99.53	99.18
4.50	100.00	100.00	100.00	100.00	99.99	99.98	99.95	99.90	99.81	99.65	99.38
4.60	100.00	100.00	100.00	100.00	99.99	99.98	99.97	99.93	99.87	99.74	99.53
4.70	100.00	100.00	100.00	100.00	100.00	99.99	99.98	99.95	99.90	99.81	99.65
4.80	100.00	100.00	100.00	100.00	100.00	99.99	99.98	99.97	99.93	99.87	99.74
4.90	100.00	100.00	100.00	100.00	100.00	100.00	99.99	99.98	99.95	99.90	99.81
5.00	100.00	100.00	100.00	100.00	100.00	100.00	99.99	99.98	99.97	99.93	99.87

Table 2.4. Probabilities for a Biased Gaussian vs. Fraction of Root Mean Square

TABLE SHOWING PER-CENT OF READINGS TAKEN FROM A GAUSSIAN DISTRIBUTION WITH SIGMA=1 AND THE INDICATED BIASES

ERROR-BAR -TO+ BIAS= FRACTION OF R.M.S.	.00	.20	.40	.60	.80	1.00	1.20	1.40	1.60	1.80	2.00
.00	.00	.00	.00	.00	.00	.00	.00	.00	.00	.00	.00
.10	7.97	7.06	7.92	7.76	7.41	6.84	6.08	5.18	4.22	3.30	2.47
.20	15.05	15.05	15.76	15.45	14.78	13.69	12.22	10.49	8.67	6.91	5.30
.30	23.50	23.57	23.45	23.01	22.06	20.52	18.47	16.07	13.54	11.07	8.81
.40	31.08	31.07	30.03	30.30	29.21	27.33	24.06	21.99	18.97	16.01	13.26
.50	38.29	38.20	30.11	37.49	36.17	34.09	31.38	20.28	25.02	21.02	18.00
.60	45.15	45.14	44.95	44.29	42.90	40.75	30.01	34.90	31.68	28.50	25.47
.70	51.61	51.59	51.40	50.73	49.35	47.27	44.67	41.78	38.03	35.93	33.17
.80	57.63	57.61	57.43	56.78	55.40	53.57	51.26	48.78	46.30	43.90	41.63
.90	63.19	63.17	63.00	62.40	61.24	59.60	57.70	55.74	53.86	52.11	50.49
1.00	68.27	60.26	68.10	67.57	66.59	65.20	63.05	62.40	61.26	60.22	59.33
1.10	72.07	72.06	72.72	72.20	71.50	70.55	69.61	68.03	68.27	67.90	67.71
1.20	76.99	76.08	76.86	76.52	75.96	75.36	74.09	74.66	74.66	74.09	75.20
1.30	80.64	80.63	80.55	80.30	79.96	79.69	79.63	79.05	80.31	80.97	81.70
1.40	83.05	83.04	83.78	83.63	83.49	83.50	83.78	84.34	85.12	86.05	87.09
1.50	86.64	86.64	86.60	86.54	86.56	86.00	87.33	88.11	89.07	90.12	91.21
1.60	89.04	89.04	89.03	89.04	89.20	89.61	90.30	91.19	92.20	93.25	94.27
1.70	91.09	91.09	91.09	91.17	91.43	91.95	92.72	93.63	94.60	95.55	96.42
1.80	92.01	92.02	92.84	92.96	93.29	93.07	94.65	95.51	96.30	97.17	97.06
1.90	94.26	94.26	94.29	94.45	94.02	95.41	96.14	96.92	97.64	98.27	98.77
2.00	95.45	95.45	95.50	95.67	96.05	96.62	97.20	97.94	98.51	98.98	99.33
2.10	96.43	96.43	96.48	96.66	97.03	97.55	98.12	98.66	99.09	99.42	99.65
2.20	97.22	97.22	97.27	97.46	97.00	98.26	98.73	99.15	99.46	99.68	99.82
2.30	97.06	97.06	97.91	98.08	98.40	98.79	99.16	99.47	99.69	99.83	99.92
2.40	98.36	98.36	98.41	98.57	99.04	99.17	99.46	99.68	99.83	99.92	99.96
2.50	98.76	98.76	98.81	98.95	99.10	99.44	99.66	99.81	99.91	99.96	99.98
2.60	99.07	99.07	99.11	99.24	99.43	99.63	99.79	99.89	99.95	99.98	99.99
2.70	99.31	99.31	99.35	99.45	99.61	99.76	99.87	99.94	99.98	99.99	99.99
2.80	99.49	99.49	99.52	99.61	99.73	99.85	99.92	99.97	99.99	99.99	100.00
2.90	99.63	99.63	99.66	99.73	99.82	99.90	99.96	99.98	99.99	100.00	100.00
3.00	99.73	99.73	99.75	99.81	99.02	99.94	99.98	99.99	99.99	100.00	100.00
3.10	99.01	99.01	99.03	99.07	99.07	99.96	99.99	100.00	100.00	100.00	100.00
3.20	99.06	99.06	99.00	99.91	99.91	99.98	99.99	100.00	100.00	100.00	100.00
3.30	99.93	99.90	99.94	99.94	99.94	99.99	100.00	100.00	100.00	100.00	100.00
3.40	99.95	99.93	99.96	99.96	99.96	99.99	100.00	100.00	100.00	100.00	100.00
3.50	99.97	99.95	99.97	99.97	99.97	99.99	100.00	100.00	100.00	100.00	100.00
3.60	99.98	99.97	99.98	99.98	99.98	100.00	100.00	100.00	100.00	100.00	100.00
3.70	99.99	99.98	99.99	99.99	99.99	100.00	100.00	100.00	100.00	100.00	100.00
3.80	99.99	99.99	99.99	99.99	99.99	100.00	100.00	100.00	100.00	100.00	100.00
3.90	99.99	99.99	99.99	100.00	100.00	100.00	100.00	100.00	100.00	100.00	100.00
4.00	100.00	100.00	100.00	100.00	100.00	100.00	100.00	100.00	100.00	100.00	100.00
4.10	100.00	100.00	100.00	100.00	100.00	100.00	100.00	100.00	100.00	100.00	100.00
4.20	100.00	100.00	100.00	100.00	100.00	100.00	100.00	100.00	100.00	100.00	100.00
4.30	100.00	100.00	100.00	100.00	100.00	100.00	100.00	100.00	100.00	100.00	100.00
4.40	100.00	100.00	100.00	100.00	100.00	100.00	100.00	100.00	100.00	100.00	100.00
4.50	100.00	100.00	100.00	100.00	100.00	100.00	100.00	100.00	100.00	100.00	100.00
4.60	100.00	100.00	100.00	100.00	100.00	100.00	100.00	100.00	100.00	100.00	100.00
4.70	100.00	100.00	100.00	100.00	100.00	100.00	100.00	100.00	100.00	100.00	100.00
4.80	100.00	100.00	100.00	100.00	100.00	100.00	100.00	100.00	100.00	100.00	100.00
4.90	100.00	100.00	100.00	100.00	100.00	100.00	100.00	100.00	100.00	100.00	100.00
5.00	100.00	100.00	100.00	100.00	100.00	100.00	100.00	100.00	100.00	100.00	100.00

$$\langle x^2 \rangle = \langle [(x - \mu) + \mu]^2 \rangle$$

$$= \langle (x - \mu)^2 + 2\mu(x - \mu) + \mu^2 \rangle$$

$$= \langle (x - \mu)^2 \rangle + 2\mu \langle (x - \mu) \rangle + \mu^2$$

$$= \sigma^2 + \mu^2$$

We therefore finally state that

$$P\{|x| \geq \Delta\} \leq \text{rms}^2/\Delta^2$$

meaning that the probability that x is outside the interval $[-\Delta, \Delta]$ cannot exceed $(\text{rms}/\Delta)^2$. Thus the probability, or confidence, that the error x is within this interval is at least $1-(\text{rms}/\Delta)^2$.

We may use this result to obtain an upper bound for the half width Δ of the confidence interval, such that the probability that the error x is within this interval is at least a desired value α:

$$\Delta \leq \text{rms}/(1-\alpha)^{1/2} \tag{2.3}$$

We note that the upper bound given by the right hand side of Eq. (2.3) for 68.2% confidence is 1.75 rms, compared to 1.0 rms for Gaussians, as indicated by Table 2.4. For 95% confidence the upper bound given by Eq. (2.3) is 4.47 rms, compared to 1.96 rms for Gaussians. Futhermore we note that the interval half-width Δ from Eq. (2.3) can never be less than one rms.

2.1.2.4 Applications to Atmospheric Density Model Errors

GL has collected a substantial data base of in-situ satellite drag measurements in the lower thermosphere [Marcos, 1985]. The densities derived from this data can then be compared with models such as the previously mentioned MSIS-86 [Hedin, 1986] model. Thus, the following statistics have routinely been computed:

$$M = \Sigma\, r_i/N \tag{2.4}$$

$$s = [\Sigma\, (r_i - M)/(N-1)]^{1/2}/M \tag{2.5}$$

where r_i is the ratio of the ith measured density to the density predicted by the model for that case, and N is the number of measurements. With these two parameters, the model user may imply that a corrected model obtained by multiplying the original model by M will have relative errors with estimated standard deviation s. There are at least two problems with this approach. One is that the user may need to know the error in the model itself, rather than in a corrected version. The second problem is that the data base may have systematic error, which introduces uncertainty in the mean M, although not in the standard deviation s. The following examples will show how to characterize the error in the model itself (not the corrected model) given that we have a sample estimate M of the mean ratio, such that a sample estimate of the mean relative error μ is M-1, where M is given by Eq. (2.4), and a sample estimate of the standard deviation σ given by Ms, where s is given by Eq. (2.5). The reason for using Ms instead of s is that we are interested here in the relative error of the original model, not the relative error of the corrected model. The factor M is generally close to one, unless the model is very poor.

2.1.2.4.1 Model Developed from a Data Base

We assume that a model has been developed empirically from a data base. This is generally the case for models such as the MSIS-86. This data base is then used to "evaluate" the model. The mean relative model error is found to be zero, and the standard deviation is found to be 15%.

A. Assume there are no errors in the data. The rms model error is therefore 15%. If the error distribution is Gaussian, we may then use column 1 of Table 2.4, to find the ±error range for any desired probability. Simply find the row containing the desired probability in column 2 and multiply the number in column 1 by 15%. If the distribution is strongly non-Gaussian, we may use Eq. (2.3) to find an upper bound for the error range.

B. We find out later that there is a 10% systematic error in the data, i.e., the measurements should have been 10% higher. Therefore, using the hypothetically corrected data base to evaluate the model obtained on the basis of the uncorrected data, we would obtain a mean model error of 10% and a σ of (15 x 1.1)% = 16.5%. Thus our model error is characterized by:

$$\text{rms}(\%) = [10^2 + 16.5^2]^{1/2} = 19.3\%.$$

C. We find out later that, instead, there was uncertain systematic error in the data, in the range ± 10%. Then the total error is the sum of the measured and systematic errors. Assuming that the latter may be characterized by a probability density function with zero mean and standard deviation 10%, we obtain for the total error:

$$\text{rms} = [10^2 + 15^2]^{1/2} = 18.0\%$$

If the probability density functions of both the measured systematic errors are Gaussian, then the probability density function of the total error is also Gaussian [Brunk,1975], and we may use Table 2.4, as above, to determine the confidence limits for any specified probability. If either distribution is non-Gaussian, we may use Eq. (2.3).

There is another view of the systematic error which is sometimes considered: the systematic error is known definitely to be within a certain range, but its pd within that range is unknown. Thus the total error pd may be biased by some unknown amount, within this range. If the measured error distribution is Gaussian, then the actual error distribution is the same Gaussian biased by the systematic error. From Table 2.3 it can be seen that the probability of occurrence within an interval centered about zero decreases with the increasing magnitude of the bias. Therefore the worst case, within this specification, would occur if the systematic error had the maximum value, 10%. Using this worst case we get the same total rms as just given for the 10% σ uncertainty in the systematic error. The same rms is applicable if the measured error distribution is unspecified or strongly non-Gaussian, since the modified Chebyshev's inequality applied to this worst case rms produces the worst case confidence interval.

Another method of handling the systematic error, when it is known to lie within a definite finite range, is to add the maximum absolute value of the systematic error to the rms random measurement error. This is the approach suggested by Cameron [Cameron et al., 1996O]. It is clear that our result, using the rms of the systematic and random errors, yields tighter confidence limits.

2.1.2.4.2 Model Compared With Independent Data Base

A. The mean ratio is 1.0, the standard deviation is 15%, and there is no systematic or random measurement error. Then the rms is the same as in 2.1.2.4.1 A, 15%.

B. Same as A, except that the mean ratio is 1.1. Then, following our discussion in Sections 2.1.2.2 and 2.1.2.3,

$$rms = [10^2 + 15^2]^{1/2} = 18.0\%.$$

C. Same as B, except that the data has uncertain systematic error, and therefore an uncertainty in the mean error, within 10%. If this uncertainty is characterized by a probability density function with zero mean and standard deviation 10%, then the overall pd (measured + systematic error) is characterized by:

$$\sigma = [10^2 + 15^2]^{1/2} = 18.0\%$$

$$\mu = 10\%$$

For this biased distribution we may again define an effective rms

$$rms = [\sigma^2 + \mu^2]^{1/2} = 20.6\%$$

If we take the second approach, mentioned above, for the systematic error, namely that we know only that it is in the interval $\pm 10\%$, then, taking the worst case, as we did previously, we get a distribution whose mean is the sum of the measured mean and the largest possible bias value:

$$\mu = 10\% + 10\% = 20\%$$

The standard deviation is as measured, 15%. Then, we obtain, for the rms:

$$rms = [20^2 + 15^2]^{1/2} = 25\%$$

D. Same as C, except that the data has random error of 5%. In this case, we know that the measured σ, estimated by s, is the standard deviation for the sum of two independent unbiased random errors: the true model (random) error (true value - model value) and the measurement error (measured value -true value). Then it is evident that the true model random error has the standard deviation

$$\sigma = [15^2 - 5^2]^{1/2} = 14.1\%.$$

Then we obtain for the rms, assuming that the systematic error uncertainty is characterized by 10% standard deviation and zero mean:

$$rms = [14.1^2 + 10^2 + 10^2]^{1/2} = 20.0\%$$

For the second view of systematic error, assuming the worst case value of 10%:

$$rms = [14.1^2 + 20^2]^{1/2} = 24.5\%$$

For Gaussian distributions we must caution that, for the conservative worst case systematic errors assumed in the last two examples, the biases obtained were larger than one sigma (1.33σ in

example C, and 1.4σ in example D). For biases this large, Table 2.4 indicates moderate decrease in the probability of occurrence within intervals smaller than the rms, relative to the probabilities of occurrence in the same intervals for zero bias. At one rms, the probability has decreased from 68.2% to approximately 63%. However, it is seen that this trend eventually reverses as the interval increases.

2.1.3 Correlation of Atmospheric Density with Geomagnetic Activity Indices

2.1.3.1 Introduction

The neutral thermosphere is is an extremely complex system. Nevertheless accurate and efficient modeling of the thermosphere is important for many applications. Empirical modeling attempts to use simple indices as measures of energy sources to the thermosphere in the hope that the thermospheric density variations may be simply related to variations in these indices. For geomagnetic sources Kp has been the most prominently used index. This report compares the correlations with thermospheric density of the Evans particle precipitation indices POW and PPE, the auroral electrojet index AE, and KP.

The POW values are direct satellite-based measurements of the precipitation power level at the specific location of the measuring satellite. The PPE index is an estimate of the global precipitation obtained by using POW to normalize a pre-exisiting model. Since POW, PPE, and AE monitor specific processes thought to be important sources of energy deposition into the auroral thermosphere, it has been suspected that they may be more useful than Kp for modeling the geomagnetically disturbed thermosphere.

The thermospheric density data used in this study are obtained from the SETA-1 and SETA-2 accelerometer data bases. The SETA-1 satellite collected data over a 21 day period in March-April, 1979. The SETA-2 satellite was active May-November, 1982. Both satellite orbits were sun-synchronous (96° inclinations) with perigees in the mid-northern latitudes at approximately 10 hours local time. The SETA-1 processed date set contains 62649 measurements; the SETA-2 set contains 443.805.

This section describes the computation of normalized thermospheric drag from satellite accelerometer data, and the computation of correlation coefficients of normalized drag with the various indices. The normalization removes most density variations due to altitude variations of the satellite and non-geomagnetic energy sources. Thus the geomagnetic variations are emphasized. Software was developed for these computation and for graphical display of the drag-index correlation coefficients as functions of latitude and time lag.

2.1.3.2 Analysis

2.1.3.2.1 Normalized Drag

As we are interested primarily in the variations related to geomagnetic activity, we compute, for each orbit, the following:

$$D_t = \Sigma \, \rho_i / \Sigma \rho_i^* ; \tag{2.6a}$$

$$D_a = \Sigma' \, \rho_i / \Sigma' \, \rho_i^* , \tag{2.6b}$$

where ρ_i is the measured density for the ith sample, ρ_i^* is the density predicted for the ith sample by the Jacchia [1971] Model with K_p fixed at 1.0, and the summations in equations (2.6a) and (2.6b) extend over the entire orbit, and over a specific latitude/local time bin, respectively. The bins in equation (1b) have 5° widths with separate bins for day (4.5-16.5 hours local time) and night, plus one 90° bin each for day and night. Only northern hemisphere bins are studied. Both geographic and geomagnetic latitude bins are employed.

The variations not related to geomagnetic activity, including those caused by altitude variation in the satellite's orbit, are thus effectively removed, to the extent that they are modelled accurately by the Jacchia 1971 model. Extensive statistical comparisons of the measured density with various models [Marcos, 1985] have indicated that this model is nearly as accurate as more complex recent models. The use of the ratio of sums, rather than the sum of ratios, permits a simulation of total drag effects, which are of significant operational interest in predicting satellite orbit decay. Except for multiplication by a ballistic coefficient, each summation is the total drag over the appropriate range (total orbit or bin). This factor is canceled out in the normalization (division by the model prediction).

For each orbit the starting and ending times are tabulated, along with the normalized drag for the total orbit, and the 38 latitude-local time bins. Of these bins, the 85-90° bins are empty when the sorting is by geographic latitude, since the 96° satellite inclination precludes coverage in this region.

2.1.3.2.2 Correlation Coefficient

The correlation coefficient of two quantities r_a and r_b is defined as

$$C_{ab} = \Sigma_i[(r_{ai}-\bar{r}_a)(r_{bi}-\bar{r}_b)]/\sqrt{[\Sigma_i(r_{ai}-\bar{r}_a)^2\Sigma_i(r_{bi}-\bar{r}_b)^2]}, \qquad (2.7)$$

where r_{ai} is the ith sample of r_a, r_{bi} is the ith sample of r_b, and, for any quantity x, $\bar{x}$ is its mean value. For our application r_a is the normalized drag defined above, and r_b is the index with which the drag is being correlated. The sequence r_b is said to be lagged with respect to the sequence r_a by time lag L if

$$t_{ai}-t_{bi} = L,$$

where t_{ai} is the time of the ith sample of r_a, and t_{bi} is the time of the ith sample of r_b. The drag samples are time-tagged with the start times of the satellite orbits from which they were obtained. Then for each such sample, we must determine the value of the index at the time preceding the drag sample time by L. This has been done as follows:

For indices available at uniform increments (such as the 3-hour K_p values) the index is assumed to be a step function, its value a constant over each incremental period. If the index is given on a time-ordered, but non-uniform grid, the period of validity of the sample at time t_k on this grid is defined as

$$t_k-dt_k \le t \le t_k+dt_k,$$

where

$$dt_1 = 0.5(t_2-t_1);$$

50

$$dt_N = 0.5(t_N - t_{N-1});$$

$$dt_k = 0.25(t_{k+1} - t_{k-1}), \ 1 < k < N,$$

where N is the total number of index values available on the time ordered grid. The closest sample times before and after t are located. If t lies in only one of the associated periods of validity, the index value for that period is selected. Otherwise (either t is in a gap between the two periods, or in an overlap) the mean of the two values is selected. If t is before the first validity period, or after the last, the index value at t is undefined. The use of constant value periods for non-uniformly spaced sequences, rather than some form of interpolation, to obtain the value of the index at arbitrary times, has been done to simulate the step-function approach used with uniformly spaced sequences, to minimize artificial differences that might result from different methods of extracting the index values.

We have also computed correlation coefficients between the time-averaged drag and the various time averaged-indices, varying the duration of the averaging period from 90 minutes to 1 day. The averaging is performed on the time series pair constructed as we have just described. In the averaging, each sample is weighted equally.

2.1.3.3 Software

Figure 2.2 shows an overview of the software system developed to conduct this study. Since the density data base resides on the CYBER, the computation of the normalized drags has been performed there. The results are then transferred via the hyperchannel to the VAX 8650, where the correlation coefficients are generated. Initially this was done to make the drag data available to a VAX user, who possessed a VAX-resident particle index data base. Later the particle index data became available on tape, which could be used with either system. However, since extensive use of the IDL [Research Systems, Inc., 1987] software, available only on the VAX, had evolved for generating contour plots of the results, it was decided to retain this portion of the system on the VAX. At present, the particle indices are initially processed on the CYBER in order to use its greater temporary storage facility. Data for the relevant time periods are extracted and sent via hyperchannel to the VAX. With the recent availability of scratch disk space on the VAX, the need to use the CYBER for processing the particle indices may be eliminated.

2.1.3.3.1 Normalized Drag

The normalized drag data bases are generated in two steps. In the first step, a modified reduced data base (MRDB) is constructed from a density data base by inserting, for each data sample, the Jacchia 1971 ($K_p=1$) model value and the K_p values at various lagged times relative to the sample time. This is accomplished with either program MRDB, or MRDBPK, depending on whether the data is packed or unpacked. The second step employs program OADB to generate the normalized drags, and program OACNVT to convert the output file from binary to coded for transfer to the VAX.

2.1.3.3.2 Geomagnetic Activity Indices

The indices included in this study are the Evans POW and PPE indices, the AE index, and the K_p index. The latter has been routinely received and maintained on data files for years, and as mentioned above, is already incorporated into the reduced drag data bases. The others have been received separately for this study, and reformatted when necessary into separate files. Since
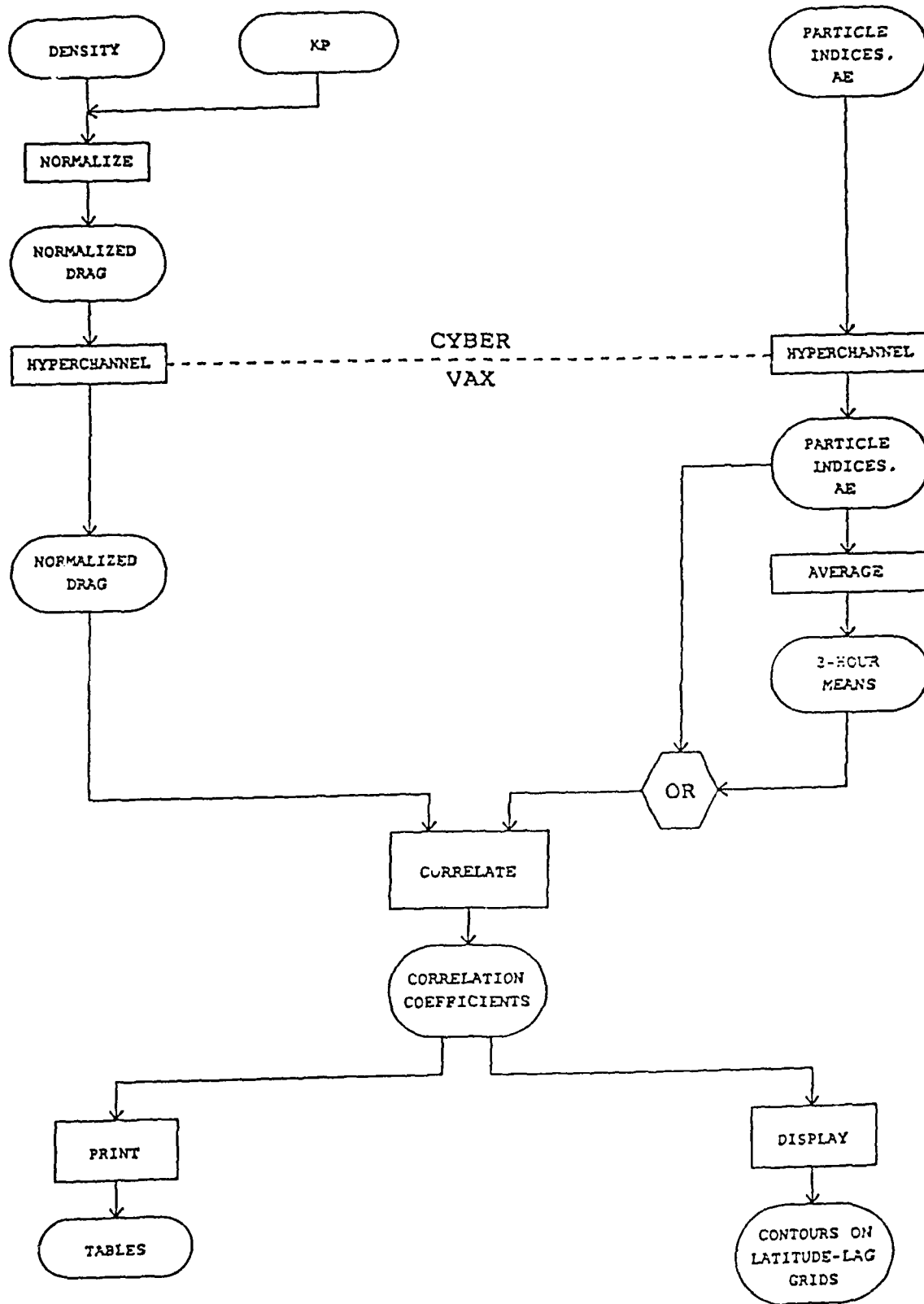
Figure 2.2. Software system for atmospheric density correlation studies

52

the smallest time resolution for which K_p is available is 3 hours, files of 3-hour averages were created for the other indices. Program MAKCO3 was written to generate the 3-hour files for the Evans Index, by averaging the data within each 3-hour period. The AE data was made available on an hourly basis from which 3-hour values are similarly generated by program MAKAE3.

2.1.3.3.3 Correlation Studies

The correlation studies have been performed on the VAX 8650. Program DRAGMCOR performs the numerical computations of the correlation coefficients using IBM subroutine CORRE [IBM, 1968]. It has the capability of inputting any of the 3-hour files, or the Evans per pass file described above. The coefficients are then computed, for a user-specified segment of the data, for the drag-particle index and drag-K_p correlations (the "particle index" in this case may be the Evans POW, Evans PPE, or AE index). Latitude-local time binning is permitted. The results are generated for lag times 0-15 hours in increments of 3 hr. The basic output is an ASCII summary file (Figure 2.3) which may be easily viewed and printed, and which serves as input to an IDL package which generates contours of constant correlation coefficient in lag-latitude space (Figure 2.4).

Program DRAGMCOR

The drag and index data are input from the appropriate files. Then the subsets required for each correlation coefficient are selected, the drag values time-tagged, and the index values at the properly lagged times obtained according to the procedures described in Section 2.1.3.2.2. If requested, the drag and index values are averaged over consecutive time periods of specified length. Thus a sequence of drag-index pairs is available for correlation. This is fed to subroutine CORRE for the computation of the correlation coefficients. The results are tabulated for output to the summary file, which will contain a table of drag-particle index correlation coefficients plus a corresponding table for drag-K_p correlation coefficients. In addition, if requested by the user, 3 optional files, primarily for debugging purposes, may be generated: a general detailed output file listing the particle index (3 hour values only) and drag data read in and stored by the program, and the input and output parameters of each call to subroutine CORRE; a file listing only the inputs and outputs of each call to CORRE for the drag-particle index correlations; and a file listing only the inputs and outputs of each call to CORRE for the drag-K_p correlations.

2.1.3.3.4 IDL Software

Several small IDL procedures have been written to interactively perform contour generation and other functions. To enter IDL from the GL VAX 8650 VMS operating system, one simply enters the command XIDL. Then to compile the procedures, simply enter the command

> @BEGIN

The command file BEGIN.PRO is then executed, compiling the procedures, opening a plot output file, and performing certain parameter initializations. To save the compiled procedures, enter the command

> SAVE,filnam

where filnam is the character string (in single quotes) name of the file (default extension: .DAT) on which the procedures would be saved. In subsequent sessions the command

DRAG-ROW CORRELATION COEFFICIENTS
SATELLITE: SETA-2   SEASON(S): ALL
GEOMAGNETIC LATITUDE BINNING: ALL
0 HOUR LAG KP RANGE: 0 TO 9

BIN	LAG (HOURS) 0	3	6	9	0	12	15	SD (DRAG)	NODS
ALL	0.5804	0.5920	0.5768	0.5005	0.4331	0.3700	0.0020	1765
DAY N. HEM.	0.5818	0.5833	0.5704	0.5030	0.4387	0.3020	0.0911	1751
NITE N. HEM.	0.4849	0.4851	0.5120	0.4005	0.4156	0.3427	0.1125	1746
DAY 0 – 5	0.4024	0.5513	0.4848	0.4251	0.3041	0.3209	0.0708	1028
DAY 5 – 10	0.4907	0.5454	0.4677	0.3984	0.3001	0.3201	0.0700	1590
DAY 10 – 15	0.4051	0.5477	0.4741	0.3984	0.3780	0.3530	0.0700	1570
DAY 15 – 20	0.4823	0.5598	0.5105	0.4485	0.4055	0.3772	0.0772	1542
DAY 20 – 25	0.4809	0.5504	0.5404	0.4605	0.4200	0.3702	0.0785	1401
DAY 25 – 30	0.4807	0.5477	0.5572	0.4828	0.4329	0.3002	0.0707	1403
DAY 30 – 35	0.4050	0.5675	0.5027	0.5225	0.4604	0.4015	0.0813	1440
DAY 35 – 40	0.5078	0.5670	0.5715	0.5241	0.3011	0.3011	0.0833	1435
DAY 40 – 45	0.4923	0.5494	0.5474	0.4920	0.4271	0.3751	0.0870	1434
DAY 45 – 50	0.4858	0.5242	0.5231	0.4680	0.3970	0.3484	0.0807	1400
DAY 50 – 55	0.4824	0.4960	0.4936	0.4546	0.3853	0.3308	0.0088	1504
DAY 55 – 60	0.4000	0.4780	0.4551	0.4308	0.3024	0.3200	0.1124	1570
DAY 60 – 65	0.5092	0.4703	0.4593	0.4189	0.3703	0.3108	0.1206	1632
DAY 65 – 70	0.5300	0.4832	0.4585	0.4098	0.3512	0.2952	0.1433	1078
DAY 70 – 75	0.5121	0.4710	0.4470	0.3983	0.3329	0.2022	0.1544	1700
DAY 75 – 80	0.4830	0.4095	0.3516	0.3092	0.2835	0.2473	0.1001	1323
DAY 80 – 85	0.4847	0.4157	0.3970	0.3552	0.3050	0.2041	0.1631	1024
DAY 85 – 90	0.3693	0.3400	0.3624	0.3490	0.2938	0.3140	0.1529	703
NITE 0 – 5	0.4707	0.5473	0.5062	0.4392	0.3374	0.2332	0.1402	1075
NITE 5 – 10	0.4853	0.5520	0.5121	0.4540	0.3553	0.2510	0.1411	1075
NITE 10 – 15	0.4758	0.5463	0.5161	0.4640	0.3692	0.2010	0.1362	1075
NITE 15 – 20	0.4671	0.5208	0.5030	0.4500	0.3767	0.2724	0.1310	1670
NITE 20 – 25	0.4401	0.4996	0.4793	0.4398	0.3714	0.2774	0.1209	1072
NITE 25 – 30	0.4438	0.4834	0.4801	0.4420	0.3702	0.2855	0.1251	1073
NITE 30 – 35	0.4332	0.4627	0.4660	0.4317	0.3707	0.3009	0.1211	1676
NITE 35 – 40	0.4434	0.4687	0.4733	0.4367	0.3843	0.3137	0.1104	1079
NITE 40 – 45	0.4623	0.4835	0.4766	0.4262	0.3607	0.3127	0.1108	1083
NITE 45 – 50	0.4507	0.4662	0.4715	0.4314	0.3774	0.3274	0.1107	1004
NITE 50 – 55	0.4553	0.4569	0.4703	0.4304	0.3754	0.3438	0.1104	1683
NITE 55 – 60	0.4726	0.4610	0.4683	0.4533	0.3880	0.3557	0.1202	1690
NITE 60 – 65	0.4045	0.4543	0.4803	0.4522	0.3803	0.3450	0.1308	1718
NITE 65 – 70	0.4052	0.3568	0.4313	0.4275	0.3603	0.3027	0.1420	1720
NITE 70 – 75	0.3584	0.3280	0.3810	0.3962	0.3590	0.2718	0.1373	1728
NITE 75 – 80	0.3690	0.3272	0.3550	0.3628	0.3321	0.2940	0.1307	1313
NITE 80 – 85	0.3608	0.3378	0.3859	0.3553	0.3002	0.2910	0.1427	1024
NITE 85 – 90	0.3344	0.2857	0.3310	0.3188	0.2768	0.2701	0.1428	680

Figure 2.3.   ASCII summary file of correlation coefficients
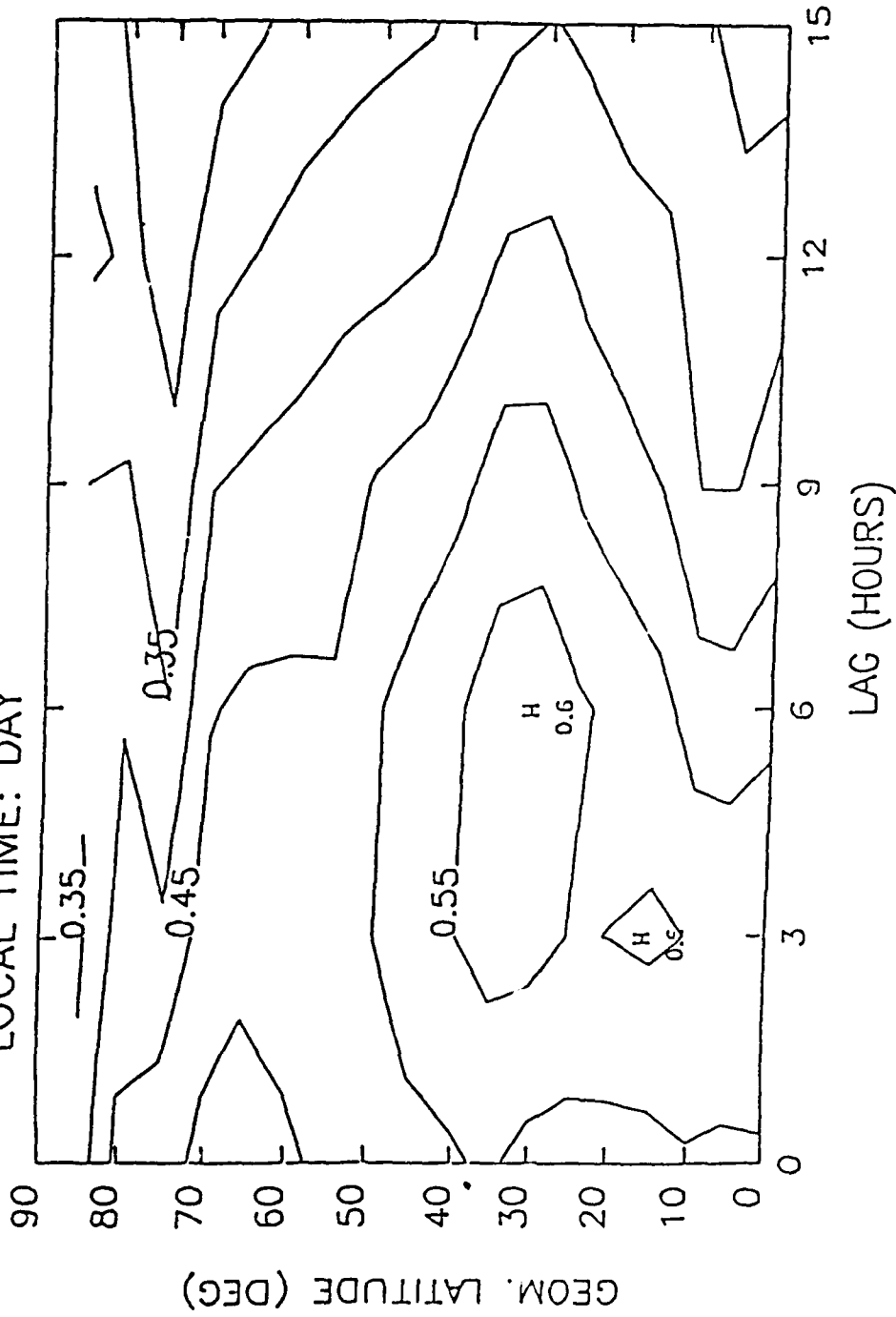
Figure 2.4. Sample contour plot for data of Figure 2.3

@BEGINR

may be used instead of @BEGIN to restore the saved compiled procedures, instead of recompiling them, and perform the other initializations.

Both @BEGIN and @BEGINR invoke a small program file SETVAR which allocates arrays for the plot header and data, invokes procedures SETRVAR and UDEFLAB to, respectively, define certain IDL system variables, and define a common block which will contain labeling information, and requests a name for a plot output file, which it subsequently opens to unit 10, with the specification that the plots also be sent to the terminal. The plot file may be sent to the VAX laser plotters with the VMS commands LASERTEK FILNAM or LT3 FILNAM. This may be done while still in IDL by first closing the file (CLOSE,10) and then executing the laser command prefixed by a dollar sign ($). To leave IDL, enter CTRL/Z, which automatically closes the file.

The other callable procedures are:

    READCOR, IOPEN, FILNAM, HEAD, COR, ICLOSE

A single page, as in Figure 2.3, is read into the HEAD and COR arrays.

IOPEN	if not 0, the file FILNAM is opened as unit 1. Otherwise unit 1 is assumed already open.
FILNAM	character string (in single quotes) name of the file to be read
HEAD	the 40 character string array, initially dimensioned size 8 by SETVAR, which will receive header information
COR	the 6 by 39 floating point array which will receive the correlation coefficients
ICLOSE	if not zero, the file is closed upon return; otherwise it is left open for subsequent input

    CPLOT, DN, HEAD, COR

A contour plot is generated for the day (DN='DAY') or night (DN='NIGHT') data in the array COR. HEAD supplies information for titling and labeling. The IDL-supplied plotting routine CONTOURXY is invoked to do the actual contouring.

    CORRATFGEN, INFILNAM, IOPEN, OFILNAM, ICLOSE

Writes on the file OFILNAM a matrix containing the ratios of the drag-particle index correlation coefficients to the drag-Kp correlation coefficients, in the same format as the correlation coefficients were written.

INFILNAM   the name of the input file, which must start with a page of drag-particle index correlation coefficients, as in Figure 2.3, followed by a page of drag-Kp correlation coefficients; the name must be a character string in quotes

IOPEN   if non-zero, the output file is opened to unit 2 in this call; otherwise it is assumed to be already opened.

OFILNAM   character string name of the output file, in single quotes

ICLOSE   if non-zero, the output file is closed before returning; otherwise it remains open to receive additional output in subsequent calls

2.1.3.4 Results

The SETA-1 and SETA-2 drag data were considered in this study. Figure 2.5 shows the Kp, AE, PPE, and POW indices for the 21 day period when SETA-1 was active. The three-hour values appear in histogram form, that is they are depicted as constants within the three-hour intervals 0-3, 3-6 ,6-9, 9-12, 12-15, 15-18, 18-21, and 21-24 hours UT of each day. For the PPE and POW indices, the instantaneous values are plotted point-to-point and superimposed upon the three-hour plots. The major variations are seen to correlate well among these indices. For this period the correlation coefficients of Kp with AE, PPE, and POW, using three-hour values, are, respectively, .813, .823, and .802.

2.1.3.4.1 Total Orbit, Day, and Night Correlations

Table 2.5 indicates the maximum correlations of each index with the total orbit drag, total northern hemisphere day-side drag, and total northern hemisphere night-side drag. In parentheses are the lags in hours for which these maxima occur. Often the night-side results contain two maxima in their dependence on lag, one at zero lag, and the other at a higher lag. In these cases the table shows the higher of the two.

2.1.3.4.2 Latitudinal Variations

Figures 2.6-2.13 show the correlation coefficients vs. latitude and lag on the day and night sides for the SETA-1 satellite. The Kp correlations are shown first, in Figs. 2.6 and 2.7. The correlation coefficients of the other indices with drag are shown as ratios to the Kp-drag correlation coefficient: the PPE results are shown first (Figs. 2.8 and 2.9), followed by the POW results (Figs. 2.10 and 2.11), and the AE results (Figs. 2.12 and 2.13). A ratio larger (smaller) than one indicates that the correlation of drag with the designated index is larger (smaller) than the correlation of drag with Kp.

The results for SETA-2 over all seasons covered by the data are shown in Figs. 2.14 - 2.19, beginning the drag-KP correlations in Figs. 2.14 and 2.15, followed by the ratios of the drag-PPE and drag-POW correlations to the drag-Kp correlation.

57

Figure 2.5. Geomagnetic activity, 1979

Table 2.5 Maximum Correlation Coefficients
(Lags in hours in parentheses)

SETA-1

	Total Orbit	Total North Day	Total North Night
Kp	0.70 (3)	0.66 (3)	0.43 (9)
PPE	0.65 (6)	0.64 (6)	0.39 (9)
POW	0.62 (6)	0.60 (6)	0.36 (6)
AE	0.60 (6)	0.59 (6)	0.39 (0)

SETA-2 All Seasons

	Total Orbit	Total North Day	Total North Night
Kp	0.62 (3)	0.64 (0)	0.54 (6)
PPE	0.54 (0)	0.55 (0)	0.47 (6)
POW	0.59 (3)	0.59 (3)	0.51 (6)

SETA-2 Spring

	Total Orbit	Total North Day	Total North Night
Kp	0.85 (0)	0.83 (0)	0.81 (9)
PPE	0.76 (0)	0.77 (0)	0.73 (6)
POW	0.81 (0)	0.82 (0)	0.76 (6)

SETA-2 Summer

	Total Orbit	Total North Day	Total North Night
Kp	0.60 (6)	0.64 (3)	0.49 (6)
PPE	0.56 (0)	0.60 (0)	0.44 (6)
POW	0.64 (3)	0.64 (3)	0.54 (6)

SETA-2 Autumn

	Total Orbit	Total North Day	Total North Night
Kp	0.71 (3)	0.71 (3)	0.63 (0)
PPE	0.65 (3)	0.65 (3)	0.56 (6)
POW	0.69 (3)	0.69 (3)	0.58 (6)

DRAG— KP CORRELATION COEFFICIENTS
SATELLITE: SETA—1   SEASON(S): SPRING
LOCAL TIME: DAY
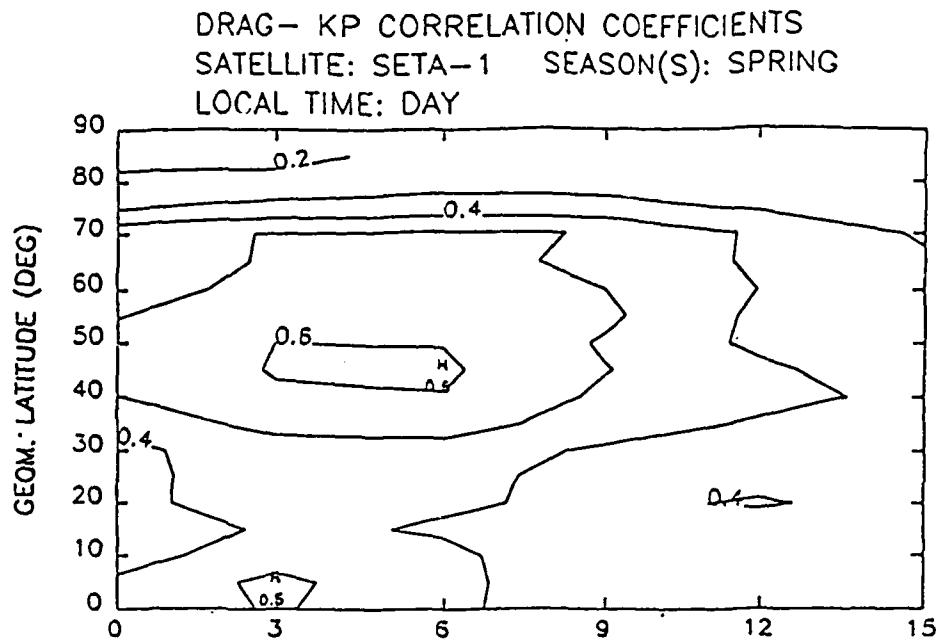
Figure 2.6. Contours of constant daytime drag-Kp correlation ratio, spring: SETA-1

DRAG— KP CORRELATION COEFFICIENTS
SATELLITE: SETA—1   SEASON(S): SPRING
LOCAL TIME: NIGHT
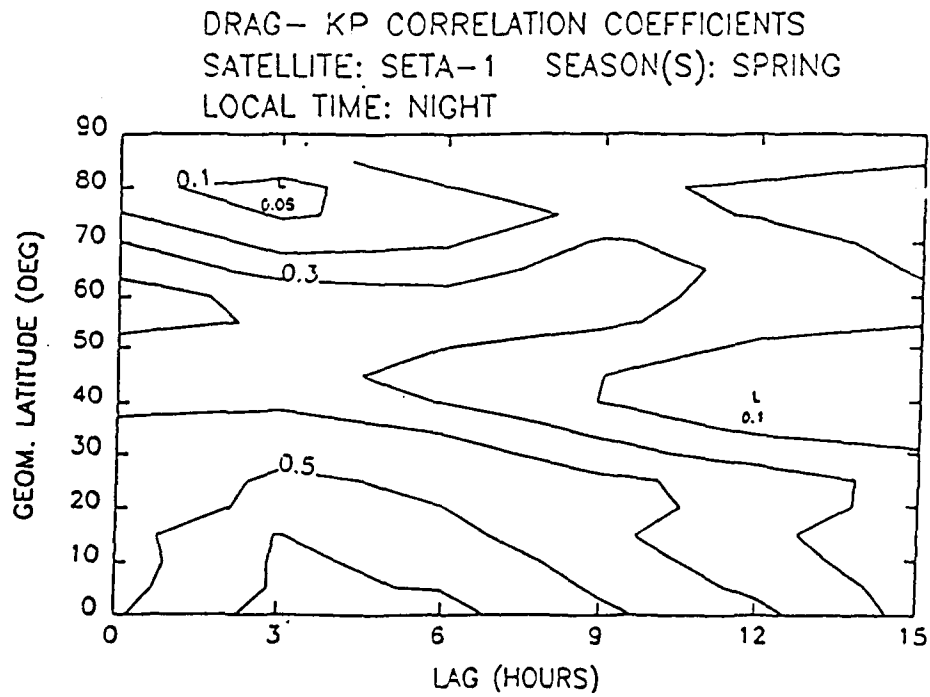
Figure 2.7. Same as Figure 2.6, except night

DRAG–PPE/DRAG–KP CORRELATION RATIO
SATELLITE: SETA–1   SEASON(S): SPRING
LOCAL TIME: DAY
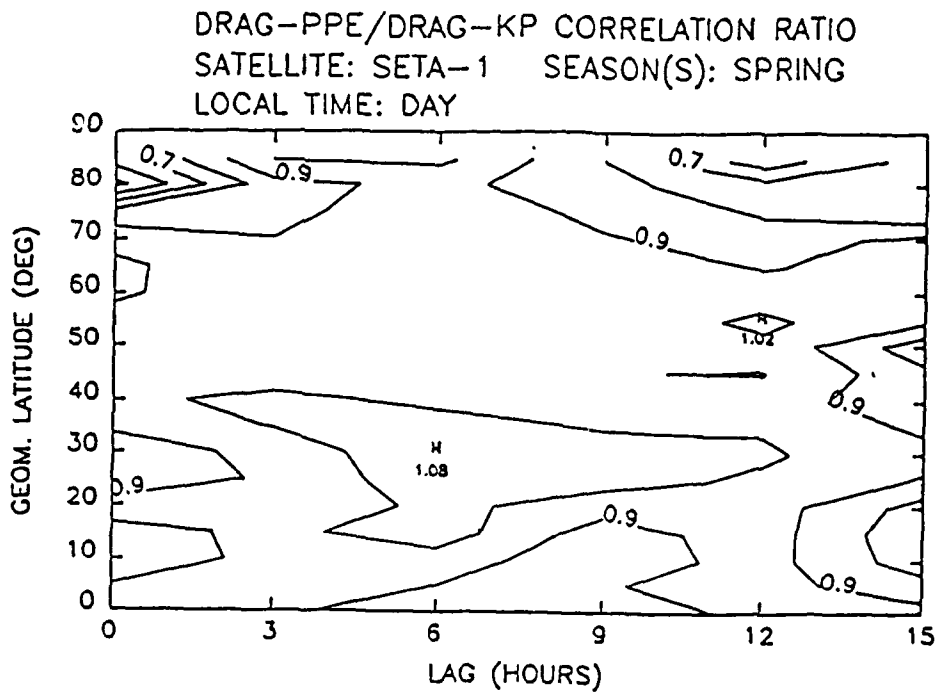
Figure 2.8. Contours of constant daytime drag-PPE/drag-Kp Ccrrelation ratio, SETA-1

DRAG–PPE/DRAG–KP CORRELATION RATIO
SATELLITE: SETA–1   SEASON(S): SPRING
LOC.L TIME: NIGHT
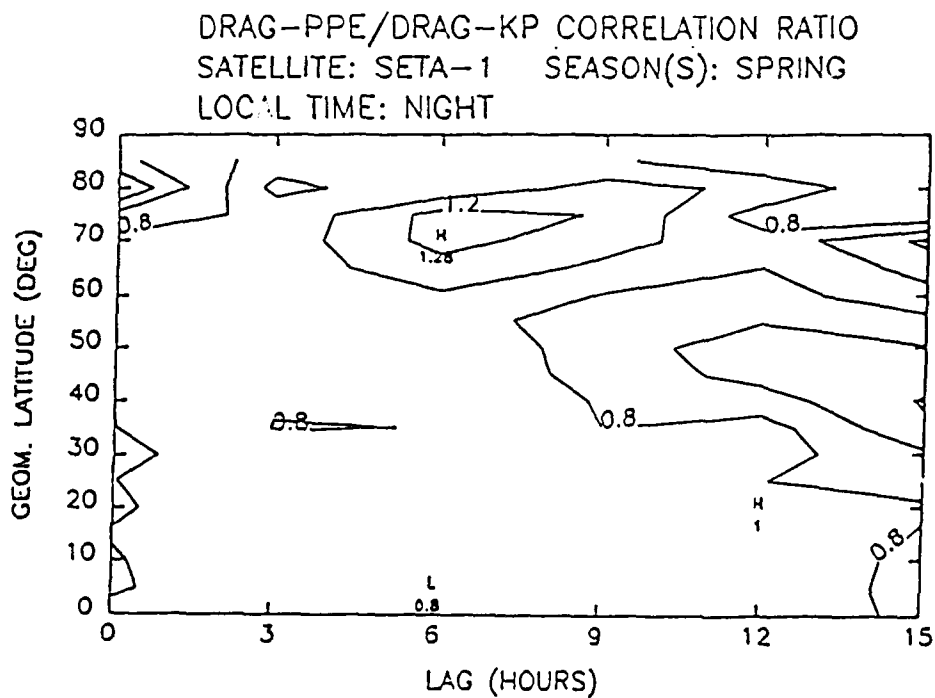
Figure 2.9. Same as Figure 2.8, except night

61

DRAG—POW/DRAG—KP CORRELATION RATIO
SATELLITE: SETA—1   SEASON(S): SPRING
LOCAL TIME: DAY
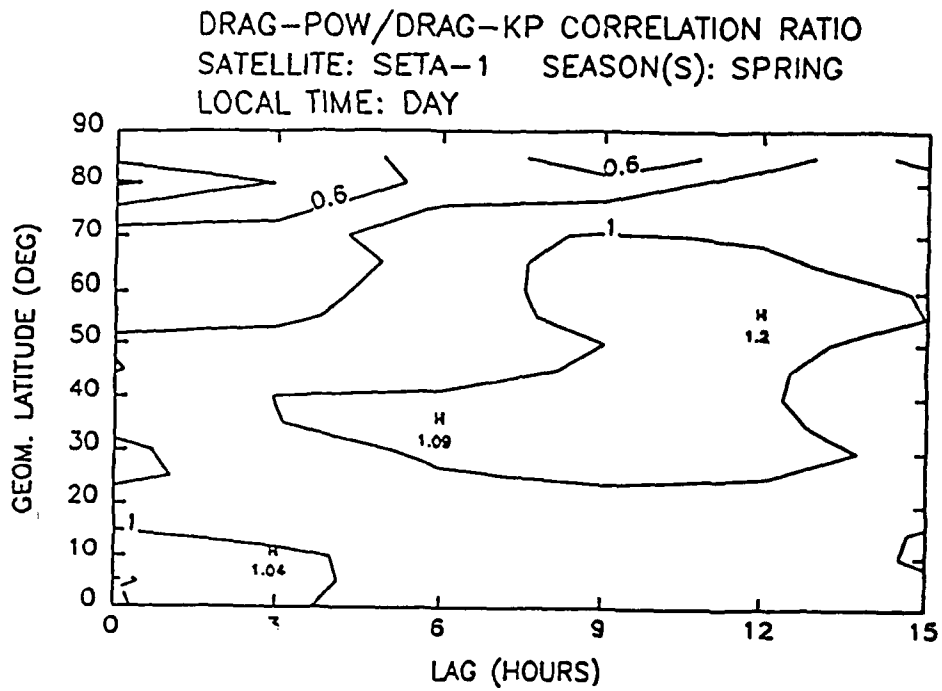
Figure 2.10. Same as Figure 2.8, except POW instead of PPE

DRAG—POW/DRAG—KP CORRELATION RATIO
SATELLITE: SETA—1   SEASON(S): SPRING
LOCAL TIME: NIGHT
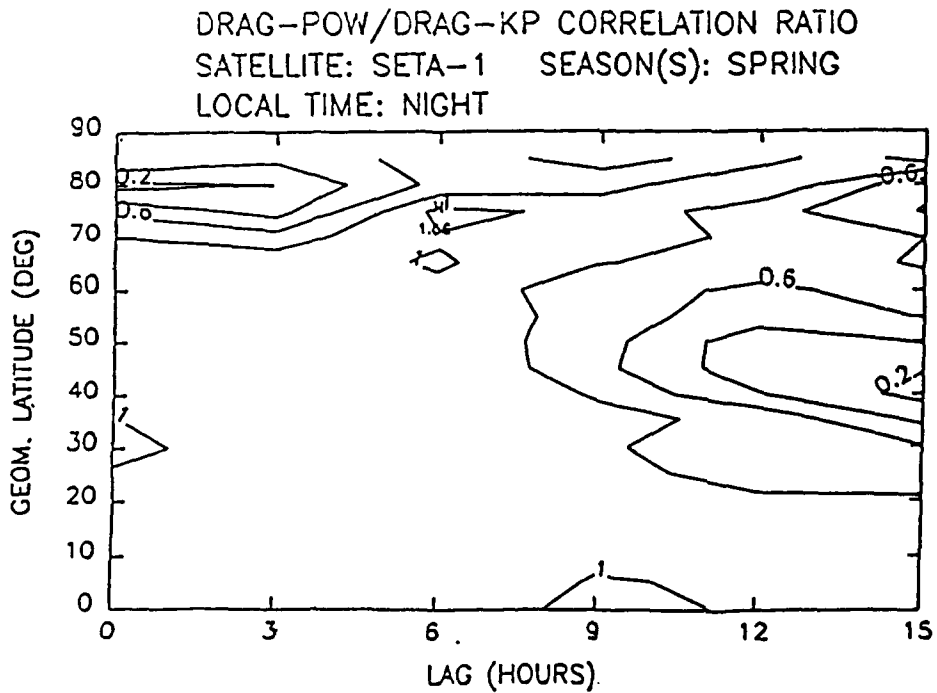
Figure 2.11. Same as Figure 2.10, except night

DRAG—AE /DRAG—KP CORRELATION RATIO
SATELLITE: SETA—1   SEASON(S): SPRING
LOCAL TIME: DAY
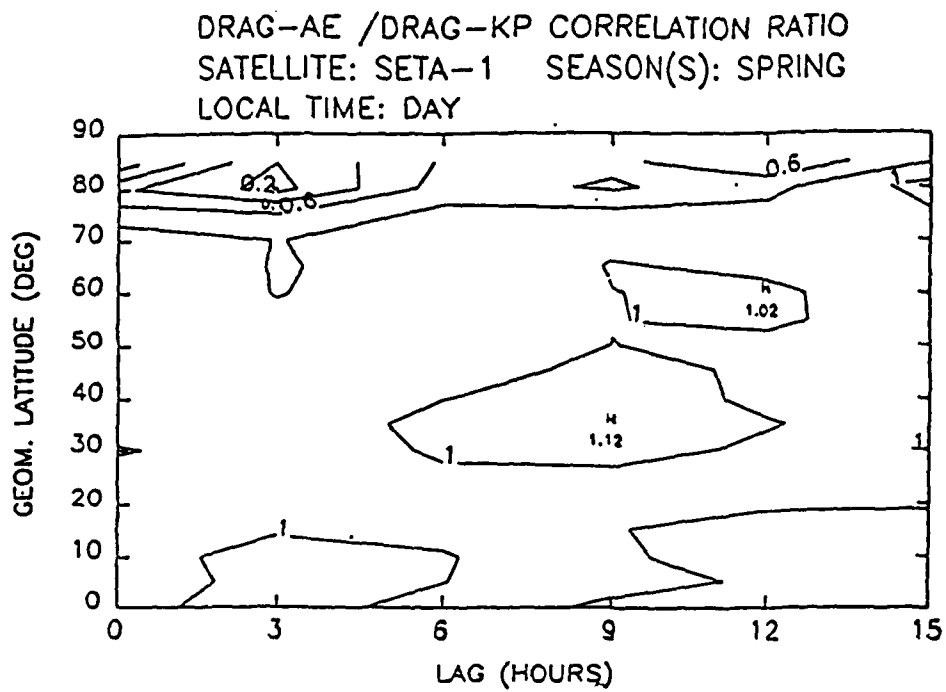
Figure 2.12. Same as Figure 2.8, except AE instead of PPE

DRAG—AE /DRAG—KP CORRELATION RATIO
SATELLITE: SETA—1   SEASON(S): SPRING
LOCAL TIME: NIGHT
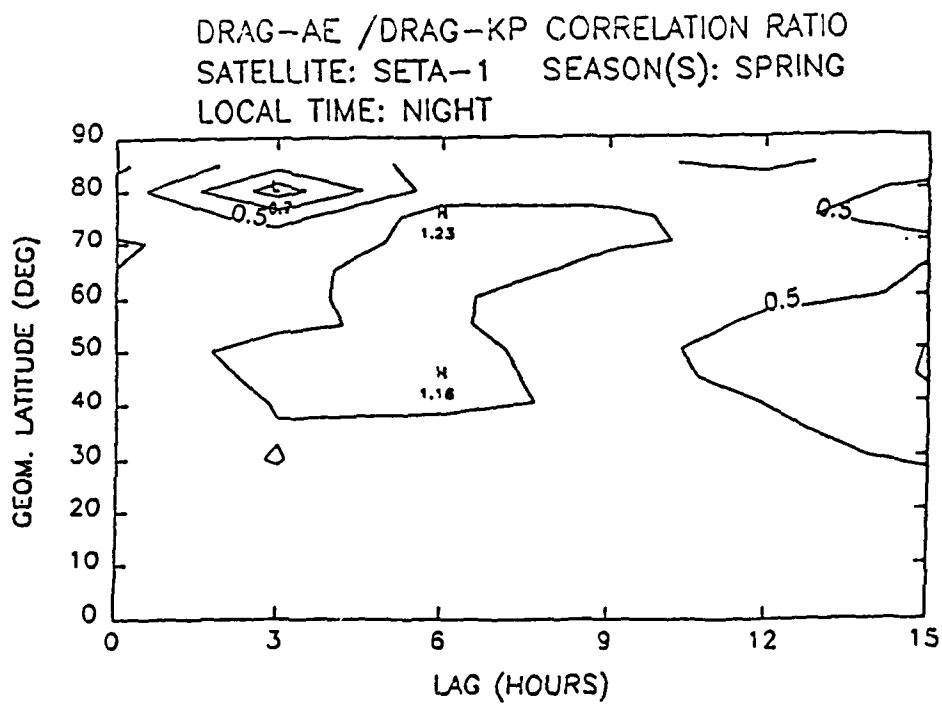
Figure 2.13. Same as Figure 2.12, except night

DRAG— KP CORRELATION COEFFICIENTS
SATELLITE: SETA−2   SEASON(S): ALL
LOCAL TIME: DAY
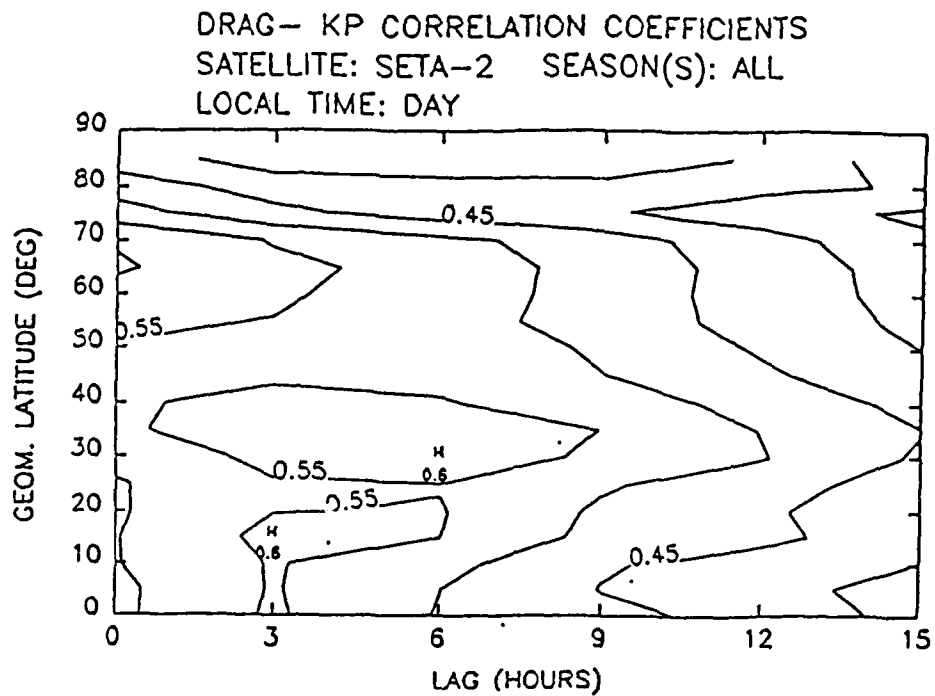
Figure 2.14. Same as Figure 2.6, except SETA-2, all seasons

DRAG— KP CORRELATION COEFFICIENTS
SATELLITE: SETA−2   SEASON(S): ALL
LOCAL TIME: NIGHT
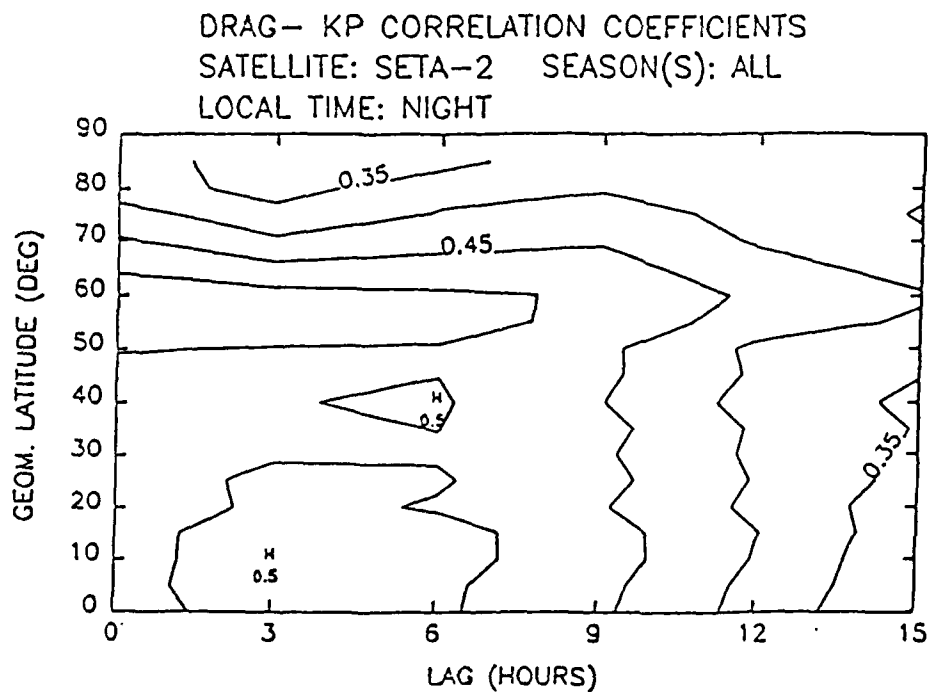
Figure 2.15. Same as Figure 2.14, except night

64

DRAG−PPE/DRAG−KP CORRELATION RATIO
SATELLITE: SETA−2   SEASON(S): ALL
LOCAL TIME: DAY
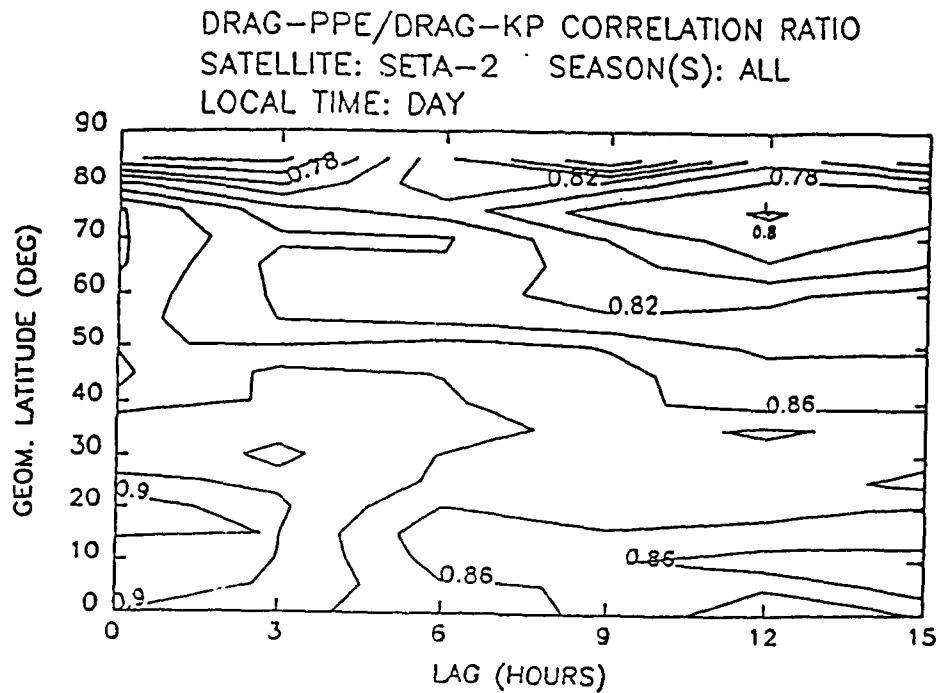
Figure 2.16. Same as Figure 2.8, except SETA-2, all seasons

DRAG−PPE/DRAG−KP CORRELATION RATIO
SATELLITE: SETA−2   SEASON(S): ALL
LOCAL TIME: NIGHT
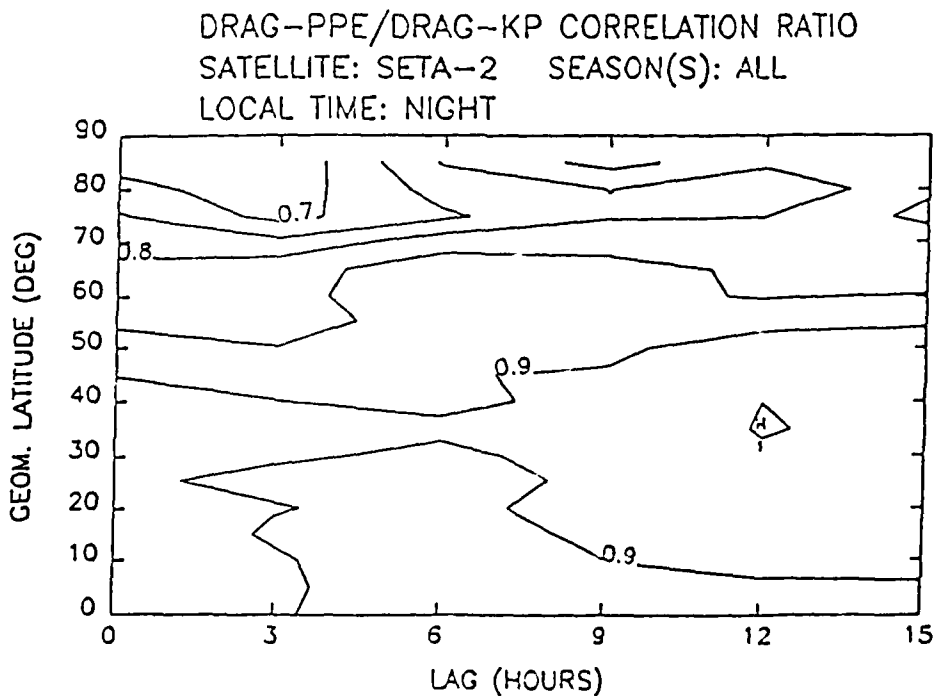
Figure 2.17. Same as Figure 2.16, except night

DRAG—POW/DRAG—KP CORRELATION RATIO
SATELLITE: SETA—2   SEASON(S): ALL
LOCAL TIME: DAY
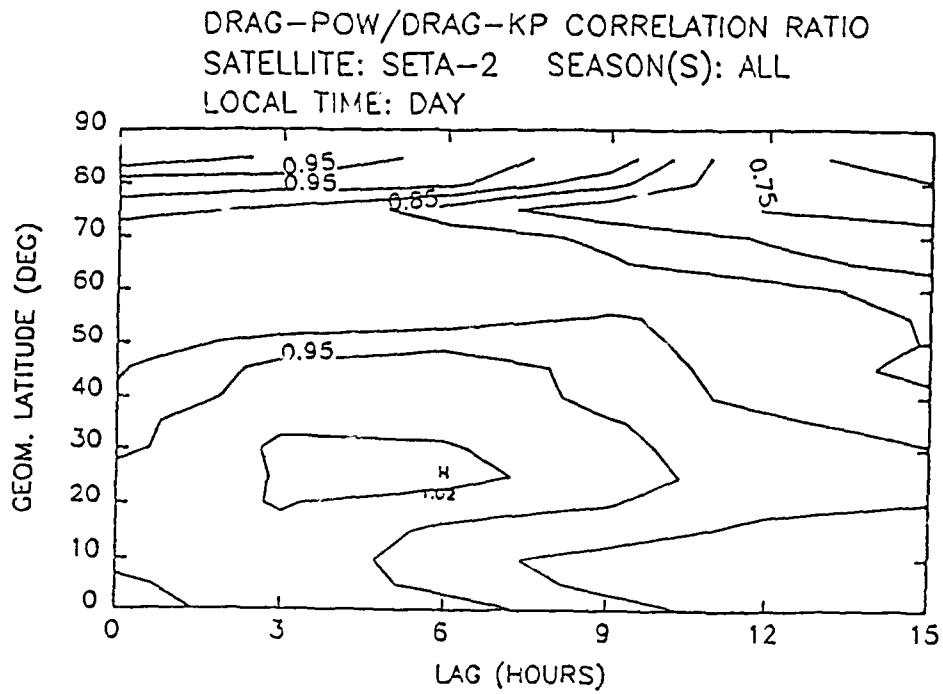
Figure 2.18. Same as Figure 2.10, except SETA-2, all seasons

DRAG—POW/DRAG—KP CORRELATION RATIO
SATELLITE: SETA—2   SEASON(S): ALL
LOCAL TIME: NIGHT
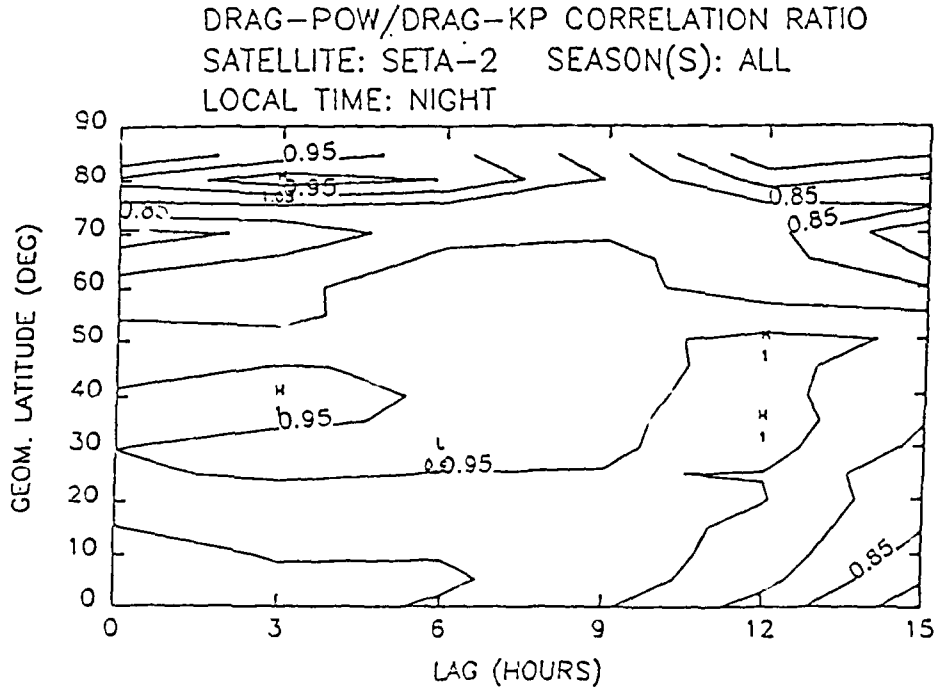
Figure 2.19. Same as Figure 2.18, except night

66

2.1.4 3-D and Color Ratio Plots

In many scientific applications, plots must be constructed from data with more than one independent variable. For example, atmospheric density may be shown as a function of both latitude and time. A Cartesian plot is clearly inadequate for such a presentation, unless a series of strips are drawn at fixed values of one of the variables. Contour plots perform smoothing, and so are unsuitable if the actual data must be presented. In addition, contouring requires a continuous dependence on both dependent variables.

In the atmospheric density example, measurements were taken from a satellite over a series of orbits. Due to variations in conditions such as geomagnetic activity and solar flux, successive passes did not necessarily have a strong correlation. Data was not available over the entire grid, and the gaps needed to be shown. Therefore neither a Cartesian plot nor a contour plot could provide an appropriate presentation.

GraphiC, a C language plotting library distributed by Scientific Endeavors Corporation, was used to create a three-dimensional plotting program (3DSURF) suitable for the presentation of the atmospheric density data. The *GraphiC* package provides a number of mathematical and scientific plotting routines, along with support for a number of different graphics boards and printers. Source code is available for all routines, allowing tailoring to suit a particular problem.

The 3DSURF program constructs a surface from a uniformly-spaced data set. Where data is not present, grid values are set level with the X-Y plane, permitting ready determination of latitude and time correspondence. Peaks and valleys are clearly visible due to the cross-hatch pattern. A number of user-selectable settings, such as axis lengths and extrema, are available for interactive modification, and may be chosen from a menu. The input file is expected in ASCII format, so data may be transferred from mainframes or created on PC's. High quality hard copies may be obtained on a number of printers; support is provided for our Canon laser printers and the HP Laserjet series, as well as a number of other printers.

A typical plot from 3DSURF appears as Figure 2.20, showing atmospheric density data as a function of time and latitude over an eight day period. In order to provide sufficient detail along the time axis, two separate four day passes were required to draw the entire surface. The associated Kp values are indicated along the time axis in the form of a bar graph, created with a separate program and superimposed on the surface plot.

Presentations of this type suffer from several problems not ordinarily encountered in Cartesian plotting. Much of the data remains hidden, and the association with the time and latitude axes is not clear in some regions. The actual ratio values are difficult to determine except for points near the 7 axis, so if precise information is required, it is necessary to rely on tabulated data.

Attempts to improve on this format led to the development of an alternative presentation utilizing the high-resolution color graphics mode of the Enhanced Graphics Adapter (EGA). A two-dimensional grid is created, with time and latitude presented along the axes. Data is provided in "bins" created by averaging groups of points at regular intervals. These averages are scaled to fit a spectrum of fourteen colors, with higher values indicated by bright colors. Each average is shown as a colored block, with gaps in the data indicated by unshaded blocks.

Time and latitude correspondence may be more precisely determined in this format, while the pattern of ratio values is easily seen by observing the flow of color through individual orbits. While the determination of precise ratios is still not possible, approximate values are obtained more easily than from the surface plots by reading the markings along the color "stick." The
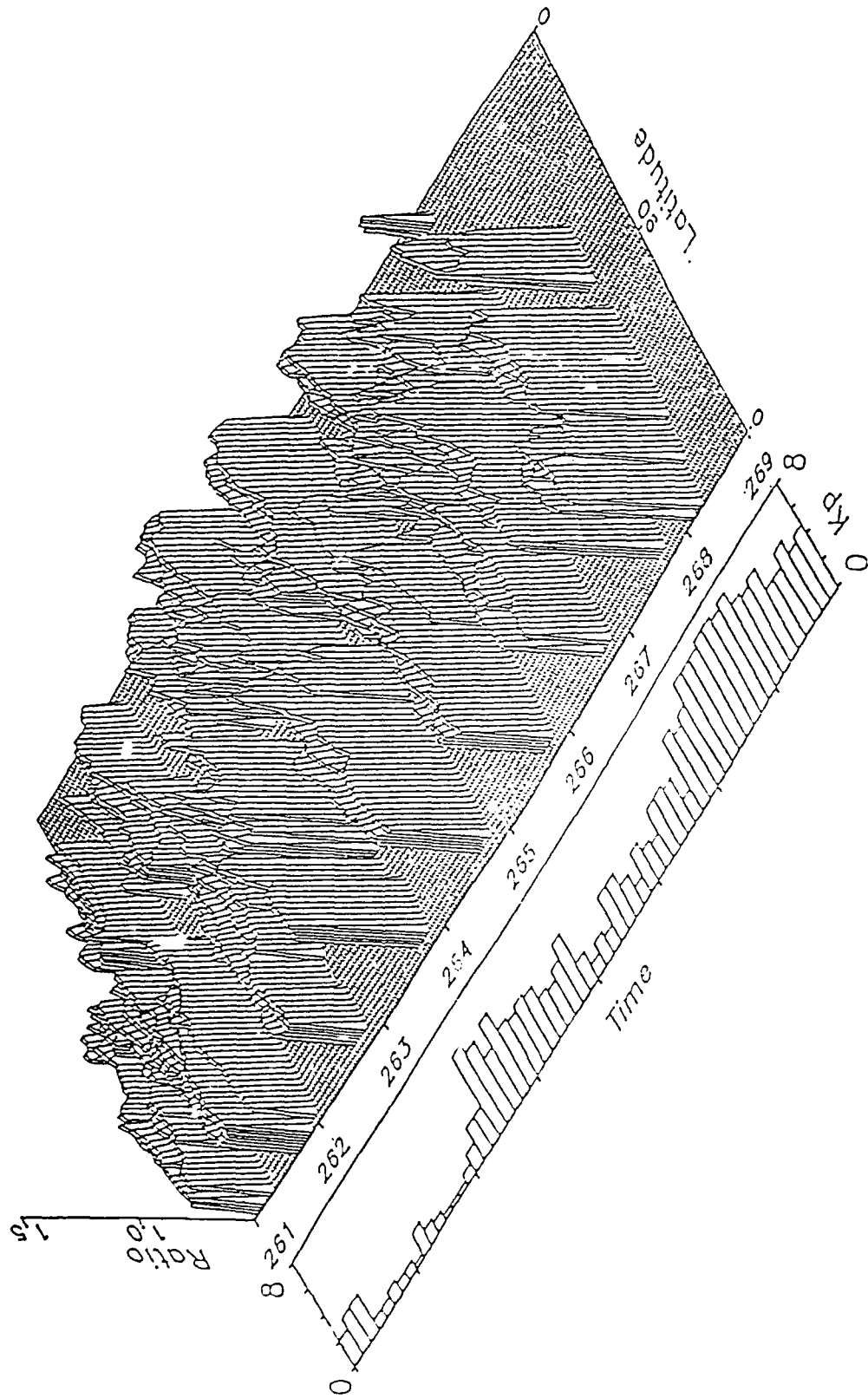
Figure 2.20. Atmospheric density as a function of time and latitude over an eight day period

68

gaps in the data are clearly evident, and there are no cases of hidden or obscured data. As with the surface presentation, Kp values are indicated on a bar graph.

Figure 2.21 shows a typical plot created with this program (reproduced in black and white) using the same data as in Figure 2.20. A hard copy was obtained by using *Pizazz* to dump the graphics screen to a Tektronix 4696 color printer. Transparencies suitable for viewgraphs may also be obtained in this fashion.
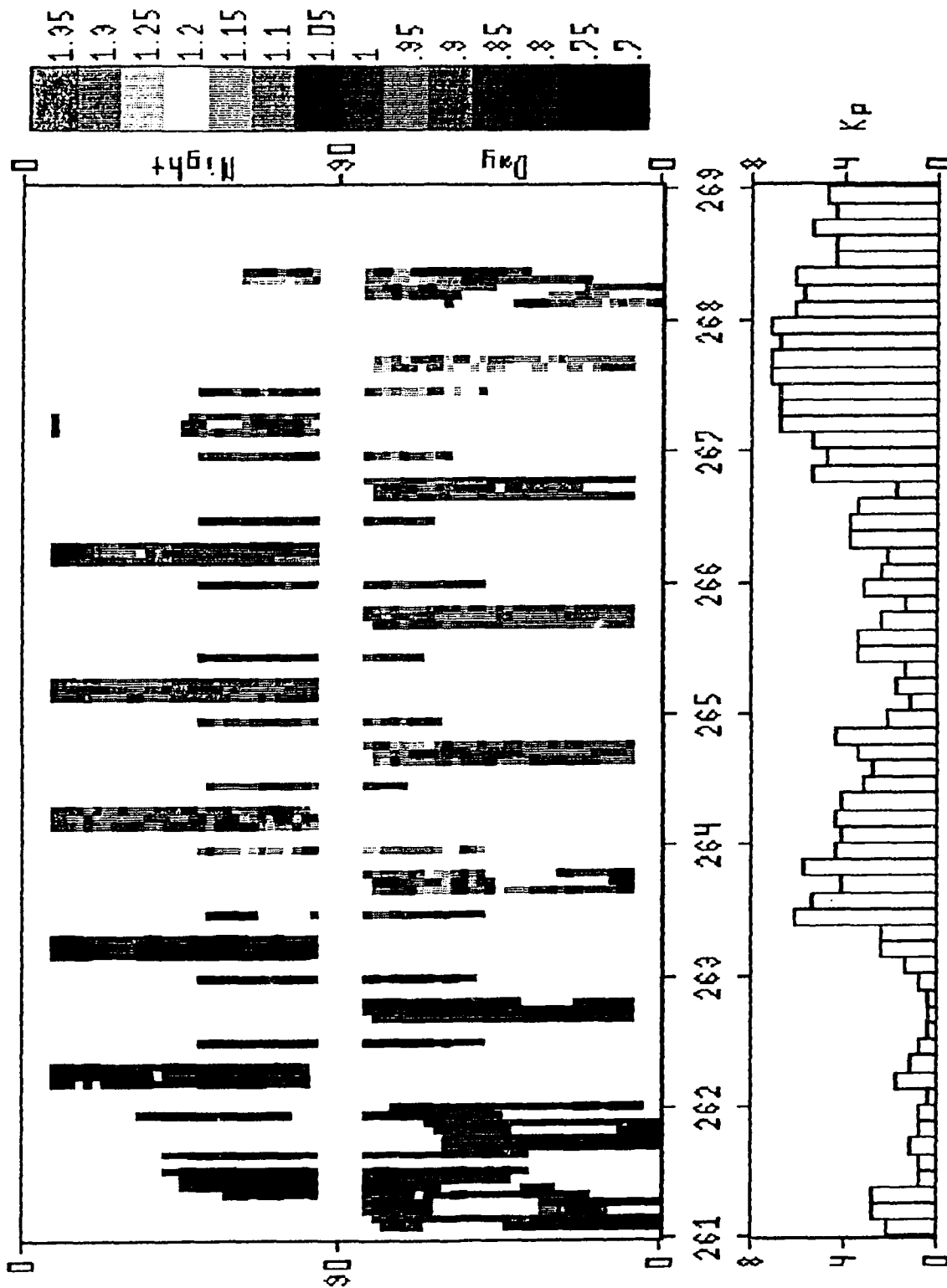
Figure 2.21. Atmospheris density ratio plot using the same data as in Figure 2.20.

(This is a copy of a color plot)

70

2.2 ATMOSPHERIC STRUCTURE

2.2.1 LIDAR Experiment

2.2.1.1 Introduction

A lidar (light detection and ranging) system was implemented in Poker Flat, Alaska to measure relative densities in the upper stratosphere and mesosphere from February to April 1986. The transmitter is a Nd:YAG laser, which outputs a signal at 532 nm wavelength (Green light) and another at 355 nm wavelength (Ultraviolet). Rayleigh scattering of the laser beam at altitudes ranging from 20 km to 100 km has been employed to determine the density of atmospheric molecules. Observations were restricted to night-time due to the high background of scattered sunlight present during the day [Philbrick et al, 1988].

The lidar signal was recorded in 400 channels, each of which corresponds to a 2 μs time duration or about 300 m range. Two data inputs were simultaneously measured. The measurements for the 532 nm wavelength signal were obtained by means of a detector on the 32 cm telescope. The detector is a photomultiplier operating in the photon counting mode. 3 to 5 measurements for the 355 nm wavelength signal were taken for a given night. The other measurements were those for the 532 nm wavelength signal on the 62 cm telescope. The output detector from the 62 cm telescope for the Green light was used to extend the range of measurements.

The Green light signals on the 32 cm telescope are stored in files denoted by Gymmddrr. The Green light signals on the 62 cm telescope are in files denoted by Hymmddrr. Here y stands for year (y=6 for 1986), mm for month, dd for day, and rr for the run number. The ultraviolet signal is stored in files denoted by Uymmddrr.

The data analysis consists of four major steps: summarizing, editing, filtering, and main processing. A description of each of these steps is given by the diagrams in Figure 2.22. The program names are given with the required inputs. The outputs from each program are also shown. The parameter files specified must also be available. For a complete description of these programs, the reader is advised to refer to the manuscript by Bounar et al [May 1988].

2.2.1.2 Summarizing the Data

The raw data for both the low altitude Green light signal (G file) and the high altitude Green light signal (H file) were preedited. This consists of a quick look at the raw data files, checking the quality of the lidar signal. A channel number is then provided to indicate at which point the signal becomes too noisy. Generally, noisy channels are at the end of the altitude range (above 65 km for G files and 85 km for H files).

2.2.1.3 Editing the Data

Editing the data consists of making the necessary corrections to the raw data [Bounar et al., May 1988]. Editing of the G files is done by routines SHIFT and SHFTADD. Editing of the H files is done by EDIT.

2.2.1.3.1 Low Altitude Files

The shutter timing relative to the laser firing was drifting during February and March 1986 measurements. Part of the problem is due to the shutter motor malfunction [Philbrick et al, May

(a)

(b)

(c)

(d)

(e)
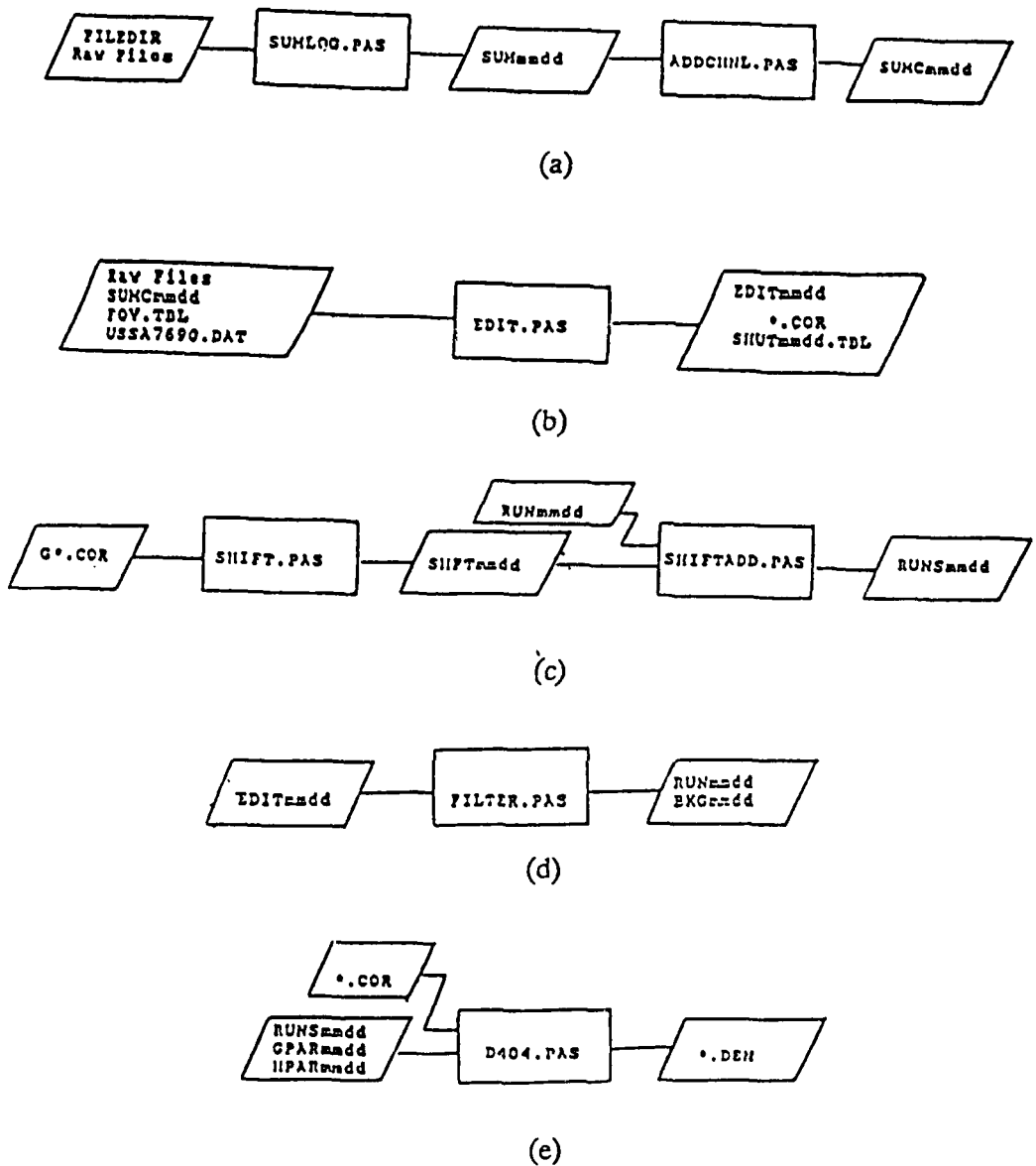
Figure 2.22.   Program flow of lidar processing

(a) summarizing raw files;
(b) editing H files, *.COR files generated;
(c) editing G files and computing shutter shift;
(d) filtering G and H files;
(e) main processing, *.DEN files generated.

1987]. The timing of the laser firing and the shutter opening is critical. The drift in the shutter position was corrected as follows: From the white light shutter functions obtained during day-time measurements, geometrical models for the shutter function were devised for each month. Routine SHIFT is based on a piecewise smoothing, which uses a cubic polynomial fit. It computes the shift of the shutter function of a particular G file from the model shutter function. The shift value is in fractions of a channel. In general, the shutter drifts by about ± 3 channels of 2 μs duration each. The other routine SHIFTADD adds the shift value to a file containing pertinent information on all the files in a given day of measurements.

2.2.1.3.2 High Altitude Files

Three corrections are applied to the H files by routine EDIT. The deadtime correction is first applied on the raw data. The deadtime correction is based solely on the photon count rate in a 2μs bin.

Next, the field of view correction is applied. For proper operation, the centers of the laser beam and the field of view of the receiver must coincide. Prior to April 14, 1986, there was a mismatch in the centers. To apply the field of view correction, one must compute the field of view overlap, which is a two dimensional Gaussian integral over a circular region whose displacement from the center of the Gaussian depends on altitude. The field of view correction factor was tabulated for periods when this problem prevailed; namely, high altitude measurements prior to 14 April 1986.

The last correction of the H files is the shutter correction. The shutter for the high altitude measurements is phase-locked to the shutter for low altitude measurements. At times there is a synchronization loss between the two shutters which lasts a few seconds. Prior to April 14, 1986, the sync-loss reoccurred frequently. For measurements up to this date, a shutter correction was applied.

The shutter correction applied to the high altitude data measurements is based on the Gaussian shape of the second partial derivative of a signal, which is given by the ratio of the photon counts times the altitudinal range to the US Standard Atmospheric (USSA76) model. The Gaussian curve is completely defined by its center and half-width. The best estimates of these two parameters are those for which the Chi-squared value is minimum. Using these parameters, the correction factor is obtained from the normalized integral of the Gaussian curve, and is applied to the data to be corrected.

2.2.1.4 Filtering the Data

Filtering is done by a routine called FILTER. Filtering the data consists of accumulating all information possible on the background scatter on a given night of measurements. The background counts are obtained from 400 channels at the beginning of each raw file, prior to the collection of the lidar signal. Smoothing using Hanning window coefficients is then applied to the background counts. G or H files with too high background values introduce a high noise level making it impossible to extract the lidar signal. Such files are flagged, and will not be processed.

The smoothed curves represented the mean values for the background. Standard deviations were also computed for the smoothed curves. A 4σ-line, four standard deviations above the mean curve, was constructed. Each of the non-smoothed background values are then compared to the

73

4σ-curve. If the background values exceed the 4σ-curve, the corresponding data file will be flagged. Background flags are an indication of the presence of large background noise pulses in the data.

2.2.1.5 Final Processing

Altitude profiles of atmospheric density are retrieved from the lidar data as

$$\rho(z_i) = A \cdot (N_c(i) - N_B) \cdot z_i^2$$

where $N_c(i)$ is the photon count at the ith channel, corrected for a photon counter deadtime of 9 ns; N_B is the background noise photon count; and z_i is the altitude at the ith channel in km. Here A is a normalizing constant which equals the ratio of the area under the calibration density curve to the area under the density curve being calculated. These areas are obtained over a range of 2 to 5 km. The calibration range for the G files is generally between 30 and 32 km. The range for the H files is generally between 40 and 45 km. The G density profiles are tied onto the rawinsonde files obtained from rocket measurements on the same date. The H density profiles are tied onto the corresponding G density profiles already processed. In order to show the deviations of the density profile from the USSA76 model, the final curves are a ratio of the measured density to the USSA76 model.

The final processing routine is called D404. The input files consist of a file containing statistics and other pertinent information on all files obtained in one day of measurements, and the parameter files for processing the G and H files. A parameter file contains information about the site altitude, the channel number after which the data becomes useful, and the channel number at which the laser was fired. It also contains the file name for the USSA76 model, the file name for the shutter function to be used, and the calibration file name.

Once the density ratios are processed, they are smoothed using the Hanning window described above. The smoothing interval must be changed as a function of altitude depending on the count level. The number of points being smoothed varies from 1 to 9 according to the number of the photon counts in each 2 µs bin. A sample of the processed low altitude Green light G6021432.DEN file collected on 14 February 1986 is shown in Table 2.6. The raw and smoothed density, and its ratio to the USSA76 model is given for different altitudes. The altitude increments are 300 m. For this particular file, the density drops to about 30 or 50% below the USSA76 model. In Table 2.6, the standard deviation and the signal to noise ratio are also provided. The parameter NF is the length of the Hanning window, which was used to obtain the filtered density.

2.2.1.6 Other Processing

The processing of over 2000 low and high altitude Green light files was done using the processing routines described above. The Ultraviolet wave density profiles were also obtained and compared to the those of the low altitude Green light obtained at the same time. On a given night, there were about 3 to 5 ultraviolet density profiles. Density profiles of other files were also generated using the same processing scheme that was used in processing individual files. These other files are a combination of several individual files. To improve the signal to noise ratio and to reduce the variance of the lidar signal, individual files were combined hourly and also daily to produce mean density ratio profiles.

To compare the performance of the lidar measurements with concurrent measurements, the individual files were combined to match the time span during which measurements, such as the

Table 2.6.   Sample of G6021432.DEN with the raw and smoothed density, its ratio to the USSA76 model. The standard deviation and the signal to noise are also provided.

G6021432.DEN   860214   0815 UTC   VERSION 4.00   OCTOBER 1987
SHUTTER FILE   S6021301.FIT   MODEL FILE USSA7690.DAT   FILTER LEVEL 2
CALIBRATION FILE R021490.DAT   CALIBRATION ALTITUDES 28.0 KM TO 30.0 KM
SITE ALTITUDE 0.393 KM   ELEVATION ANGLE 90.0   DEADTIME 25.0 NSEC
BACKGROUND 0.39   ENERGY 1057.86   MAX. CHANNEL 299

#	ALTITUDE KM	RAW DENSITY	FILTERED DENSITY	RATIO TO MODEL	SIGMA	NF	TEMP K	S/N RATIO
63	35.019	6.470E-003	6.533E-003	0.77416	0.01023	2	-999.9	48.8
64	35.319	6.176E-003	6.162E-003	0.76478	0.01049	2	-999.9	47.8
65	35.619	5.844E-003	5.798E-003	0.75350	0.01078	2	-999.9	46.6
66	35.919	5.370E-003	5.460E-003	0.74299	0.01111	2	-999.9	44.8
67	36.219	5.086E-003	5.176E-003	0.73735	0.01137	2	-999.9	43.7
68	36.518	5.076E-003	4.925E-003	0.73427	0.01159	2	-999.9	43.7
69	36.818	4.591E-003	4.676E-003	0.72947	0.01192	2	-999.9	41.7
70	37.118	4.396E-003	4.411E-003	0.72002	0.01225	2	-999.9	40.8
71	37.418	4.240E-003	4.157E-003	0.70992	0.01261	2	-999.9	40.1
72	37.718	3.773E-003	3.924E-003	0.70096	0.01300	2	-999.9	37.9
73	38.017	3.823E-003	3.690E-003	0.68930	0.01336	2	-999.9	38.1
74	38.317	3.410E-003	3.470E-003	0.67792	0.01383	2	-999.9	36.0
75	38.617	3.197E-003	3.273E-003	0.66843	0.01426	2	-999.9	34.8
76	38.917	3.175E-003	3.111E-003	0.66423	0.01460	2	-999.9	34.6
77	39.217	2.912E-003	2.982E-003	0.66536	0.01496	2	-999.9	33.1
78	39.516	2.900E-003	2.828E-003	0.65940	0.01332	3	-999.9	32.9
79	39.816	2.713E-003	2.675E-003	0.65176	0.01378	3	-999.9	31.8
80	40.116	2.420E-003	2.539E-003	0.64630	0.01425	3	-999.9	29.9
81	40.416	2.356E-003	2.431E-003	0.64628	0.01460	3	-999.9	29.4
82	40.716	2.379E-003	2.341E-003	0.64987	0.01486	3	-999.9	29.4
83	41.015	2.358E-003	2.245E-003	0.65095	0.01524	3	-999.9	29.0
84	41.315	2.131E-003	2.124E-003	0.64303	0.01586	3	-999.9	27.4
85	41.615	1.961E-003	1.991E-003	0.62912	0.01661	3	-999.9	26.1
86	41.915	1.776E-003	1.877E-003	0.61927	0.01725	3	-999.9	24.7
87	42.215	1.749E-003	1.797E-003	0.61847	0.01765	3	-999.9	24.3
88	42.514	1.807E-003	1.730E-003	0.62154	0.01799	3	-999.9	24.5
89	42.814	1.720E-003	1.633E-003	0.61206	0.01532	5	-999.9	23.8
90	43.114	1.544E-003	1.549E-003	0.60576	0.01591	5	-999.9	22.4
91	43.414	1.406E-003	1.466E-003	0.59784	0.01653	5	-999.9	21.2
92	43.714	1.317E-003	1.383E-003	0.58814	0.01714	5	-999.9	20.4
93	44.013	1.274E-003	1.305E-003	0.57857	0.01773	5	-999.9	19.9
94	44.313	1.312E-003	1.236E-003	0.57144	0.01832	5	-999.9	20.0
95	44.613	1.164E-003	1.177E-003	0.56722	0.01892	5	-999.9	18.8
96	44.913	1.026E-003	1.124E-003	0.56496	0.01950	5	-999.9	17.5
97	45.213	1.053E-003	1.076E-003	0.56361	0.02003	5	-999.9	17.6
98	45.512	1.102E-003	1.032E-003	0.56316	0.02055	5	-999.9	17.9
99	45.812	9.666E-004	9.922E-004	0.56410	0.02107	5	-999.9	16.6
100	46.112	9.477E-004	9.553E-004	0.56581	0.02162	5	-999.9	16.4
101	46.412	9.065E-004	9.196E-004	0.56736	0.02220	5	-999.9	15.9
102	46.711	8.676E-004	8.843E-004	0.56827	0.02280	5	-999.9	15.4
103	47.011	8.972E-004	8.503E-004	0.56898	0.02342	5	-999.9	15.6
104	47.311	8.121E-004	8.188E-004	0.57050	0.02406	5	-999.9	14.8
105	47.611	6.945E-004	7.924E-004	0.57331	0.02136	7	-999.9	13.6
106	47.911	8.482E-004	7.643E-004	0.57398	0.02188	7	-999.9	14.9
107	48.210	7.045E-004	7.375E-004	0.57492	0.02240	7	-999.9	13.5
108	48.510	7.016E-004	7.111E-004	0.57541	0.02293	7	-999.9	13.4
109	48.810	6.867E-004	6.842E-004	0.57463	0.02349	7	-999.9	13.1
110	49.110	6.792E-004	6.557E-004	0.57164	0.02413	7	-999.9	13.0
111	49.410	5.983E-004	6.252E-004	0.56576	0.02489	7	-999.9	12.1
112	49.709	6.713E-004	5.926E-004	0.55654	0.02583	7	-999.9	12.8
113	50.009	5.632E-004	5.590E-004	0.54494	0.02695	7	-999.9	11.6

meteorological rocket measurements, were conducted. The density profiles of these combined files were obtained using the processing scheme described above. The density profiles were then compared to those obtained from the rocket measurements.

2.2.2 Analysis and Processing of Falling Sphere Data

Data from ten falling sphere experiments conducted over a number of years had been processed and analyzed previously in order to obtain atmospheric density and winds [Radex Final Reports, 1983, 1986]. A revised effort was undertaken to incorporate improved processing techniques as they had evolved from the previous efforts, and to include some new considerations:

a) Greatly reduced smoothing as part of the processing, in order to retain more information about atmospheric structure and turbulence.

b) Re-examination of pertinent concurrent meteorological data that were available, including Robin sphere, radar and chemical release data, to achieve improved tie-down.

Because absence of spin modulation as well as long damping time-constants characterized the sensing of accelerations along the spin axis, use of Z-sensor data proved unreliable and were dispensed with in the new analyses. Further, for altitudes below the start of upleg data, where analytical computation of in-track wind was not possible, rather than assuming a zero in-track wind, the approach adopted was to fix the in-track wind as obtained from tie-down met-data. Complete AC06 processing was carried out for the first time. Major factors involved in the new effort are outlined below:

1) Uniform analysis procedures were applied on all flights, with emphasis on obtaining greater fine scale structure, viz. uniform 0.1 km spacing comparable to the maximum vertical travel in one half spin. Overall, the new results concur with our original work, but greater atmospheric structural resolution is provided.

2) Since tie-down considerations introduced overriding constraints, no rework of calibrations based on in-flight uncaging resonance analysis procedures was performed.

3) Sphere axis tilts were established so as to match results from the analyses of concurrent met-rocket or radar data in the 60-65 km range, as available from the investigator.

4) Wind analysis was conducted without use of Z-sensor data.

5) Unwanted instrument beat frequencies are evident in the sensor signals. This problem was circumvented previously by using rather heavy ($\pm$1 km window) smoothing, since turbulence profiles were of less interest. In the new effort $\pm$0.1 km windowing was used, and spline approaches were evaluated to implement an optimum signal-to-noise trade-off. Though the resonance signals were somewhat alleviated, they were never satisfactorily eliminated.

6) An AC15 smoothing study made showed that density and temperature profile solution are not significantly altered if greater noise is allowed through the initial processing, i.e. noisy results may be smoothed subsequently. Thus, the problem of distinguishing between turbulence and remaining resonance features was left to the investigator.

7) Except for the higher spatial resolution, tabulations and plots were conveyed in previously established formats.

Table 2.7 shows sphere spin and some related parameters that were applied to each of the flights. Figures 2.23 thru 2.25b show typical density, temperature, and wind profiles for AC13. In Figure 2.23, which shows density ratio, solid lines show the new results, which retain greater structural detail, but sometimes at the expense of unwanted resonances. The dashed lines show the relatively smoothed results from our earlier processing. The relative density profiles remain similar, but the overall levels differ due to the low altitude tie-down constraint in the latter study.

Comparative plots of density ratio from the present and the original work were prepared for reference. A comparison of the finally adopted spin parameter values showed little change from the original axis orientation and spin estimates. Results of the analyses for all ten rocket sphere files were conveyed on floppy disk. Detailed results and support files conveyed included print-outs and corresponding summary plots of density, density ratio, winds, and temperature solutions.

The following items were conveyed to the researcher, either on floppy files with hard copy, or as laser plots:

a) Tabulation of files containing all the data that were generated in our analyses, performed at 100 meter increments.

b) Summary density, temperature, and wind profiles at 1 km increments.

c) An experiment data file containing all the updated resource data, except tie-down information, that were used for each rocket sphere analysis.

d) Files containing the data and Richardson Number that were used for the results plots.

e) Laser plots at standard scales were produced using these files. These plots were restricted to 140 km on the top side, since results in the top 10 km of most flights tended to be noisy. Similarly, for AC17, AC08 and AC18, where the peak altitude reached was below 140 km, plotted results in the top 10 km are questionable.

Table 2.7   <u>Parameters for Comprehensive Analysis of Falling Sphere Data</u>

Flight Date Time Spin Characteristics Altitude Analysis Breaks Downleg Upleg Top	Range Tie-Down Data	Campaign
AC06 18MAY77 1343Z Spin axis tilt = 11.0 Spin rate 5.643200 RPS Spin-down Phase Model .040 x (85-Alt)² 55 90 150 Km	KMR	
AC10 26FEB79 1628Z Spin axis tilt = 13.5 Spin rate 5.922188 RPS Spin-down Phase Model .050 x (90-Alt)² 55 90 150 Km	RED LAKE	ECLIPSE 79
AC12 16NOV80 0447Z Spin axis tilt = 6.0 Spin rate 6.253840 RPS Spin-down Phase Model .060 x (85-Alt)² 50 85 150 Km Tie-down: chemical release and Robin sphere	ESRANGE	EBC SALVO B
AC13 01DEC80 0009Z Spin axis tilt = 15.0 Spin rate 5.932616 RPS Spin-down Phase Model .045 x (85-Alt)² 55 85 150 Km Tie-down: Robin sphere	ESRANGE	EBC SALVO A2
AC14 07MAR81 0838Z Spin axis tilt = 13.0 Spin rate 5.564330 RPS Spin-down Phase Model .051 x (85-Alt)² 58 75 150 Km Tie-down: MST radar data	PFRR	AURORAL E

Flight Date Time Spin Characteristics Altitude Analysis Breaks Downleg Upleg Top	Range Tie-Down Data	Campaign
AC15 29JUN82 1101Z Spin axis tilt = 25.0 Spin rate 6.111438 RPS Spin-down Phase Model .095 x (85-Alt)² 65 75 145 Km Tie-down: Robin sphere wind & density	WALLOPS	TRACER
AC16 04AUG82 0016Z Spin axis tilt = 7.0 Spin rate 6.419824 RPS Spin-down Phase Model .060 x (85-Alt)² 55 75 150 Km	ESRANGE	CAMP
AC17 16JUN83 0651Z Spin axis tilt = 6.0 Spin rate 4.250335 RPS Spin-down Phase Model .060 x (85-Alt)² 55 75 130 Km Tie-down: radar data from 15th & 17th.	PFRR	STATE
AC08 31JAN84 1853Z Spin axis tilt = 24.0 Spin rate 5.552080 RPS Spin-down Phase Model .092 x (80-Alt)² 66 66 110 Km Tie-down: Robin sphere	ANDOYA	MAPWINE
AC18 10FEB84 0305Z Spin axis tilt = 20.5 Spin rate 4.459859 RPS Spin-down Phase Model .060 x (80-Alt)² 66 66 110 Km Tie-down: Robin sphere	ANDOYA	MAPWINE

78

AC13   01DEC80   0009Z   ESRANGE
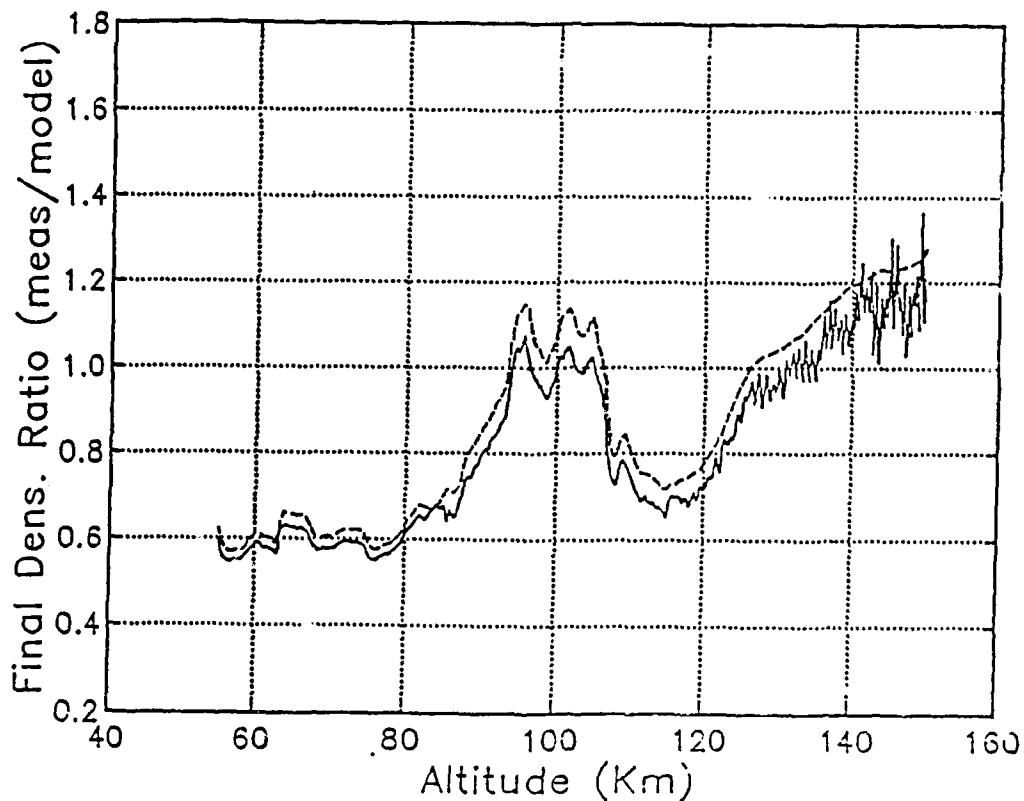
Figure 2.23. Density ratio vs. altitude (km) for AC13

AC13   01DEC80   0009Z   ESRANGE
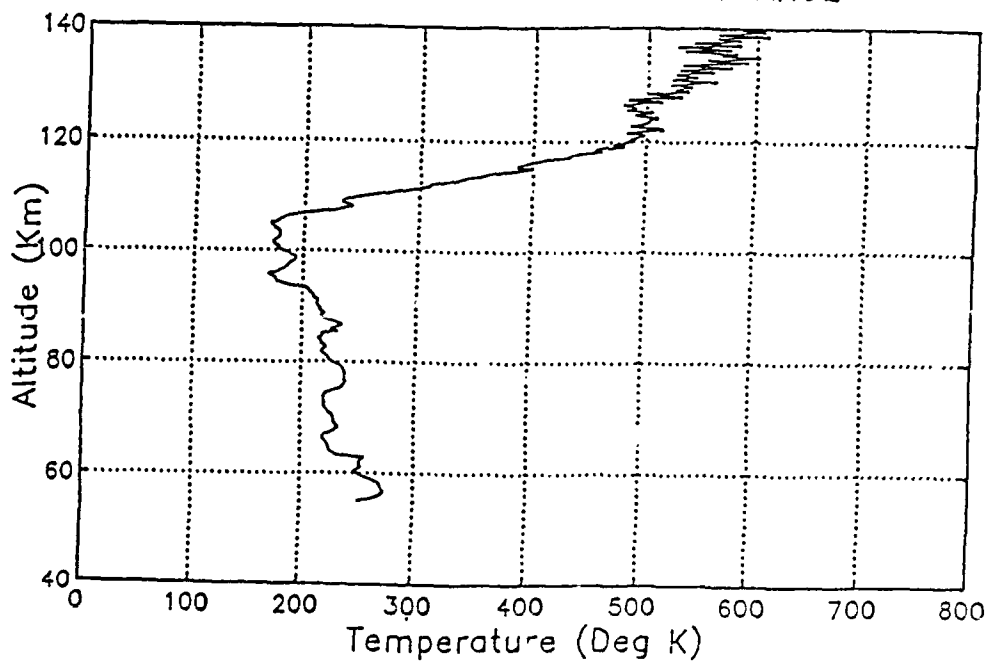
Figure 2.24. Temperature profile for AC13

AC13 01DEC80 0009Z ESRANG⁻
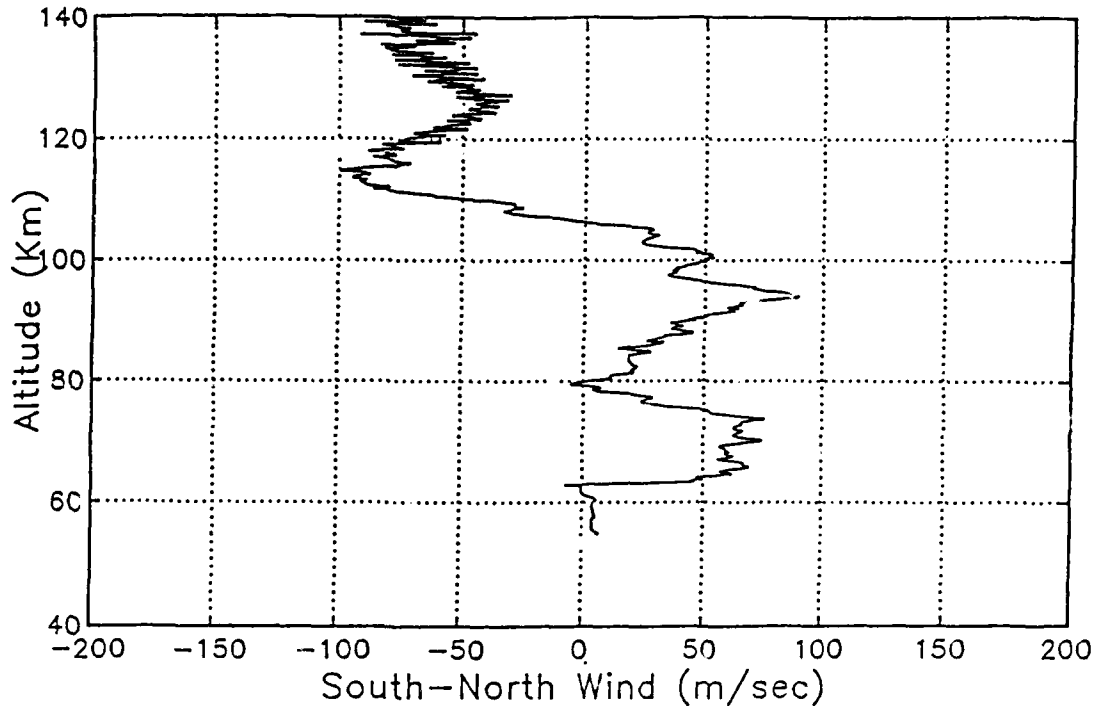
Figure 2.25a. Wind profile for AC13 (south-north)

AC13 01DEC8C 0009Z ESRANGE
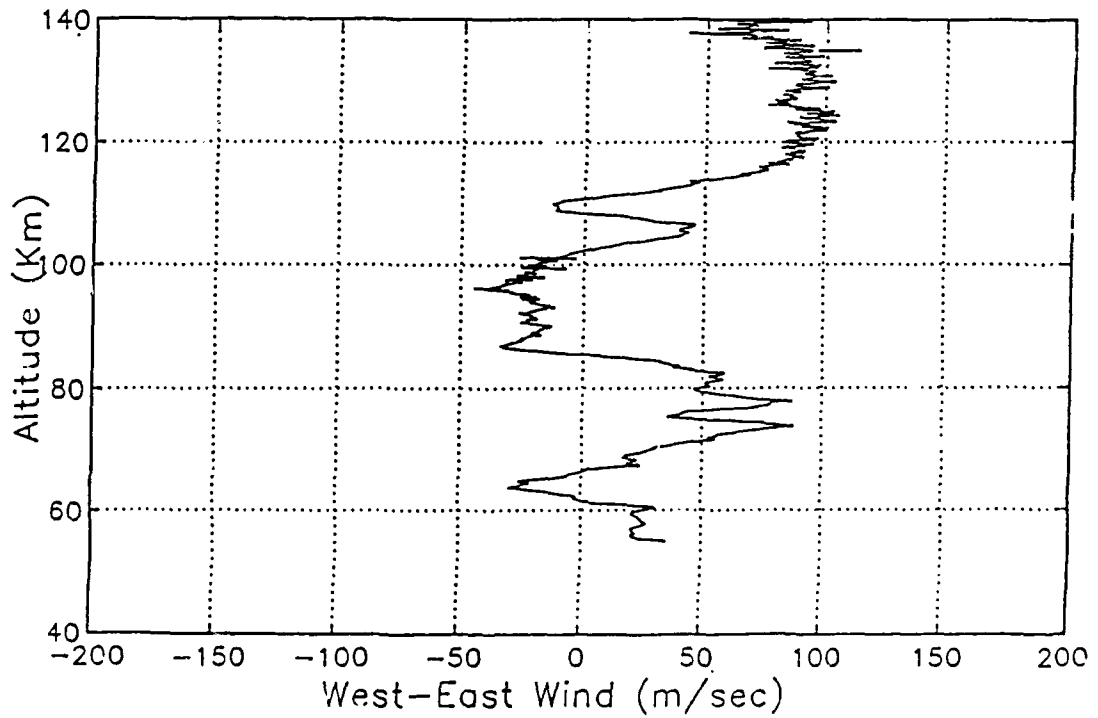
Figure 2.25b. Wind profile for AC13 (west-east)

2.2.3 Vertical Correlation using Falling Sphere Data

A vertical density autocorrelation study was performed using the density profiles obtained from analyses of falling sphere data, as described in the previous section, viz. AC06, AC08, AC10, AC12, AC13, AC14, AC15, AC16, AC17, AC18. Figure 2.26a shows AC16 profiles of ratio to USSA76 and to MSIS86. Note that MSIS86 provides no densities below 85 km, and each MSIS model in this range was obtained by requiring continuity using the USSA76 model. Unavoidably, the highest 10 km of each falling sphere flight had poor geometry for reliable calculation of the winds and profiles, so data above 140 km were disregarded. For AC17 profiles above 120 km, and for AC08, AC18 profiles above 100 km are similarly unreliable. Since this leaves little of value, the latter two flights were disregarded in this study. The autocorrelation calculations were performed on density ratios for distances up to 60 km, with the proviso that at least 25 km of overlap still remained available.

The density ratio profiles have varying average trends or slopes and, in Figure 2.26a, it is seen that this can include a model dependence, with the ratios crossing-over rapidly around 95 km, because of the significantly different scale heights of the USSA76 and MSIS86 models. In fact, this indicates that in some cases model dependence may affect short distance correlations. To the extent that these variations are due to incorrect models, some type of model de-trending may be in order.

For the conditions of the AC16 experiment, Figure 2.26b shows the uncertainty beyond 40 km as the autocorrelation plots for the two ratios diverge. However, even on this limited set cf flights, model cross-overs occur in both directions, and no attempt was made to determine any altitude dependence. The basis for forcing this slope to be zero or some other value is not clear, and eventually no de-trending was performed.

Figure 2.27 presents correlation results for all USSA76 ratio profiles (except AC06 which was unavailable originally) in one plot. As expected, these show the positive correlation at closer distances, within about 20 km of any measurement. A subsequent negative correlation which reaches below -0.75 around 40 km is often found, suggesting a vertical half-wave length of 30-40 km.
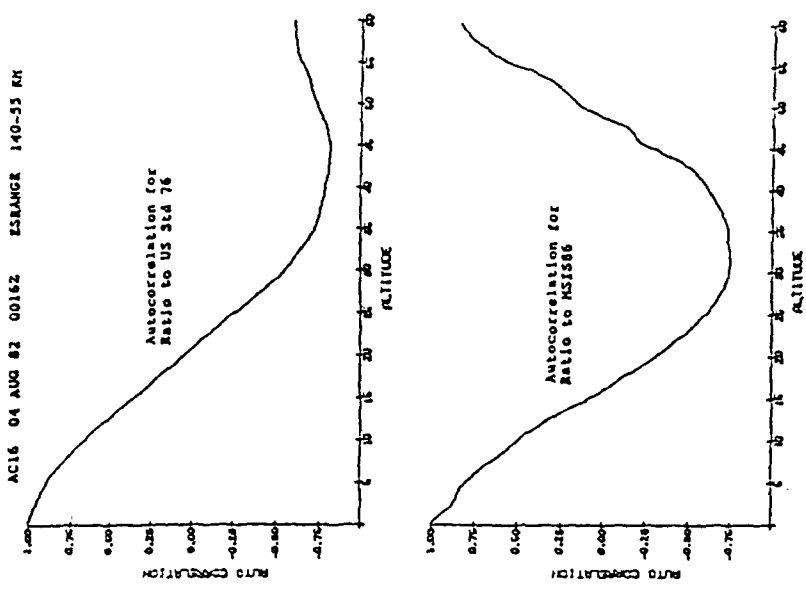
Figure 2.26b. Vertical autocorrelation of density ratio for the two profiles in the adjoining figure
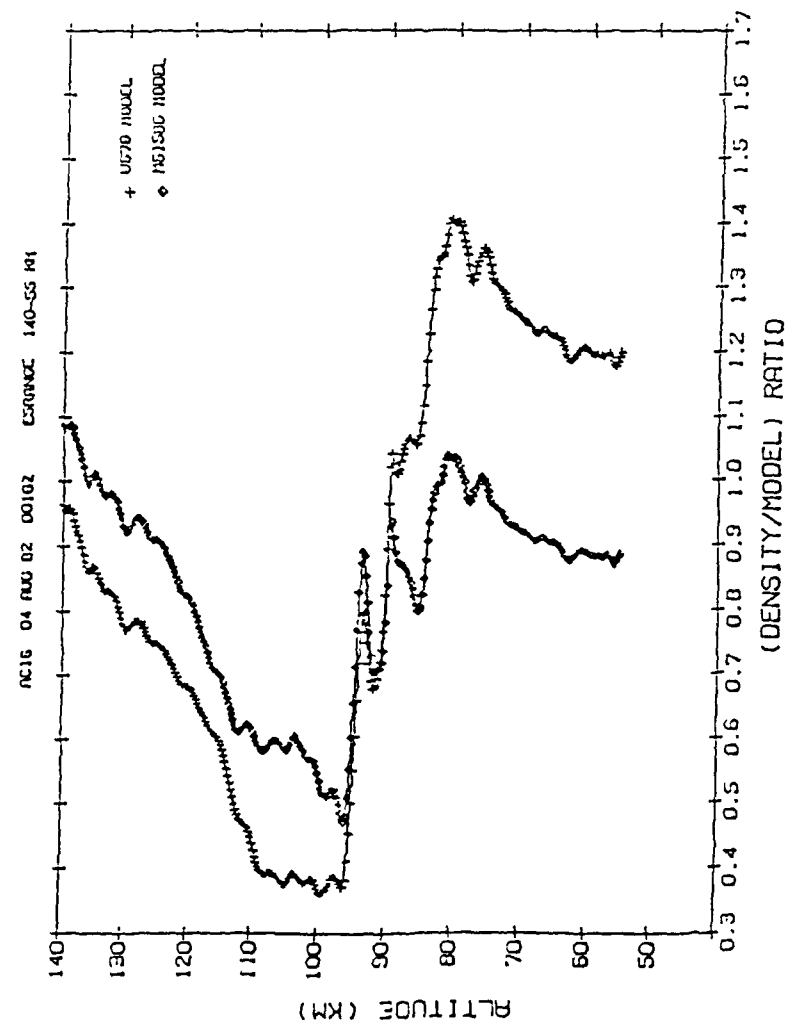
Figure 2.26a. Profiles of density ratio to US Std 76 and MSIS86 from falling sphere analysis

COMBINED AUTOCORRELATION PLOTS
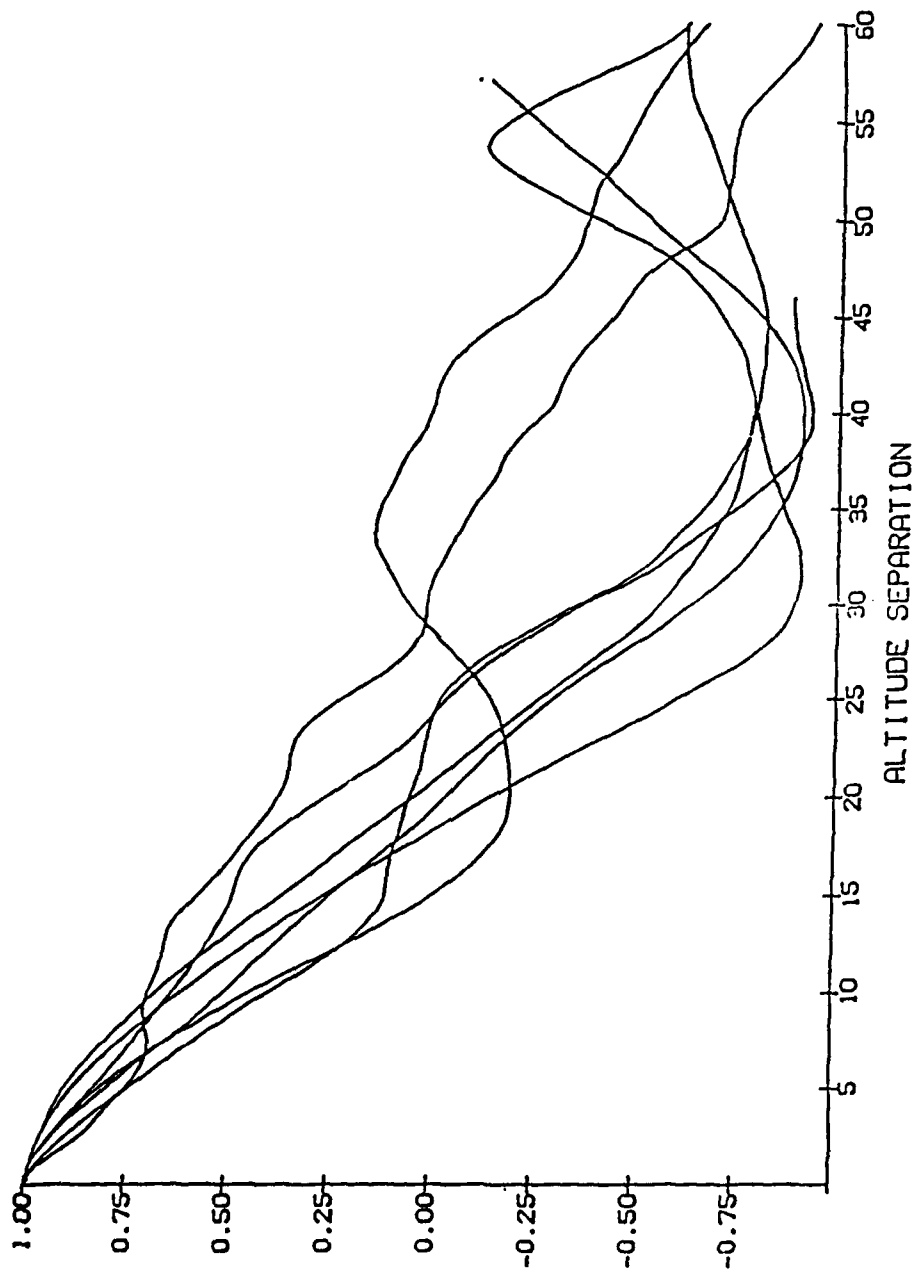
Figure 2.27. Combined plot for autocorrelations for profiles of density ratio to US Std 76

References

Bounar K., et al., Private Communication, May 1988.

Bramson. A.S., and Slowey, J.W., Some Recent Innovations in Atmospheric Density Programs, Technical Report No AFCRL-TR-74-0370, Air Force Cambridge Research Laboratories, Hanscom AFB, MA, 1974.   AD786414

Bhavnani, K.H., and McInerney, R.E., SUATEK Interactive Graphics User's Guide, Air Force Geophysics Laboratory/LCY, Hanscom AFB, MA, 1988.

Bass, J.N., Bhavnani, K.H., Bonito, N.A., Bryant, C.M., Jr, McNeil, W.J., Roberts, F.R., Sannerud, D.A., and Kantor, A.J., "Integrated Systems with Applications to the Multi-Phases of the Ephemerides, Physics, and Mathematics of the Upper Atmosphere", AFGL-TR-87-0064, February 1987.   ADA185748

Brunk, H.D., An Introduction to Mathematical Statistics, Xerox College Publishing, Lexington, MA/Toronto, 1975.

Cameron, J.M., "Chapter 2. Statistics", in Fundamental Formulas of Physics, Vol 1, Menzel, D.H., ed., Dover Publications, Inc., New York, 1960.

COESA (U.S. Committee on Extension to the Standard Atmosphere), "U.S. Standard Atmosphere, 1976", U.S. Government Printing Office, Washington, D.C., 1976.

Cole, A.E., and Kantor, A.J., "Air Force Reference Atmosphere", AFGL-TR-78-0051, ADA058505, 1978.

Evans, D.E., "Physics and Observations of High Latitude Energy Deposition", Pp 179-191 in Proceedings of a Workshop on Satellite Drag, Space Environment Services Center, Space Environment Laboratory, Boulder, CO, 1982.

Forbes, J.M., Temperatures, pressures, and densities in the 80-120 km region, in "Thermospheric Structure Variations During High Solar and Magnetic Activity Conditions", Final Report, AFGL-TR-86-0009, Pp 18-53, 1987.   ADA171350

Groves, G., "A Global Reference Atmosphere from 18 to 80 Km", AFGL-TR-85-0129, 1985. ADA1624⁹

Groves, G., "Modeling of Atmospheric Structure, 70-130 Km", AFGL-TR-87-0226, 1987. ADA201077

Hedin, A.E., A revised thermospheric model based on mass spectrometer and incoherent scatter data: MSIS-83, "J Geophys Res 88", No A12, Pp 10,170-10,188, 1983.

Hedin, A.E., MSIS-86 thermospheric model, "J Geophys Res 92", No A5, Pp 4649-4662, 1987.

International Business Machines, Corporation, System/360 Scientific Subroutine Package Version III Programmers's Manual, White Plains, NY, 1968.

Jacchia, L.G., "Revised Static Models of the Thermosphere and Exosphere with Empirical Temperature Profiles", Smithsonian Astrophysical Observatory Special Report No 332, Cambridge, MA, 1971.

References (cont'd)

Jacchia, L.G., "Thermospheric Temperature, Density, and Composition: New Models", Smithsonian Astrophysical Observatory Special Report No 375, 1977.

Logicon, Inc., Analysis and Research for Integrated Systems in Physics of the Upper Atmosphere, Final Report, AFGL-TR-77-0265, Air Force Geophysics Laboratory, Hanscom AFB, MA, 1977. ADA051126

Marcos, F.A., McInerney, R.E., and Fioretti, R.W., Variability of the Lower Thermosphere Determined from Satellite Accelerometer Data, Technical Report No AFGL-TR-78-0134, Air Force Geophysics Laboratory, Hanscom AFB, 1978. ADA058982

Marcos, F.A., "Requirements for Improved Thermospheric Neutral Density Models", Paper No AAS 85-312, AAS/AIAA Astrodynamics Specialist Conference, AAS Publications, San Diego, CA, 1985.

Philbrick, C. R., et al., Private Communication, May 1987.

Radex, Inc. Final Report, "Analysis of Spacecraft Charging, Particle Beams and Geophysical Data Bases", AFGL-TR-83-0140, July 19983, ADA138632.

Radex, Inc. Final Report, "Analysis of Geophysical Data Bases and Models for Spacecraft Interactions", AFGL-TR-86-0221, October 1986, ADA184809.

Research Systems, Inc., IDL User's Guide, Denver, CO, 1987.

3. INVESTIGATION OF SPACECRAFT INTERACTIONS

The charging of spacecraft and/or spacecraft surfaces by energetic electrons has been observed at geosynchronous orbits (GEO) and Medium ($\approx$1000 km) altitudes with the GL satellites SCATHA and DMSP. It has been predicted that auroral electrons can cause large objects to charge in low Earth orbit (LEO). In addition, high spacecraft potentials can be produced by the effect of unneutralized particle emitters.

The reliable estimation of the charging effects on present and future space vehicles has been a concern of the Air Force and NASA for several years, and a subject of considerable R&D activity. The inclusion of all factors that are significant for spacecraft charging presents a formidable problem. Complex three dimensional geometries with diverse surface materials and internal electrical properties have to be taken into account. The surface-plasma interactions which involve secondary emission, backscattering, photoemission and charge transport must be considered in detail. The magnetospheric environment may include solar, magnetic field, substorm and space charge effects. Charging dynamics can exist due to varying photoemission over a rotating or eclipsing satellite, changing plasma conditions, active control by electron or ion beams, and switching of electrically connected satellite configurations.

GL is perhaps the leading investigator of spacecraft charging, and is involved in theory, experiment, and modeling. Briefly, GL experiments include the SCATHA satellite, intended specifically to study charging at GEO; the DMSP satellites which have observed auroral charging at medium altitude.

3.1 SPACECRAFT CHARGING

GL has placed a strong emphasis on accurate modeling of charging phenomema, and has contracted for the production of two sophisticated models, first NASCAP [Katz et al., R-79; Stannard et al., R-82; Katz et al., R-83] and then POLAR [Cooke et al., R-83; Lilley et al., R-86] both written by S-Cubed. The NASCAP program represents an attempt to faithfully simulate and depict spacecraft charging at GEO by numerically solving the full three dimensional problem.

The POLAR code extends the analysis to lower earth and near polar orbits, where the higher density plasmas that are encountered requires the consideration and treatment of more complicated processes. The numerical procedures must solve, in a mutually consistent way, the Poisson-Vlasov system of non-linear coupled equations, as depicted in Figure 3.1.
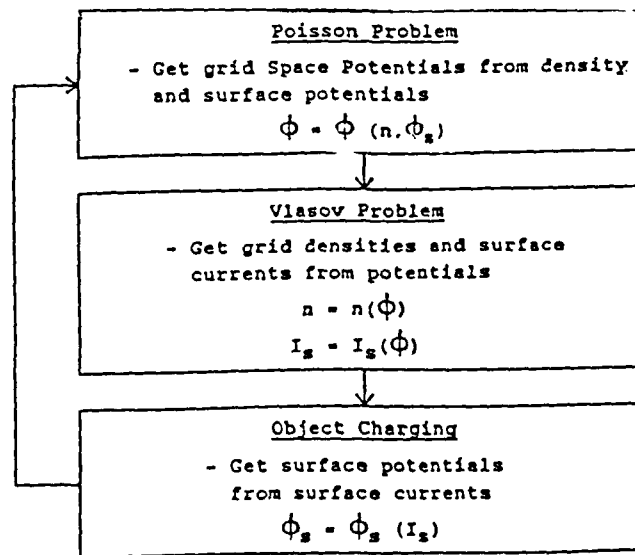
Figure 3.1. Flow Chart for Poisson-Vlasov Iterations

POLAR is a fully self-consistent three dimensional Poisson-Vlasov code, that provides quasi-steady state solutions by iterating between a finite element potential (Poisson) and a density (Vlasov) solution. A versatile set of building elements can be combined to form complex objects with a variety of surface material and electrical connections. A surface charging module, based on a circuit model analogy, can be added to the iteration to provide the spacecraft charging response to both natural and induced charge drivers. The grid space potentials in POLAR are obtained by the conjugate gradient method. Particle densities are calculated by a method that divides space into sheath and non-sheath regions separated by a sharp sheath edge. External to the sheath regions, densities are determined by geometric ray tracing with first order electric field corrections. This approach has been shown to correctly predict wake formation about the Space Shuttle Orbiter [Katz et.al., 1987]. Internal to the sheath, POLAR uses outside-in tracking of ions and/or electrons to obtain densities and currents. The electrical charging circuit model is solved by the ICCG method. The progress of new space missions in these orbits, such as the space shuttle and the space based radar, signals that the charging of large space structures is of concern. The POLAR code is designed to simulate and investigate these conditions.

The NASCAP program was first installed at GL in 1978. NASCAP is still being maintained and used, but GL is now focusing on POLAR and other supportive models such as MACH [Tautz & Cooke, TR. 1988] (which is described in Section 3.1.3). POLAR was installed at GL in 1983, and is now the object of an extensive validation effort. The true centers of effort in the validation process are S-Cubed, and GL/PHK.

3.1.1 System Implementation and Operation at GL

In 1984 a Ridge 32C computer was aquired by PHK for dedicated POLAR and MACH running. In 1986 an IRIS 3030 workstation was obtained for 3D color graphics display of modeling results. In 1988, a second Ridge computer (3200) was acquired with faster CPU speed (approximately a factor of four) and 600 Megabytes of storage to increase our ability to model large simulations. Since all three of these machines are self-contained mini-computers, most of the system management tasks fall to the user. System implementation support for the Ridge 32C, Ridge 3200 and the IRIS 3030 includes:

a) a working knowledge of UNIX operating systems (Bourne and C shells)

b) administration of system setup and account files;
    archiving results files on cartridge tape

c) monitoring disk usage and doing periodic compactions of the hard disk

d) interfacing with Ridge and IRIS personnel regarding system problems and
    hardware breakdowns.

e) overviewing the operation of the QMS laser printer;
    setting up various font options and providing for Tektronix output.

f) setting up port connections for terminal and modem use and providing
    for transport of files to and from the VAX-780 for printing or QMS output.

g) Setting up ethernet connections to the three computers.

Operational support for running POLAR and MACH on the RIDGE requires:

a) creating job input files for start and continue runs

b) configuring and modifying spatial objects and their charging properties

c) interpreting intermediate and final results to determine further runs
    or changes

d) execution of auxiliary codes e.g. TEKPLOT (2D contour plotter) for
    graphical display

The option of remote operation on a supercomputer has also been explored. The MACH code has been brought up and run on the Weapons Lab Cray 2. The access to the Cray was done through a Telnet connection. Output and plot files were shipped back to GL via telnet for detailed analysis. This operation enabled us to obtain a speed increase of approximately 30 over the Ridge 32C with, however, limited access time and difficulties with the remote connections.

3.1.2 Three Dimensional Color Display of Modeling Data

After the IRIS 3030 Workstation was aquired by PHK, we developed a program called IRMA (for IRis MAnipulater) to provide three-dimension color display of modeling results. Such a program is indispensible, not only to present results, but also to comprehend complex 3D distributions which are difficult to understand using only 2D projections. The IRMA program is comprised of both FORTRAN and C coding. Assembly language wrapper routines provide entry point interfaces for FORTRAN-C calls. The program uses the multiple windowing capability (MEX) to manage up to 10 windows which display viewports, graphics parameter lists, text port messages, and clipping plane locations.

The input files to IRMA can be of two types, surface polygons or grid node data. The surface polygon input can be used to draw complex geometrical objects e.g., the Space Shuttle. The node data specifies scalar functions of physical variables such as potentials or densities. The IRMA program is driven interactively by pop-up menus which are under mouse control. Practically all of the IRIS graphics library options are available to the user by means of a slider bar interface which enables one to pick out and adjust parameters using the curser. There are modules for controlling the observers viewpoint, for formatting the screen, and for building and managing 2D contour surfaces imbedded in three dimensions. There are many display options including slicing the data to produce color coded contour maps, stripping contour sufaces to give more transparent views of multiple surfaces and depth-cueing effects. IRMA is compatible with both the MACH and POLAR and is being used to display solutions obtained from these codes. In addition IRMA can read files written by the SOCRATES code [Elgin et al., in publication] to display the neutral particle number density distributions representing the shuttle plume.

An important aim of the SOCRATES program is to accurately depict the radiation distributions around the space shuttle, as measured at an arbitrary viewing point. To this end we have added an option to IRMA to calculate integrated column densities for an observer at any given location

and with a specified viewing window. This option will be refined to enable line of sight radiation intensities to be computed, thus providing a direct link between contamination results obtained by SOCRATES and experimental data.

3.1.3 Research and Analysis with POLAR and MACH

As part of the effort involved in the verification of the POLAR code, we have developed an independent computer code, called MACH, designed to validate the physical and numerical methods of POLAR. The methodology of MACH (Mesothermal Auroral Charging) is somewhat closer to first principles than POLAR. MACH solves the same Vlasov-Poisson equations as POLAR but under different conditions. The most important difference is that no assumption about the sheath edge is made; the sheath and wake are determined as self-consistent solutions to the Vlasov-Poisson equations. However, the geometry of MACH is restricted to two dimensions, precluding detailed application to real spacecraft. The MACH program is an adaptation of TDWAKE [Parker, CR-144159]. Figure 3.2 gives a brief comparison of MACH and POLAR.

The MACH program was first brought up on the CYBER-750 and then ported to the RIDGE and converted from Fortran 5 to Fortran 77. A considerable development effort has been put into MACH in order to make it an effective analysis tool. The most recent changes are:

a) development of the VSTS (velocity space topology search) algorithm
for calculating particle densities

b) extension of the charging algorithm to enable the case of positively
charged objects to be treated

c) modification of the outer grid boundary conditions to enable the
code to handle plasma chamber simulations

MACH has passed a variety of Laplacian and Poisson (non-zero plasma density) tests and shows agreement with simple analytic models. The largest modification of the MACH code was the implementation of the VSTS procedure, which constituted a complete rewrite of the Vlasov algorithm. This procedure is described below.

In the inside-out method each point in the velocity space integral for obtaining density must be generated by calculating a particle trajectory, which can become computationally prohibitive. The original TDWAKE Vlasov algorithm was abandoned, as it did not provide adequate efficiency and resolution for many of our needs. The new method is called Velocity Space Topology Search (VSTS). The central idea here is to adjust track generation to the topology of the distribution function (as obtained from previous tracks) in velocity space at each grid point (R,Z) instead of following any preset pattern. To facilitate the computation of the density quadrature, a transformation is made from velocity components to energy and angles (polar and azimuth). The analysis is then carried out in the angle space corresponding to each energy value in the quadrature sum. The topology of the angle space is inspected and regions needing better resolution are identified. On the next pass, the angle space is bisected in the identified regions and the process is repeated. The procedure stops when no further tracks are required to resolve the region, as determined by a significance test for each angle space point. Figure 3.3 shows how the VSTS analysis fits into the density quadrature loops. The basic VSTS method as

89

	MACH	POLAR
Dimensions	2D axially symmetric	3D
Objects	simple geometries	complex geometries
Surface charging	fixed	solution by ICCG
Potential solver	SOR	conjugate gradient
Sheath edge	no assumption	sharp division between sheath and presheath
Density solver	inside-out tracking	outside-in tracking from sheath edge

Figure 3.2. Comparison between MACH and POLAR

Energy loop

VSTS loop

Angle space loop

Track all significant points

Do angle space quadrature sums

Bisect angle space

Evaluate significance of all points

Reduce angle space frame

no — Exit test

yes

Do energy quadrature sums

Finish
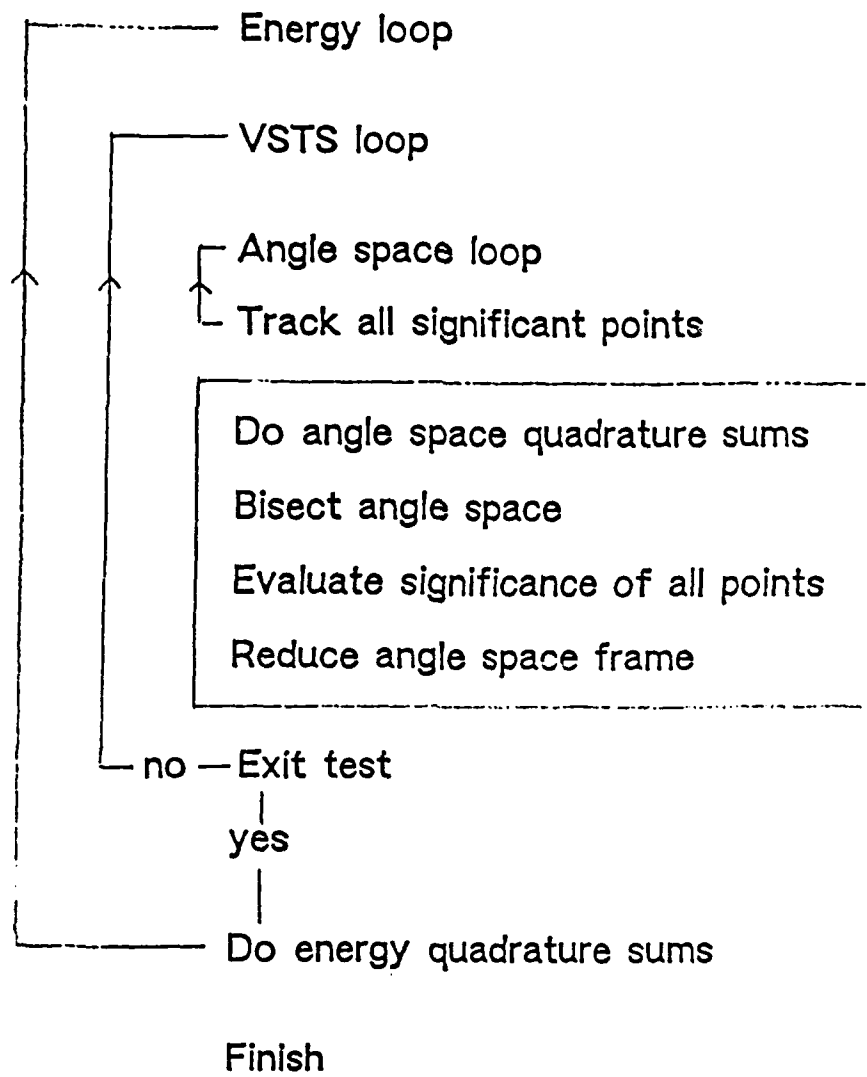
Figure 3.3. Flow chart for VSTS algorithm

91

described above has been tested on many cases. For the default energy quadrature setting (6 intervals) the method generates on the order of a thousand trajectories, which can be compared to the ~ 200,000 tracks which would be needed for equivalent resolution (~1 degree) with uniform velocity space gridding. The procedure works for both ions and electrons. The only parameters that need to be changed to go from ions to electrons are the Mach number and the sign of the potentials (so that the particle tracker sees a reversed electric field). Higher order velocity space moments, for ob.. .ning fluxes and temperatures, are calculated by including suitable factors in the quadrature integrand.

To compute models of the spacecraft interaction, we have specialized the spacecraft in both MACH and POLAR to charged disks in flowing plasmas [Heinemann, et al., 1986]. These studies of the charged disk have shown that the POLAR and MACH solutions for the wake and sheath are essentially the same. Both codes find a near sheath which is approximately symmetric in ram and wake. The far wake is quasineutral and similar to the geometrical shadowing of the downstream flow of a disk. The substantial agreement between MACH and POLAR on this problem, obtained by very different numerical techniques (see Figure 3.2), gives a good indication of the consistency and validity of the two codes.

The capabilities of the MACH code have been extended so that it can handle some problems that are not currently addressable by POLAR. One such problem is that of a positively charged object in a flowing plasma [Cooke, Tautz & Rubin, 1987; Tautz & Cooke, 1988], which has application to space vehicles charged by beam emission and for Langmuir probes. This case is more difficult to solve than negative charging because the density of the repelled particles (positive ions) is not Boltzmann and therefore both species must be tracked. We have used MACH to determine the current-voltage (I-V) characteristics for a disk in a drifting Maxwellian plasma and for a stationary plasma.

The electron currents collected by the object as the positive bias is increased from 0 through the stagnation potential of +16 kT/e and up to 100 kT/e are shown in Figure 3.4. The currents are normalized to the appropriate electron random thermal current, $I_o = N_o e (kT/2\pi m)^{1/2}$. The circles represent the results for ion mach number M = 4 and the triangles give the results for M = 0. The other line in the plot is data taken from Laframboise [1966], and gives the currents for a spherical conductor in a non-flowing plasma. Since MACH uses a disk rather than a sphere, we do not expect perfect agreement with this reference data. From the figure it is evident that the electron current is larger for the flowing plasma than for the stationary case. This effect comes about because of the enlargement of the sheath, and hence of the effective collection area for electrons, brought about by the build up of positive charge at the front of the disk due to reflected ram ions. Figure 3.5 shows the dimensionless electrostatic potentials at probe voltage 50kT/e. One can see here the distortion of the potentials due to the reflected ram ions. The electrons dominate in the wake and drive the potentials a few kT/e negative.

Another problem that can be handled by MACH is that of two charged objects aligned on the flow axis of symmetry [Cooke & Tautz, 1988]. We have looked at the case of a cylindical probe situated in the wake of disk. In our initial investigation of this problem we have calculated the I-V characteristic of a probe located behind an uncharged disk. This configuration is shown in Figure 3.6a. A negative potential of a few kT/e would develop behind the disk even if the probe were absent, because ambient electrons diffuse into the wake, and the probe acts as a perturbation to this background field. When the probe potential is less than the background potential there exists a barrier field which shields out some current. Because of this, the electron current shows a knee structure as the probe potential passes through the background level. This
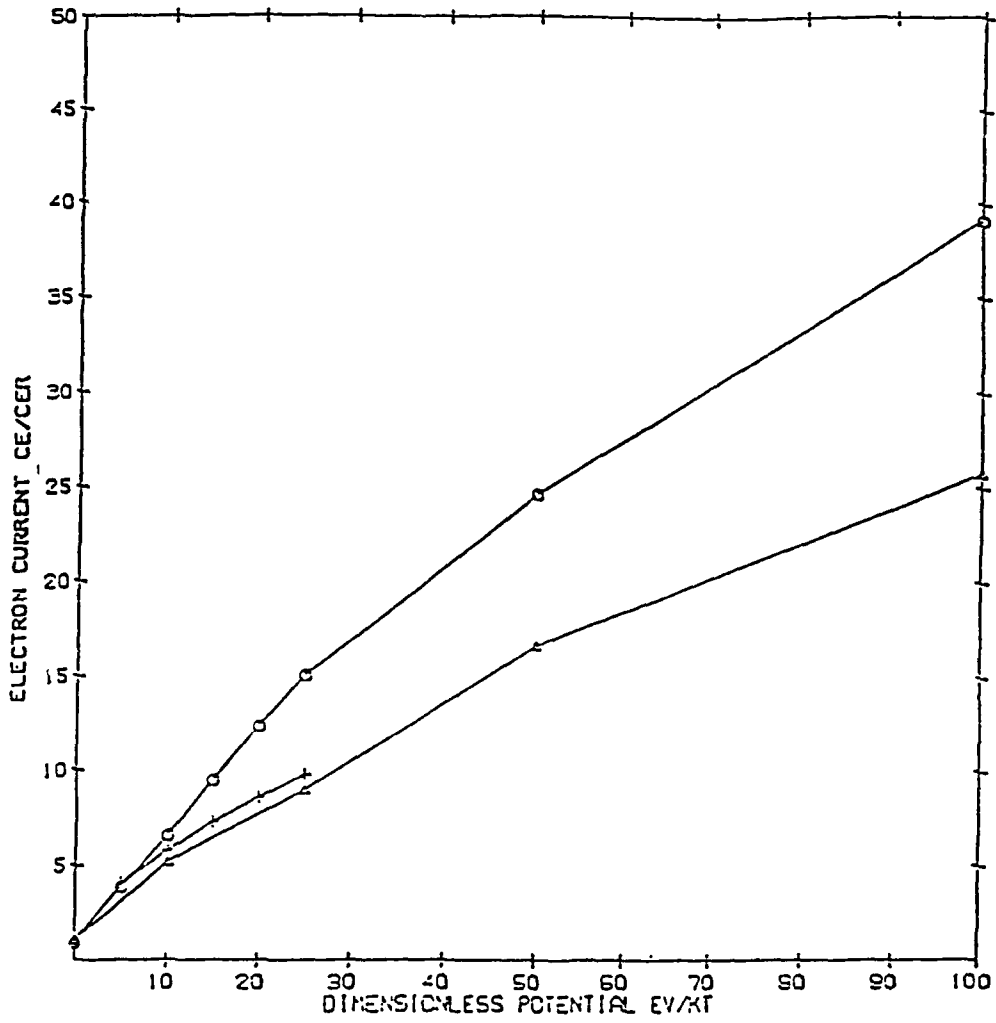
Figure 3.4. MACH solution for the I-V curve for a disk with positive bias
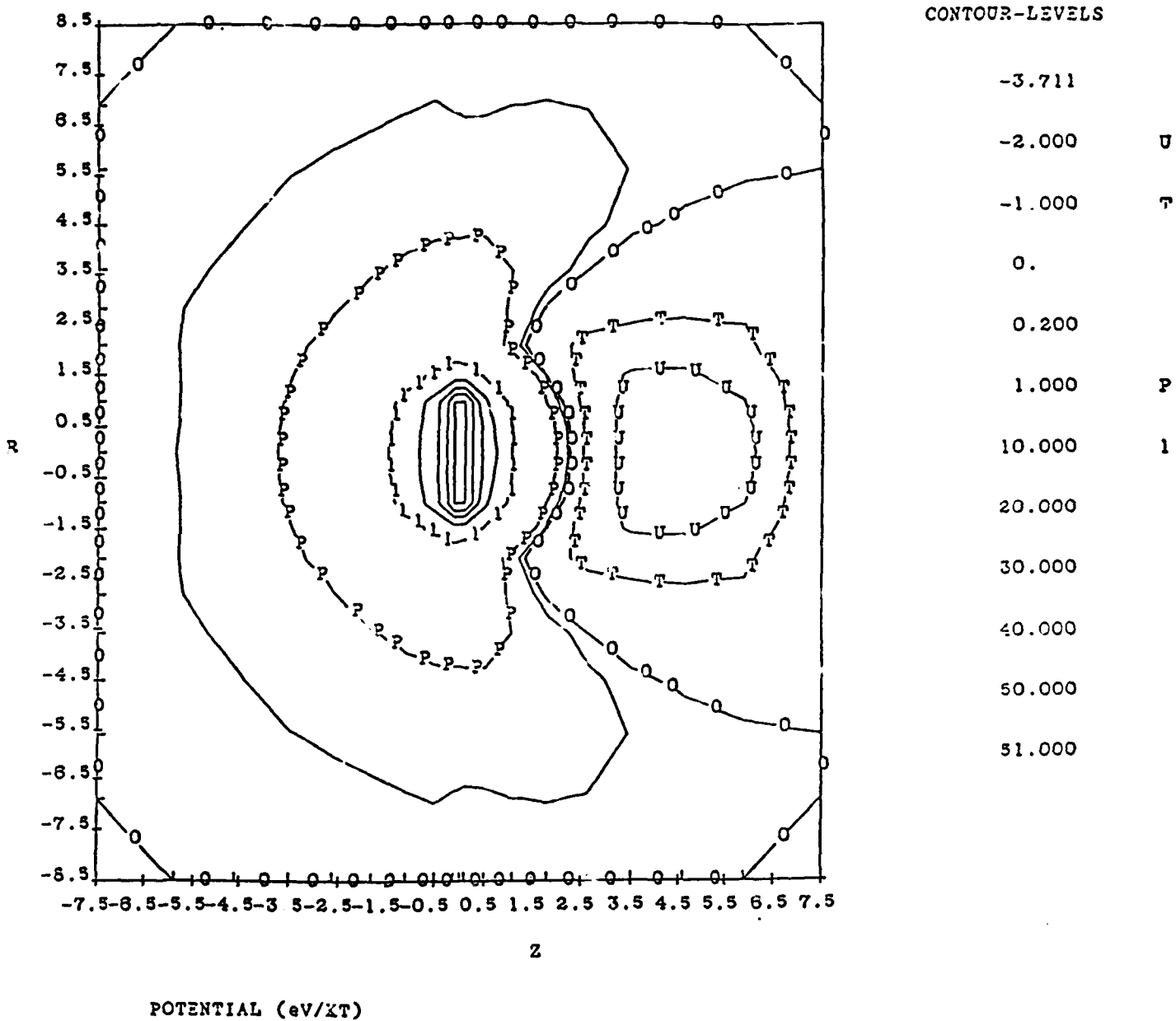
Figure 3.5. MACH solution of electrostatic potentials surrounding a positively charged disk

CONTOUR-LEVELS

-4.500
-4.000
-3.500
-3.000
-2.500
-2.000
-1.500
-1.000   T
-0.100

DIMENSIONLESS POTENTIAL
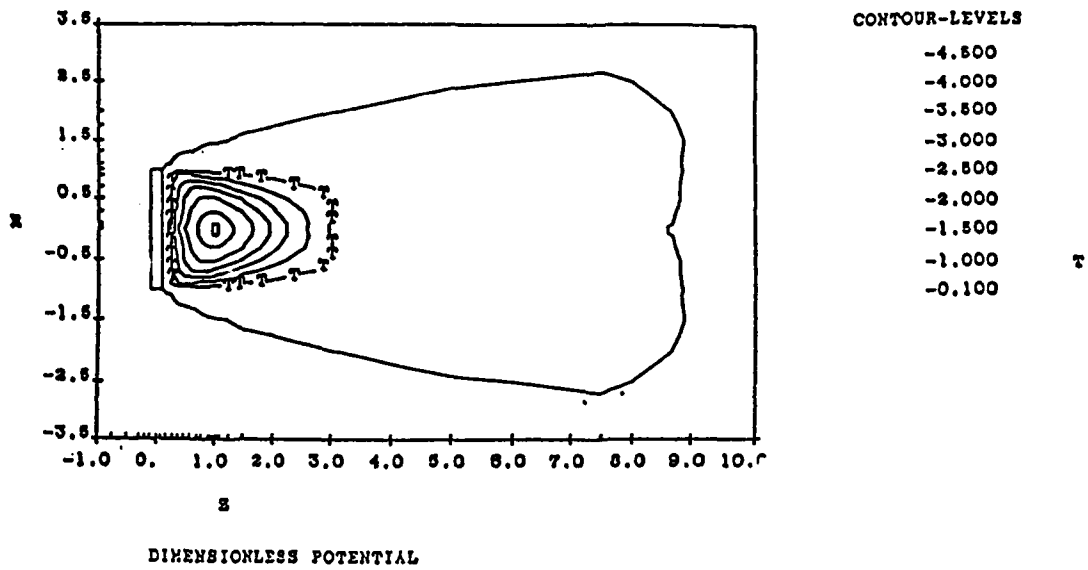
Figure 3.6a. MACH solution for electrostatic potentials for a probe in the shadow of an uncharged disk

CONTOUR-LEVELS

-70.000
-60.000
-50.000
-40.000
-30.000
-20.000
-10.000
-1.000   T
-0.100

DIMENSIONLESS POTENTIAL
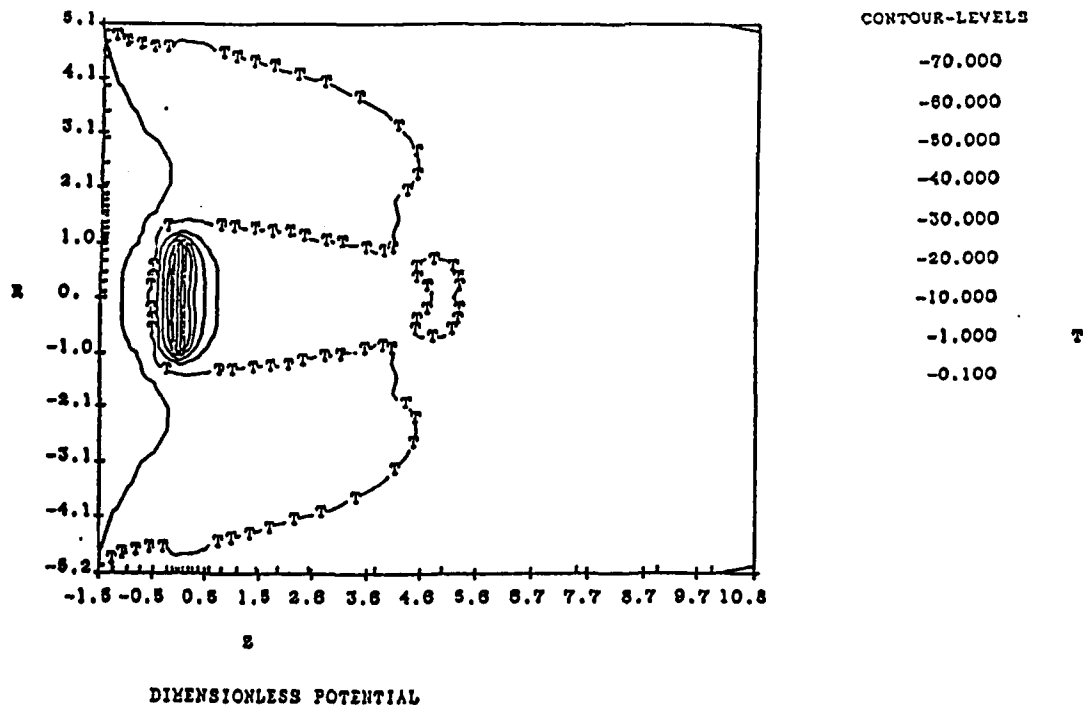
Figure 3.6b. MACH solution for electrostatic potentials in the Northeastern chamber experiment

could be interpreted as a temperature enhancement effect if the location of the knee is not well resolved experimentally. Thus our model may be able to explain some experiments where temperature enhancements have been observed. We intend to use this two body capability of MACH to also investigate the man-in-the-wake problem, where we will compute currents and floating potentials for a 'man' located in the shadow of a larger object.

The MACH program has also proven useful in simulating the behavior of charged probes in a plasma chamber [Morgan, Chan et al., in publication]. Figure 3.6b shows the MACH solution for electrostatic potential for the Northeastern experiment [Chan, Morgan, Allen et al., 1986] which investigated probe charging in a modified double plasma device. The code can solve this case, in steady state, when the outer grid boundary conditions are set to allow for the absorption of particles by the chamber walls. Our preliminary results for this case are somewhat uncertain, due to the lack of exact knowledge of the boundary conditions at the throat of the chamber. We have investigated a few different scenarios by changing the throat boundary conditions, but CPU time restrictions preclude exploring the total parameter space. The solution shown in Figure 3.6b appears to be the most reasonable one, and does show a small electron density bump in the wake which is consistant with the experiment. In the future we will use MACH to simulate the MIP (Multi-body Interactions in Plasma) chamber experiment being carried out at GL. The MACH simulations will provide guidelines for more comprehensive models to be incorporated into the POLAR code.

The verification of the POLAR code has progressed through the comparison of code results with the MACH program [Heinnemann, et al., 1986] and through simulation of charging phenomena on SPEAR [Cooke et al., 1987] and DMSP [Cooke et al., 1987]. The simulation of a DMSP charging event is described below.

Many of the DMSP (Defense Meteorological Satellite Program) Satellites have been observed to undergo charging while passing through auroral electron streams [Gussenhoven et.al., 1985]. So far, the most extreme satellite frame potential appears to have been about 440 Volts negative, and no serious satellite misfunctions have been attributed to these charging events. For a given environment though, the maximum spacecraft potential increases with size [Katz and Parks, 1983], indicating that larger systems in polar orbit, planetary missions, and electrically active spacecraft, will face more severe charging problems. Because they are well instrumented, and surviving, the DMSP satellites provide an excellent experimental platform for the validation of spacecraft charging concepts, and in particular, the POLAR code.

High and low resolution POLAR models of the DMSP satellite are shown in Figure 3.7. In order to save CPU time, the low resolution model was mostly used in this study. A fit to the differential electron flux measured for the DMSP eclipse charging event of Dec 1, 1987 at UT 1458 was made using the POLAR code parameterization in terms of a power law, a Gaussian, and an energetic Maxwellian distribution. The ambient plasma was taken to have temperature 0.2 eV and density of $3.55 \times 10^9/m^3$ based on on-board DMSP measurements. The potentials around the satellite obtained from the POLAR code simulation are shown in Figure 3.8. In the figure, the direction of plasma flow is from left to right at Mach number 6.7. The contours represent the electrostatic potential in Volts. The contour marked "T" represents the 1 KT level and corresponds to the approximate location of the sheath edge (the downstream part of the solution has been truncated). Figure 3.9 shows the POLAR time history of charging for selected surfaces composed of kapton, teflon, and solar material and the satellite ground potential. The observed spacecraft frame potential, based on ion spectrograph measurements, was -215 Volts, in excellent agreement with the POLAR result for ground potential as shown in the figure.
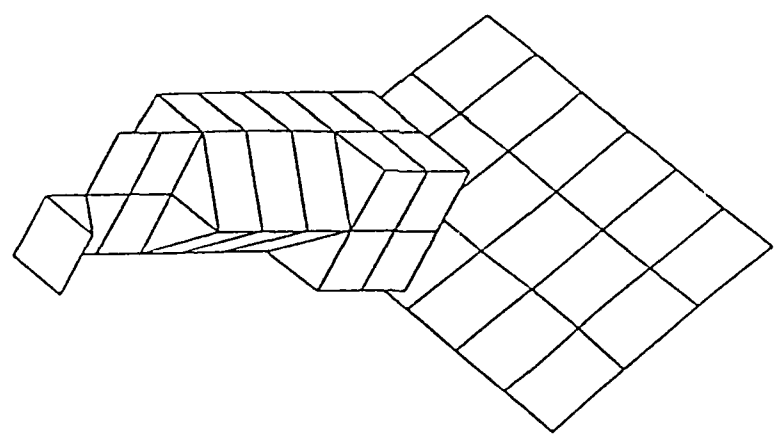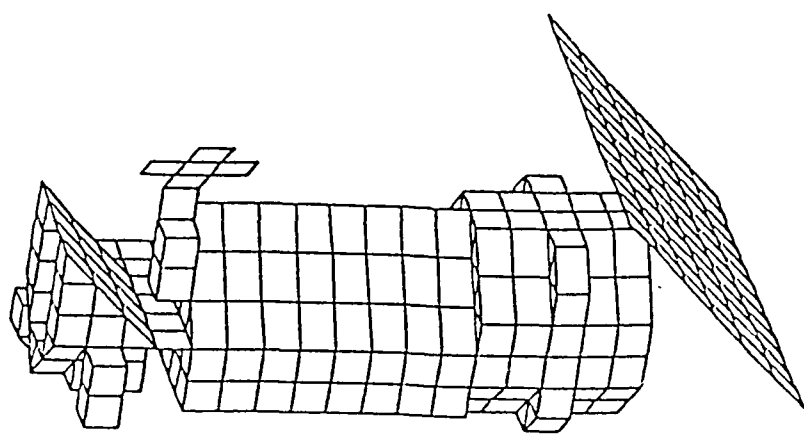
Figure 3.7. POLAR models of the DMSP satellite

CONTOUR-LEVELS VOLTS

-500.000

-400.000

-300.000

-200.000

-100.000

-.200   T

-.020
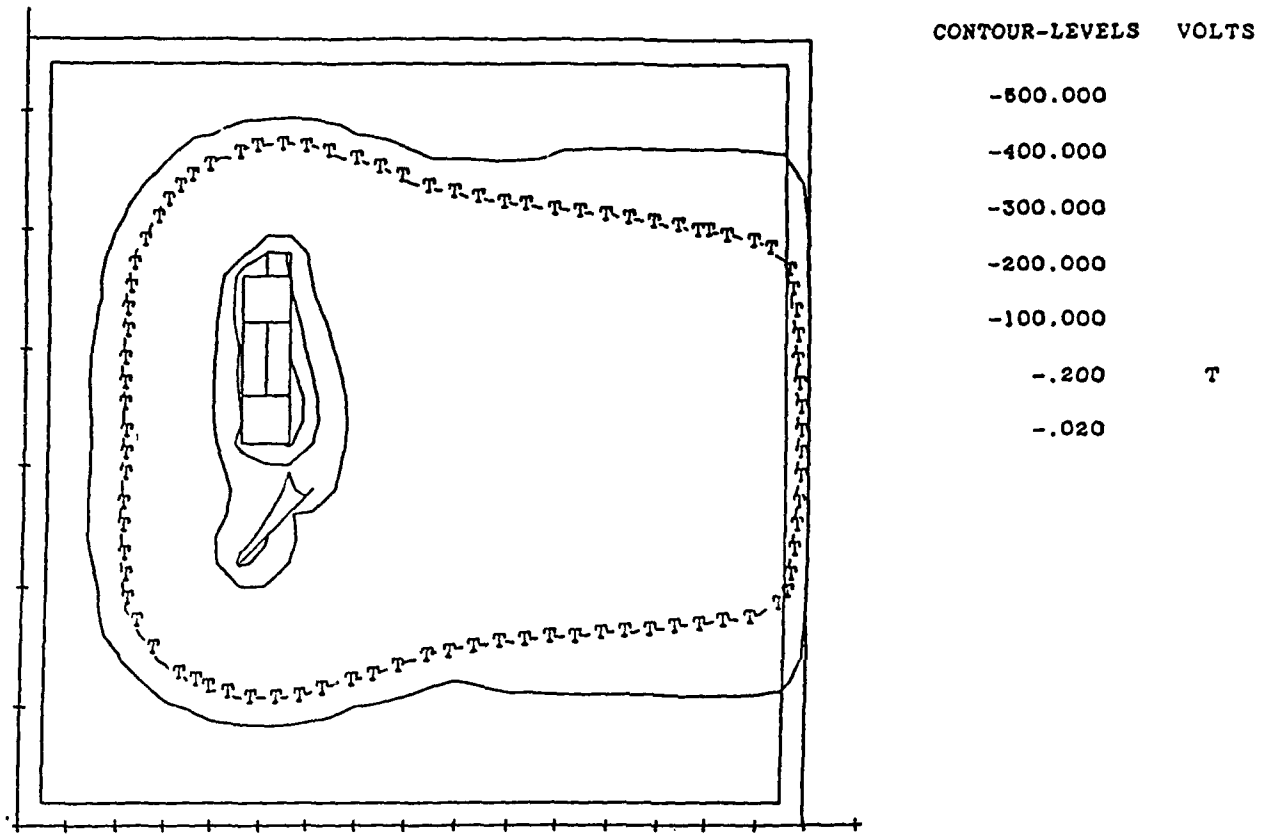
Figure 3.8. POLAR solution for electrostatic potentials surrounding the DMSP satellite
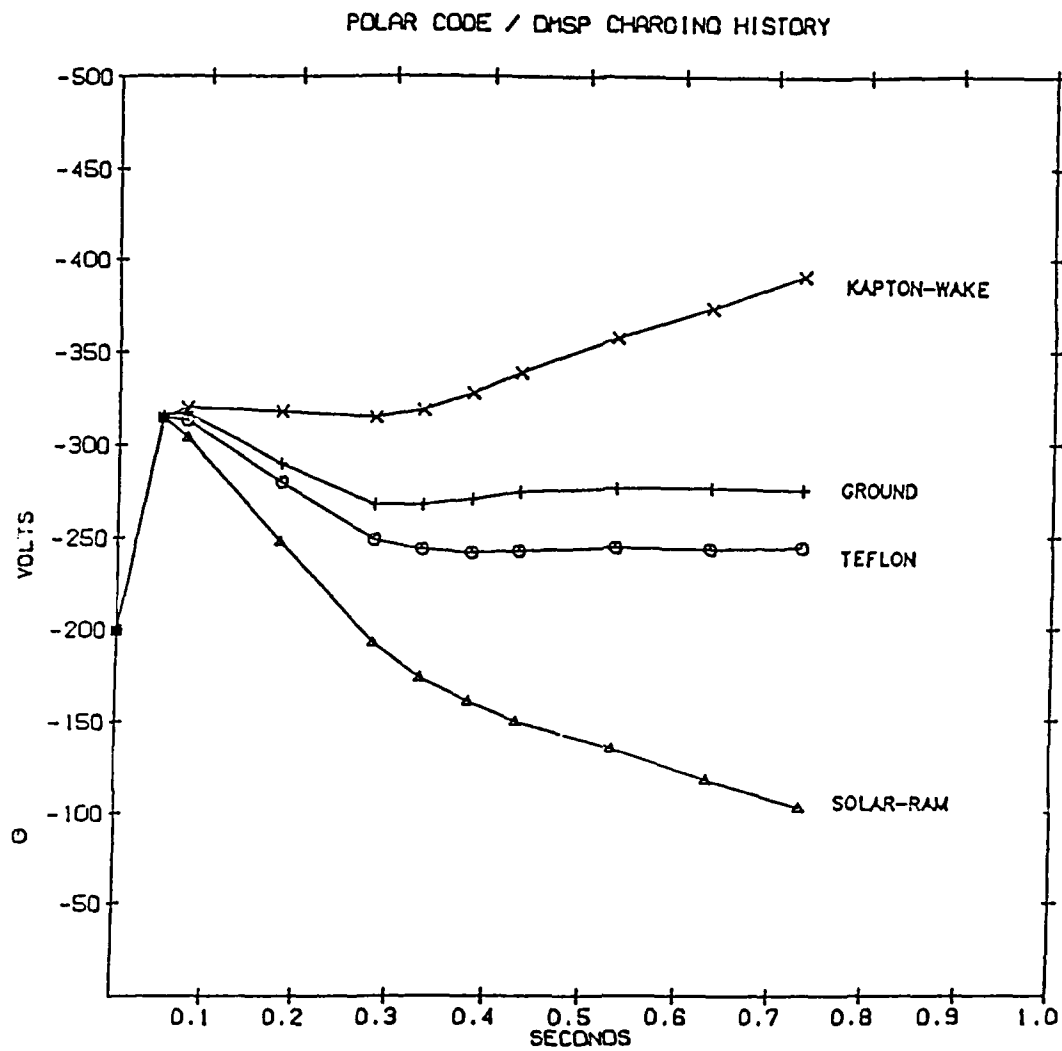
Figure 3.9. POLAR solution of DMSP charging history for selected surfaces exposed to an electron environment observed by DMSP-F7 on 01 Dec 1987

99

The comparison of POLAR charging results and DMSP observations indicates that POLAR is capable of predicting auroral charging within reasonable interpretations of the experimental and model uncertainties. Experimental uncertainty arises in the determination of background plasma parameters at all times, and in the extrapolation of energetic electron fluxes to pitch angles not measured by DMSP. There are no free parameters in the POLAR calculations, but the degree of faithfulness in the satellite description and model preparation can contribute significant uncertainty.

3.2 EVALUATION OF THE CHEMICAL PROCESSES LEADING TO SPACECRAFT CONTAMINATION

The environment surrounding an orbiting spacecraft is a dynamic system created not only by ambient and outgassed molecules, but also by a myriad of chemical reactions between these molecules. Realistic modeling of this environment must therefore be predicated upon a thorough understanding of the chemistry between the various species of contaminant molecules. Such modeling efforts often attempt to incorporate spacial asymmetry of spacecraft geometry in a fully three-dimensional way. However, inclusion of complex chemical and plasma processes has generally been impossible due to prohibitive computational cost or necessary physical approximations which obscure the detailed molecular and plasma interactions. Many aspects of these processes can be addressed and understood without recourse to a full three-dimensional model through chemical kinetics and through electrostatic plasma simulation methods including chemical processes. In addition, solutions to the dispersion relations obtained from linear plasma theory give important insight into the wave-particle interactions. The use of these and other simplifying models allows for the inclusion of a large number of processes, which would not be tractable in a model with realistic geometries. Results from these studies can often provide significant clues in and of themselves. The results also indicate important processes that must be included in the more complex modeling efforts and identify other processes that can be safely neglected.

Two aspects of contamination in which chemical processes must be of particular importance are the observations of enhanced regions of ionization and of significant illumination of the shuttle ram surfaces, the so called "shuttle glow" [Green, et. al., 1985]. One possible explanation that has been offered [Papadopoulos, 1984] arises from the interaction of flowing neutrals with the ambient plasma. This is the Critical Ionization Velocity (CIV) process, first proposed by Alfven [1954] to explain the accretion of matter in the universe and the formation of planets in our solar system. Many theoretical attempts have been made to understand the CIV process and several recent experimental investigations have been undertaken in an effort to prove or disprove the existence of CIV in space. Results of these experiments are generally inconclusive and there is need for a more detailed understanding of these data.

After a brief overview of the CIV concept and a description of the observations pertinent to spacecraft contamination, we present a summary of the efforts undertaken in the investigation of chemical processes relevant to CIV and to other contamination problems.

3.2.1 The CIV Hypotheses

The concept of CIV was first proposed by Alfven to explain two aspects of the formation of the solar system; why the dust and gas did not fall directly into the sun and why the chemical composition of the inner planets is so different from the outer planets. His explanation rests in part on the selective ionization of the neutral gas cloud as soon as the velocity of a particular constituent exceeds a critical velocity given by

$$V_* = \sqrt{(2\phi/M)} \qquad (3.1)$$

where ϕ is the ionization potential and M is the mass of the constituent gas. In order for CIV to occur, it is necessary that the neutral molecules be moving almost perpendicular to an external magnetic field. Once ionized, the molecule is trapped by the magnetic field and separated from the other as yet un-ionized components of the cloud.

Many laboratory experiments have confirmed the existence of the process and have shown that energy is transferred to the electrons through a plasma instability likely to be the modified two stream instability. The cyclic process is likely to consist of the following steps. The neutrals transfer energy to the ambient ions through charge exchange or elastic collisions. The ions then move through the ambient electrons, which are pinned to the field lines. This creates an instability and transfers the ion energy to the electrons. The heated electrons then ionize more neutrals, creating more fast moving ions to complete the cycle. Some aspects of this cycle are diagrammed in Figure 3.10.

3.2.2 Experimental Evidence

The observations that implicate CIV as a possible contamination source come from two general sources; observations made on the Shuttle and in space experiments designed especially to test the CIV hypotheses. The most striking evidence was provided by photographs from the third and fourth shuttle flights revealing a significant illumination of the ram surfaces [Banks et al., 1983]. Other evidence comes from the Plasma Diagnostics Package (PDP) measurements [Shawhan and Murphy, 1983] on STS-3. Among these results were (1) evidence of plasma density in the vicinity of the shuttle up to ten times the ambient plasma density, (2) energetic electrons of up to 100 eV, and (3) intense electrostatic noise up to 20 kHz. The glow on the ram surfaces was postulated by Papadoupolos [1984] to be due to the CIV discharge of ambient Oxygen bouncing off the ram surfaces and thus acquiring twice the Shuttle velocity (8 km/sec) to exceed the critical velocity given by Equation 3.1. The other three observations show a high degree of ionization in the shuttle vicinity and the heating of electrons, possibly by electrostatic waves around the lower hybrid frequency. The CIV concept is consistent with these features.

The other source of data on space CIV comes from experiments designed to test the hypotheses. The majority of these involve the explosion of a shaped cloud of neutrals in the ionosphere. Usually Sr or Ba are used since these atoms have clearly identifiable spectral lines that can be used to differentiate the ion from the neutral species and have low critical velocities. Overall, the results of the experiments carried out to date is inconclusive, with two giving positive results and the rest apparently failing to show CIV. Even if all the experiments were to give negative results, it would be important to understand why CIV failed to occur in these instances. Otherwise, one could not preclude the occurrence of CIV under other conditions on the Shuttle or on other space vehicles.

101
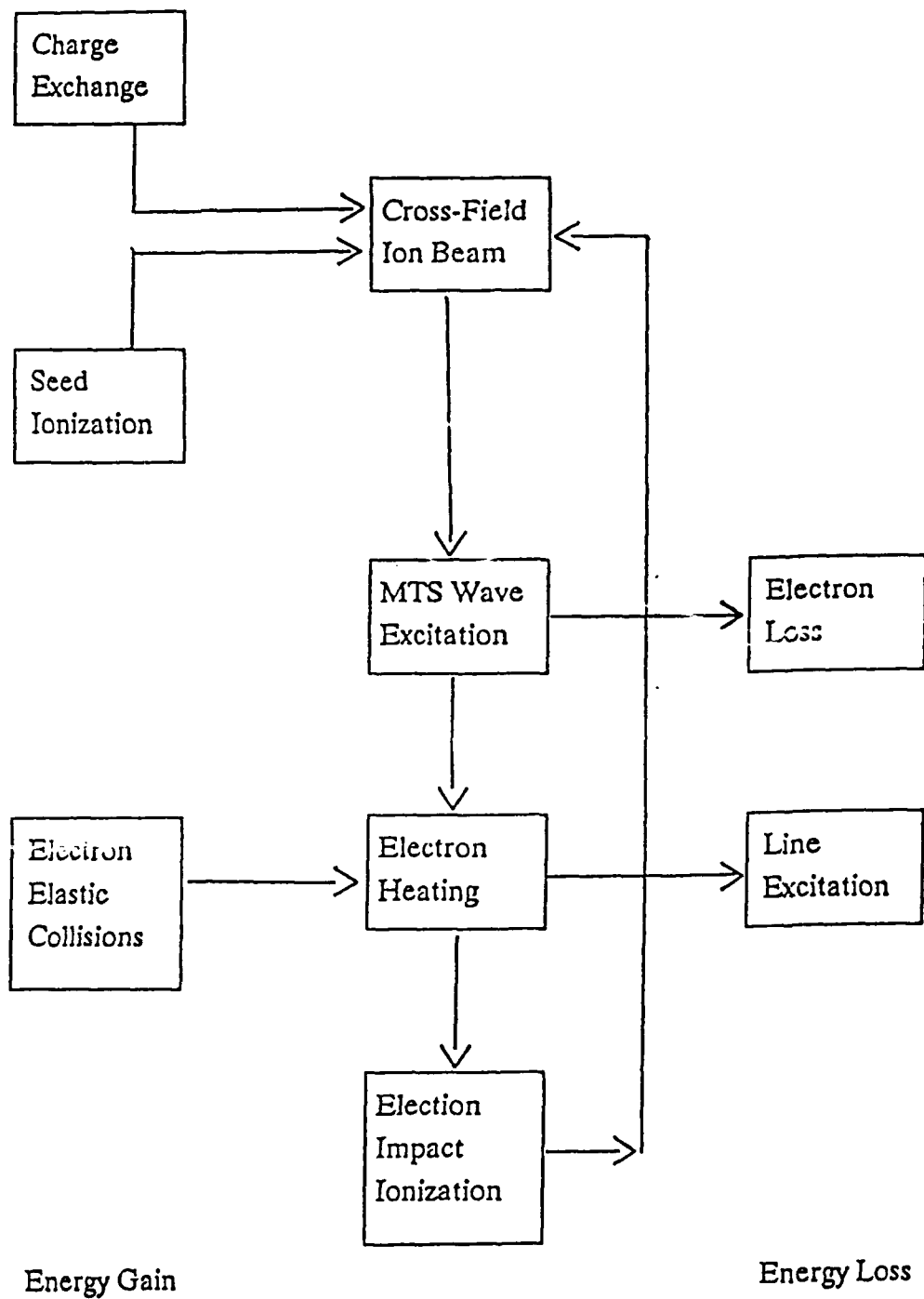
Figure 3.10. Schematic diagram of the flow of energy in a CIV discharge

102

3.2.3 Kinetic Studies

In order to understand spectral or mass concentration measurements, one must model the concentrations of various components in the system. Since steady state or transient concentrations of many components depend on the various chemical reactions taking place in the system, such calculations can be used to justify one's choice of a reaction scheme when comparisons with data are favorable, and to reject other schemes when they are not. One way to arrive at steady state concentrations is to follow the evolution in time of a system through chemical kinetics.

This type of analysis begins with a set of chemical components that are thought to be present in the system. Next, a set of reactions between these components is decided upon. Calling the components of the system A, B, etc, the reactions are of the form

$$n_A A + n_B B + \ldots = n_X X + n_Y Y + \ldots \tag{3.2}$$
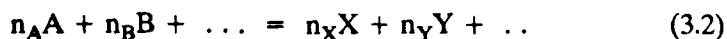
The products X, Y, etc. may be the same as those originally determined as components of the system or they may be new components that arise because of the reactions. The time dependence of any component, W, is then given by

$$d[W]/dt = \Sigma_i n_{iW} k_i [A]^{nA} [B]^{nB} \ldots - \Sigma_j n_{jW} k_j [A]^{njA} [B]^{njB} \ldots \tag{3.3}$$

where the summation i is taken over all reactions in which species W appears on the right hand side and that over j taken over all in which W appears on the left. For almost all cases of interest, reactions like 3.2 will be bi-molecular, meaning that there will be only two components A and B on the left hand side and that n_A and n_B will be unity. In this case, the rate constant k_i can be calculated with knowledge of the distribution of *relative* energy between A and B, $f_{AB}(E)$ and the reaction cross-section for reaction i, $\sigma_i(E)$.

$$k_i = (2/\mu)^{1/2} \int E^{1/2} \sigma_i(E) f_{AB}(E) dE \tag{3.4}$$

These values, coupled with an assumption for the initial concentrations in the system can be used to follow the time evolution of all components. Using these results, one can assess the importance of specific reactions, compare concentrations with mass spectra, and calculate relative intensities of spectral lines.

One difficulty encountered in the solution of a system of kinetic equations is the correct construction of a subroutine to express Equation 3.3 for all components in the system. When dealing with several tens of reactions, the transformation of the elementary reactions into rate equations can be extremely tedious and often leads to errors in coding which can be nearly impossible to detect. To ease this burden, we have written a program KINEQ which reads a file of the elementary reactions (Equations like 3.2), sorts out and labels the components of the system, and writes a subroutine expressing the rate equations for each component. To ensure that the input file is correct, KINEQ also performs a mass and charge balance check on each reaction. A second problem often arises because many large kinetic equation systems are inherently stiff. This makes solution difficult by conventional means. To aid in this situation, KINEQ also writes a subroutine expressing the derivative of each rate equation with respect to its representative component. The program then writes a Runge-Kutta based stiff equation

solver which uses the derivative routine. The subroutine of kinetic equations is free-standing, however, and can be used with almost any differential equation package.

3.2.3.1 Metastable States

Applying kinetic simulations to problems in CIV, and in contamination in general, has shown that the metastable states of many atoms and molecules are important in the CIV process [Lai et al., 1988]. A metastable state is an excited state of a molecule with a very long lifetime. If a neutral and an electron collide, resulting in an ionization,

$$A + e = A^+ + 2e \tag{3.5}$$

the electron must necessarily possess at least an energy equal to the ionization potential of A. However, since the energy of the metastable A^* lies somewhere between the energy of A and that of A^+, the two-step reaction

$$A + e = A^* + e$$
$$A^* + e = A^+ + 2e \tag{3.6}$$

can be accomplished by two electrons, each having energy substantially less than the ionization potential. This process of "energy pooling" dramatically increases the ionization rate in CIV at velocities near V_*. Figure 3.11 shows the enhancement of ionization in the four species considered in this study.

3.2.3.2 Ion-Molecule Reactions

In another kinetic study related to CIV, we have examined the influence of ion/molecule reactions. One such reaction of particular interest is the sequence

$$H_2 + e = H_2^+ + 2e$$
$$H_2^+ + N_2 = N_2H^+ + H$$
$$N_2H^+ + e = N_2\ddagger + H$$
$$N_2\ddagger = N_2^* + h\nu \tag{3.7}$$
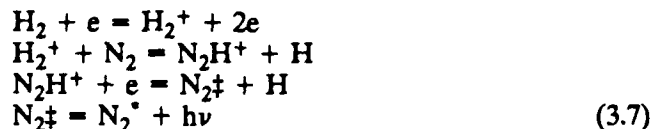
In this reaction, H_2 is first ionized then undergoes an ion/molecule reaction with N_2 forming N_2H^+. This undergoes molecular dissociative recombination forming H atom and an N_2 molecule in an excited state. This excited state decays, leading to the metastable N^* and emitting characteristic radiation of the transition. Through kinetic analysis, we showed that the majority of radiation emitted at this characteristic frequency (approximately 1.18 eV) came from this reaction, thus demonstrating the importance of ion/molecular reactions in spectral calculations [Lai et al., 1989].

3.2.3.3 Oscillating Reactions

In addition to the Ion-Molecule reactions mentioned above, a molecular ion can also undergo a process called Molecular Dissociative Recombination (MDR)

$$A_2^+ + e --> 2A \tag{3.8}$$
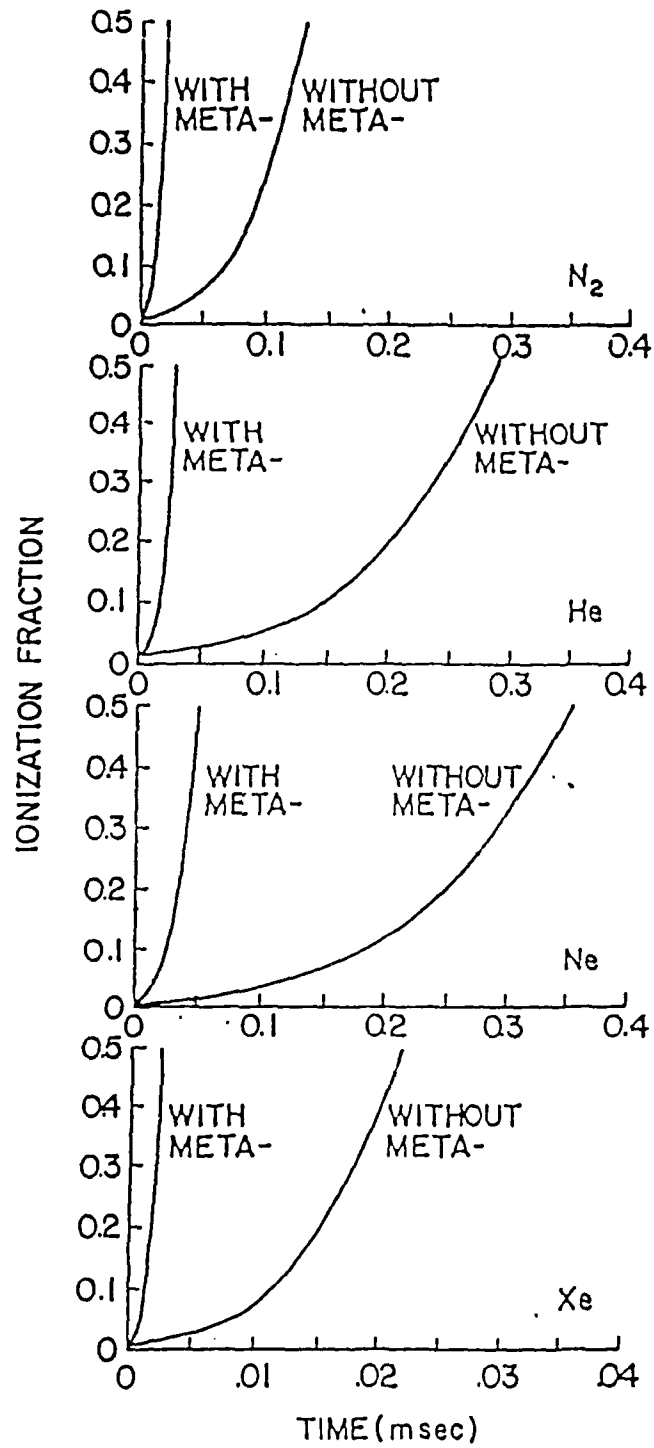
Figure 3.11. Enhancement of ionization in four species

We have investigated the possibility that MDR could lead to oscillatory behavior in systems undergoing CIV. [Lai, et al. 1987] Since the atomic species A has only one-half the mass of the molecular species A_2, it may be that a neutral beam of A_2 could be capable of sustaining CIV while one of the atomic A could not. As ionization and MDR proceed, the average mass of the system will be reduced. Ionization would be quenched whenever this average mass falls below the critical mass which, from Equation 3.1 should be given by

$$M_c = 2<\phi>/V^2 \tag{3.9}$$

To demonstrate the critical-mass concept, we consider a simple scenario. Suppose critical velocity ionization of A_2 has occurred. As the density A_2^+ and e^- increases, so does the probability of MDR, thus the average mass $<M>$ drops below the critical value. When this point is reached, ionization ceases. The atomic fragments A will be swept away by diffusion and we can suppose that fresh A_2 is introduced continuously by a "snow plow" effect. Thus in the absence of ionization, the average mass begins to increase. Eventually, the average mass will rise above M_c and CIV is again ignited. Figure 3.12 shows the behavior for one set of parameters in this model.

3.2.3.4 Electrostatic Particle Simulations

One major drawback of the kinetic studies presented above is the fact that electron and ion distributions must be assumed a priori and used to calculate rate coefficients that then stay constant during the simulation. This approximation, though necessary in kinetic theory, suffers both because the assumed distribution function may not be correct and because various chemical reactions can greatly affect the distribution of both ions and electrons. This problem can be overcome by the use of "particle in cell" (PIC) codes which calculate a time dependent distribution of electrons and ions directly as the result of simulated plasma instabilities. When coupled with chemical reactions between constituents in the system, PIC codes can be a powerful tool in predicting the results of CIV interactions for moderately complex chemical systems.

Beginning with a PIC code developed some time ago [McNeil et al., 1984], we have developed a code capable of simulation of several of the important chemical processes that should occur in the CIV discharge of Neon [McNeil and Lai. 1988]. The code allows for (1) ground state ionization of beam neutrals, (2) charge exchange between neutral beam atoms and Neon ions, (3) excitation and (4) ionization of metastable states, (5) energy loss due to the excitation and subsequent decay of allowed states and (6) elastic collisions between neutrals and electrons. With this code, we have been able to generate several interesting results [McNeil et al., 1988]. We have confirmed that metastable states play an important role in the total ionization when the beam energy is near the critical energy. We have shown that charge exchange is essential in sustaining a CIV discharge at low beam energy. We have shown that the energy loss due to line excitation does not quench the discharge but merely raises the threshold for CIV.

We have recently extended this work to include similar models for Helium, Xenon and Barium. Among the interesting results of these studies was the realization that the magnitude of the line excitation cross-section can lead to profound differences in the threshold for CIV for various gases. This means that a low critical velocity may not be the best criterion for choosing an experimental gas, since species with low ionization potentials frequently have a high probability of line excitation as well.

$$\tau_1 = 0.5 \text{ms} \quad S = 10^3 \text{s}^{-1}$$
$$\tau_2 = 0.5 \text{ms} \quad M_* = 0.8$$
$$D = 10^3 \text{s}^{-1} \quad \text{Onset Delay} = 50 \mu \text{s}$$
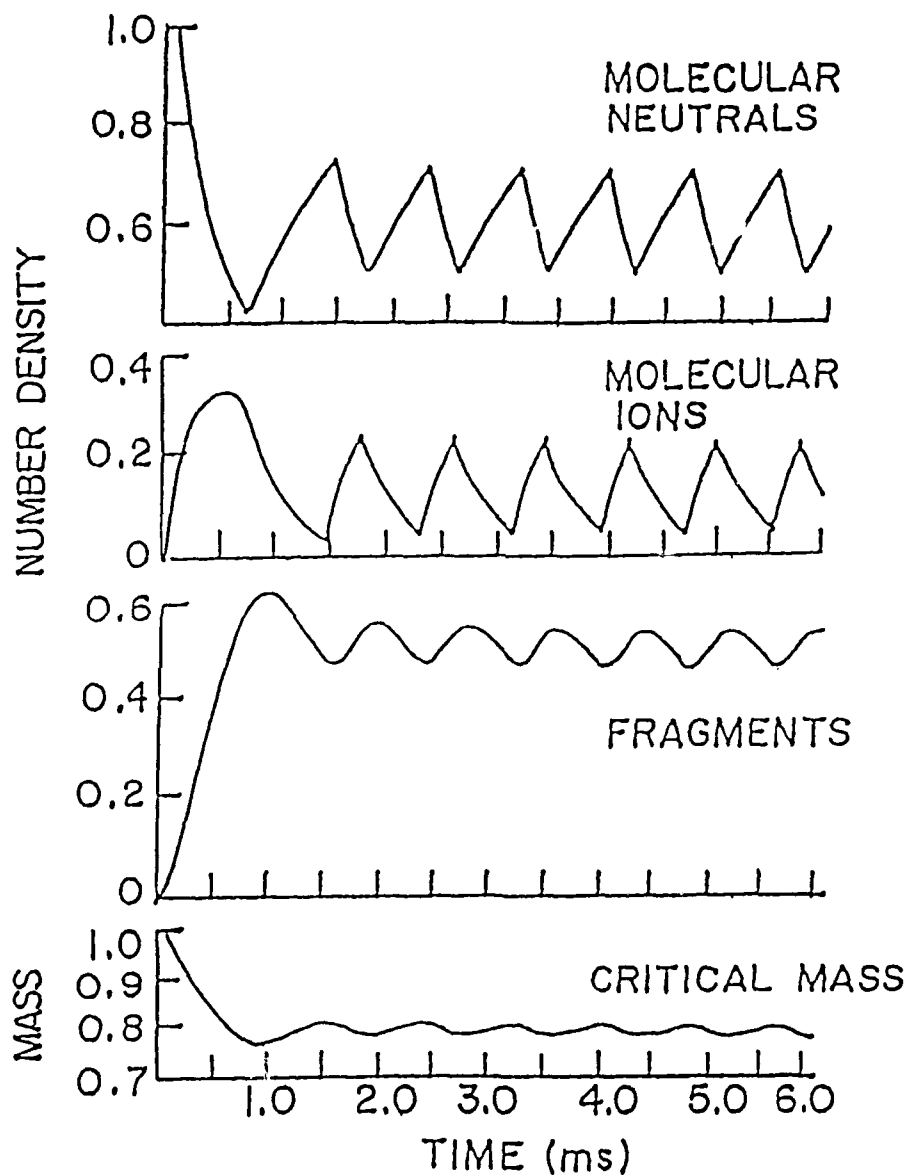
Figure 3.12. Behavior for one set of parameters in the model

3.2.3.5 Dispersion Relations

One tool of particular importance in the investigation of many plasma processes is the dispersion relation obtained from linear Vlasov theory. This equation relates the frequency and rate of growth of an unstable wave to other system parameters such as wavelength, density, and dimension. The dispersion relation is a complex function of a complex frequency

$$\omega = \omega_r + i\gamma \tag{3.10}$$

with all other quantities in the expression being, in general, real. Even for most simple systems, analytical solutions to the relation cannot be obtained and one must resort to numerical methods. Even then, the manipulation of these equations becomes somewhat of an art. This section describes the program DISPER, which has been used extensively in dispersion relation work, with emphasis on providing valuable hints on its operation.

As an example, we consider the dispersion relation for the Modified Two-Stream instability, which is the basis for the plasma simulation described before. The equation to be solved is

$$1 = \omega_{pe}^2/(\omega^2 - \Omega^2)\cos^2\theta + \omega_{pe}^2/\omega^2\sin^2\theta$$

$$+ \omega_{pi}^2/(\omega - kv_0\cos\theta)^2 \tag{3.11}$$

where ω_{pe} is the electron plasma frequency, ω_{pi} is the ion plasma frequency, Ω is the electron cyclotron frequency, v_0 is the ion beam velocity, k is the wave number and θ is the angle between the ion beam and the magnetic field. The first step in attacking 3.11 is to perform a reduction of variables, generally so that the frequency ω is expressed in terms of some fundamental frequency of the system. For example, if we define

$$\omega = \omega/\omega_{pe}$$

Equation 3.10 can be written as

$$1 = \cos^2\theta/(\omega^2 - h^2) + \sin^2\theta/\omega^2 + 1/M(\omega - f\cos\theta)^2$$

where $h = \Omega/\omega_{pe}$, $f = kv_0/\omega_{pe}$ and $M = M_i/M_e$. This reduced relation is then introduced into DISPER through the function FDISP. One of the variables (typically the one containing the wavevector k) is chosen as the independent variable, a second (typically ω) is chosen as the dependent variable and all others are set to chosen constants. The solution process then begins.

Figure 3.13 shows a typical solution for the Modified Two Stream instability, produced by DISPER. The lower panel is the imaginary part of ω and the upper the real. DISPER can only solve for one ω_r and γ at a time, so the branch that can be seen on the right hand side must be calculated in two separate runs. In order to initialize DISPER, one must be able to come reasonably close to one solution on each branch of the dispersion curve. This is far easier if one begins at a value of f where the solution for ω is entirely real, such as along the dotted line in Figure 3.13. When DISPER begins, it asks for a starting and ending value for the independent variable and a step size. It then asks for a range of the dependent variable. Using the starting value of the independent variable, it then displays the value of the dispersion relation at several points in the dependent variable range, assuming that the imaginary portion of ω is zero. In this way, one can find the appropriate zero on each curve. When found, this value is supplied to

108

Modified Two−Stream Instability

$M_i/M_e = 100 \quad \omega_{pe}/\Omega_e = 1 \quad \theta = 6°$

$$1 = \omega_{pe}^2/(\omega^2 - \Omega_e^2)\cos^2\theta$$
$$+ \omega_{pe}^2/\omega^2 \sin^2\theta$$
$$+ \omega_{pi}^2/(\omega - kv_o\cos\theta)^2$$

ω/ω_{pe}

γ/ω_{pe}

kv_o/ω_{pe}
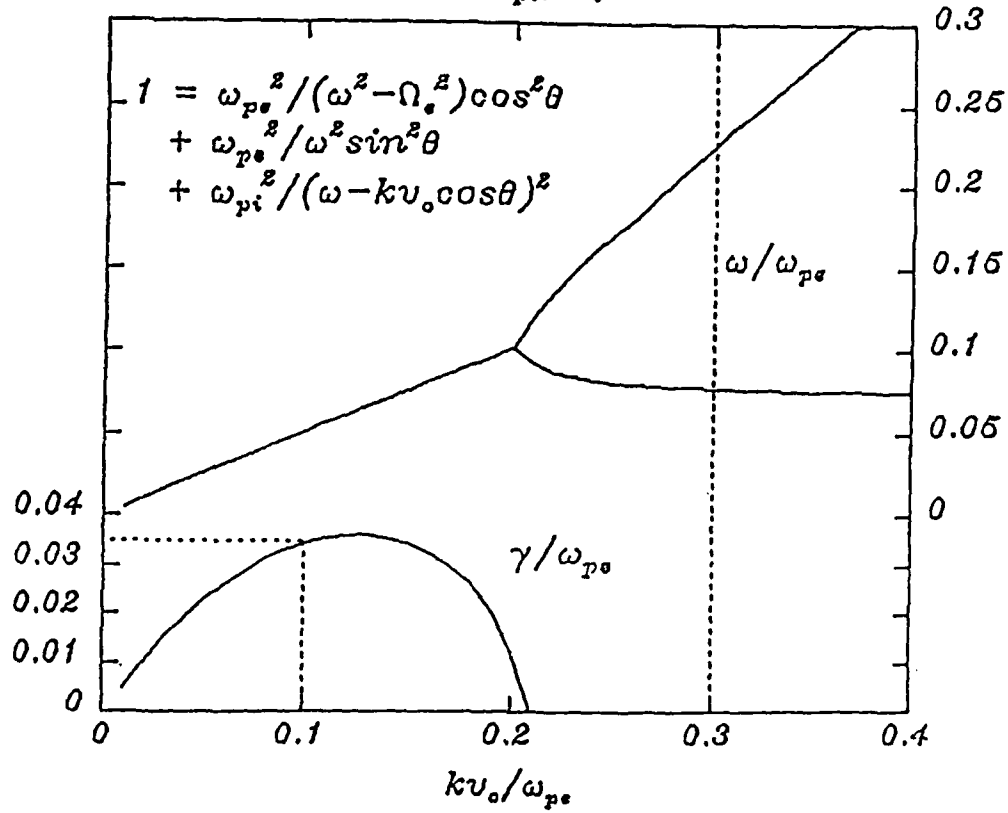
Figure 3.13. Dispersion of the modified two stream instability

DISPER in the second phase and the search begins for the root. If the search is successful, DISPER asks for one additional value of ω at the next value of the independent variable. This should be chosen close to the first value to ensure that roots on the same branch are obtained. Once two points along any branch have been found, the remaining points should be found automatically, if the function is reasonably well behaved and if the step size is chosen small enough. The entire process can then be repeated for other branches.

3.2.4 Summary

The combined application of chemical kinetics and plasma simulation has proven to be a valuable tool in the investigation of contamination processes. We have demonstrated the importance of several molecular processes in the determination of the macroscopic behavior of systems undergoing CIV. We have also demonstrated the important interconnection between chemical and plasma processes in the determination of thresholds for a CIV discharge. In the course of this work, several important software tools have been developed, including routines for particle simulation of plasma, for setting up complicated systems of kinetic equations and for the solution of dispersion relations.

3.3 FUNCTIONAL MODELING OF GEOPHYSICAL PROPERTIES

It is often advantageous to express the contents of large data sets in terms of functional fits. These parameterized models can then be incorporated into software without the need for large tables and interpolation schemes. Also, the fitting process itself achieves a degree of smoothing of the data set, which is usually desirable. The process also allows for differentiation of the functions, either analytically or numerically, without excessive problems of noise. Sometimes, when the model functions are physically representative, examination of the magnitude of various terms can even give insight on the properties under consideration. We have been involved in the functional modeling of several data sets in various applications. Here, we report on two such modeling efforts: the Epstein function modeling of auroral ion flux, and the modeling of the polar electrostatic potential by spherical harmonics.

3.3.1 Auroral Ion Number and Energy Flux

In past effort, models of the auroral electron flux and conductivities have been provided using Epstein functions [Hardy, et. al., 1987]. This effort extended the model to the ions. The data were obtained as an average over several hundred orbits in a matrix of 1350 values at seven integral values of the magnetic activity index K_p. Each matrix contained data at 48 magnetic local time (MLT) values and 30 corrected geomagnetic latitude values. Although in the electron model, a single Epstein function was employed at each MLT, the broadness of the ion peak in certain areas required the utilization of a second order function which is defined below.

$$e(h) = r_0 + s_0(h-h_0) + (s_1-s_0)\ln\{(1+e^{h-h0})/2\}$$

$$+ (s_2-s_1)\ln\{(1+e^{h-h1})/(1+e^{h0-h1})\} \tag{3.12}$$

with

110

$$s_1 = (r_1 - r_0 - s_0(h_1-h_0) + s_0\ln\{(1+e^{h1-h0})/2\} +$$

$$s_2\ln\{2/(1+e^{h0-h1})\}) / (\ln\{(1+e^{h1-h0})/2\} - \ln\{(2/(1+e^{h0-h1})\})$$

where h is the latitude, h_0 is the first set point at which the value of e is r_0, h_1 is the second set point at which the value of e is r_1, s_0 is the slope for h $<<$ h_0 and s_2 is the slope for h $>>$ h_1. The choice to calculate s_1 from r_1 instead of including s_1 as a parameter was made to keep the six model parameters as physically meaningful as possible, r_0 and r_1 thus representing actual values of the property.

Once the coefficients for each Epstein function were obtained at all MLT values, a Fourier expansion was carried out to bridge MLT.

$$\alpha_i(T) = \Sigma \ C_n\cos(2\pi T/24) + \Sigma \ S_n\sin(2\pi T/24) \qquad (3.13)$$

where α_i is one of the Epstein coefficients r, s, or h.

After an attempt at automatic fitting for all MLT values, each MLT was plotted and the interactive phase of fitting began. The software allowed for the repositioning of either set point and for the readjusting of the slopes. Also, the entire set of MLT's could be expanded and replaced by the fourier results at any time during the interactive fitting. In this way, one could see the results of the full model at any point.

Figure 3.14 shows the resulting model for one K_p value both as comparative contour plots and as a histogram of the deviation of the model from the data. The full set of coefficients and a more complete description of the fitting will be made available soon [McNeil and Hardy, 1989].

3.3.2 The Heppner-Maynard Electrostatic Potential

In this work, a series of patterns of the electrostatic potential, which were available only as hand drawn plots, were digitized and fit to spherical harmonics so that they could be used in conjunction with the conductivity [Hardy, et al., 1987] in the calculation of electric fields. The contours of seven Heppner-Maynard patterns were traced on a digitizing tablet. The electrostatic potential values were interpolated from the contours onto regularly spaced grid points in magnetic latitude, from 50° to 90° by 1° increments and by 5° increments in MLT. These were then interpolated further to a 91 x 91 grid for integration in order to determine the expansion coefficients. The series fit was

$$\phi = \Sigma_{n=0,11} \ \Sigma_{m=-1,1} \ C_{n,m} \ k_{n,m} \ Y_{n,m}(\lambda,\cos\theta) \qquad (3.14)$$

where λ is the magnetic local time, θ is (magnetic latitude -70°)/20°, $Y_{n,m} = \cos(m\lambda)P_{n,m}(\cos\theta)$, $b_{n,m}$ is a coefficient that makes the square integral of each Y equal unity and $C_{n,m}$ is the expansion coefficient. The expansion coefficient was calculated by carrying out the integral

$$C_{n,m} = < F(\lambda,\cos\theta) \mid b_{n,m}Y_{n,m}(\lambda,\cos\theta) > \qquad (3.15)$$

Figure 3.15 shows comparitive contour plots for one model. These results are presented more elaborately elsewhere [Rich and Maynard, 1989].

111
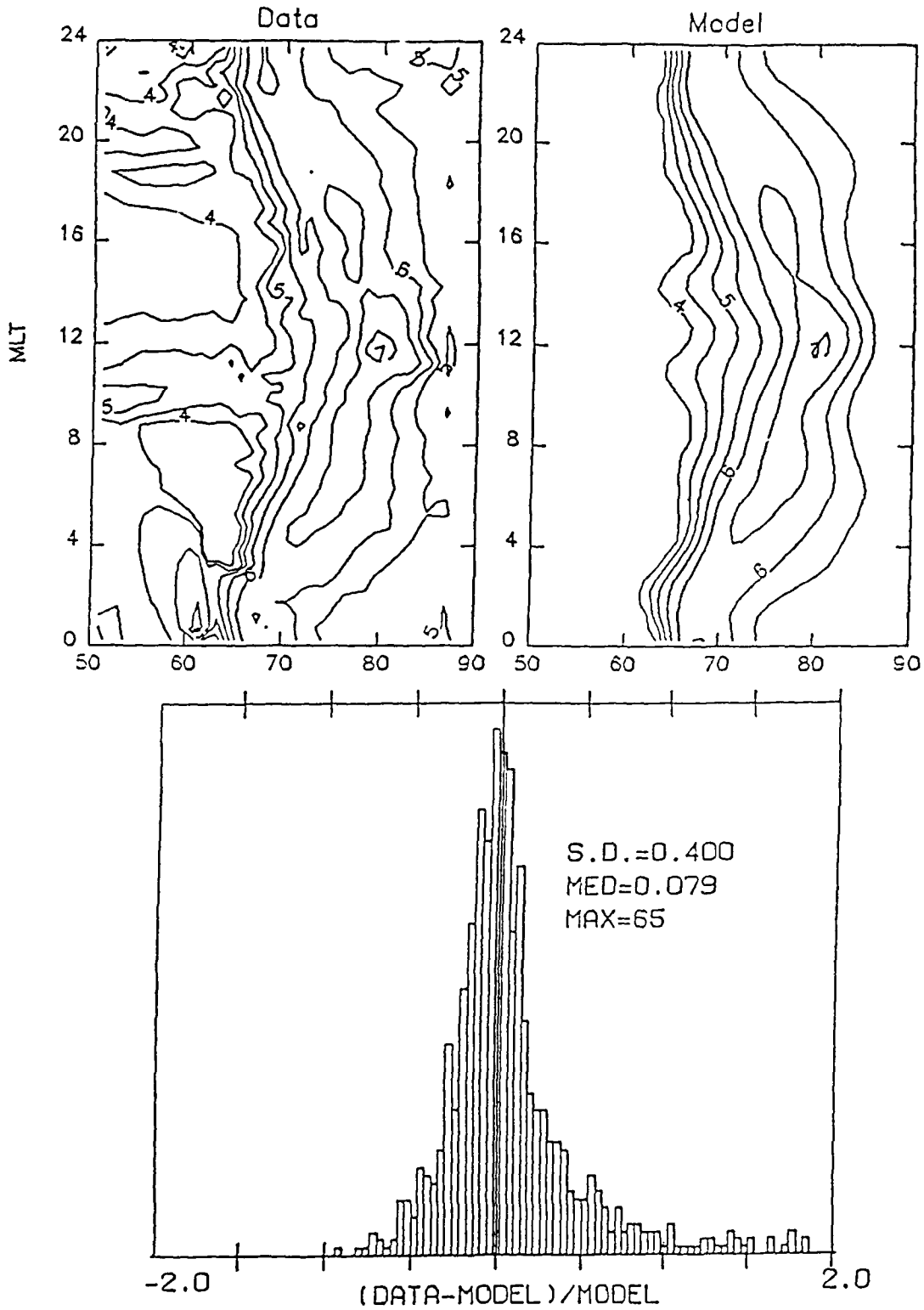
Figure 3.14. Resulting model for one Kp value

112

Figure 3.15. Comparative contour plots for one model

113

References

Alfven, H., *On the Origin of the Solar System*, Oxford University Press, New York, 1954.

Banks, P.M., Williamson, P.R. and Raitt, W.J. (1983) Space Shuttle glow observations, *Geophys. Res. Lett.*, 10, 118.

Cooke, D.L. et al., "Prelimimary Documentation for the POLAR Code", SSS-R-83-6027, October 1984, S-Cubed, LaJolla, CA.

Cooke, M., and Tautz, M., "The Sheath Edge of a Charged Object in a Flowing Plasma", AGU Presentation, Fall Meeting, Dec 1986.

Cooke, D.L., Tautz, M.F., and Rubin, A.G., "The Sheath of a Positive Probe in a Flowing Plasma", presented at Am. Phys. Soc. Numerical Simulation of Plasmas Conference, Sept. 1987.

Cooke, D.L., Tautz, M.F., "Steady State Computer Simulation of Wake-Electron Temperature Enhancement", AGU Presentation, Fall Meeting, Dec. 1988.

Cooke, D.L., Lilley Jr., J.R., and Tautz, M.F., "POLAR Code Simulation of DMSP Charging" presented at the AIAA Aerospace Sciences Meeting at Reno, Nevada, May 1989.

Elgin, J.G. and Sundberg, R.L., "Model Description for the SOCRATES Contamination Code", AFGL-TR-88-0303, October 1988, ADA205181.

Elgin, J.G., Cooke, D.L., Murad, E., and Tautz, M.F., "The SOCRATES 3D Monte Carlo Shuttle Contamination Model", in publication.

Green, B.D., Caledonia, G.E. and Wilkerson, T.D., The shuttle environment: gases, particles, and glow, *J. Spacecraft Rockets* 22, 500, 1985.

Gussenhoven, M.S., Hardy, D.A., Rich, F. Burke, W.J., and Yeh, H.C., "High-Level Spacecraft Charging in the Low-Altitude Polar Auroral Environment", J. Geophys. Res. V90, Nov., 1985.

Hardy, D.A., Gussenhoven, M.S., Raistrick, R., O'Neil, R.R., and McNeil, W.J., "Statistical and Functional Representation of the Patterns of Energy Flux, Number Flux and Conductivity", *J. Geophys. Res.*, 11, 12,275 (1987).

Heinemann, M. et al., "Computer Models of the Spacecraft Wake", AGARD conference, The Hague, Netherlands, June 1986.

Katz, I. et al., "Extension, Validation and Application of the Nascap Code", Final Report, SSS-R-79-3904, January 1979, S-Cubed, LaJolla, CA.

Katz, I. et al., "Plasma Interactions of Spacecraft in Polar Orbit", SSS-R-83-6050, S-Cubed, LaJolla, CA.

Katz I., and Parks, D.E., "Space Shuttle Orbiter Charging", J. Spacecraft and Rockets V20, Jan. 1983.

References (cont'd)

Katz I., Jongeward, G.A., Lilley Jr., J.A., Mandell, M.J., "Polar Code Calculations of the Shuttle Orbiter Plasma Wake and Direct Comparisons with Spacelab II Measurements", AFGL-TR-87-0041, 1987, ADA181160.

Laframboise, J.G., "Theory of Spherical and Cylindrical Langmuir Probes in a Collisionless Plasma at Rest", UTIAS Report #100.

Lai, S.T., McNeil, W.J., and Murad, E., "Time evolution of critical ionization velocity process in a spacecraft environment" (extended abstract), *The Third International School for Space Simulation*, (Beaulieu, France), 1987, pp. 152-155.

Lai, S.T., McNeil, W.J., and Murad, E., The role of metastable states in critical ionization velocity discharges. *J. Geophys. Res.* **92** 5871, 1988.

Lai, S.T., Murad, E., and McNeil, W.J., An Overview of Atomic and Molecular Processes in Critical Velocity Ionization. *IEEE Trans. Plasma Sci.*, special issue dedicated to Alfven's 80th birthday, **17**, 135, 1989.

Lilley, J.R. et al., "POLAR Users Guide", SSS-R-86-7563, AFGL-TR-85-0246, ADA173758.

McNeil, W.J., Cohen, H.A., and Lai, S.T., Private Communication, 1984.

McNeil, W.J. and Lai, S.T., Private Communication, 1988.

McNeil, W.J., Lai, S.T., and Murad, E., Simulation of Collisional Processes in a Critical Ionization Velocity Discharge, *EOS*, **69**, 1373 (abstract), 1988.

McNeil, W.J. and Hardy, D.A., Private Communication, 1989.

Morgan, M.A., Chan, D., Cooke, D.L., and Tautz, M.F., "The Dynamics of Charged Particles in the Near Wake of a very Negatively Charged Object - Laboratory Experiment and Numberical Simulation", in publication.

Papadopoulos, K., On the Shuttle glow (the plasma alternative), *Radio Sci.* **19**, 571, 1984.

Parker, L.W., "Computation of Collisionless Steady-State Plasma Flow Past a Charged Disk", NASA CR-144159.

Radex, Inc. Final Report, "Analysis of Geophysical Data Bases and Models for Spacecraft Interactions", AFGL-TR-86-0221, October 1986, ADA184809.

Rich, F.J. and Maynard, N.C., "Consequences of Using Simple Analytical Functions for the High-Latitude Convection Electric Field", *J. Geophys. Res.*, **94**, 3687 (1989).

Shawhan, S.D. and Murphy, G.B., Plasma diagnostics package assessment of the STS-3 orbiter environment and systems for science, AIAA-83-0253, AIAA 21st Aerospace Sciences Meeting, Reno, Nevada, 10-13 January 1983.

Chan, C., Morgan, M.A., and Allen, R.C., "Electron Dynamics in the Near Wake of a Conducting Body", IEEE Transactions on Plasma Science, VOL PS-14, NO. 6, Dec. 1986.

References (cont'd)

Stannard, P.R. et al., "NASCAP Programmer's Reference Manual", SSS-R-82-5443, March 1982, S-Cubed, LaJolla, CA.

Tautz, M.F. and Cooke, D.L., "Preliminary Documentation for the MACH Code, AFGL-TR-88-0035, Jan 1988, ADA198956.

Tautz, M.F., Cooke, D.L., "Computer Models of Langmuir Probes in a Flowing Plasma", AGU presentation, Fall Meeting, Dec 1988.

4. CRRES

4.1 BASELINE MAGNETOSPHERE

The Baseline Magnetosphere is defined as the one in which the energy transfer from the solar wind to the magnetosphere is minimized. This occurs when the solar wind velocity is minimized, and when B, and in particular B_z, is near-zero. The purpose of studying the baseline magnetosphere is to specify the initial conditions that may apply to more dynamic situations, to verify magnetic field models, and to understand, in detail, processes that may occur in isolation from other processes during the baseline conditions.

For the baseline period 20 April, 1979, SCATHA particle data was analyzed to look at average (over 1/20 of an R_E, or ~10 min) electron and ion flux variations in altitude and pitch angle. Using a simple model magnetic field for this region, the assumption that the electric field may be neglected, and conservation of the first two adiabatic invariants, the specification of these variations was extended from just the single SCATHA orbit on that day to the entire altitude range 5.4 - 8.1 R_E for all local times [Bass and Gussenhoven, 1988]. This specification was compared to the SCATHA Atlas average variations for the conditions K_p = 0-1.

Figure 4.1 shows the calculated stand-off distance (balancing kinetic and magnetic pressures) for 19 and 20 April. The stand-off distance was relatively constant over the first half of 19 April, at between 9.6 and 10 R_E; it expanded to 10.5 R_E over the second half of 19 April; it then contracted steadily from 10.5 to 9.3 R_E during 20 April, a 10% decrease overall.

4.1.1 Particle and Field Data along the SCATHA orbit for 4/20/79

The SCATHA Satellite orbit is a 5.3 R_E x 7.8 R_E, low-inclination (7.9°) orbit with an easterly drift rate of about 5° per day. The satellite is spin stabilized at approximately 1 rpm, with the spin axis of the satellite located in the orbital plane of the satellite and normal to the Earth-Sun line. On 20 April the perigee of the orbit was at 1600 MLT and the apogee at 0300 MLT.

The data used here was taken from the Geophysics Laboratory Rapid Scan Particle Detector and the NASA Goddard magnetic field monitor. The Rapid Scan Particle Detector measures fluxes of electrons and ions in the energy ranges from 100 eV to approximately 1 MeV, and from 100 eV to approximately 5 MeV, respectively. The SCATHA magnetometer is a triaxial fluxgate magnetometer with the three sensors mounted in a mutually orthogonal configuration. The magnetometer sensors are located at the end of a 4-m boom. Each axis has a range of approximately 500 nT and accuracy of about 1 nT at the 1-sigma confidence level.

4.1.2 Particle and Field Modeling

A Mead-type magnetic field model was used for this period. Its scalar potential is of the form

$$V = -B_0 \cos\theta/r^2 - B_1 \, r \cos\theta + B_2 \, r^2 \sin\theta\cos\theta\cos(t-\phi), \qquad (4.1)$$
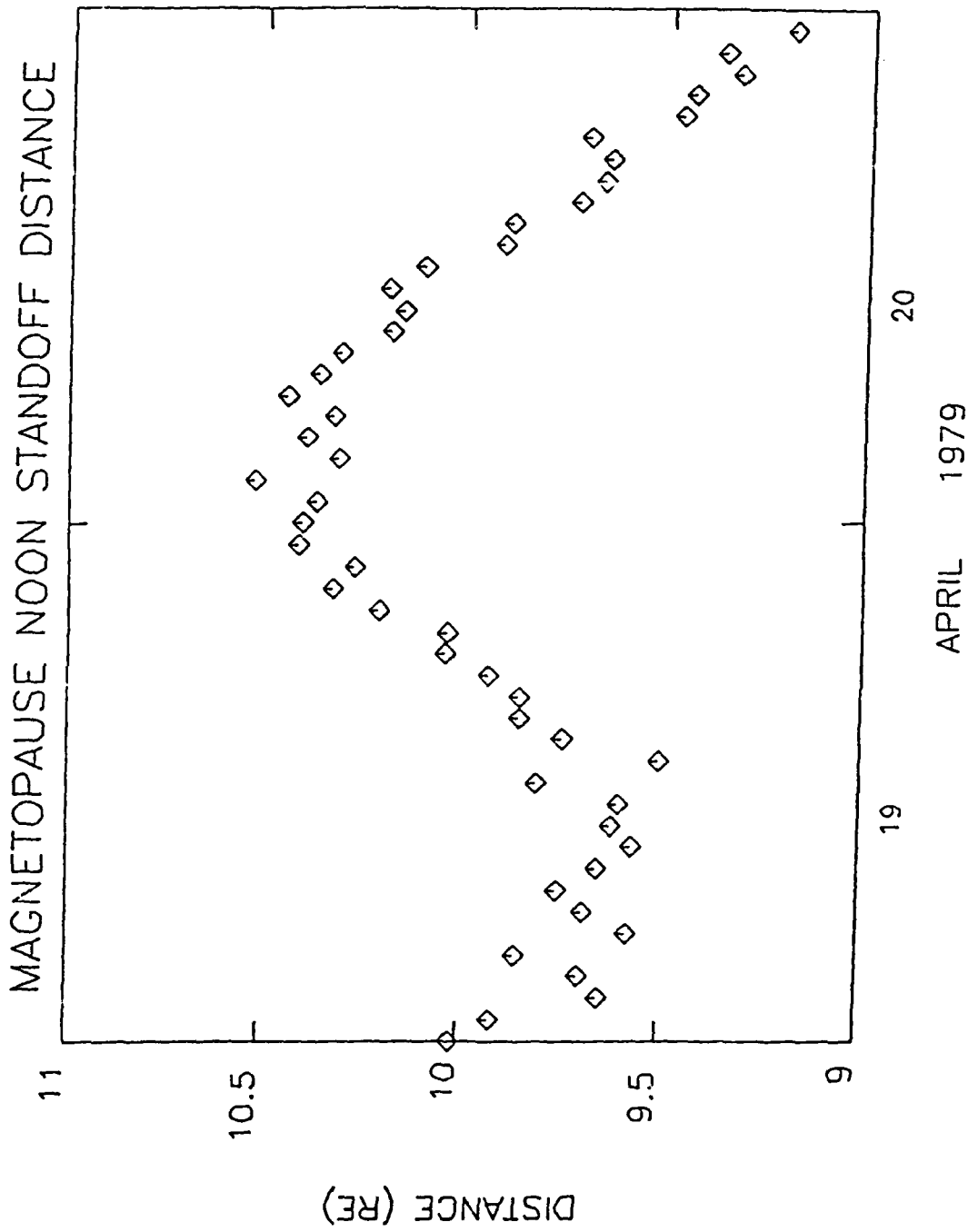
Figure 4.1. Noon magnetopause standoff distance for 19 - 20 April 1979

where B_0 is the Earth's dipole magnetic moment, r is the radial distance in R_E from the center of the Earth, θ is the geomagnetic colatitude, t is the geomagnetic local time (midnight = 0°) and ϕ is a phase angle which rotates the axis of symmetry. The local time values must be converted to the appropriate degrees. For 20 April we find that the magnetometer data fit well to this model if we take

$$B_1 = -10 \text{ nT};$$

$$B_2 = 2.5 \text{ nT};$$

$$\phi = -3 \text{ hours.}$$

Figure 4.2 shows the measured (circles) and the model (solid line) field values along the equatorial plane ($\vec{B} = B_z \hat{z}$)for 20 April. The measured values of B_z are averaged over $1/20 \, R_E$. The differences are great only where the field value is large (at lowest altitudes).

The observed particle populations were mapped to local noon [Bass and Gussenhoven, 1988] by calculating the drift orbits and applying the Louiville theorem. The drift orbits were calculated from the conservation of the first two adiabatic invariants. These permit determination of the noon equatorial crossing position and pitch angle of a particle given its observed position at the satellite's local time.

The Louiville theorem states that the particle's distribution function is preserved along their trajectory; thus the distribution function at the noon equatorial crossing is equal to the observed distribution function at the satellite position.

The resulting noon radial and pitch angle dependencies for each SCATHA energy channel were fit to analytic functions. We implicitly assumed that all the observations are on the magnetic equator, although this is not exactly true. On 20 April, the magnitude of the geomagnetic latitude of SCATHA never exceeded 5°.

4.1.3 Equatorial Maps

From the noon equatorial model particle populations were computed at other local times by first obtaining the noon equatorial crossings from the drift orbits as described above. Then the Louiville theorem was applied to obtain the population at the desired location from the model population at the noon location.

From these results we can derive properties such as energy and particle densities, average energy, pressures and beta parameters. These require the calculation of moments of the distribution function similar to those discussed by Mullen and Gussenhoven [1983]. In our case, we performed double integrations over pitch angle and momentum, of the form

$$M_{nm} = \int\int F(E,\alpha)E^n(\sin\alpha)^m p^2 dp 2\pi \sin\alpha d\alpha, \tag{4.2}$$

where F is the distribution function at a point in space for particle energy E and pitch angle α. M_{00} gives us the particle number density, M_{10} the total energy density, and M_{12} the energy density perpendicular to the magnetic field. The integration over pitch angle is approximated as a sum over the 10 degree bins. Thus the element $2\pi d\alpha$ is replaced by:

$$2\pi d\alpha = 2\pi(\pi/180)10 = \pi^2/9. \tag{4.3}$$

119

20 APRIL 1979   MAGNETIC FIELD BZ
MEASURED (SYMBOLS) AND ADJUSTED MEAD MODEL (LINE)
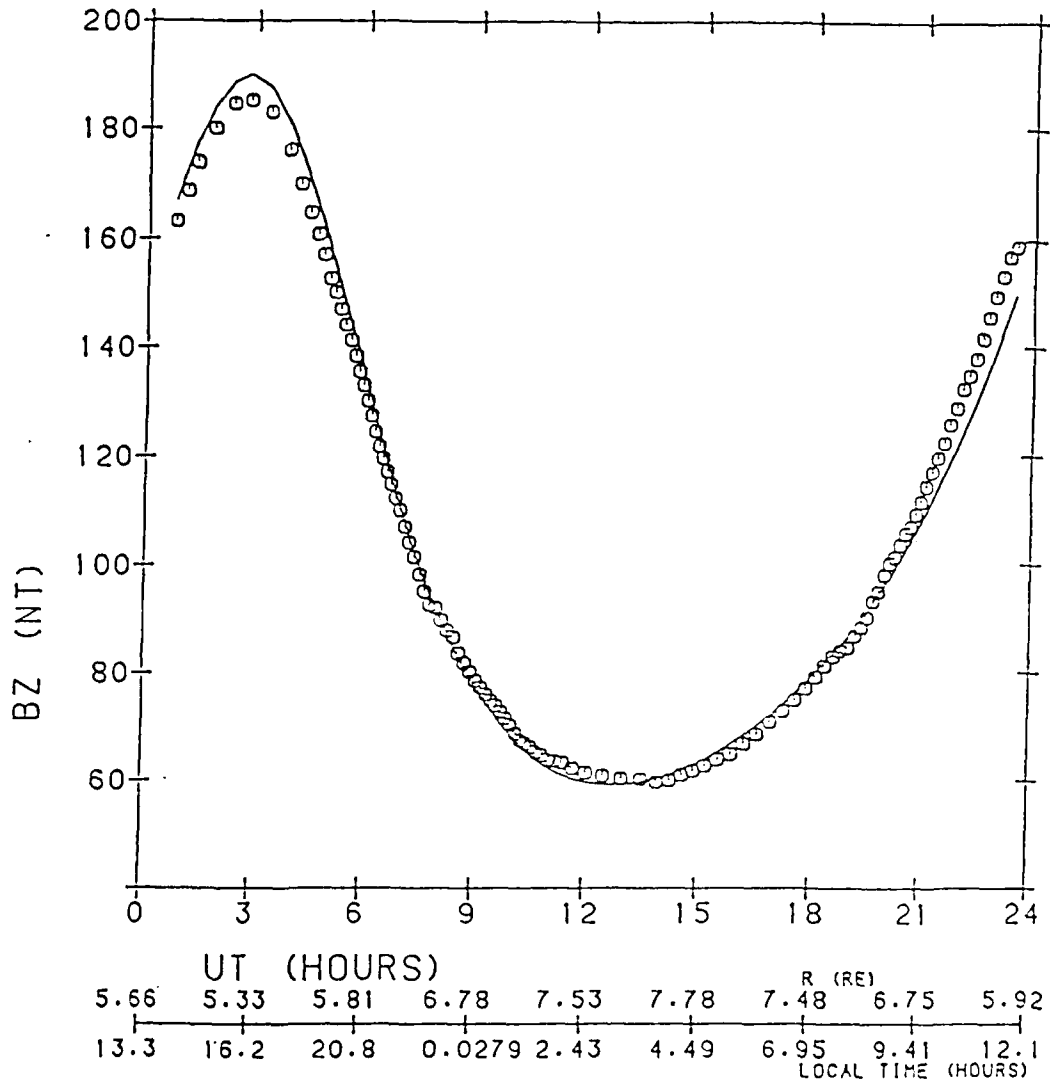
Figure 4.2. Comparison of the observed Z component of the magnetic field on 20 April 1979 with the adjusted Mead model

120

To perform the integration over momentum, we transform relativistically to an integral over energy:

$$p^2 dp = [(E_0 + E)\sqrt{(E^2 + 2E_0 E)}/c^5] dE, \qquad (4.4)$$

where E_0 is the particle rest energy and c is the speed of light.

Also of interest is the pitch angle anisotropy index defined by Mullen and Gussenhoven [1983]:

$$AI = F_{90}/F_{45} - 1, \qquad F_{45} > F_{90}, \qquad (4.5a)$$

$$AI = -(F_{45}/F_{90} - 1), \qquad F_{90} \geq F_{45}, \qquad (4.5b)$$

where F_{90} is the particle distribution function perpendicular to the magnetic field and F_{45} is the distribution function at 45° to the magnetic field. This index ranges from -1 for extremely field-aligned (butterfly) distributions, through 0 for an isotropic distribution, to +1 when the particle velocities are predominantly normal to the magnetic field.

4.1.4 Results

4.1.4.1 Equatorial Maps

Figure 4.3 shows the energy densities for the 20-400 keV electron and ion populations, and the anisotropies for 96 keV electrons and 126 keV ions. The energy density maps show nearly circular contours. The ion energy densities decrease from 20 keV/cm³ at 5.4 R_E to 5 kcV/cm³ at 8.1 R_E. The electron energy densities are nearly 2 orders of magnitude smaller and vary only by 20% over the radial range. For both the ions and electrons, the anisotropies reflect the transition from dayside normal to nightside butterfly (field-aligned) pitch angle distributions observed for electrons by West [1979], including the appearance of the butterfly distribution in the afternoon.

The appearance of afternoon butterfly distributions in our results is due entirely to the rotation of the local time axis of symmetry from the noon-midnight meridian to the 0900-2100 meridian, reflecting the similar rotation of the axis of symmetry in the adjusted Mead model used for this period. Although this rotation may be an artifact of incomplete specification of the magnetic field model, for example, the lack of a realistic ring current representation, we will later show indication of a real dawn-dusk asymmetry in the ring currents. Although West's results may be influenced by interaction of the electrons with the magnetopause, this cannot be the case here, since our model does not take that into account. Our model forces the particle populations to have the same local time symmetry as the magnetic field, since the drift orbits must have that symmetry. When interaction with the magnetopause is a dominant factor, ion pitch angle distributions, not measured by West, would exhibit morning butterflies, rather than afternoon, since the ions and electrons drift in opposite directions.

Figure 4.4 shows comparison of the total (electron + ion) energy densities derived adiabatically from the April 20, 1979 SCATHA data, with a similar map in the SCATHA Atlas [Mullen and Gussenhoven, 1983] (although for the entire SCATHA energy range), derived statistically for K_p = 0-1, typical for baseline conditions. Note the dawn-dusk asymmetry in the Atlas results, compared to the near-circular symmetry in the adiabatic results. In particular, a maximum in total energy density extends at geosynchronous altitude well into the dusk side of the midnight meridian. The ring current distribution inferred from the zero density gradient (westward at a larger radii,

Figure 4.3. Adiabatically trapped particle populations according to the Empirical model constructed for 20 April 1979

TOTAL ENERGY DENSITY

(keV/cm^3)

CURRENT WORK

SCATHA ATLAS

Kp0,1
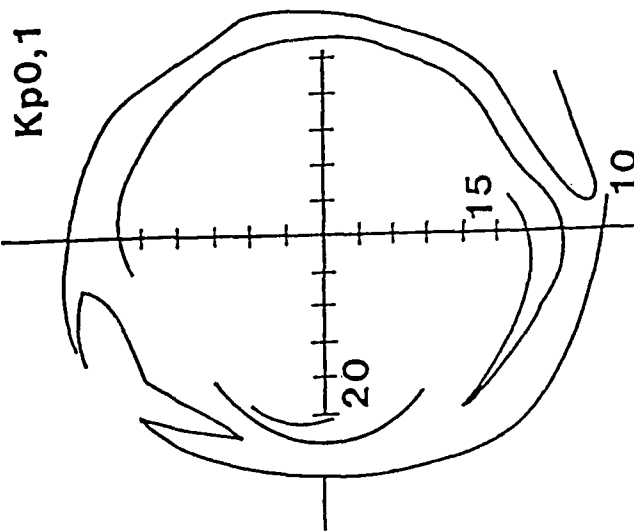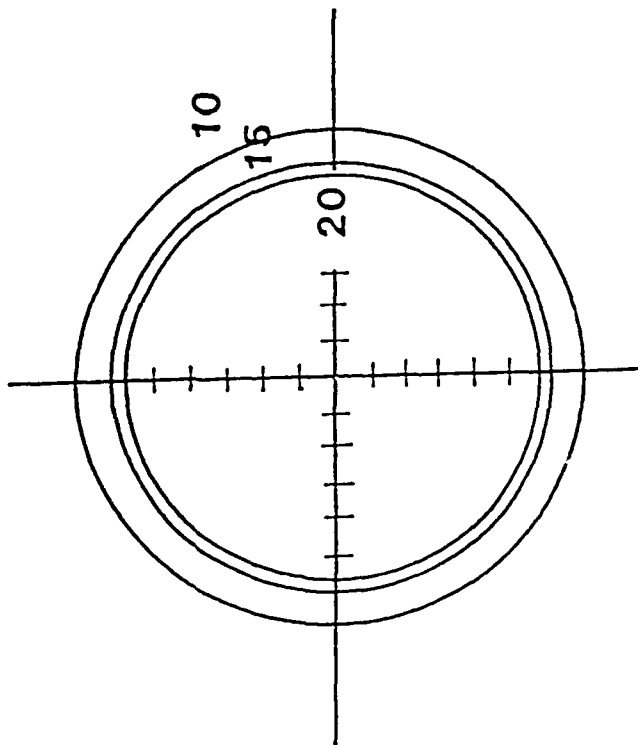
Figure 4.4. Total energy density: Comparison between results of this work and SCATHA Atlas

123

eastward at smaller) could produce a depression in the magnetic field in the dusk-midnight sector relative to the midnight-dawn sector. A convection electric field of the type found by Baumjohann, et. al., [1985] could produce such a distribution, since it is strongest on the dawn side, where it could convect particles out of the radial region of interest.

4.1.4.2 Shell Splitting

Shell-splitting [Roederer,1970] has often been invoked to explain the commonly observed trend from normal pitch angle distributions (peaked at $90°$) on the dayside to butterfly (peaked at lower or higher angles) on the nightside. In the adiabatic form of shell-splitting, particles are found on a common field line at a particular local time drift to or from different field lines at other local times, depending on their pitch angles. Thus $90°$ particles found at midnight on a particular equatorial radial distance have drifted from a larger distance at noon than particles at lower or higher pitch angles. This difference generally increases with distance, i. e., the shell-splitting effect increases as distance increases. If the noon pitch angle distribution is normal, and changes slowly with L, then a negative gradient in the radial distribution dictates that the $90°$ population on the nightside will decrease more rapidly with distance than the populations at lower or higher pitch angles, leading to a trend from normal to butterfly distributions. In the nonadiabatic form of shell-splitting, the $90°$ particles actually drift outside the noon magnetopause, where some or all of them are lost, resulting in a precipitous drop of that population.

These features are illustrated (Figure 4.5) in the pitch angle distributions found over the SCATHA orbit on April 20, 1979. The left-hand panel shows a schematic diagram of the orbit, on a local time-L grid, where L is the McIlwain [McIlwain, 1961] parameter. Beginning at perigee, during the late afternoon local time, the satellite moved counter-clockwise, completing the ascending portion of the orbit post midnight LT (noon UT). The high energy electron pitch angle distributions changed from normal in late afternoon local time to isotropic in the midnight sector, then to butterfly in the early morning sector. The switchover from isotropic to butterfly coincides with the beginning of a sharp drop in the $90°$ population at L = 7.7 seen in the right-hand panel for the ascending portion of the data (circles). In that panel, we also see the $90°$ population observed during the descending portion of the orbit (triangles), as well as the fit to both sets of data (line). The differences in the ascending and descending results is puzzling at first, since for purely adiabatic motion in negligible electric field, one would expect the population of $90°$ equatorial pitch angle particles to depend only on L and E. Upon further examination of the effects of a non-zero electric field and SCATHA's non-zero magnetic latitude [Bass and Gussenhoven, 1988], it was determined that neither of these could account for the differences.

4.1.4.3 Moving Magnetopause

In the left-hand panel of Figure 4.6 is shown the noon magnetopause stand-off distance for April 20, 1979, calculated from the pressure balance between a dipole field and the solar wind and densities for that period. It is seen that the stand-off is relatively level at 10.4 R_E until 0900 UT, and then decreases steadily to 9.4 R_E at the end of the day. When the satellite is at L = 7.5 R_E (case 1) the stand-off distance is 10.2 R_E and the noon side of the $90°$ drift orbit (solid line) is just inside the magnetopause (dashed line), as shown in the right-hand panel. When the satellite reaches the same L-shell on the descending portion of the orbit (case 2), the magnetopause has moved to 9.6 R_E, causing particles to run into it and be lost. Calculations of the L-shell at the noon magnetopause crossings give 7.6 and 7.2 R_E, for stand-off distances 10.2 and 9.6 R_E, using the dipole + parabolic magnetopause model of Stern [1985]. These are in reasonable agreement with the values 7.7 and 7.3 found experimentally, if we interpret these

Figure 4.5. Ascending-descending mismatch on 20 April 1979

MAGNETOPAUSE CROSSINGS
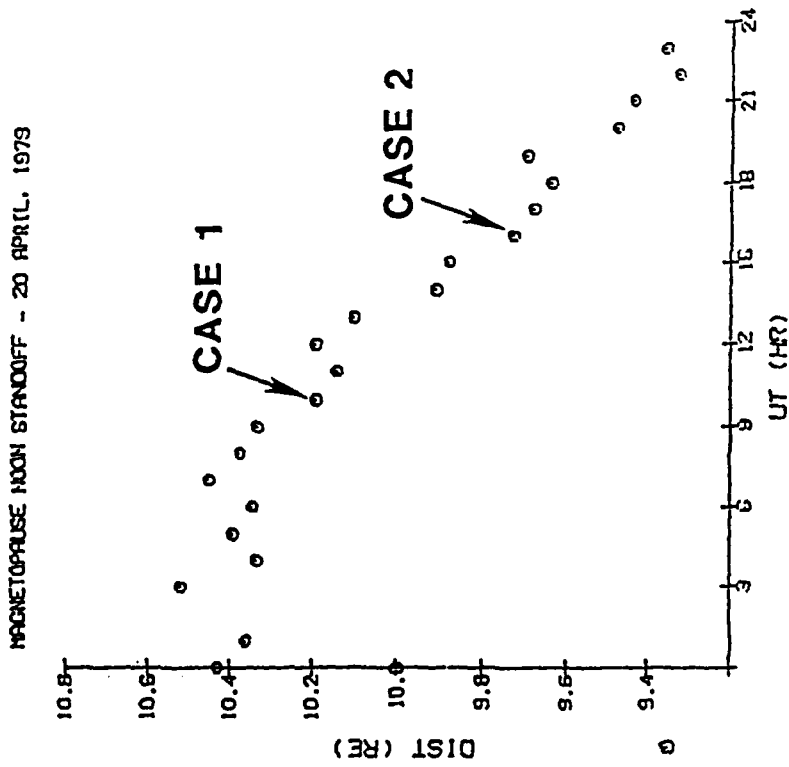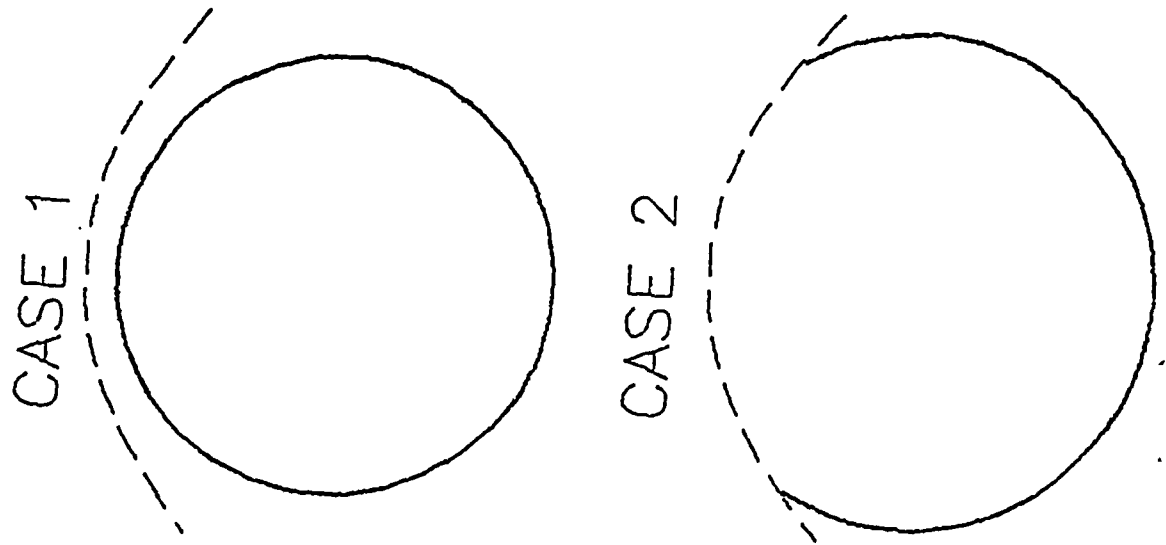
Figure 4.6. Noon Magnetopause Crossings

values to be for the drift orbits which just touch the noon magnetopause. The magnetopause loss sink may be a source for energetic electron precipitation observed near the cusp [Matthews, et. al, 1988]. The L-shell dependence of the populations crossing the magnetopause, since they do not drop off to zero, might be used to infer something about the dynamics of the magnetopause, for example, the strength of the wave-particle interactions there. The magnetopause loss sink, in this case at least, appears to be the primary cause of the butterfly pitch angle distributions seen in the electron populations.

However, one also expects that the magnetopause would interact with the ions. That this is not apparent here is due possibly to the relatively steep radial slope in the ion population, over the entire radial range, which may mask the magnetopause cutoff seen more clearly in the electron population. Furthermore, the cutoff may not be as sharp for ions as for electrons, due to the larger ion gyromagnetic radius.

4.1.5 Summary

In conclusion, we have derived a model of the baseline trapped population which crosses a single SCATHA orbit, assuming conservation of the adiabatic invariants and total energy, and negligible electric field. Although reasonable agreement has been found with statistically derived populations, a significant dawn-dusk asymmetry is found in the statistically derived pressure gradient which is not found in our model. This could be the source of a ring current dawn-dusk asymmetry, which could produce a similar asymmetry in the magnetic field. Small baseline convection electric fields may be responsible for this asymmetry. We have definitively identified a significant magnetopause loss sink, brought about by the inward moving magnetopause to deplete formerly trapped particles, as the primary cause of nightside electron butterfly pitch angle distributions. Such a process could supply energetic electrons for dayside precipitation near the cusp.

4.2 INTERNAL FIELD MODELS

Four internal magnetic field models were compared on the basis of their L-shell and subsequently their B field determination. Each of these spherical harmonic models was determined to a different degree and order. The higher the degree, the more complex the structure becomes and thus, the more easily contributing components (i.e. the crustal component) may be analyzed. IGRF 1985 was truncated to 10 to isolate the core component of the field, but this may not be the best representation of the internal field. Barraclough and Cain limited their models due to the global coverage and accuracy of the data (to 12 and 15, respectively). Magsat goes to a high degree due to superior global coverage of the satellite combined with highly accurate observatory data and less accurate scalar data from remote regions (to 50, truncated from 66).

Barraclough et al. [1975] derived Schmidt quasi-normalized main field coefficients from five data sets: survey, observatory, oceanographic, ships' compass, and satellite data. The first four groups came from the World Digital Data Centre C1 at Herstmonceux and spanned the years 1955 to 1975. The data was reduced to sea level and to a common epoch, 1965. The satellite data was obtained from a model [Cain, August 1973] based on the OGO series of satellites (2, 4, and 6, collectively called POGO).

127

The Magsat model described here was derived by Cain et al. [1988a] using only the radial component of the Magsat data, plus observatory data taken within two hours of midnight for Kp limited to about 1⁺. Magsat data covers a very short time span, thus the observatory data was selected from 1978 to 1983 to minimize annual variations which show up in short data sets. For our comparisons, the additional computation time required for n=50 is unjustifiable, so this model was truncated to n=15.

IGRF 1985 was put out by the International Association of Geomagnetism and Aeronomy (IAGA) Division I, Working Group 1. The group selected GSFCMF80 [Langel and Estes, 1985] truncated to n=10 for the DGRF 1980. They applied an SV 1980-1985 model and a predictive 1985-1990 model to this to obtain the IGRF 1985 coefficients. Both the SV and predictive models were the mean of three models submitted to the group. The GSFCMF80 model is based on Magsat data (Nov. 1979 - April 1980) supplemented by data from 91 magnetic observatories (1978-1982). The final data set was composed primarily of dawn data and augmented by dusk data for optimal geographic coverage. A discontinuity (jerk) seen in the SV model in 1978 required the data to be fit with two lines. Cain found a shift in SV after 1982 (possibly another jerk), therefore IGRF 1985 might not project very well to 1990. Thus, Cain started with his n=15 Magsat model, then used observatory data, Project Magnet, and ship-towed magnetometer data sets to get a SV model to extrapolate the Magsat model to future epochs. The observatory data was comprised of Kp < 2 and data taken within four hours of local midnight. Due to the possibility of a jerk in 1983, supplemental data was used. Project Magnet data excluded data within two hours of local noon and where Kp > 2. Ship-towed data was kept for Kp < 1⁺ within four hours of local midnight.

McIlwain's L parameter is used to organize the radiation belt data. It maps the real Earth's field onto that of a dipole. In a time-independent magnetic field (dipole or otherwise) and zero electric field, trapped particles conserving their adiabatic invariants mirror at points of fixed B_m and I as they drift longitudinally around the Earth. In a dipole field this means that they drift on field lines of fixed L. Thus, McIlwain defined L for a non-dipole field as that given by the same functional relationship with I and B_m as for a dipole field. That is, I and B_m are computed for a given point in the non-dipole field and the McIlwain functional relationship,

$$\frac{L^3 B_m}{M} = F\left(\frac{I^3 B_m}{M}\right)$$

(where, M is the dipole moment, B_m is the magnetic field at the mirror points, I is the invariant integral, and L is the maximum equatorial radius) is applied to get L at that point. Particles thus mirror at points of fixed L. The simple geometric interpretation of L that holds for a dipole field, that L is the radial distance in R_E of equatorial crossing of the field line is approximately valid for the internal models discussed here. L is less useful by about $5R_E$ where the effects of the imbedded plasma become comparable to the internal field significantly distorting the field lines and the conservation of adiabatic invariants may be violated. Also, L is not conserved if the electric field is significant.

Comparisons of the L-shell values determined by each of the models (Table 4.1) incorporated into a software package currently available at GL (OPTRACE), showed very good agreement between IGRF 1985 and Cain 1990. MAGSAT 1980 and Barraclough 1975 also agreed pretty well with IGRF 1985, but not quite as closely as Cain 1990.

Originally, L was determined for each point by the full evaluation of the integral I from the point in space to its conjugate mirror point. Thus, as L gets longer, the line gets longer, and the

Table 4.1. MAXIMUM L-SHELL DIFFERENCES BETWEEN ±20° LATITUDE
All models Compared to IGRF 1985 (Model-IGRF)

Year	Alt. (x10³km)	Barr (x10⁻³)	Magsat (x10⁻³)	Cain (x10⁻³)
1980	0.0	4.10	1.32	2.86
	2.0	4.13	1.08	1.98
	4.0	4.42	1.13	1.61
	6.0	5.13	1.03	-0.57
	8.0	4.98	1.28	1.04
	10.0	4.73	1.06	-0.54
1986	0.0	13.36	6.21	2.07
	2.0	13.78	6.05	1.49
	4.0	14.96	5.65	2.08
	6.0	16.16	5.91	2/04
	8.0	17.62	6.20	1.82
	10.0	19.40	6.56	2.16
1990	0.0	19.89	11.19	3.26
	2.0	20.31	10.57	2.10
	4.0	22.50	10.40	2.45
	6.0	24.59	11.27	2.44
	8.0	25.99	11.59	2.64
	10.0	28.77	12.30	3.51

computation becomes more time consuming. The length of the line goes as the inverse of $\sin^2\theta$, where θ is the colatitude. So as one nears the poles, the length of the line increases sharply. Hence, the computation time increases sharply. To alleviate this problem, numerical techniques have been used to try to compensate for this. These tend to result in discontinuities due to dropping terms in the expansion with increasing altitude. There are also difficulties at low altitudes where the field deviates significantly from the dipole.

OPTRACE uses such numerical techniques. The linear relationship between the number of steps and the length of the trace breaks down for the short field lines. Thus, a three-dimensional model representing the field line length vs. the dipole equatorial radius, geomagnetic latitude and longitude for the $0.5R_E$ to $2.0R_E$ range is used. Several routines were evaluated to find the optimum combination for the line trace. LINTRA (from MAGFLD?) [Stassinopoulos and Mead, 1971] uses the fourth-order Adams formula in cartesian coordinates. It doesn't have a self-starting algorithm, it needs four points in the history of the trajectory to proceed. Hence, three fourth-order Runge-Kutta steps are done to initiate the trace. Once started, only one field evaluation per step is required. All steps have equal size. The algorithm is controllable via the step size, since the step size determines the number of steps and hence, the CPU time. To determine L-shell, CARMEL [INVAR by McIlwain, 1965] was chosen. It converts the field values to their logarithms and integrates over the change in variables. For the CRRES orbit, it was decided that the algorithm was sufficiently accurate when there were 100 steps for a fixed line length of $2R_E$. OPTRACE is very accurate to $\pm40°$ (which is more than adequate for CRRES, which doesn't exceed $\pm20°$). However, if one is interested in higher latitude calculations, the algorithm should be improved for the longer line length.

To get around the problems generated by numerical techniques, Kluge [1972] transformed to inverse coordinates before computing the field. Using a natural coordinate system centered on a dipole, inverse coordinates are straight, thereby simplifying the integration and interpolation. This alleviates the truncation problem and the problem of integrating over the poles. Cain recreated this work, updating the interpolation tables using his current models.

To compare the accuracy of the various codes, plots were made of the differences between L-shell values calculated from interpolation tables, Cain's integration code, using Cain's model in OPTRACE, and using IGRF 1985 in OPTRACE. A discrepancy was found between the results obtained from OPTRACE and the two codes sent from Cain. The problem was attributed to Cain's use of a twenty year old value for the dipole moment. The dipole moment has been found to be decreasing over time. Even over a span of twenty years the change has been been sufficient to be discernible in L calculations. When the updated dipole moment (as determined by the IGRF 1985 spherical harmonic coefficients) replaced the old value coded in the integration code sent by Cain, the results much more closely coincided with those obtained from OPTRACE. Since the interpolation tables were determined from the output of Cain's integration code using the old value for the dipole moment, the results from the interpolation code could not be brought into agreement with the integration codes.

Finally, the models were compared on the basis of their determination of the B field and its components (Tables 4.2 - 4.5). Here, some variations were found. The models agreed very well in terms of L; so well in fact, that the differences are barely distinguishable experimentally. The B field and its components also agree fairly well, however there are measurable differences between the models.

130

Table 4.2. MAXIMUM B_{mag} DIFFERENCES BETWEEN ±20° LATITUDE
All models Compared to IGRF 1985 (Model-IGRF)

Year	Alt. (km)	Cain (nT)	Magsat (nT)	Barraclough (nT)
1990	350	257.34	-306.22	-639.74
	850	162.72	-175.11	-409.83
	1500	97.12	-98.37	-249.93
	10000	3.28	-5.58	-14.37
	15000	1.19	-2.36	-5.39
1985	350	95.57	-159.15	-442.93
	850	60.16	-90.13	-287.49
	1500	36.33	-51.14	-175.70
	10000	1.59	-2.65	-9.50
	15000	0.61	-1.13	-3.54
1980	350	163.59	66.05	-249.10
	850	105.47	40.45	-165.36
	1500	63.34	23.26	-106.03
	10000	1.95	-1.60	-4.97
	15000	0.72	-0.71	-1.73

Table 4.3. MAXIMUM B_r DIFFERENCES BETWEEN ±20° LATITUDE
All models Compared to IGRF 1985 (Model-IGRF)

Year	Alt. (km)	Cain (nT)	Magsat (nT)	Barraclough (nT)
1990	350	-294.66	-719.18	-1073.37
	850	-189.53	-473.74	-772.41
	1500	-115.02	-298.27	-530.36
	10000	-3.95	-14.00	-32.09
	15000	-1.40	-5.37	-12.76
1985	350	-99.83	-356.79	-695.26
	850	-64.34	-228.41	-493.11
	1500	-39.19	-139.94	-334.51
	10000	2.05	-6.00	-19.35
	15000	0.82	-2.29	-7.53
1980	350	203.63	-95.77	-317.15
	850	128.06	-64.05	-213.80
	1500	76.54	-41.49	-139.39
	10000	2.34	2.40	-6.70
	15000	0.81	1.02	-2.40

131

Table 4.4. MAXIMUM B_θ DIFFERENCES BETWEEN ±20° LATITUDE
All models Compared to IGRF 1985 (Model-IGRF)

Year	Alt. (km)	Cain (nT)	Magsat (nT)	Barraclough (nT)
1990	350	192.72	-409.73	-530.87
	850	119.87	-274.11	-368.74
	1500	69.15	-172.56	-244.80
	10000	1.85	-6.34	-14.60
	15000	0.67	-2.28	-5.61
1985	350	62.09	-196.02	-361.87
	850	34.48	-129.86	-248.02
	1500	20.21	-81.72	-161.66
	10000	1.02	-3.01	-9.11
	15000	0.40	-1.09	-3.51
1980	350	131.44	68.87	244.99
	850	83.42	38.26	155.15
	1500	49.78	19.18	91.74
	10000	1.88	-0.88	-4.05
	15000	0.65	-0.37	-1.49

Table 4.5. MAXIMUM B_ϕ DIFFERENCES BETWEEN ±20° LATITUDE
All models Compared to IGRF 1985 (Model-IGRF)

Year	Alt (km)	Cain (nT)	Magsat (nT)	Barraclough (nT)
1990	350	139.07	312.77	-495.48
	850	96.18	190.35	-316.94
	1500	62.82	-113.93	-220.78
	10000	2.70	-7.30	15.06
	15000	0.96	-2.97	05
1985	350	-54.71	-141.24	-336.16
	850	35.45	-90.84	-215.31
	1500	23.01	-55.42	144.23
	10000	1.08	-3.03	9.38
	15000	-0.41	-1.22	3.70
1980	350	-98.85	71.28	-201.41
	850	-65.16	48.37	-125.84
	1500	-39.71	31.36	75.72
	10000	-1.09	1.59	3.70
	15000	-0.39	0.62	1.34

4.3 HMIN MODELS

Models of Hmin in the South Atlantic Anomaly (SAA) region (0° - 60°S, 60°W - 40°E) were constructed for use in analyzing data from the Defense Meteorological Satellite Program (DMSP). Two models were generated, one for epoch 1985.0 and the other for epoch 1987.0. These may be updated to future epochs (to be used with data from the Combined Release and Radiation Effects Satellite, CRRES, for example) using the same software which was used to develop these two models.

A data base was generated by finding Hmin as a function of latitude and longitude in the SAA. At any given longitude, a system of two non-linear equations is solved for H and latitude, given B and L, using a discrete version of the Newton-Raphson Technique. A quadratic line search was then performed for the epoch 1985.0 model such that the minimum H was obtained as a function of longitude. Problems arise with this method occasionally in finding appropriate starting values of H that bracket the minimum for a given B and L, particularly for the extreme values of L. Hence, a manual search was used to find those points for which the quadratic line search did not converge. To alleviate these problems, the 1987.0 model used a search routine which selected three points along a given longitude and tested for the minimum. This procedure was repeated until the three points converged to within 0.25 km (an improvement in accuracy by a factor of four compared to the epoch 1985.0 database).

Initially, the data base was selected for a range in L of 1.2 to 3.0 R_E. These points were fitted with a fourth order polynomial and the coefficients were used to evaluate Hmin for a given B and L. Later, the range was extended down to 1.1 R_E, at which time an unexpected upturn of Hmin was found as the equatorial limit of $L = (B_o/B)^{1/3}$ was approached. This upturn precludes the use of polynomial fitting due to the required accuracy limit. Thus, a bicubic spline fit was done.

A two-dimensional (bicubic) spline fit requires a rectangular grid of data points. The equatorial limit on L cuts off data points at low L and low B. Thus, one must invent suitable points to fill out the missing data. For 1985.0, a first approximation for these points was obtained using an eighth order polynomial. This filled database was then fit with a bicubic spline. The coefficients from this fit were used to calculate Hmin given any B and L. Note, that the filled in data base contains only even values of B. The odd values ot B and the boundary values of B and L were used to test the fit. This procedure of filling the data base, fitting it, and testing it was repeated until the values obtained from the model agreed with those of the database to within 1.0 km. For 1987.0, the starting values for the filled data were the final values used to fill the 1985.0 model. This time the fit was done to an accuracy of 0.5 km. Beware that near the boundary, the accuracy of the model may not be relied on too greatly. The program itself will not allow values below L = 1.1 R_E, however, for low B, the boundary cut-off is higher than this. Thus, caution is urged when considering values within 0.05 R_E of the boundary L value for a given B.

On the Cyber (using the NOS operating system), the model is run using HM85(87). This program requires the file CHM85(87). This file is opened within the program, so one needs only to make sure that it is available. This code prompts for B and L and then returns the Hmin value. A BASIC version of this code is also available. It was written on a Zenith Z-100 using Z-BASIC. This program is called HMB.85(87) and requires CEFS.85(87). Like the Fortran code, HMB.85(87) opens CEFS.85(87) during execution. Make sure that CEFS.85(87) is available in disk drive A when running HMB.85(87). This code also prompts for B and L, then returns Hmin. Error messages are included in both versions to ensure that one stays within the accepted ranges of B and L values.

4.4 SCATHA SPECTROGRAM DISPLAY

Efficient yet comprehensive display of CRRES data will be an important aid to researchers. The SCATHA data base has been used for the development of prototype survey plots of averaged binned data. In this section we describe software for the statistical analysis of SCATHA data, and the generation of spectrogram survey plots suitable for distribution to researchers world-wide. The spectrograms portray radial, pitch angle, and energy distribution of trapped particles.

4.4.1 Statistical Analysis

Program SC5STAT [Radex,1987] has been updated to include all the active energy channels on the SC5 instrument. The total range now covered is 100 eV to 1 MeV for the electrons (12 channels) and 100 eV to 5 MeV for the ions (17 channels). A switch in the code provides the option to convert the data counts in each channel to fluxes. This option was activated for the present application. The measurements (flux or counts) in each channel are sorted into L-shell bins 0.05 R_E wide, centered on multiples of 0.05 R_E. Each L bin is in general encountered twice, in the ascending and descending portions of the orbit, respectively. These are treated as separate bins, and so labeled. A bin at the boundary between ascending and descending portions of the orbit is counted twice, once as an ascending bin, and once as a descending bin. The data within each bin are further sorted into 19 pitch angle bins, the first at 0-5°, followed by 17 10° bins centered at multiples of 10°, and terminating with a bin at 175-180°. The binary output file format, as presently constituted, is as follows:

Header record #1.

Two 50-character strings: the first gives the day number, the second indicates the type of output, fluxes or counts (presently fluxes)

Header record #2

Three integers indicating, respectively, the number of data channels (29), the number of ephemeris variables (23), and the number of 30-character (52) labels which follow. Each label describes an ephemeris variable or a data channel. The ephemeris labels (at present there are 23) come first, followed by the data channel labels.

Header record # 3

An integer indicating the number of pitch angle bins (19) followed by 19 real numbers, giving the central pitch angles for these bins.

Data records

One record for each L bin. The record begins with the 23 ephemeris values, in the following order:

> Mean time (real) (Day number + fraction of day)
> Number of readouts (integer)
> Central L-shell value (real)
> Ascending-descending flag (real): +1.0 if ascending, -1.0 if descending
> Altitude, km (real)
> Magnetic latitude, deg (real)
> Magnetic east longitude, deg (real)
> Magnetic time, hours (real)
> Solar-magnetic latitude, deg (real)
> Solar-magnetic local time, hours (real)
> Geocentric solar-magnetospheric latitude, deg (real)
> Geocentric solar-magnetospheric local time, hours (real)
> Solar-magnetic x, y, and z components of model magnetic field, nT (3 reals)
> Magnitude of model magnetic field, nT (real)
> Minimum of model magnetic field magnitude along field line, nT (real)
> ECI x, y, and z coordinates of Sun, km (3 reals)
> ECI x, y, and z components of dipole moment, nT (3 reals)

The altitude and all parameters following apply to the mean time of the bin. The ephemeris list is followed by the measurement statistics, grouped in the following manner:

> Mean measured fluxes, part/cm^{2}sec/eV/sr (551 reals)
> Standard deviations (551 reals)
> Number of measurements (551 integers)

In each group all the results for the first pitch angle bin are provided first, followed by all the results for the second, etc. Within each pitch angle bin, the results for the 12 electron channels are listed first, in order of increasing energy, followed by the results for the 17 ion channels.

4.4.2 Presentation

This data was then represented by color spectrograms. Due to the volume of data which will be obtained from CRRES, a set of survey plots with which to scan the particle flux distributions of the electrons and ions would be useful. Thus, to examine what sort of format would be suitable, the SCATHA data was used to develop the color spectrograms which represent this multi-dimensional data in a concise manner. The accompanying Figure, 4.7, (available in both paper and transparent media) shows the ion distributions observed by SCATHA as it was ascending on Day 110 of its orbit. Energy has been plotted versus the L-shell parameter (in Earth radii). The local and universal times corresponding to these L observations have been plotted on an axis below the L-axis. The data is binned into .05 R_E sections with further divisions of 19 pitch angles (0 to 180 degrees). Additionally, the colors represent the particle flux. Clearly, as energy increases, the flux decreases. The color bar is the same for electrons and ions so that one may see the correlation between their distributions.

These plots were developed on the Cyber (available on NOS and NOS/VE) using TEKSIM which is a graphics package developed for use on Tektronix terminals. The software which produces these plots from the data set described previously consists of three separate routines. The first routine (SCUFFL on NOS/VE) reads in the data from the SCATHA file and writes a file which contains the flux data for the electrons or ions in each L-bin, pitch angle, and energy channel. The second routine (SCFLX on NOS/VE) groups this data into 60 groups of seven records where each group represents an L-bin of .05 R_E. The first record contains the L-bin value, the local time, and the universal time. The third routine (SCPLT on NOS/VE) plots the flux data by color (the flux is binned into 15 groups each represented by a different color) according to L-bin and energy.

The plots have since been implemented on a PC using both a Tektronix emulation package and a graphics package with a playback feature. The Tektronix emulation allows the original code to be run with fairly few modifications on a PC. The package with the playback feature captures the plotfile as it is generated on the screen. Once the plotfile has been captured, one no longer needs to start from scratch each time the plot is desired. Thus, the plots may be distributed to researchers with access to a PC and this graphics package. They may then be rapidly replotted and scanned as survey plots.
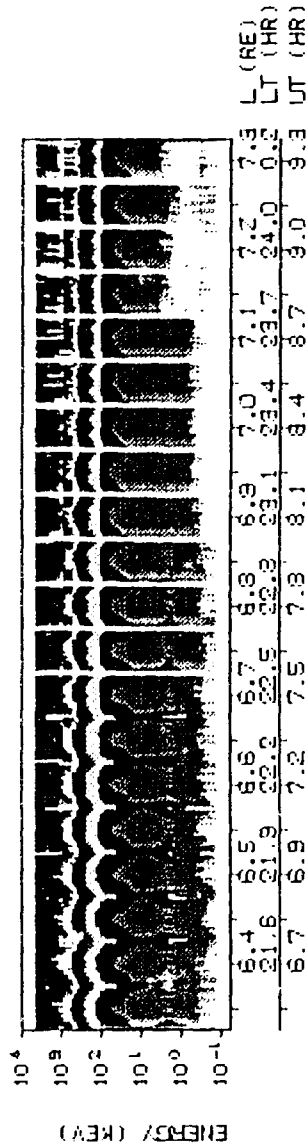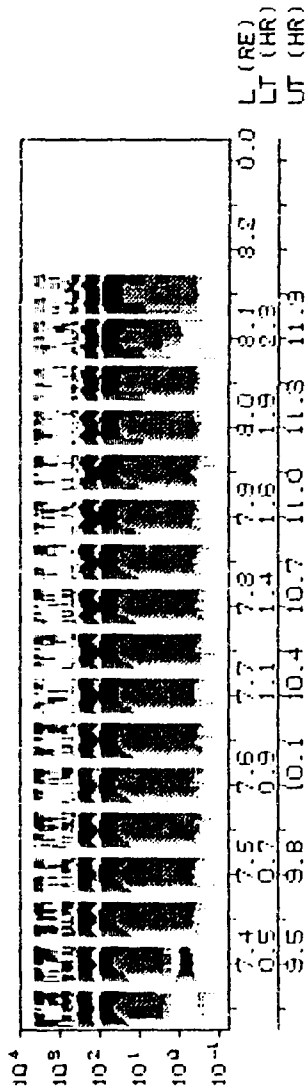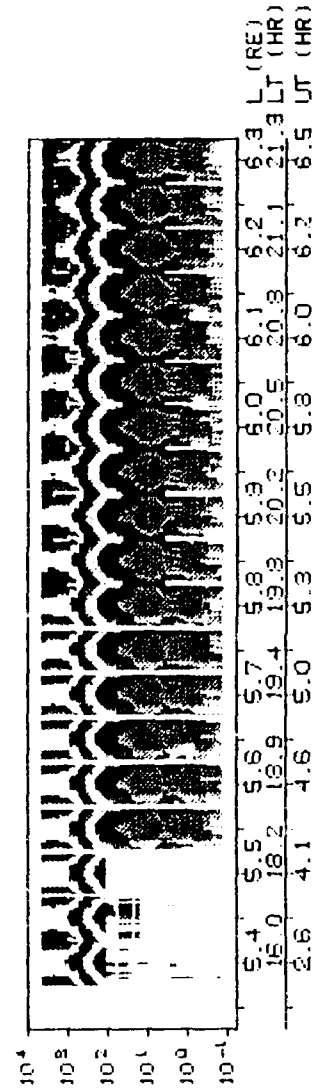
Figure 4.7. Ion distribution observed by SCATHA on day 110 of its orbit

137

4.5 ON-ORBIT CALIBRATION OF MAGNETOMETERS

The success of many spacecraft born experiments designed to detect and characterize distributions of ambient charged particles depends to a large extent on accurate knowledge of the magnitude and direction of the external magnetic field. This is because the distributions are strongly dependent on the angle between the field and the look direction of particle sensing instruments, the so called pitch angle. Accurate pitch angle determination, in turn, depends on two factors: (1) knowledge of the calibration factors to be used in the conversion of magnetometer signals to geophysical units and (2) knowledge of the orientation of the magnetometer axis in respect to the coordinate system chosen for the spacecraft. We have been involved for some time in the development of algorithms to provide accurate calibration factors and orientation information, with specific application to the fluxgate magnetometer to be flown on the CRRES satellite.

In this section, we describe these algorithms and the computer program RCAL which has been designed to implement these algorithms. We also describe the analysis of a precession maneuver, by which we are able to measure calibration factors that are not attainable under nominal operation. We will briefly describe the construction of a data base to be utilized by the system. Finally, we present an example of the use of on-orbit calibration on data from the DE satellite.

4.5.1 Calibration Algorithms

The purpose of calibration as it is defined here is the determination of the factors (gains and offsets) necessary to obtain from a magnetometer sensor signal the magnitude of the magnetic field external to the spacecraft along that sensor axis. It should be clear from this definition that the calibration process will not give us all the information necessary for conversion of the field to spacecraft coordinates. As a by-product of the calibration, however, we will be able to obtain quantities that will be helpful for this conversion.

The general method is to determine the way in which each sensor responds to the field and then, through analysis of the signal characteristics, to determine various parameters in that relationship. The conversion of field to sensor signal can be derived by the use of three coordinate systems. The first of these is called the spinning spacecraft (SSC) and is defined such that the z axis is along the spin axis and the spacecraft x axis is in the xz_{SSC} plane. The environmental magnetic field external to the spacecraft is defined in the SSC system by its projection onto the spin axis and onto the xy plane, b_z and b_{xy}, and by the angle that the xy plane projection makes with the SSC x axis, ϕ_b.

Assuming that the environmental field is constant, the field signal will oscillate in the SSC system due to the fact that the SSC system rotates around the spin axis with respect to an inertial frame. The signal in the SSC frame has the form

$$
\begin{bmatrix}
b_{xy}\cos(\omega t+\phi) \\
b_{xy}\sin(\omega t+\phi) \\
b_z
\end{bmatrix}
\tag{4.6}
$$

where ω is the spin rate and ϕ is the value of ϕ_b at some chosen time zero. As it turns out, the value of ϕ_b never enters the calibration equations. The SSC system is close to the CRRES spacecraft (SC) frame, since plans are for the satellite to rotate around z_{sc}. If the spin axis is truly along z_{sc}, then the two coordinate systems are identical. The two systems will not coincide exactly, due to deviations from design specifications, but this is not important for calibration as it is defined here. It should be helpful, though, to be able to convert the field into a system quite near the actual spacecraft frame as a first approximation for despinning and pitch angle determination.

The second system to be defined has axes close to those planned for the magnetometer axes. This will be called the orthogonal magnetometer (OM) system. It is defined by first making the transformation

$$x_{OM} = -x_{SSC} \quad y_{OM} = -z_{SSC} \quad z_{OM} = -y_{SSC}$$

and further carrying out a rotation around x_{SSC} by the angle γ and another about y_{SSC} by the angle μ. The SSC coordinate system has been defined such that the third possible rotation, around z_{SSC}, is defined to be zero since x_{OM} is in the xz_{SSC} plane. The angles γ and μ will be calculated in the calibration process and are planned to be near 2.5° and 0° respectively.

The last coordinate system to be used is defined by the magnetometer axes. This will be called the sensor (SEN) system and is not necessarily orthogonal. It is defined by the angles between each pair of sensor axes and further by the fact that x_{SEN} is the same as x_{OM} and that y_{SEN} lies in the xy_{OM} plane. The angles w_{ij} have been found by ground calibration to be no more than 0.2° off orthogonal and will be assumed to be known in this analysis.

Now that the transformation matrices between an external field and the sensor signals have been determined, the equation describing the sensor signals can be written. The details of the derivation will be omitted here.

$$
\begin{bmatrix} s_x \\ s_y \\ s_z \end{bmatrix} = \begin{bmatrix} g_x & 0 & 0 \\ 0 & g_y & 0 \\ 0 & 0 & g_z \end{bmatrix} \begin{bmatrix} 1 & 0 & 0 \\ \cos w_{xy} & \sin w_{xy} & 0 \\ \cos w_{xz} & \cos c & \cos d \end{bmatrix}
$$

$$
x \begin{bmatrix} -\cos\mu & 0 & \sin\mu \\ -\sin\mu\cos\gamma & -\sin\gamma & -\cos\mu\cos\gamma \\ \sin\mu\sin\gamma & -\cos\gamma & \cos\mu\sin\gamma \end{bmatrix} \begin{bmatrix} b_x \\ b_y \\ b_z \end{bmatrix}
$$

$$
+ \begin{bmatrix} d_x \\ d_y \\ d_z \end{bmatrix} \tag{4.7}
$$

where
$$\cos d = \sqrt{(\,1 - \cos^2 w_{xy} - \cos^2 c\,)}$$
and
$$\cos c = (\cos w_{yz} - \cos w_{xy} * \cos w_{xz})/\sin w_{xy}$$

where g is the gain and d is the offset of each sensor.

4.5.2 Spin Fit Representation

There is a simpler way of writing each sensor signal. The signal detected by a single magnetometer axis m has the form

$$s_m = g_m \sin\theta_m b_{xy}\cos(\phi_m + \omega t - \phi_b) + g_m b_z \cos\theta_m + d_m \tag{4.8}$$

where θ_m is the angle that the magnetometer axis makes with the spin axis. If the environmental field is constant, then the signal can be fit to a function of the form

$$s_m = \alpha_m \cos\omega t + \beta_m \sin\omega t + \delta_m \tag{4.9}$$

In practice, the environmental field is modeled as a polynomial of chosen order by the addition of terms such as

$$t^n \cos\omega t \quad t^n \sin\omega t \quad \text{and} \quad t^n$$

The constant portion is then evaluated by discarding the coefficients of the higher order terms.

140

4.5.3 Calculation of the Spin Axis Angles

The calculation of the angles θ, or equivalently of γ and μ, relies on the ratio of the coefficients of the modulated portion of the sensor signals and on the variation of the sensors' dc component with the background field. Each dc component has the form

$$\delta_m = g_m b_z \cos\theta_m + d_m \tag{4.10}$$

which follows directly from Equation M.3. The slope of δ_m against δ_n is

$$\sigma_{mn} = d\delta_m/d\delta_n = g_m \cos\theta_m/g_n \cos\theta_n \tag{4.11}$$

By comparing Equation M.2 to Equation M.3, it can be shown that

$$\begin{bmatrix} \sin\mu \\ -\cos w_{xy} \sin\mu - \sin w_{xy} \cos\mu \cos\gamma \\ \cos w_{xy} \sin\mu - \cos c \cos\mu \cos\gamma + \cos d \cos\mu \sin\gamma \end{bmatrix}$$

$$= \begin{bmatrix} \cos\theta_x \\ \cos\theta_y \\ \cos\theta_z \end{bmatrix} \tag{4.12}$$

Furthermore, if we square each α and β of Equation 4.9 and and compare to Equation 4.12 we can find the quantities

$$r_{nm} = g_n/g_m = (\kappa_n/\kappa_m)(\sin\theta_m/\sin\theta_n) \tag{4.13}$$

with

$$\kappa_n = \sqrt{(\alpha_n^2 + \beta_n^2)}$$

This information is sufficient to uniquely define γ and μ. One can solve for γ and μ iteratively by first calculating θ_x, θ_y and θ_z from the previous value of γ and μ. Next, r_{xy} and r_{xz} are found. Then a new γ and μ are obtained from the equations

$$\tan\gamma = (\cos c - (a/b))\sin w_{xy})/\cos d$$

$$\tan\mu = -\cos\gamma\sin w_{xy}/a$$

with

$$a = r_{xy}\sigma_{yx} - \cos W_{xy}$$

$$b = r_{xz}\sigma_{zx} - \cos W_{xz} \tag{4.14}$$

4.5.4 Calibration Factors

The spin axis angles are calculated first in the analysis. The second step is the calculation of the calibration factors, which is done in two parts. First, a set of gain ratios between sensor axes and two independent offsets perpendicular to the spin axis are calculated. From these and knowledge of the spin axis offset and the gain in any one of the sensors, the calibration factors can be calculated. We later describe methods for the independent calculation of absolute gain and spin axis offset [McNeil and Singer, 1986].

Each sensor has two gain states, high and low. Additionally, the y sensor can be switched to multiply its signal by approximately a factor of six. It is assumed that each sensor in each gain state can have different gains and offsets. The y sensor may also have different gains and offsets when the times-six multiplication is in effect.

4.5.5 Gain Ratios and Spin Perpendicular Offsets

The ratio of gains between the three sensors in any one operational mode can be found through Equation 4.13. Additionally, the ratio of gains between sensors in high and low gain operational mode can be found. In addition to the variable gain channels, there is in the data base a fixed low gain set of signals. When the variable gain channels are in high gain, these ratios can be found by comparing the coefficients of fixed and variable gain signals as shown below.

$$
\begin{aligned}
r_{xlh} &= \kappa_{xl}/\kappa_{xh} \\
r_{ylh} &= (\delta_{yl} - d_{yl})/(\delta_{yh} - d_{yh}) \\
r_{zlh} &= \kappa_{zl}/\kappa_{zh}
\end{aligned}
\tag{4.15}
$$

This calculation requires prior knowledge of the dc offsets for the y sensor. These values can be estimated from earlier calculations or earlier iterations on the same data set. The modulated portion of the signal is chosen for the x and z sensor because they are nearly perpendicular to the spin axis and thus the signal is strongly modulated. The y sensor, being nearly along the spin axis, has a small modulated component.

In order to define dc offsets that are independent of the offset along the spin axis, which cannot be calculated from spin fits, the offsets are defined along two not necessarily perpendicular axes that lie in the spin plane. The offsets along these are defined as

$$
\begin{aligned}
\Delta_1 &= \cos\theta_y\delta_x - r_{xy}\cos\theta_x\delta_y \\
\Delta_2 &= \cos\theta_z\delta_y - r_{yz}\cos\theta_y\delta_z
\end{aligned}
\tag{4.16}
$$

These can be shown to be independent of the external magnetic field. Again, the values for r_{xy} and r_{yz} are necessary. They can be taken from previous calculations on other data sets, from previous iterations of the same data set, or from the value calculated from each individual spin fit, since values for r_{ij} are produced from each fit.

4.5.6 Relation to the Calibration Factors

In order to apply the quantities calculated above to the task of creating a calibrated magnetometer signal, it is necessary to generate the g's and d's of Equation 4.8. Although there are several possible ways to do this, we have adopted a scheme which worked well in simulated data tests.

First, it is assumed that g_{xh} and g_{xl} are known. In high gain, we use g_{xh} and r_{xyh} or r_{xzh} to find g_{yh} or g_{zh}. In low gain, we use g_{xl} and r_{xzl} to find g_{zl}. Since the y-sensor is nearly parallel to the spin axis, there is little modulation in the y-sensor signal. Thus the ratio r_{yl} contains substantial error because of the +/- 20 nT uncertainty in low gain. In fact, the modulation of the y-sensor is often less than this uncertainty. Because of this, an alternate procedure was used to find the value of g_{yl}. We used g_{yh} and the low to high gain ratio in the y-sensor r_{ylh}. This gave more accurate results in our simulation.

$$
\begin{aligned}
g_{xl} &= g_{xh}{}^{*}r_{xlh} \\
g_{yh} &= g_{xh}/r_{xyh} \\
g_{zh} &= g_{xh}/r_{xzh} \\
g_{yl} &= g_{yh}{}^{*}r_{ylh} \\
g_{zl} &= g_{xl}/r_{xzl}
\end{aligned}
\tag{4.17}
$$

This means that, if model field calibration is not used, all gains will be proportional to the gain in the x-sensor in high gain operation. This would give the correct pitch angle, but an incorrect magnitude.

Next, we assume that Δ_3, the offset along the spin axis, is defined as

$$
\Delta_3 = d_x\cos\theta_x + d_y\cos\theta_y + d_z\cos\theta_z
\tag{4.18}
$$

The values for d_x, d_y and d_z are then obtained from the solution to the matrix equation

$$
\begin{bmatrix} \Delta_1 \\ \Delta_2 \\ \Delta_3 \end{bmatrix}
=
\begin{bmatrix}
\cos\theta_y & -r_{xy}\cos\theta_x & 0 \\
0 & \cos\theta_z & -r_{yz}\cos\theta_y \\
\cos\theta_x & \cos\theta_y & \cos\theta_z
\end{bmatrix}
\begin{bmatrix} d_x \\ d_y \\ d_z \end{bmatrix}
\tag{4.19}
$$

by inversion.

4.5.7 Model Field Comparisons

The process described above results in gains that are correct relative to the x sensor in each operational mode. If it is desired to find the absolute gain in the x sensor and thus in y and z, a comparison can be made to the magnitude of a model field. This calculation is made as follows. The calculated offsets d are subtracted from each of the three sensor components. Then the y sensor signal is multiplied by r_{xy} and the z sensor is multiplied by r_{xz}. This makes the y and z sensor have the same gain as the x sensor signal. As long as the sensors have the same gain, the

sensors can be transformed to the OM frame by multiplication of the signals by the inverse of the orthogonality matrix in Equation 4.7. The magnitude of the sensor signal is related to the magnitude of the true field by

$$|s| = g_x|b| \tag{4.20}$$

where s is the magnitude of the sensor signal and b is the magnitude of a model field. If a model field is available and is reasonably close to $|b|$, at least on average, then model field calibration can be used to find g_x. The advantage of this method is that it uses the magnitude rather than the individual components of the model field. The magnitude of the field is generally better known than the direction. The method is also independent of attitude information.

4.5.8 Calculation of the Spin Axis Bias

In Section 4.5.6, we relied on a knowledge of the value of the offset along the spacecraft spin axis, Δ_3. This was done simply because there is no way to calculate this value while the spacecraft is undergoing pure rotation. If the spin axis moves relative to the external field, however, this value can be calculated. Such movement will occur when the attitude is adjusted during a precession and will also occur for long periods of time during the nutation that naturally follows a precession of the axis. To take advantage of this situation, a large angle precession of the spacecraft is planned within a few orbits of deployment of the magnetometer.

The first half of this analysis is carried out on data from nominal operation, during pure rotation. It involves calculation of the angles γ and μ and the gain ratios r_{xy} and r_{xz}. These are applied to the data to transform the signals into the spacecraft frame. The offsets in the spin plane Δ_1' and Δ_2' are then determined from spin fitting. (These values are primed because they are not exactly equal to the Δ values used above. They are easily converted to Δ values, however.) The identical transformations are then applied to the data taken during nutation. The spin plane offsets are subtracted. If s_1 is the converted signal taken during one orientation of the magnetic field and s_2 is that taken from another, it can be seen that

$$s_{1x}^2 + s_{1y}^2 + (s_{1z}-\Delta_3')^2 = s_{2x}^2 + s_{2y}^2 + (s_{2z}-\Delta_3')^2$$

assuming that the magnitude of the external field has not changed between the two data points. From this relation, we can obtain

$$\Delta_3' = \{s_{1x}^2+s_{1y}^2+s_{1z}^2-(s_{2x}^2+s_{2y}^2+s_{2z}^2)\}/2(s_{1z}-s_{2z})$$

In addition to this, we have developed a second algorithm which does not require the external field to remain constant [McNeil and Singer, 1989].

4.5.9 The Calibration System RCAL

A major aspect of this effort in the recent past has been the development of an efficient and user friendly code to implement the calibration algorithms described above. This effort has produced the system RCAL [Radex, Inc., 1987]. The system performs all the functions of calibration, including fits of the sensor signals, calculation of the alignment angles, calculation of the gain ratios and spin axis perpendicular offsets, transformation of these into calibration factors, and absolute calibration of gains through the use of a model field.

144

The system contains a parser which understands several variations of user commands used to direct the processing. It is screen oriented and menu driven and has several interactive editing features. One example of a screen used in the editing is shown in Figure 4.8. Movement of the cross-hairs and selection of one of the options listed in the upper right of that figure allows for selection of the best data for inclusion in the average. The RBIAS system, described above, also operates with much the same characteristics and includes the same type of editing screens.

4.5.10 Other Applications of Calibration

Even prior to the launch of CRRES, we have had the opportunity of applying the technology discussed above to other applications. One recent instance involved data from the DE satellite. The data, which was preprocessed to some extent, appeared to have ripples at the spin rate when despun. The top panels of Figure 4.9 show these ripples. These features, aside from being astetically unpleasant, made difficult the analysis of ripples caused by actual waves. A modification of the above process was applied to the data, from which it was determined that the ripples arose from incorrect alignment of the magnetometer axis. This could be compensated for in the despinning, producing the plots shown in the lower portion of Figure 4.9, allowing the waves to be more clearly visible.

4.5.11 Data Bases and Simulation Systems

Several data bases are used and produced in the course of processing the magnetometer data from CRRES. The **Magnetometer Experiment File** (MEF) contains the 16-samples per second magnetometer sensor signals and is used by the program MAKOSDB to generate a time-averaged **One-Second Averaged Data Base** (OSDB). This is used by the calibration system and is also despun to a **Five-Second Data Base** (FSDB).

The process of despinning and the conversion of data to inertial coordinate frames requires knowledge of the attitude of the spacecraft. This can be gained from the results of the Attitude Determination Program (ADP) in conjunction with the program AGMOD, which produces inertial look directions of arbitrary spacecraft frame vectors. It is quite possible, however, that accurate despinning will require a more detailed calculation of spacecraft attitude, especially if one attempts to use the data during periods of nutation or in periods where the ADP fails to produce attitude at all or produces an unreliable attitude. This is especially true in the calculation of the phase, which can be determined to a higher accuracy than that derived from AGMOD by simple algorithms. The MEF will be used as the source of some of this data, since it contains the times of Sun hits and of magnetic field zero crossings for the engineering magnetometer. In addition, it may be necessary to call upon the **Calibrated Attitude Data** (CAD) file, which contains, in addition, times of Earth limb crossings and Sun declination angle measurements.

In the course of development of RCAL and RBIAS, software has been generated that is capable of simulation of the MEF and the OSDB. As a result of other work concerning the generation of test files for the ADP [McNeil and McInerney, 1988], we have the capacity to generate both the CAD and RAD files corresponding to the MEF or OSDB files for any simulated orbit. We are also able to run the ADP on simulated RAD files to generate results to be used by AGMOD. This previous work puts us in a unique position to examine various ways to put together a system for despinning and analysis of the data that uses magnetic field and attitude measurements to the greatest advantage.
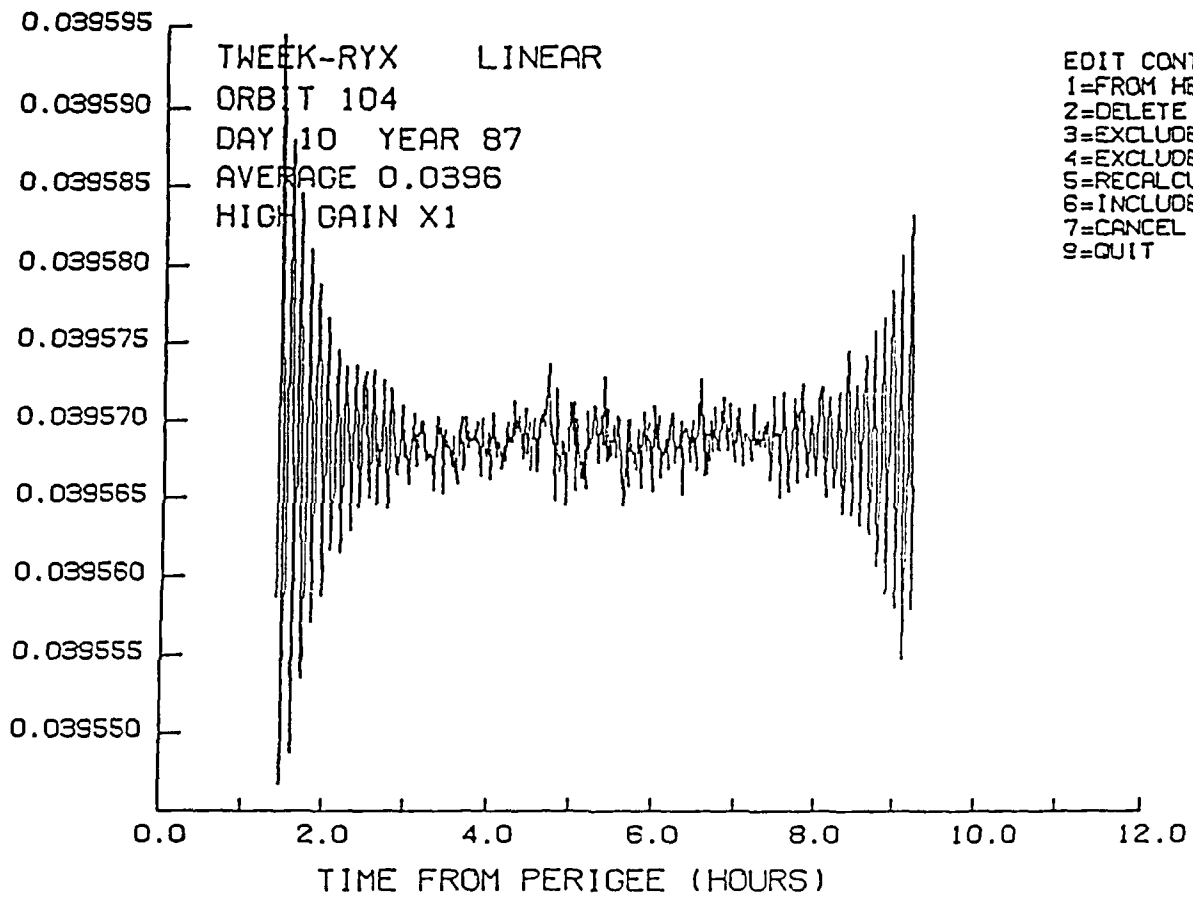
Figure 4.8. Sample editing screen from the calibration system
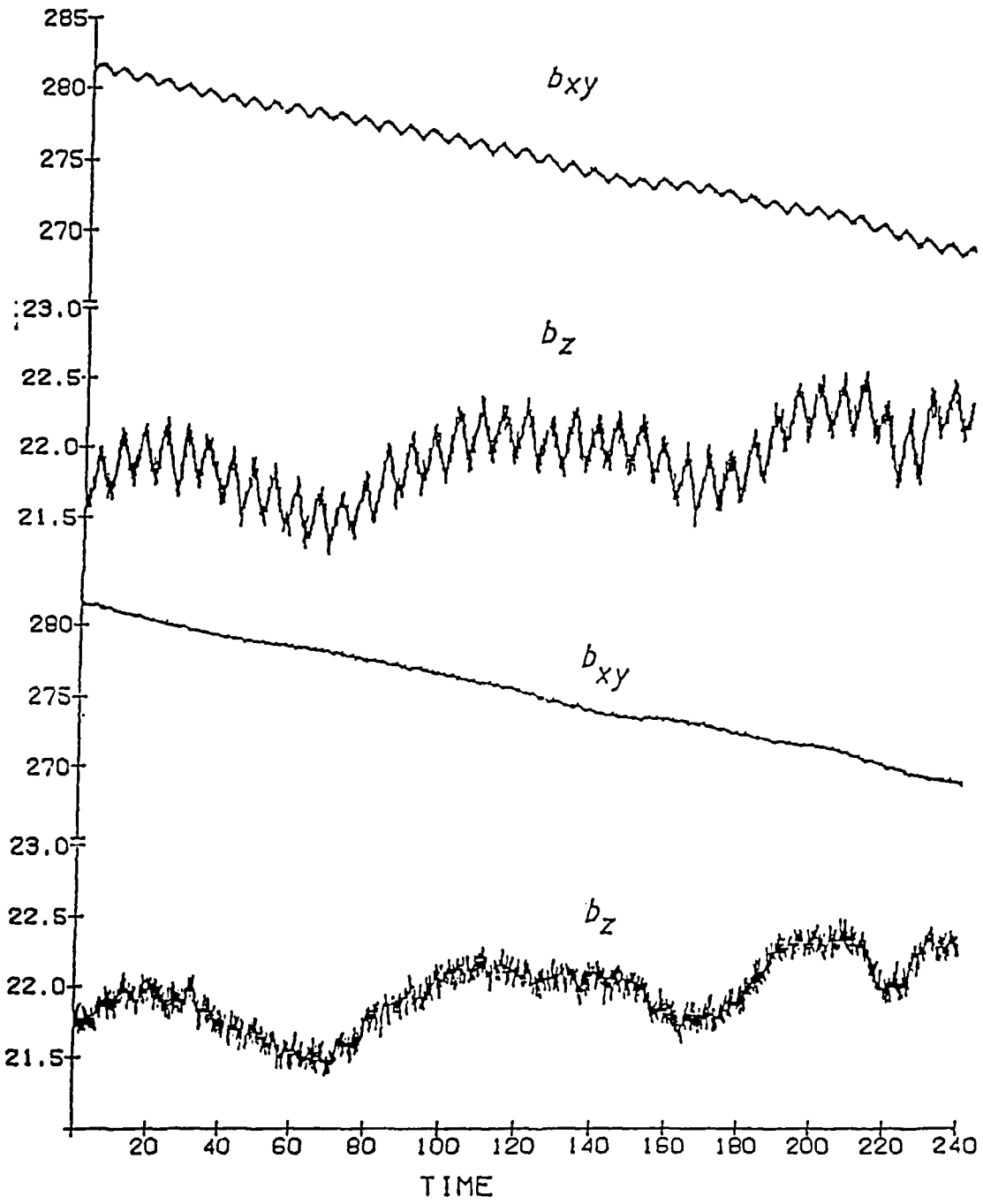
Figure 4.9. Example of the use of on-orbit calibration in the removal of oscillations in the DE satellite data

4.6 CRRES INSTRUMENTS AND RADIATION BELT MODELING

The Combined Release and Radiation Effects Satellite (CRRES) Program will measure the near-Earth radiation environment and its effects on state-of-the-art microelectronics devices and other spacecraft components. The CRRES Program supports, among other experiments, the Geophysics Laboratory Space Radiation Effects Program (SPACERAD). In order to accomplish the SPACERAD mission goals, GL has developed a space experiment complement consisting of a microelectonics experiment package, dosimeters, particle detectors, space plasma detectors, and wave and field (electric and magnetic) experiments.

The instrumentation on CRRES will provide increased sensitivity, mass and energy resolution; measurements will cover electrons, protons, the major ion species (O^+, H_e^+, H_e^{++}), measured dose, and the magnetic field. The task of radiation belt modeling does not address electron energies below 20 keV or proton energies below 40 keV. Count or other measurements for each instrument present on Agency tapes will be reduced to separate files called the Time History Data Base (THDB). This data, together with concurrent environmental geophysical data, will be collected and binned onto Product Associated Data Bases (PADB) appropriate for modeling, "event" and other science studies.

Measurements for electron population modeling are now discussed further. Eight instruments measure electron flux, however LEPA (701-6) and IMS-LO (307-8-1,2) fall below 20 keV and are not required for the electron model product data base. If after preliminary checking during the early months, it is found that the instruments operate reasonably well, the scientists have suggested that the data base creation task may be simplified by dispensing with redundancy requirements. Thus the SEP (307-3) would be available as back-up only, leaving the bulk of the modeling to be based on RPD (701-7A), HEEF (701-4), MEES (701-5A), and EPAS (701-5B). Considerations of quality control and cross-checking of instrument data will remain important until reliability and acceptance criteria are established. Each experiment has its own number of sensors, energy characteristics, angular resolution, readout intervals, geometric factors (calibration), sweep-times and look directions. The readout values vary from one experiment to another, and for some even within a given experiment. However, the sweep time is an integral multiple of 1.024 seconds for all experiments except LEPA (701-6), which is per vehicle spin.

Table 4.6 gives an overview of the measurement ranges, resolution, read-out intervals, and look direction available for the principal electron detectors for the modeling effort. Table 4.7 gives a similar presentation of the detector characteristics, energy ranges, energy resolution, and angular resolution for the instruments to be used for proton modeling. The PADB will be formed from the THDB, which will provide for each specie vs. time, the counts, energy ranges, geometric factors, differential fluxes, integral number and energy fluxes. Thus, in addition to THDB data, the PADB will be able to provide differential spectra; integral number and energy spectra; color spectrograms (energy vs. L, R_E, pitch angle, UT); distribution function plots; in conjunction with ephemeris in-situ and model magnetic field components; and DST, Kp and other magnetic substorm parameters.

Table 4.6. Principal Electron Detectors for Radiation Belt Modeling

	701-7A (RPD)	701-4 (HEEF)	701-5A (MEES)	701-5B (EPAS)	307-3 (SEP)
No. of Sensors	2	1	17	10	3
Energy Ranges	------	10 ch (1-10 MeV)	1 range per ch (40keV-2.2MeV)	15 ch. 15-300 keV	24 ch. 2 12 pt Diff. spect mode 1: 20 - 300 keV mode 2: 300 - 5000 keV 4 Integral spectra
Energy Thresholds	>200 keV, >35 MeV	1 ch > 10MeV	------	>22 keV	------
Energy Resolution	------	channel dependent	channel dependent	35%	channel dependent
Field of View (Az x El)	------	$\pm7.5^0$ conical	$(\pm3^0 - \pm11^0) \times \pm11^0$	$\pm2.0^0 \times \pm3.0^0$	6^0 conical
Readout Intervals	1.024 or 2.048 s	.512 s	.512 s	10 Integral fluxes .512 s 1 Diff. flux, 14 pts from one sensor .256s	80^0, 60^0 sensors .256 s 40^0 sensors; .512 s
Geometric Factor	------	0.0120 cm²sr	each sensor has its own value	5×10^{-5} cm²sr	3×10^{-3} cm²sr
Look Direction wrt. S/C spin axis	90^0	90^0	90^0	10^0-50^0, 80^0-120^0 in 10^0 steps	80^0, 60^0, 40^0
THDB Parameters	Counts for Integral fluxes	Diff flux 1 ch > 10MeV	17 Diff fluxes	Diff. flux per sensor 10 Int. fluxes & 1 > 22 keV	12 pt. Diff flux 4 Int. fluxes
PADB Parameters	Calc. Int. fluxes for each detector	Diff. fluxes Int. fluxes distri. func.	Diff. fluxes Int. fluxes distrib. func.	Diff. fluxes Int. fluxes distrib. func.	Diff. fluxes Int. fluxes distrib. func.

Table 4.7. Principal Proton Detectors for Radiation Belt Modeling

	701-7A (RPD)	701-8,-9 (PROTEL)	701-7B (PS)	701-5B (EPAS)	307-3 (SEP)
No. of Sensors	3	2	3	4	3 (2 protons)
Energy Ranges	------	1 - 100 MeV	20 - 80 MeV	20 KeV - 3.3 MeV	0.5 - 100 MeV
Energy Thresholds	>80 MeV, >320 MeV; >440 MeV	------	------	------	------
Energy Resolution	20 - 40 MeV 40 - 80 MeV	1 - 9 MeV 6 - 100 MeV	20 - 40 MeV 40 - 80 MeV	35%	48 channels (energy dependent)
Field of View (Az x El)	------	±10° x ±10°, LE ±12° x ±17°, HE	180° conical	±2.0° x ±5.0°	6° conical
Readout Intervals	2.048 s	1.024 s	4.096 s	0.512 s	0.512 s
Geometric Factors	------	0.0121cm²sr, LE 0.12cm²sr, HE	------	2×10^{-4} cm²sr	3×10^{-3} cm²sr
Look Direction wrt. S/C spin axis	90°	90°	------	23°, 46°, 83°, 106°	80°, 60°, 40°
THDB Parameters	Counts for Integral fluxes (count level)	Differential flux; Dose	Integral flux (count level)	Integral flux counts from 4 sensors; Differential flux from one selected sensor; Coincidence and Background count rates	Diff. and Integral fluxes from 4 modes; chan. width 0.5 - 4.5 MeV; 330 KeV 4.5 - 20 MeV; 1.25 MeV 20 - 45 MeV; 2.0 MeV 45 - 100 MeV; 4.2 MeV
PADB Parameters	Diff. fluxes Int. fluxes distrib. func.	Diff. fluxes Int. fluxes distrib. func.	Integral flux	Diff. fluxes Int. fluxes distrib. func.	Diff. fluxes Int. fluxes distrib. func.

References

Bass, J.N., Gussenhoven, M.S., Private Communication, 1988.

Baumjohann, W., Haerendel, G., and Melzner F., "Magnetospheric Convection Observed between 0600 and 2100 LT: Variations with Kp", J Geophys Res, Vol 90, No A1, Pp. 393-398, 1985.

Gussenhoven M.S., Mullen E.G., and Sagalyn R.C., "CRRES/SPACERAD Experiment Descriptions", AFGL TR-85-0017, January 1985, ADA160504.

Matthews, D.L., Rosenberg T.J., Benbrook J.R., and Bering E.A., "Energetic Electron Precipitation Near the Cusp", EOS, Vol. 69, No. 16, P. 441, 1988.

McIlwain, C.E., "Coordinates for Mapping the Distribution of Magnetically Trapped Particles", J Geophys Res, Vol 66, No 11, Pp. 3681-3689, 1961.

McNeil, W.J. and Singer, H.J., "Fluxgate Magnetometer Analysis and Simulation Software for the Combined Release and Radiation Effects Satellite", AFGL-TR-86-0222, October 1986, ADA176353.

McNeil, W.J. and McInerney, R.E., Private Communication, May 1988.

McNeil, W.J. and Singer, H.J., Private Communication, 1989.

Mullen, E.G., and Gussenhoven, M.S., SCATHA Environmental Atlas, Tech. Report, AFGL-TR-83-0002, ADA131456, Air Force Geophysics Laboratory, Hanscom Air Force Base, MA, 1983.

Radex, Inc., "On-Orbit Fluxgate Magnetometer Calibration System Product Specification and Test Results for the Combined Release and Radiation Effects Satellite", Radex, Inc., Bedford, Mass. 01730, June 1987.

Roederer, J.G., Dynamics of Geomagnetically Trapped Radiation, Springer Verlag, New York, 1970.

Stern, D.P., "Parabolic Harmonics in Magnetospheric Modeling: The Main Dipole and the Ring Current", J. Geophys. Res., Vol. 90, No. A11, Pp. 10851-10863, 1985.

West, H.I., Jr., "The Signatures of the Various Regions of the Outer Magnetosphere in the Pitch Angle Distributions of Energetic Particles", Quantitative Modeling of Magnetospheric Processes, W.P. Olson, Ed., A.G.U., Washington, 1979.

5. SHUTTLE SUPPORT SYSTEMS

5.1 AITS

The AFGL Interactive Targeting System (AITS) [Bonito et al., 1986] was designed to provide pre-mission and on-orbit planning support for the CIRRIS-1A project. It is a computer based system which displays shuttle position and sensor line of sight in various formats. Color graphic displays are used to depict the world map, the celestial sphere, and the probability of auroral activity. This system is used by researchers as a tool for evaluating in near real time, shuttle and sensor orientation during data gathering, and to determine possible shuttle attitude for auroral oval conditions. It will also determine sensor line of sight angles required to view earth and space targets.

The shuttle position and sensor line of sight are presented in realistically simulated formats. The depiction includes the world map, the celestial sphere, the probability of auroral activity, as well as a console type Mission Event Sequencing (MES) [Banks and Sannerud, 1986] display. A user friendly interactive menu allows the researcher to display and/or compute measurement mode operation. Information and displays relevant to the operation of probes flown on the space shuttle are used to augment the sensor measurements. Data displays may be used for long and short range operations planning and post-pass evaluation of data gathering conditions. The sensor line of sight and the vehicle orientation required to view target locations can be calculated. Geographic and celestial coordinate based processing is available, and may be selected by the researcher to present the information.

5.1.1 AITS Enhancements and Graphic Capability

AITS was originally designed to operate on a VAX/VMS computer utilizing the Tektronix 4109 to generate graphic displays. The original computer, a VAX-750, required approximately 50 square feet of floor space solely for the computer, which did not include the space for graphic displays and hard copy equipment. Thus the area of an average office would be required to support an on-orbit operation. The availability of space at a remote facility for a prolonged period of time pending launch could be a major complication for the research group. The AITS package was updated to operate on a Micro-VAX GPX, since these machines offer greater computational power, portability and reduced space requirements.

AITS graphics performance on the GPX is greatly improved over the older technology of the Tekronix 4109, however, for reasons of compatibility, the Tektronix version has been retained. The increased availability of Micro-VAX GPX systems has allowed for a greater application of the AITS system on other than an on-orbit support basis.

The AITS system was originally developed for CIRRIS-1A project support, however, the system has been enhanced to allow for multiple project usage. A brief description of the processes and displays available for mission planning and support is given below.

5.1.2 Shuttle Flight Monitoring

The AITS package provides displays of shuttle ground tracks on latitude and longitude grids with continental outlines, which can be displayed on linear or polar projections. In addition, the Feldstein auroral oval [Whalen, J. A., 1970] and Hardy-Gussenhoven [McNeil et al., PC-1, McNeil et al.,

152

PC-2; Gussenhoven et al., 1988] probability contours, and the day/night terminator are projected on these maps. Other displays include ground tracks of past and upcoming orbits; present time and position of the vehicle; proximity of the auroral oval and/or probability contours; and the time of the next instrument measurement occurrence.

5.1.3 Mission Event Sequencing (MES)

The Mission Event Sequencing (MES) system is a menu driven interactive computer process designed for real time sequencing of CIRRIS-1A experiments. The MES software allows for ease of entry and modification of data concerning each sensor's operation. MES calculates the internal sequence of events for sensor functions during data gathering periods, and sequences the CIRRIS-1A experiments for the mission with user entered information and vehicle position ephemeris. These main features of the software allow for dynamic mission planning given any reconfiguration of the vehicle's orbit.

5.1.3.1 MES and AITS Integration for On-Orbit Support

The MES system was integrated as a portion of the AITS system level software, allowing for redesign for greater system generality. The AITS package used a modified version of a twenty-four hour timeline, which was replaced with a more compatible version generated by the MES system. The MES system utilizes vehicle position information to determine the appropriate commencement of a measurement period. The integration of MES within the AITS package will now eliminate any database transferal errors which could occur during on-orbit operations. Launch time and major orbital changes could have generated complications in transferring information between the two packages. This condition has been eliminated since the AITS package automatically updates the mission timeline upon the addition or alteration of vehicle state vectors.

The AITS and subprocess MES were also modified to allow for multiple project usage. The AITS package requires a specific database to operate; others would be specific to a particular project. The project specific databases were isolated and organized in a manner that allows the package access to only the databases applicable to the user/research project. With this alteration, a single version of the AITS package can support multiple projects simultaneously.

5.1.4 Ephemeris Computations

Orbital parameter computation is done using a software package derived from the ephemeris calculation program LOKANGL [Minka, et al., 1965 and 1966]. The package interpolates between orbital elements to compute satellite position, or extrapolates from an orbital element set for cases of thrust or lack of further elements. Condensing and retailoring of the LOKANGL package for operation as a part of the software system minimizes the need for pregenerated ephemeris information and additional computer storage. The major advantage in having an independent ephemeris computation approach allows for online updates of the satellite position elements without waiting for regeneration of ephemeris data files.

5.1.4.1 Ephemeris Products

Ephemeris computations performed include calculation of vehicle position in geodetic and geocentric coordinates, and in corrected geomagnetic coordinates. The station look angle option provides the user with the capability to compute information relative to when the shuttle is

153

within view of a ground station. NASA, CSTC, AF Space Command, and TDRSS ground and spacial tracking stations are available. The user can select from the available or enter any ground location. Eclipse and nodal times are computed and listed when requested by the user or performed when updates to the MES system are required. All vehicle ephemeris information can be generated in hardcopy listing format or as a graphic display.

5.1.5 Celestial Support Functions

The AITS software uses various displays, symbols and colors to represent the celestial sphere and stellar sources. Stellar intensities are denoted by various colors, and symbol sizes. Each display shows the celestial ecliptic plane and planets for the time period selected. The vehicle's orbital path is projected onto the celestial sphere with directional arrows at 5 minute intervals. The celestial sphere and computed information can be depicted as spherical, Aitoff, or linear display projections. These displays are used to show what the instrument will view as background to the measurement being performed.

5.1.6 Camera Simulation

The AITS system offers a Camera View Simulation process which can graphically display a camera field of view for a selected time. The user enters the time, shuttle attitude, and camera orientation. The display contains land masses, stars, planets, and a simulated auroral boundary that are viewable using the selected information. Though static, these displays also allow for post-flight comparison with as-flown camera pictures, to evaluate the quality of the measurements.

5.1.7 Gimbal/Off-Track Celestial Tracking

This process determines the Local Vertical Local Horizontal (LVLH) angles and CIRRIS gimbal angles required to view a celestial target. The user supplies the type of target and its coordinates, the span of time desired to process, and the type of output product desired. The process creates either a tabulated print-out of the information or a graphic display of the LVLH angles versus time (Figure 5.1).

5.1.8 Gimbal/Off-Track Earth Location Tracking

This process determines the gimbal angles required to view either a ground target auroral region or location for a user entered constant vehicle attitude. The results of the computation performed for the selected span of time are tabulated on print-outs to aid the researcher in the selection of gimbal angles to use with other processes. The LVLH angles of azimuth and elevation are referenced positive down from the local horizontal toward the earth. LVLH azimuth is positive about the local vertical from the negative velocity vector on the local horizontal plane (Figure 5.2).
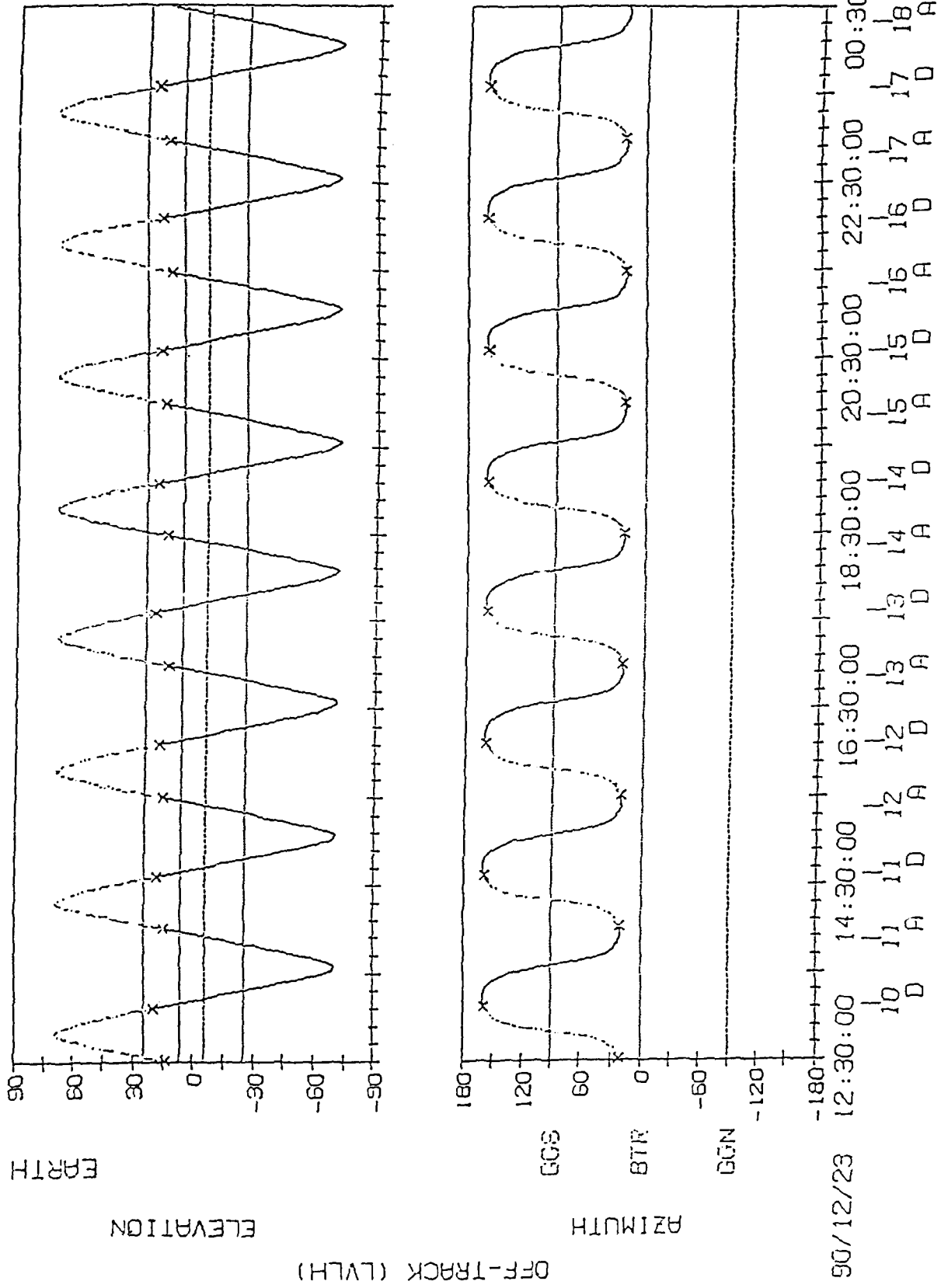
Figure 5.1. Graphic display of the LVLH angles vs. time

155
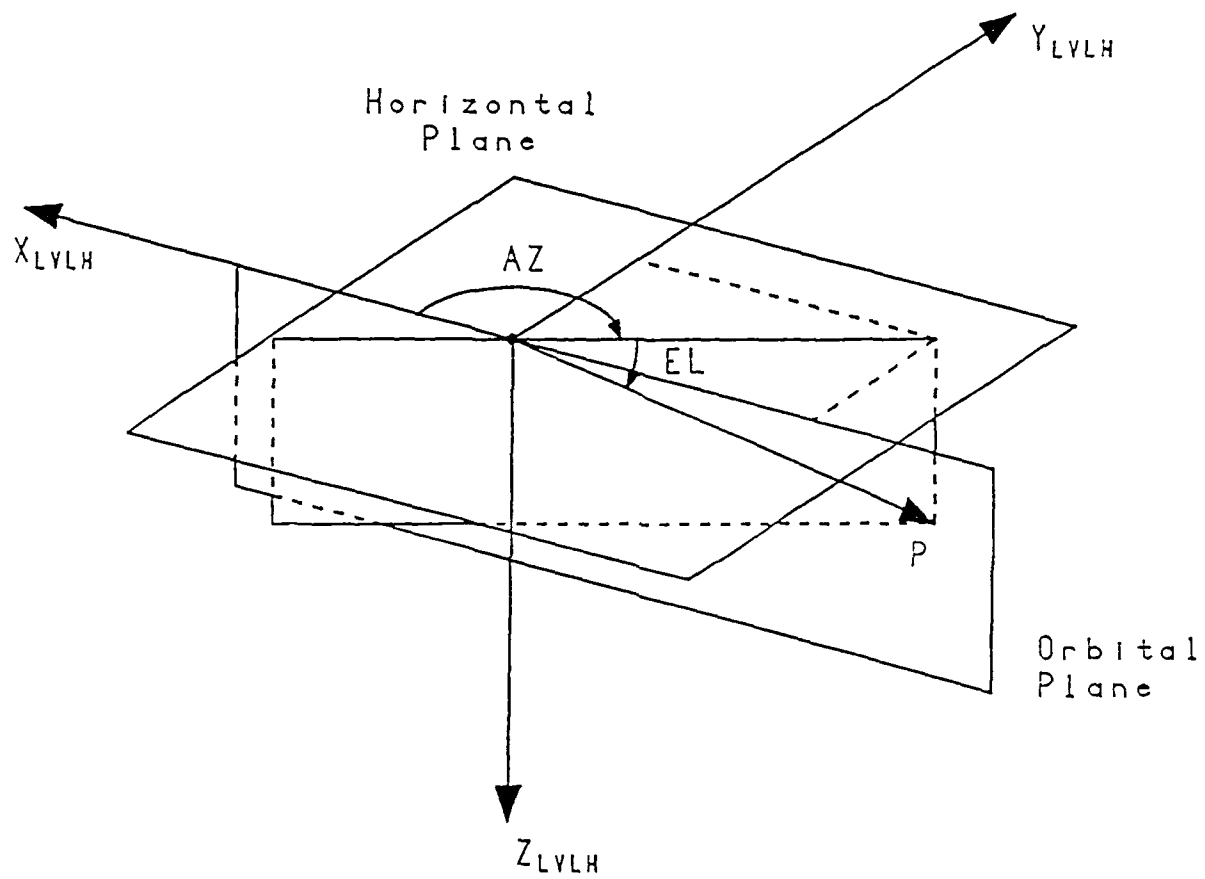
Figure 5.2. LVLH coordinate system

5.2 AITS-II, 3-D SCENE SIMULATION

The AITS-II, 3-D Scene Simulation package on an IRIS 3130 Graphic work station offers the capability of depicting in real time the earth's rotation and vehicle motion as would be seen by a sensor. Figure 5.3 demonstrates the capability of a pre-mission planning package which uses false color rendering and dynamic motion graphics.

AITS-II allows for user friendly operation and also a self explanatory usage of the package. The implementation of pull-down menus for user selection using the keyboard mouse allows for a greater flexibility of the package with less complication. This capability also allows for the integration of special options relative to experimenter needs. Real-time monitoring of flight parameters such as vehicle ephemeris, attitude, and line of sight information can also be selected via the pull-down menus.

The earth limb, land masses, and stellar objects are calculated at the refresh rate of the display using the full capability of the IRIS 3-D computer. The land masses are displayed as 50 kilometer square grids to permit a dynamic motion effect, without sacrificing either the orbital ephemeris, or the attitude transformation matrix. Figure 5.3 contains the SPAS/AIS field of view as seen, given the relative range of the SPAS from the shuttle, time in the mission, and attitude of both vehicles. False color is also used to associate specific material characteristics of the shuttle (Figure 5.4), and with the shuttle body coordinates defined in inches, measured from the NASA origin.

The application of background environment relative to a sensor field of view can assist in reducing the effort in evaluating the data. The model environment can also be applied to assist in determining the best time period to analyze. Scene simulation processing also provides unique aspects during data reduction since, due to differences in physical alignment, the simulated sensor motion may not be seen by the payload video camera.

AITS-II displays the CO_2 layer defined at 40 km altitude to represent the earth limb illumination "glow" as seen from space. Applying variation of color also allows for the representation of the sun's position with respect to the viewer's line of sight.

The Smithsonian Astronomic Observation (SAO) [1966] Star Catalog is used to represent the stellar sources in the visual magnitudes range.

With multiple payloads, such as possibly combining IBSS and CIRRIS on the same shuttle mission, simulation for visibility conditions would be required. As a planning tool, the simulation can demonstrate which measurements and/or orientations are eliminated due to other instruments or the shuttle bay structure. A three dimensional representation of the CIRRIS payload with complete gimbal motion is depicted within the shuttle bay for usage in obstruction analysis, along with the SPAS/IBSS payload.

AITS II contains five perspective viewer displays: orbital view of the orbit and vehicles; CIRRIS's camera with full gimbal motion; IBSS/SPAS camera; AIS/SPAS with full gimbal motion; and shuttle bay bulkhead window. When a viewer's position is within the shuttle bay, the applicable internal and external structures are displayed with perspective distortion applied.

The AITS-II system has the capability of applying actual ancillary data from a shuttle mission and depicting the sequence of events as they occurred. The system utilizes the attitude and position from the PATH (Postflight Attitude and Trajectory History) tapes to generate a reduced scenario data set for display purposes. The system can also generate the applicable ephemeris
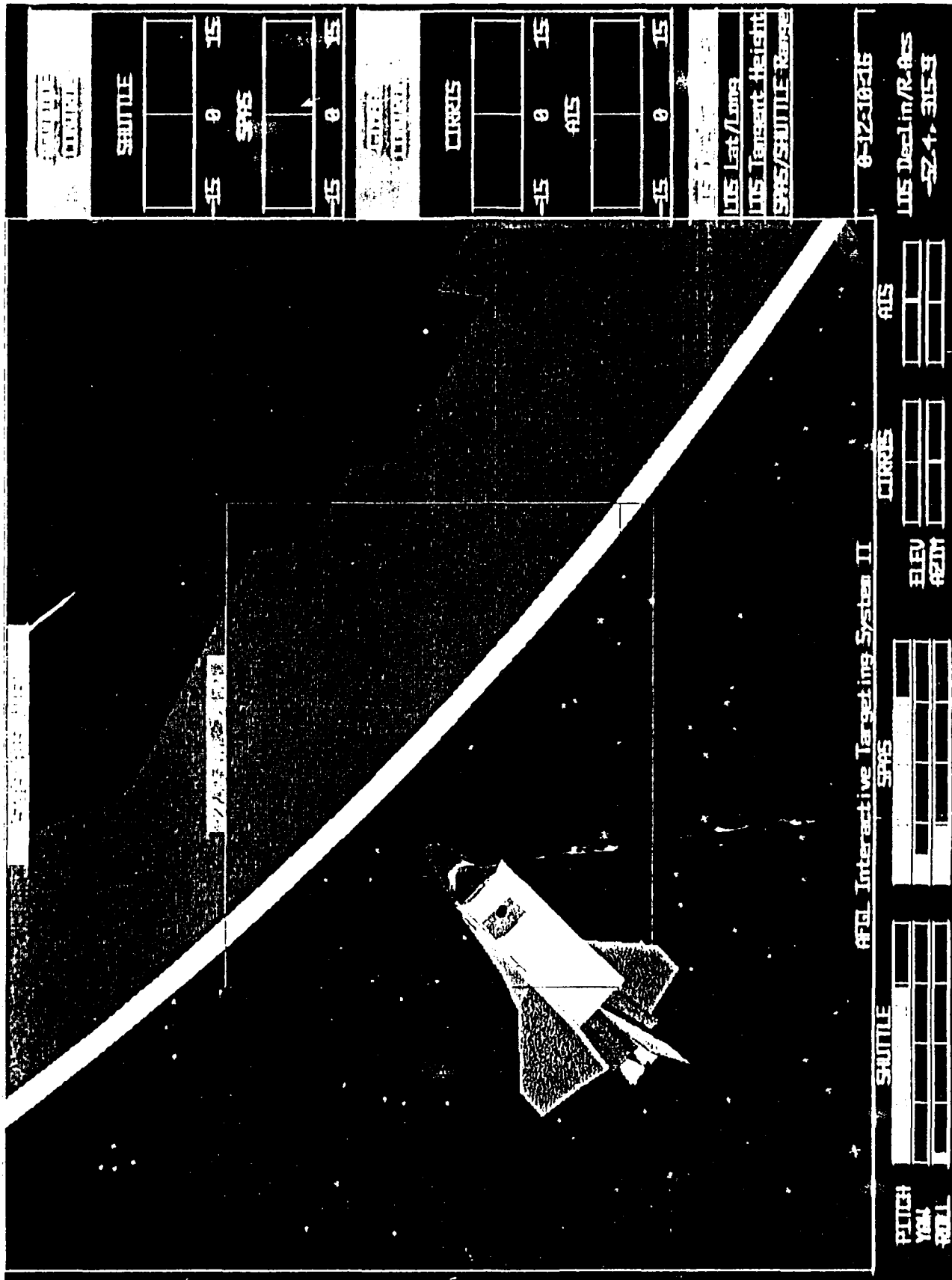
Figure 5.3. Dynamic AHS scene simulation using IRIS 3130
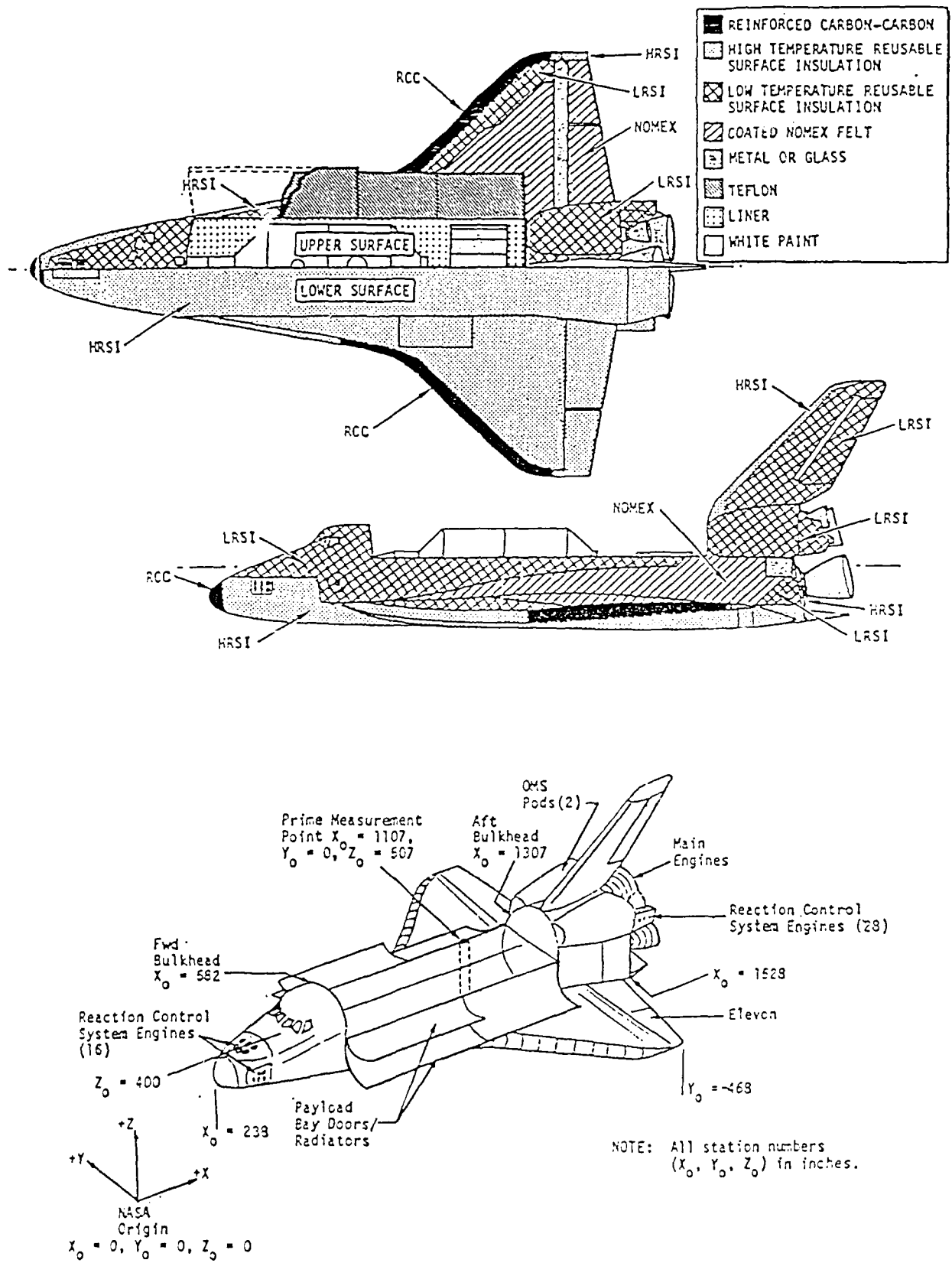
Figure 5.4. Model Shuttle Orbiter configuration. (SPACE II User's Manual, MCR-81-509)

159

information required for processing the RELBET (Relative Best Estimate Trajectory) data tapes in the same manner. This operation has been prototyped utilizing the shuttle mission 51F, which contained a TDRS satellite monitoring and RELBET tape of the information.

5.3 COORDINATE SYSTEMS

The AITS and AITS-II systems utilize a number of coordinate systems in the generation of sensor FOV, LOS and vehicle position. The most used systems and transformation matrixes are described below.

5.3.1 Local Vertical Local Horizontal (LVLH)

The LVLH coordinate system is referenced to the vehicle's position and direction of travel (velocity vector), and the primary application is for converting vehicle orientation to ECI coordinates. The LVLH coordinate system is a right-handed system (Figure 5.5) with the Z-axis along the geocentric radius positive to the center of the earth, Y-axis is the normal of the orbital plane, and the X-axis completing the right-handed system. The vehicle's body orientation is transformed by the LVLH matrix to determine the vehicle body coordinates in an ECI coordinate system.

5.3.2 Vehicle Body Orientation System (VBO)

The Euler rotation for the shuttle attitude used by the AITS system is a pitch, yaw, and roll sequence. The shuttle's body coordinate system is a right-handed system with the X-axis parallel to the vehicle's structural body axis (positive toward the shuttle nose), Z-axis parallel to the vehicle's plane of symmetry and perpendicular to the X-axis (positive down with respect to the shuttle fuselage), and Y-axis completing the right-handed system (positive toward the shuttle's right wing). The Euler angles for the shuttle are measured positive as follows: pitch up (positive X-axis to negative Z-axis), yaw right (positive X-axis to positive Y-axis), and roll clockwise (positive Y-axis to positive Z-axis) (Figure 5.6).

5.3.3 Field of View Matrix

Z-axis positive from target to viewer, Y-axis positive from target in the direction of positive Y-field of view measure, and X-axis completing the right-handed coordinate system. The primary application is for converting ECI and vehicle coordinates to camera and sensor field of view angles.

Figure 5.5. LVLH coordinate system
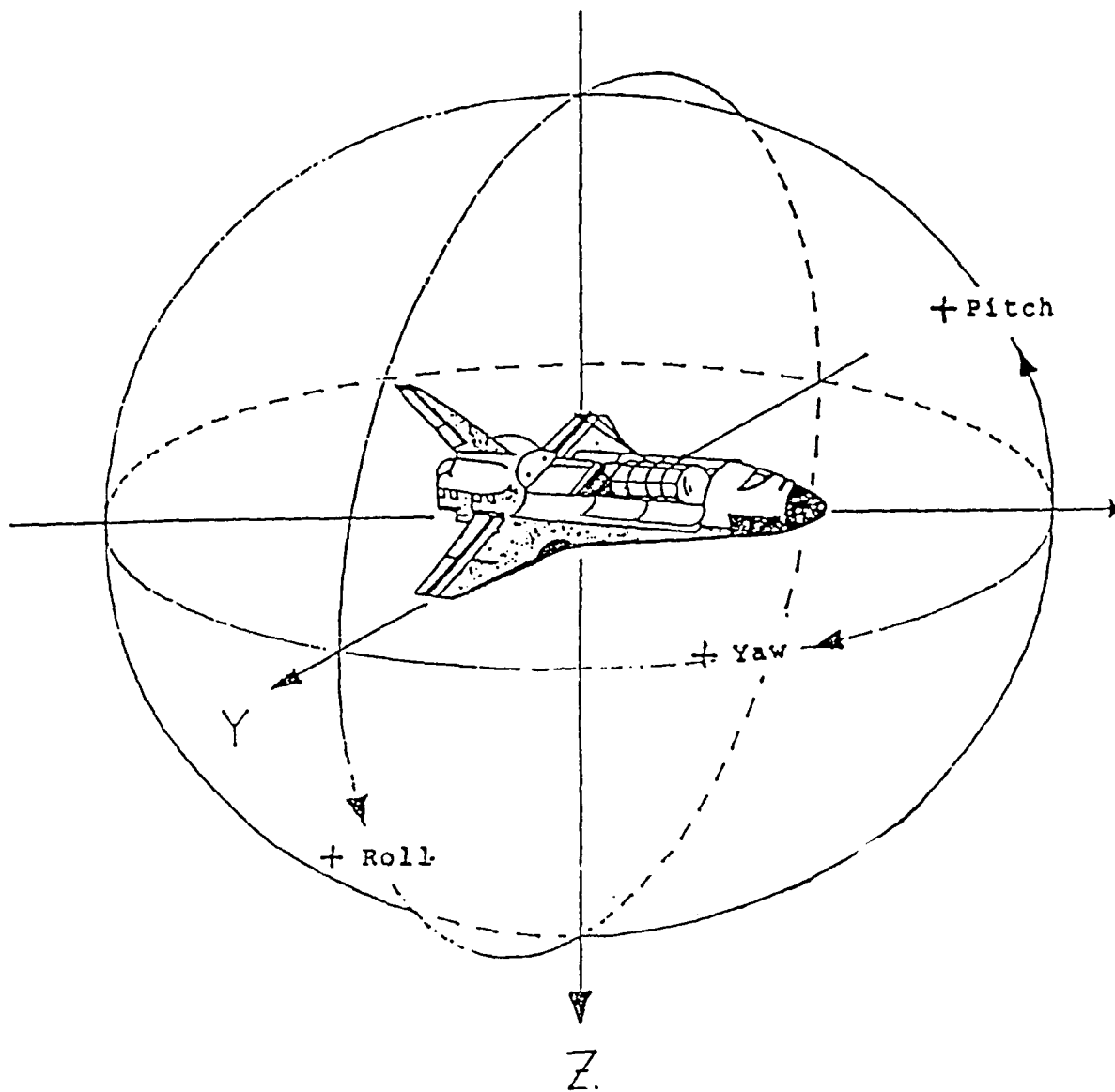
Figure 5.6. Vehicle body coordinate system and rotation

References

Banks, R. and Sannerud, D.A., Private Communication, November 1986.

Whalen, J.A., "Auroral Oval Plotter and Nomograph Determining Corrected Geomagnetic Local Time, Latitude, and Longitude for High Latitudes in the Northern Hemisphere". Environmental Research Papers, No. 327, AFCRL 70-0422, July 1970, AD713170.

McNeil, W.J., Hardy, D.A., O'Neil, R.R., Private Communication, September 1984.

McNeil, W.J., Hardy, D.A., O'Neil, R.R., Private Communication, October 1985.

Gussenhoven, M.S., Hardy, D.A., Heinemann, N., "Systematics of the Equatorward Diffuse Auroral Boundary", Journal for Geophysical Research, 88, 5692, 1983.

Minka, K., "Orbit Determination and Analysis by the Minumum Variance Method". Martin Company, Baltimore Division, Er 13950. Prepared for AFCRL, OAR (CRMXA), USAF AFCRL 65-579, August, 1965, AD625453.

Minka, K., "Orbit Determination and Ephemeris Computation. Martin Company", Baltimore Division. Prepared for AFCRL, OAR (CRMXA) USAF AFCRL 66-259, May, 1966, AD637206.

Star Catalog: Positions and Proper Motion of 258,997 Stars for the Epoch and Equinox of 1950.0., Smithsonian Institution, Washington, D.C., 1966.

6. POLAR BEAR/HILAT

The Polar Bear Auroral Ionospheric Remote Sensor (AIRS) is a multi-detector UV spectrum imager. The imager consists of four UV detectors which are uplink commanded to operate at wavelengths form 1200-6300 Å. The four detectors are co-aligned to allow the use of a single scanning mirror. A mirror scan, +65.2 to -65.2 degrees about the satellite nadir, takes three seconds to complete. The mirror scans orthogonally to the orbital plane for a gravity gradient stabilized satellite. Each scan consists of 326 pixel values for each detector and are encoded in six telemetry frames. The duration of a pass (10-12 minutes) can contain up to 260 scan lines of the region in a rectangular raster image.

The Polar Bear AIRS data is stored on magnetic tape on the CYBER. Selected items of the data for each pass have been extracted and transferred to VAX disk files for this imaging system. Figure 6.1 shows the process used to implement this conversion.

6.1 POLAR BEAR IMAGER DATABASE MANAGEMENT SYSTEM

A menu-driven database access program has been implemented as the Polar Bear Imager Database Management (PBIM) system, which provides a user-friendly method of viewing and processing archived data of the Polar Bear AIRS satellite. The system will monitor all datafiles associated with the system and prevent any duplication of data. This aspect of the PBIM system will be critical as the amount of data increases.

The capability to survey AIRS data on a GPX allows for the reduction of needless hardcopy media and greater access of the data by the researcher. The previous method of survey was graphic hardcopy on 35mm slide film with one detector per slide. This method was costly and lacked efficiency for long term survey, since the principal archive was slide film and could be misplaced. The data can now be accessed almost immediately and displayed through the imaging system eliminating needless hardcopy.

The PBIM System operates on a Digital Equipment Corporation (DEC) GPX/MicroVMS Workstation. Besides the VMS operating system sofware, the workstation also includes a User Interface Services graphics package, which is a collection of FORTRAN-referenced system routines to perform graphics operations. Using these system graphics routines, a Tektronix-emulating graphics library was developed to allow other graphics programs, such as the AFGL Interactive Targeting System, to use the faster speed and higher graphical resolution of the GPX Workstation. The workstation has additional capabilities which are unavailable on a Tektronix, such as large color maps and high-speed raster image routines. Because the current configuration of the workstation has limited hard disk space, the archived satellite data is stored on a Micro-VAX with a large hard disk capacity and is accessed via an ethernet link.

The AIRS data may be viewed in two modes; the raw, scientifically irreducible data is viewed in the form of a color-coded three-dimensional surface plot. A processed form of the data (image data) is viewed as a raster image which has been scaled, filtered and oriented in geographic or geomagnetic coordinates. The image datafiles are generated from a specified raw datafile using a selected processing mode.

A flowchart of the PBIM system is shown in Figure 6.2

Figure 6.2. Flowchart of the PBIM system

Figure 6.1. CYBER to VAX transport of data

6.1.1 Datafile Management

The PBIM system reads the directory on the Micro-VAX containing the AIRS datafiles, and stores their names for later use. Both the image and raw datafile names are coded in a manner such that the names contain the date, time and recording station. The image datafile names also relate the map type of the raster image. The file names are decoded and sorted, and the file information is displayed in several different formats for the user to choose from for viewing or processing operations.

The PBIM system prevents duplicate image datafiles from being created. This is done by maintaining lists of datafiles which already exist or are currently being created. When an image datafile is selected to be created, the system cross references the names of the files to be created to these lists. The image datafile generation selection is disabled if the file already exists or is currently being created.

6.1.2 Raw Data Display

The scientifically irreducible AIRS data is displayed on the GPX Workstation using a modifed NCAR three-dimensional surface plotting routine. This NCAR routine has been modified for use with the GPX color graphics software, and to apply graded coloring for the contour levels of the surface plot. Additional routines have been added so that the position from which the surface plot is viewed is selected using a mouse, and a specified window of the data to be viewed. The surface plot is drawn in fifteen colors with a corresponding colorbar, data value scale, and a title which identifies the detector wavelength, date and time, and the recording station. Although the sweep of detector on the earth's surface is non-linear, the surface plot is linear. Gaps are left to indicate areas where the data is absent. Figure 6.3 shows a sample of a raw data surface plot.

At the completion of the surface plot, the user has several options, one of which is a type of "zooming". To use this zooming option, a specified data value range is chosen on the colorbar scale. The corresponding range of color of the plot is then expanded to the fifteen colors, and the remaining sections of the plot are blanked out. The data value scale is also rescaled and renumbered accordingly. This ability to zoom in on a specific range allows a researcher to study small-scale variations in the data without having to redraw the plot. Figure 6.4 shows a completed zooming operation for the plot in Figure 6.3.

This zooming feature is accomplished by using the workstation's ability to manage large color maps within the display. The surface plot is actually drawn in 120 colors with blocks of eight associated to each of the fifteen colors, using the color graphics software developed for the manipulation of large colormaps. One of the other options at this level is to reset the plot to its original colors.

A majority of the datafiles have detector "roll-overs" where the detector counts became so high that it exceeded the space used for storing the number, and the highest digits were lost. These "roll-overs" usually occurred when the scan encountered the day/night terminator. The detector shuts during a scan when several "roll-overs" are encountered. Because detectors #1 and #2 became unreliable or non-functional early in the satellite life, the raw data for these detectors are not able to be displayed.

166

POLAR BEAR   02/04/1987   07:46:11 TO 07:57:14   (035-87)
RECORDED AT TROMSO   WAVELENGTH : 3914

1941.07
1807.20
1673.33
1539.47
1405.60
1271.73
1137.87
1004.00
870.13
736.27
602.40
468.53
334.67
200.80
66.93

1=SET SCALE TOP
2=SET SCALE BOTTOM
3=RESCALE
4=RESET ORIGINAL SCALE
5=NEW/NEXT PLOT
6=EXIT PROCESS
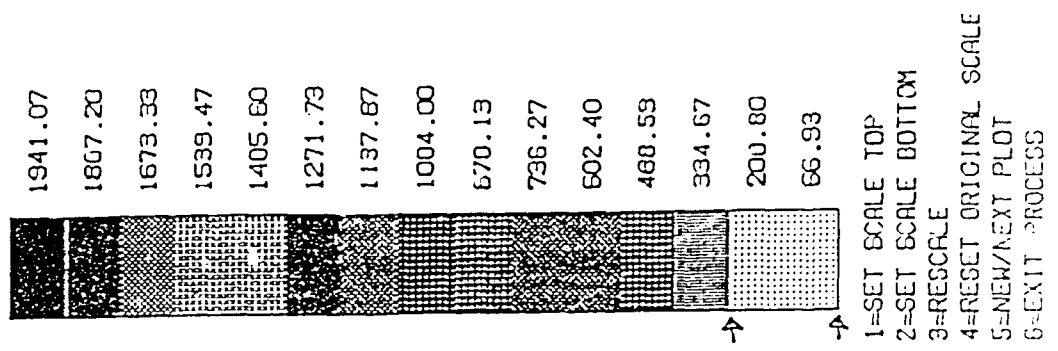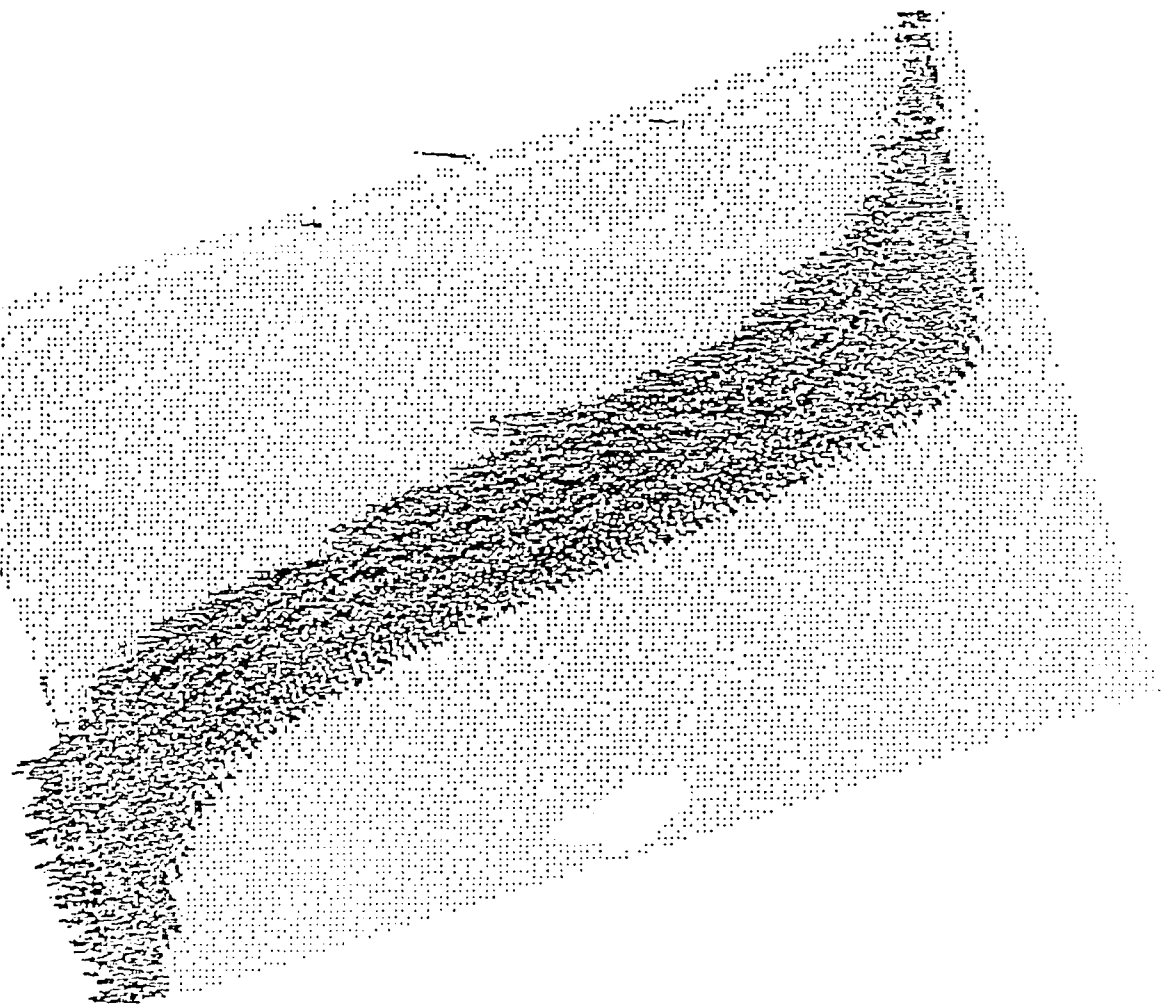
Figure 6.3. Surface plot of AHSS raw data

167

POLAR BEAR   02/04/1987   07:46:11 TO 07:57:14   (035-87)
WAVELENGTH : 3914
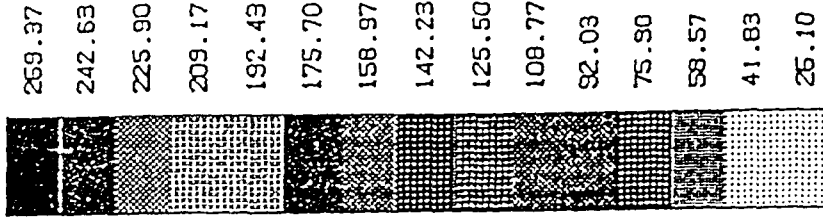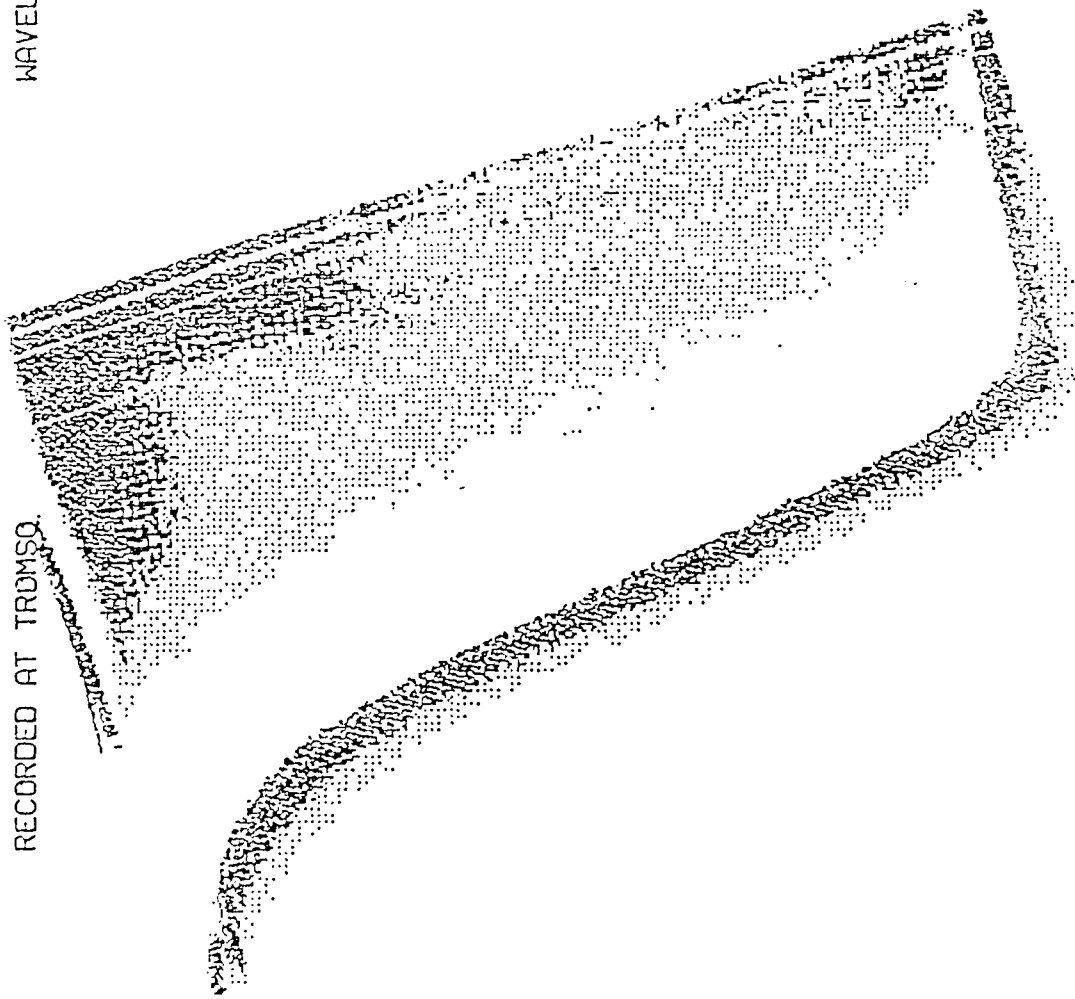
269.37
242.63
225.90
209.17
192.43
175.70
158.97
142.23
125.50
108.77
92.03
75.30
58.57
41.83
25.10

RECORDED AT TROMSO.

1=SET SCALE TOP
2=SET SCALE BOTTOM
3=RESCALE
4=RESET ORIGINAL SCALE
5=NEW/NEXT PLOT
6=EXIT PROCESS

Figure 6.4. Completed zooming operation for surface plot of AIRS raw data

6.1.3 Image Data Generation

Given a selected raw datafile and the desired image type(s), the image datafile(s) are generated in an off-line process, providing the files do not already exist. The PBIM system processes the raw data into one of five possible graphic image formats, which the user selects. The graphic image display formats available are:

- Geographic Latitude vs. Geographic Longitude as polar projections;
- Geomagnetic Latitude vs. Geomagnetic Local Time as polar projections;
- Geographic Latitude vs. Geographic Longitude as an expansion of the polar projections;
- Geomagnetic Latitude vs. Geomagnetic Local Time as an expansion of the polar projections; and
- Geomagnetic Latitude vs. Geomagnetic Longitude with the satellite ground track vertically oriented in the display area.

6.1.4 Image Data Display

An AIRS graphic image datafile contains data for the four detector wavelengths, which can be displayed one per screen or all four images in separate quadrants of a screen. This flexibility allows the researcher to study a single image in great detail or to compare the four detector wavelength images to each other. As the graphic image is accessed from the database, it is stored in the virtual memory of the GPX Workstation, and at completion, it is copied to the screen using one of the the high-speed GPX raster graphics routines. All five map types of the image datafiles offer the option of including, as an overlay, the continental outlines, day/night terminator line and the vehicle ground track. The display is annotated with the detector's wavelength, color associated scale bar, date and time, recording station, and the display coordinate system type. Examples of the five map types and two display types are shown in Figures 6.5 through 6.10.

POLAR BEAR   02/09/1987   22:19:15 TO 22:31:15   (040-87)
RECORDED AT TROMSO   TERMINATOR ALT = 0.0 KM

GEOMAGNETIC LATITUDE VS GEOMAGNETIC LOCAL TIME

WAVELENGTH
3914

Figure 6.5. Map type #1; polar projection

170
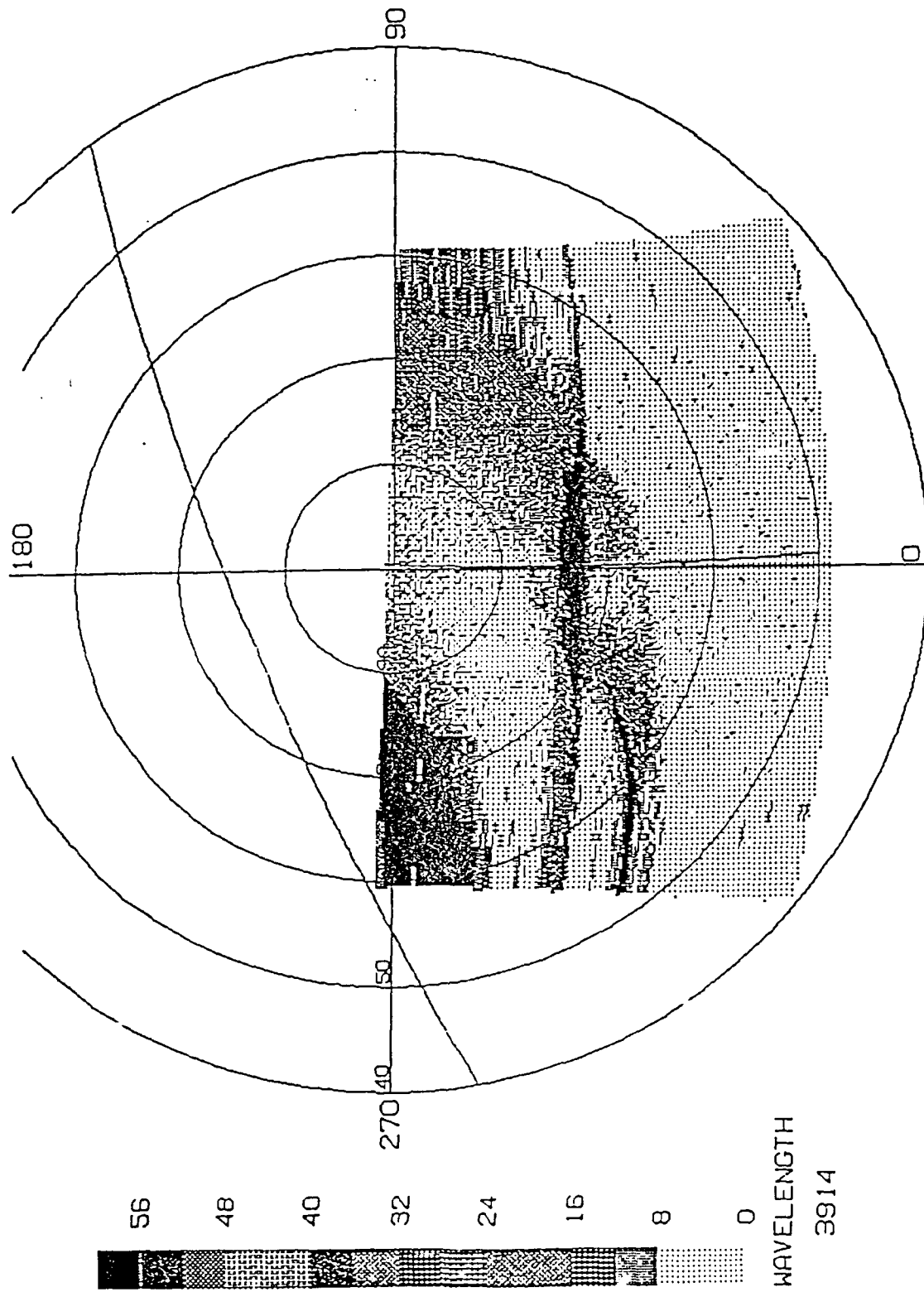
Figure 6.6. Map type #2; polar projection

171

POLAR BEAR   02/09/1987   22:19:15 TO 22:31:15   (040-87)
RECORDED AT TROMSO   TERMINATOR ALT = 0.0 KM

WAVELENGTH
3914
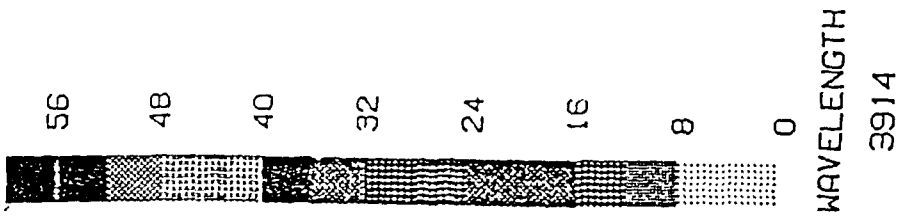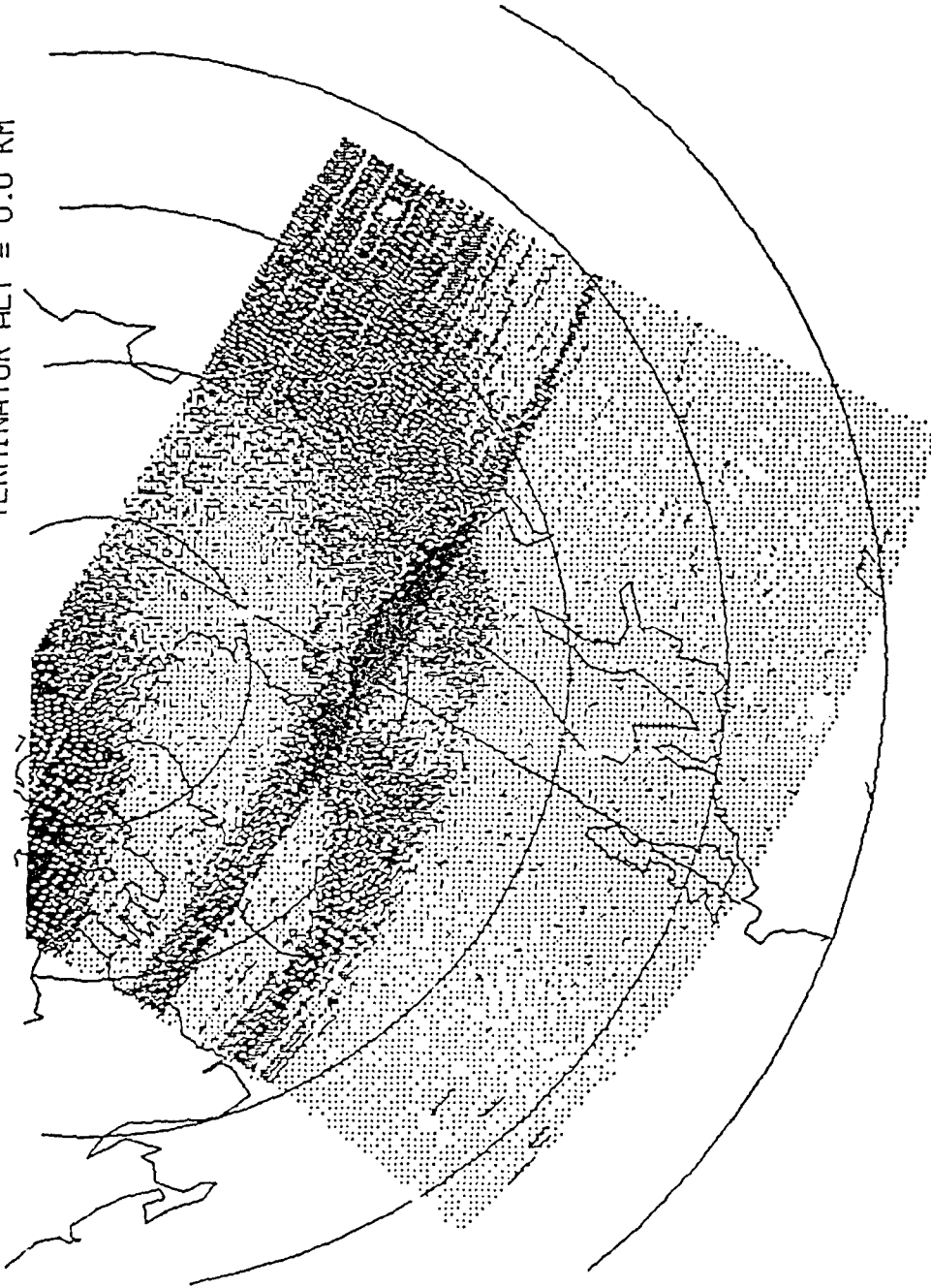
GEOMAGNETIC LATITUDE VS GEOMAGNETIC LOCAL TIME

Figure 6.7. Map type #3; expanded polar projection

172
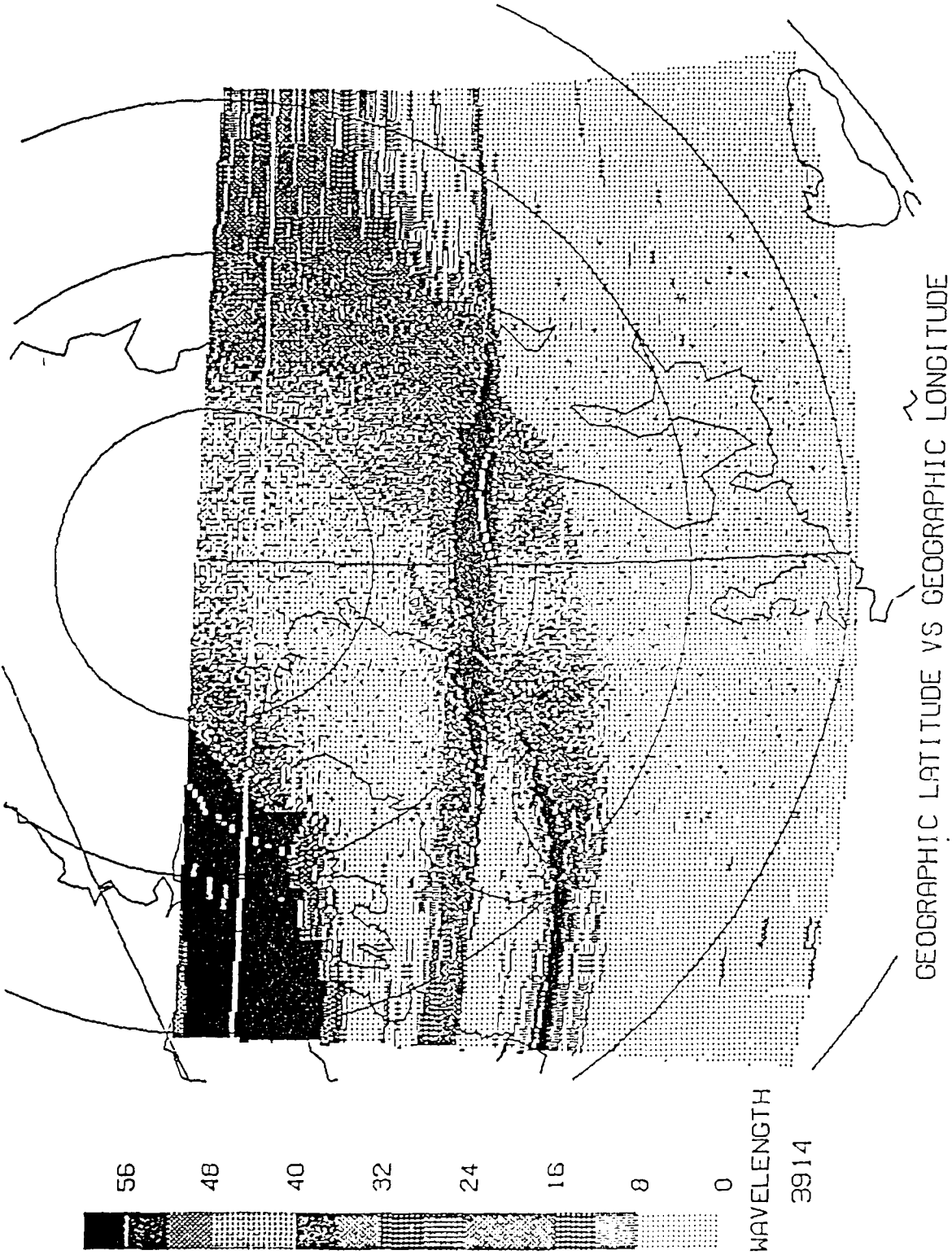
Figure 6.8. Map type #4; expanded polar projection

173

POLAR BEAR   02/09/1987   22:19:15 TO 22:31:15   (040-87)
RECORDED AT TROMSO   TERMINATOR ALT = 0.0 KM

GEOMAGNETIC LATITUDE VS GEOMAGNETIC LOCAL TIME

WAVELENGTH
3914

56
48
40
32
24
16
8
0
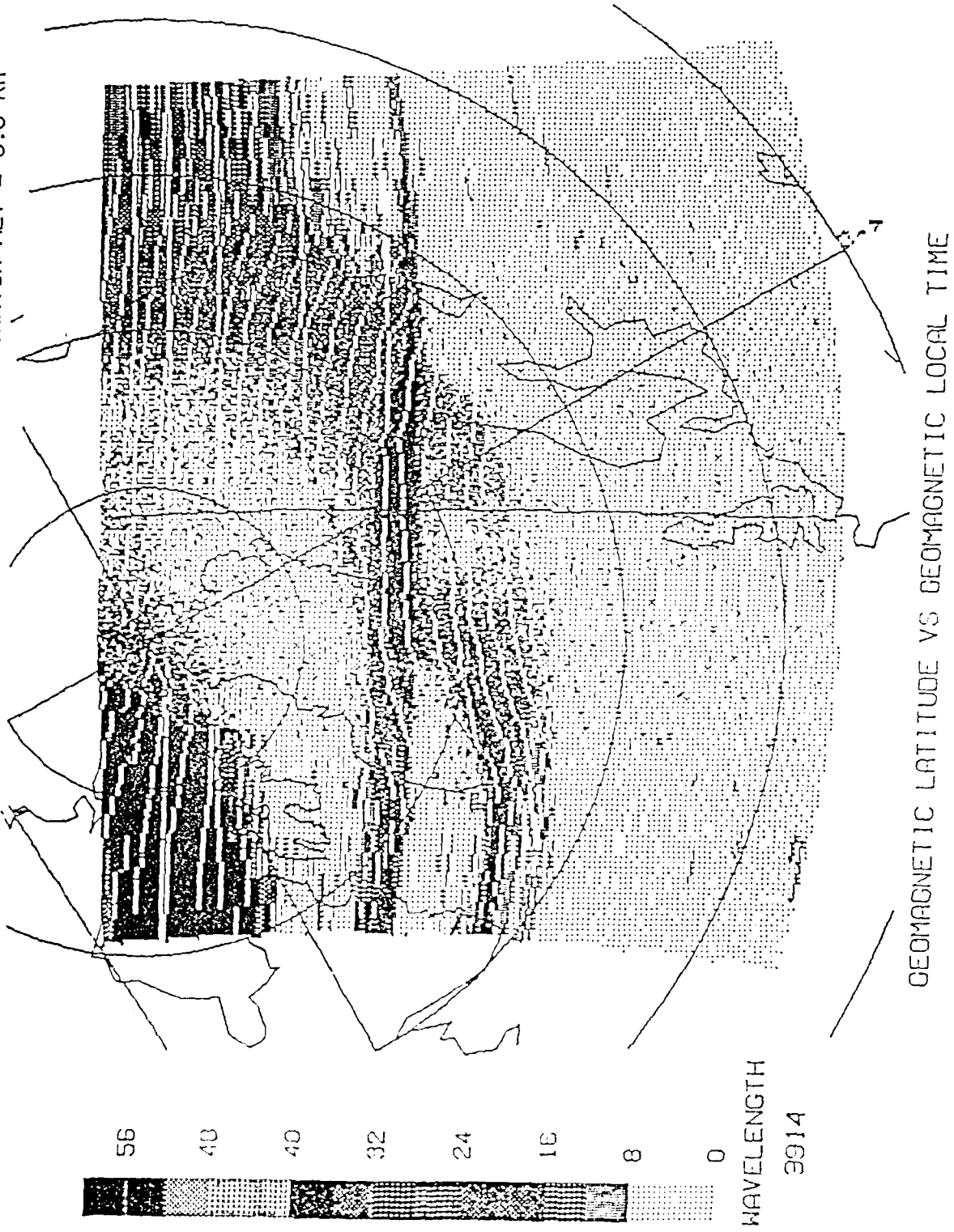
Figure 6.9. Map type #5, expansion of polar projection and vertically oriented satellite track

POLAR BEAR   02/09/1987   22:19:15 TO 22:31:15   (040-87)

RECORDED AT TROMSO   TERMINATOR ALT = 0.0 KM

Figure 6.10. Simultaneous four-detector image display

GEOMAGNETIC LATITUDE VS GEOMAGNETIC LOCAL TIME

6.2 POLAR BEAR ATTITUDE DETERMINATION

The Polar Bear satellite, which carries the AIRS, is a three axis stabilized platform. The gravity-gradient boom is designed to limit the pitch and roll angles to $\pm 10^0$ and the yaw angle is controlled by a momentum wheel, also with a $\pm 10^0$ design limit. Polar Bear carries three magnetometers and three sun sensors to allow attitude determination. The Polar Bear data base contains an attitude solution derived from the magnetometer and sun sensor data when the Euler angles (pitch, yaw and roll) were less than 45^0 in magnitude. Polar Bear was launched on November 13, 1986, and became unstable sometime in February of 1987, resulting in attitude solutions far from the design limits.

Polar Bear follows a nearly circular 1000 km orbit at an inclination of approximately 89^0. The AIRS instrument, when operating in the imager mode, provides cross-track scans in four frequencies, essentially from limb to limb. Each scan cycle, or record, requires three seconds. Details on AIRS can be found in Schenkel et al [1986]. Data are collected from Polar Bear when it is within line-of-sight of a ground station, and data is available from Seattle, Washington, Sondrestrom, Greenland, Churchill, Canada and Tromso, Norway. In this report, calculations are presented for a pass over Tromso in early February of 1987. At that time, the orbital right ascension was similar to the solar right ascension. The northerly location of Tromso, (69^0 latitude), in conjunction with the Sun/satellite geometry, resulted in passes during which the satellite was in sunlight for only part of the transmission. Attitude solutions are provided in the database only for the portions of the pass during which sun sensor data was available.

6.2.1 Polar Bear Data

The attitude solutions computed in this report use magnetometer and AIRS imager data only. The three magnetometers provide vector readings at 50 msec. intervals and are received in 0.5 second frames. The ten measurements received in each frame are averaged to give six magnetometer data points for each three second imager scan.

Figure 6.11 shows a single AIRS imager record. The four plots in this figure give the counts recorded by each detector. The bottom-most plot corresponds to detector 1 operating at 1596Å and contains little information due to the low gain. The 1356Å plot (detector 2) shows a peak near the left border which may correspond to the Earth limb. The 3914Å plot (detector 3) when followed from right to left shows a sequence of sudden drops followed by a "cutoff."

The sudden drops correspond to rollovers resulting from the saturation of the detector. The "cutoff" is caused by a large reduction in the gain applied to the output of detectors 3 and 4 when the light intensity increases above a certain level. The top plot (6300Å) shows a gradual increase in intensity leading up to the "cutoff." For this particular pass, the solar right ascension was $\sim 317.5^0$ and the orbital right ascension was $\sim 292.0^0$. Transmissions were received by Tromso (local time 0900) as the satellite passed from the pole to a latitude of 51^0. The pass consisted of 215 scan records. The records at the start of the pass covered unlit portions of the Earth while the later scans covered lit portions. Figure 6.12 corresponds to record number 100 and the ramp (going from right to left) on the top of the plot corresponds to scanning from an unlit to a lit region.
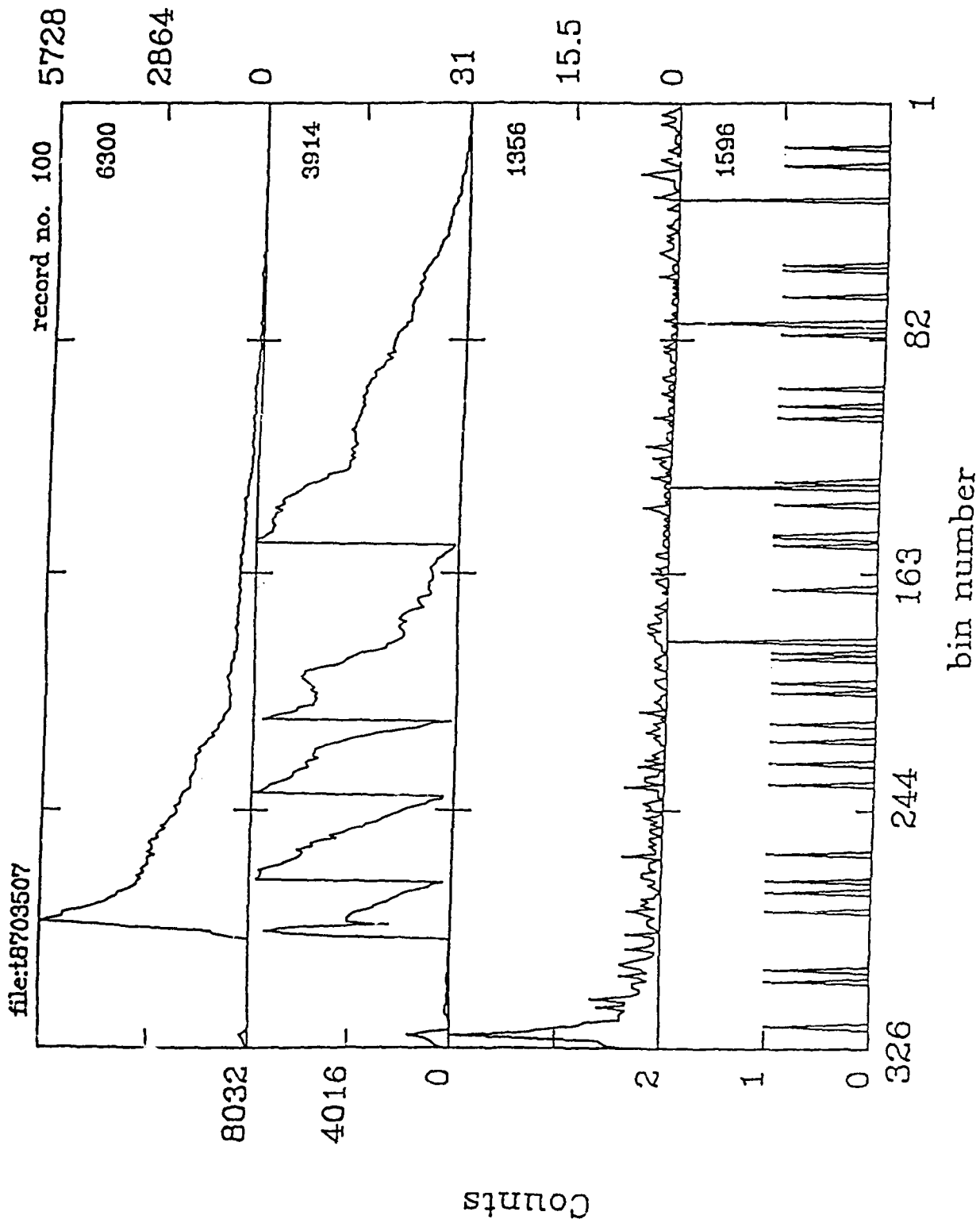
Figure 6.11. AIRS imager data

177
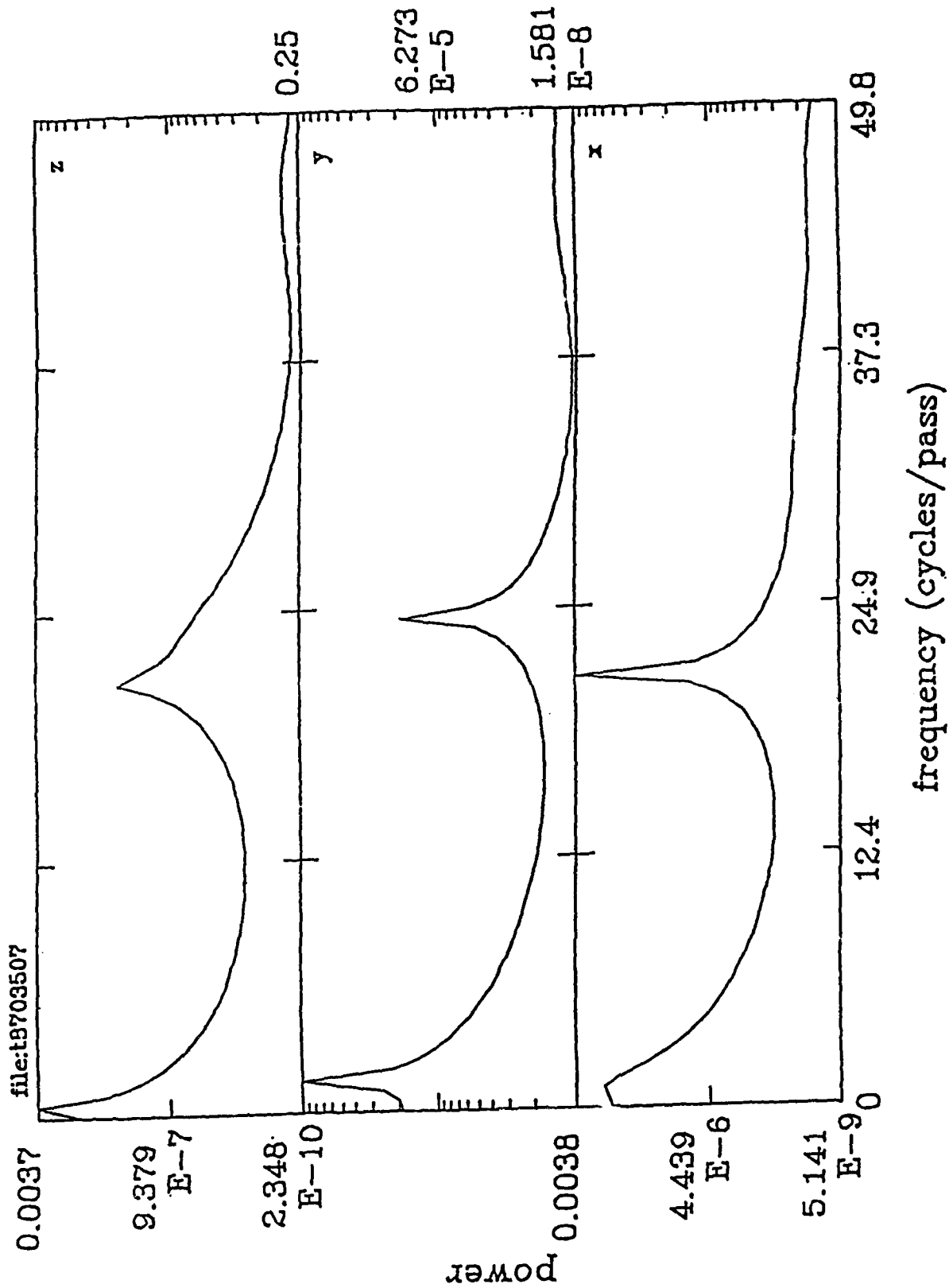
Figure 6.12 Magnetometer power spectrum density

178

6.2.2 Mathematical Formulation

There is a great deal of literature concerned with the attitude determination of a three-axis stabilized satellite. Most of this work [Wahba, 1966, Tietze, 1982] assumes there are two or more independent vector measurements available at any given time. These methods solve for the attitude matrix A by minimizing the functional,

$$J = \frac{1}{2} \sum_{i=1}^{n} \omega_i |\hat{U}_i - A\hat{V}_i|^2, \qquad (6.1)$$

where the $\hat{U}_i$ are unit measurement vectors, the $\hat{V}_i$ are unit model field vectors and the ω_i are weighting coefficients. The attitude matrix A is the orthogonal transformation which maps "model-field" coordinates into vehicle coordinates. In this report, the "model-field" will be given in local vertical-local horizontal (LVLH) coordinates and A will be parametrized by the Euler angles pitch, roll and yaw. Vehicle coordinates are defined such that the z-axis lies in the orbit plane, positive towards the Earth, the x-axis is tangent to the orbit path, positive in the direction of motion and the y-axis is normal to the orbit plane and completes the right-handed system. For a circular orbit the above definition of vehicle (body) coordinates implies vehicle coordinates are identical to LVLH coordinates when the pitch, roll and yaw are all zero. In this case, A is an identity matrix.

In this work a single vector measurement is given over a sequence of time points during which the attitude is assumed to change appreciably. The minimization functional is similar to before, only now the summation is over measurements over a period of time rather than over measurements at a single point in time. In addition, the attitude matrix becomes a function of time. It is not possible to solve this problem uniquely unless some assumption is made concerning the behavior of A as a function of time. Figure 6.12, showing the magnetometer power spectrum density, indicates that a few basic frequencies can be identified in the magnetometer data. The presence of a few strong peaks implies that a Fourier type expansion for the Euler angles involving just a few frequencies may be able to model the satellite's attitude evolution. The calculations presented here were performed by expanding the Euler angles and then minimizing Equation 6.1 to find the coefficients.

For passes during which the AIRS instrument was in the imager mode, additional attitude information is contained in the "visual data". For the pass discussed here, it appears that detector 2 encountered the Earth limb near the end of the scan sweep, from about record 20 to the end of the pass. The occurence of the limb is associated with a peak in the imager data. The bin number of the peak gives the angle from the nadir of a measured limb. Knowledge of the limb angle is not enough to locate the nadir vector so the limb angle does not provide an additional vector measurement. The limb angle can however be used as an additional constraint in the minimization functional.

Given the measured nadir angle n and the computed nadir angle η, the limb constraint is included by adding the term,

$$\Sigma (n-\eta)^2$$

to the functional J. The above summation is over those records in which the limb is detected.

179

The parameters in the Fourier expansions are determined using a standard IMSL minimization routine (DBCONG). Five frequencies are allowed ($m=5$) implying a total of 78 parameters, which makes for a rather demanding minimization problem. To reduce the CPU requirements and to enhance the probablility of convergence the solution is built up one frequency at a time and the parameters corresponding to a frequency are computed in two passes. Initially, the maximum entropy method is used to generate a power spectrum density for the magnetometer data and the resulting frequencies are sorted by power level. The frequencies are handled in the orderuency for each Euler angle.

On the first pass for a given frequency, only the amplitude and phase angle are included in the minimization problem. On the second pass all the parameters are included and the results of the first pass are used to initialize the second pass. The method is sensitive to initial estimates and to the range limits imposed on the variables.

The limb constraint is the most expensive part of the functional, and several steps are taken to lessen its impact. The idea of the limb constraint is to make sure the large scale components of the attitude solution are consistent with tual data has the resolution to resolve small scale, high frequency features of the solution. For this reason, when the high frequency solution is computed, no limb constraint is imposed.

6.2.3 Results

The data base Euler angles are shown in Figure 6.13a. It can be seen that the pitch angle undergoes small, high frequency oscillations about -2^0 while the roll and yaw angles execute lower frequency but higher amplitude oscillations. The roll varies between -2^0 and -4^0 and the yaw between 7^0 and -7^0. Figure 6.14a shows Euler angles computed using the minimization method described herein. This solution was generated using a limb height of 170 km. This value was derived by computing an Earth width angle from averaged limb data using those scan records in which both entrance and exit limbs were detected. If α is the weight for the entrance limb, β for the exit limb, then the average Earth width is given by,

$$ d = \frac{.4 \ \Sigma \alpha_i \beta_i (n_i - m_i),}{\Sigma \ \alpha_i \beta_i} $$

where i runs over those records which detected both limbs and m_i, n_i are respectively the bin numbers in which the entrance and exit limbs were detected. For this pass, the average Earth width was found to be 125.2^0 giving a layer height for the 1356Å wavelength of between 170 and 175 km. This figure is consistent with the result of 170 ± 20 found by Rosenberg [1987].

Figure 6.13b shows the measured limb data (points) and the computed limb (solid line) which resulted from the database solution. It can be seen that the computed limb differs by at least 2^0 from the measured limb. Similar results are shown in Figure 6.14b for the minimization solution. The errors are of the order of instrumentation errors. The minimization results were computed assuming there was a shift of 4 bins, or 1.6^0, in the imager data. This shift is similar to the roll adjust of 2.2^0 used by Rosenberg [1987].

180
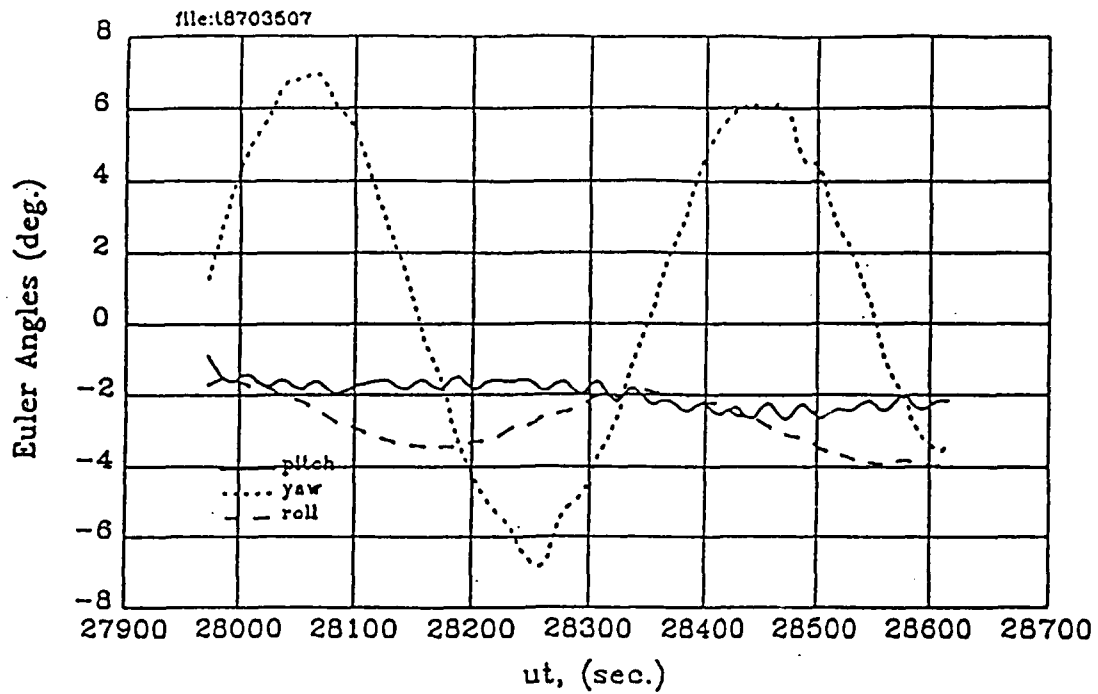
Figure 6.13a. Data base pitch, yaw, and roll
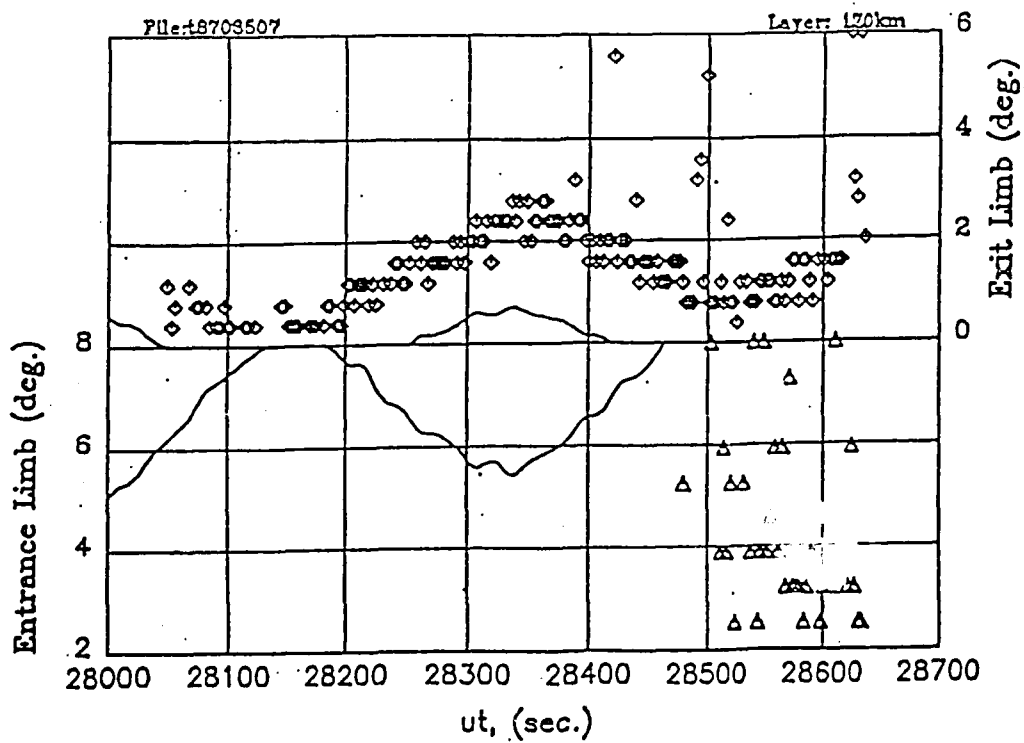
Figure 6.13b. Data base limb solution

181
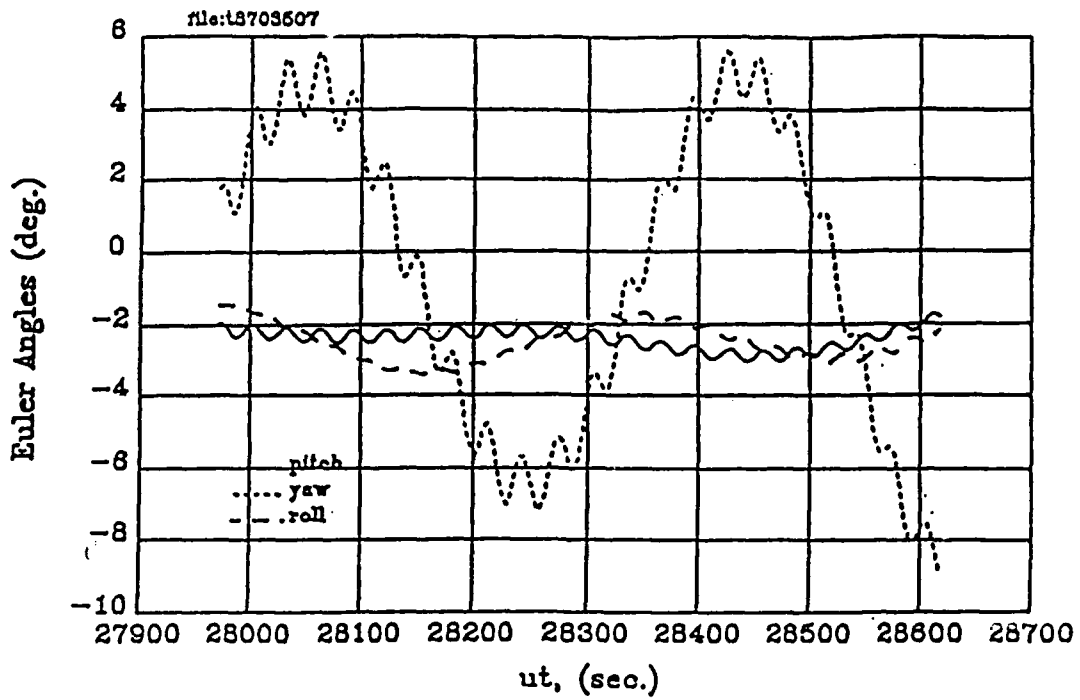
Figure 6.14a. Biased pitch, yaw, and roll
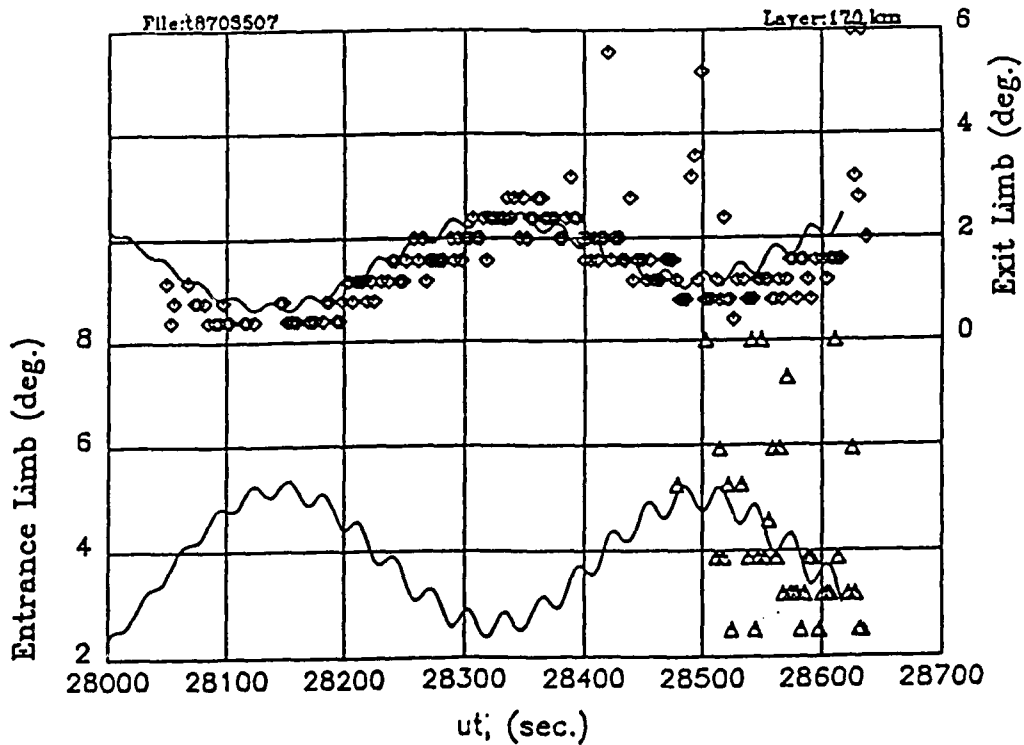
Figure 6.14b. Biased limb solution

References

Rosenberg, N. "Satellite UV Image Processing", AFGL-TR-87-0271, October 1987.

Schenkel, F.W., Ogorzalek, B.S., Gardner, R.R., Hutchins, R.A., Huffman, R.E., and Lanabee, J.C., "Simultaneous Multi-spectral Narrow Band Auroral Imagery from Space (1150 Å to 6300 Å)", SPIE, V.687 (1986), 90-103.

Tietze, J.L. "Fast Three-Axis Attitude Determination Using Vector Observations and Inverse Iteration", J.Astro.Sciences, V.XXX no.2(1982), 171-179.

Wahba, G. "A Least Squares Estimate of Satellite Attitude", SIAM Review, V.8 no.3(1966), 384.

7. IONOSPHERIC STUDIES

7.1 SCINTILLATION

7.1.1 TPSCAN Diagnostics Guide

TPSCAN is a pre-processor program which supports the statistical processing of the phase and amplitude of transionospheric VHF radio wave signals from satellite beacon transmitters. Originally intended merely to read-out salient parameters from headers, TPSCAN has undergone several metamorphoses as a result of which it now exerts major control over data evaluation and selection for subsequent processing.

The following material describes briefly the functions performed by TPSCAN, together with the content of its output products. A sample output is shown in Table 7.1.

7.1.1.1 General File Information

TPSCAN tries to anticipate various conceivable anomalies in tape formatting and to identify and diagnose such occurrences. Examples are empty files, recognizable as successive occurrences of EOF's with no intervening data. Another common fault is failure to end the tape with an EOF. These faults are identified by TPSCAN, and appropriate explanatory messages are printed:

> "Empty Tape"
> "Error-EOF Omitted-Calculate End Time Manually"
> "(# of) Empty Files"

Parity errors are summarized with appropriate printed messages:

> "Parity Error File (# of), Record (# of)"
> "Only Parity Error Records in File (# of)"

For each non-empty file there is a summary of key information, including the following:

- File number (sequential for all files on tape, including empty files)
- Mode number
- File start-time and end-time
  year
  day
  hour
  minutes
  seconds
- Indication of whether file contains calibrations or radio wave data.

184

Table 7.1. TPSCAN Diagnostics Guide

```
        PROBLEM CODE     TIME STEP GT 8 SEC:G    REPEATED TIME:R    PARITY ERROR:P

  (7)                        (1)          (5)(3)(4)                            (6)
  886.  0  0  0  0  0  0  0  0  0   0   0   3>  0  0  0  0  0  0  0  0   0   0       (2)
 1054.  0  0  0  0  0  0  0  0  0   0   2>  0   0  0  0  0  0  0  0  0   0   0
                                                                            TIME= 1038.  0 17 18
 1223.  0  0  0  0  0  0  0  0  0  20   1>  0   0  0  0  0  0  0  0  0   0   0
                                                                            TIME= 1199.  0 19 59
 1392.  0  0  0  0  0  0  0  0  0  19>  0>  0   0  0  0  0  0  0  0  0   0   0
                                                                            TIME= 1368.  0 22 48
 1561.  0  0  0  0  0  0  0  0  0  17>  0>  0   0  0  0  0  0  0  0  0   0   0
                                                                            TIME= 1537.  0 25 37
        .  .  .  .  .  .  .  .  .   .   .   .   .  .  .  .  .  .  .  .   .   .
        .  .  .  .  .  .  .  .  .   .   .   .   .  .  .  .  .  .  .  .   .   .
 5276.  0  0  0  0  0  0  0  0  4>  0   0   0   0  0  0  0  0  0  0  0   0   0
                                                                            TIME= 5243.  1 27 23
 5444.  0  0  0  0  0  0  0  0  2>  0   0   0   0  0  0  0  0  0  0  0   0   0
                                                                            TIME= 5412.  1 30 12
 5613.  0  0  0  0  0  0  0  0  1>  0   0   0   0  0  0  0  0  0  0  0   0   0
                                                                            TIME= 5573.  1 32 53
 5782.  0  0  0  0  0  0  0 19>  0>  0   0   0   0  0  0  0  0  0  0  0   0   0
                                                                            TIME= 5742.  1 35 42
 5951.  0  0  0  0  0  0  0 18>  0>  0>  0   0   0

FILE  1   1930   3   88  341  0:14:46 -  341  1:40:55        .1219E+09        RECORDS  1  THROUGH   643
           (14)  (13) (12)  (11)           (8)                 (9)                                 (10)

2 EMPTY FILES  (FILES 2 - 3)

        PROBLEM CODE     TIME STEP GT 8 SEC:G    REPEATED TIME:R    PARITY ERROR:P

55222.  0  0  0  0  0  0  0  0  0   0   0   4>  0  0  0  0  0  0  0  0   0   0
55390.  0  0  0  0  0  0  0  0  0   0   0   3>  0  0  0  0  0  0  0  0   0   0
                                                                            TIME=55383.  15 23  3
55559.  0  0  0  0  0  0  0  0  0   0   0   1>  0  0  0  0  0  0  0  0   0   0
                                                                            TIME=55543.  15 25 43
55728.  0  0  0  0  0  0  0  0  0   0  20   0>  0  0  0  0  0  0  0  0   0   0
                                                                            TIME=55712.  15 28 32
55897.  0  0  0  0  0  0  0  0  0   0  18>  0>  0  0  0  0  0  0  0  0   0   0
                                                                            TIME=55881.  15 31 21
        .  .  .  .  .  .  .  .  .   .   .   .   .  .  .  .  .  .  .  .   .   .
        .  .  .  .  .  .  .  .  .   .   .   .   .  .  .  .  .  .  .  .   .   .
59949.  0  0  0  0  0  0  0  0  0   2>  0>  0   0  0  0  0  0  0  0  0   0   0
                                                                            TIME=59925.  16 38 45
60118.  0  0  0  0  0  0  0  0  0  20   0>  0>  0  0  0  0  0  0  0  0   0   0
                                                                            TIME=60036.  16 41 26
60287.  0  0  0  0  0  0  0  0  0  19>  0>  0>  0  0  0  0  0  0  0  0   0   0
                                                                            TIME=60255.  16 44 15
60456.  0  0  0  0  0  0  0  0  0  17>  0>  0   0  0  0  0  0  0  0  0   0   0
                                                                            TIME=60424.  16 47  4
60625.  0  0  0  0  0  0  0  0 16>  0>

FILE  4   2047   3   88  341  15:20:22 -  341  16:51:45        .1219E+09       RECORDS  1  THROUGH   682

(CALIBRATION FILE   5)

6 EMPTY FILES (FILES 6 - 11)
```

185

NOTES TO TABLE 7.1

①   Twenty one record wide (i.e., 168s.) array of comments on individual 8s. records.

②   Column of times written to TAPE 19 to provide DISC the time of first of 12 successive records to be processed.

Meaning of Entries in Array

③④   During update, a phase slope threshold exceedence criterion is used to identify occurrence of update frequency. This is indicated by the > symbol if update frequency is identified anywhere within a record. A phase second derivative criterion is used to identify the onset of updating. This is indicated by an integer >1 and <20. The integer represents which of twenty time-serial subsets of the record is the one at which updating begins (in this case #2). Thus the preceding 1/24 (i.e., 0.4 sec) of the record should be good data.

Selection of Data for Processing

⑤   The zero indicates no updating activity. Moreover, this is the last record prior to the one in which updating begins. This record and its 11 predecessors have no faults, ⑤ and ⑥ are chosen as the last and first, respectively, of 12 successive records for processing. This is indicated by the value 1038 at ②.

⑦   886 is the initial time of the first record of the row. The time at record ⑥ is given by:

$$886 + 19 \times 8 = 1038$$

which is then written at ②.

Miscellaneous

⑧   Start and end times of file (hrs, min, sec).

⑨   Frequency (at beginning of file)

⑩   Total number of records in File. Needed to compute end time of last file of field tapes from which final EOF has been omitted.

⑪   Day number

⑫   Year

⑬   Mode number

⑭   An anachronism: "record serial number" taken from field tape. Invalid for multi-channel multiplexed data; e.g., approximately 3 times the actual (per-channel) number for Mode 3. Use item ⑩ to avoid ambiguity.

7.1.1.2 Rec. Specific Information

In addition to file summaries, the TPSCAN printout in Table 7.1 also displays an array of comments on each individual record, where an individual record represents eight seconds of data. The width of the printed array of comments is 21 records (168 seconds) corresponding to the period of the RF frequency update process. This should yield a stroboscopic effect: indications of frequency updating effects should exhibit nearly vertical alignment on the printed page. The symbology of this display is the following:

- P implies a parity error in record
- Q implies that the RF frequency is erroneously reported to be zero
- R implies a record-to-record time difference of less than 8 seconds----an error
- G implies a record-to-record time difference of more than 8 seconds----an error
- 0 implies no indication of initiation of frequency updating. Standing alone, it indicates good data.
- Integer ≥ 1 and ≤ 20 indicates onset of updating. Value indicates at which of twenty 0.4s. sub-intervals the updating begins.
- > implies that the computed value of the time derivative of phase suggests that frequency updating is in progress somewhere within record.

7.1.1.3 TAPE19 Generation

Unseen on the printout, but critical to subsequent processing operations, is the generation of TAPE19. Data written on TAPE19 is used by DISC to select periods of valid data for processing, while rejecting the invalid (for phase processing) frequency updating intervals. Further, for the selected data intervals, TPSCAN computes and writes to TAPE19 the corrections to be applied by DISC to raw I&Q data to suppress coherent leakage artifacts.

Manifestation of the frequency updating process typically (but by no means invariably) is characterized by a sharp onset, but a cessation that is gradual as phase lock is recovered. Therefore the data selection process is keyed to the (usually) well defined onset and its identification using a phase 2nd derivative criterion. If TPSCAN is unable to identify a sharp onset of updating for a given 168 second block of data, it will scan both the preceding and following 168 second blocks for sharp onsets. Upon finding one (which is the likely outcome), it will translate its time of occurrence ±168s (as appropriate) to get the (presumed) onset for the particular 168 second block under examination.

Once onset is identified, TPSCAN looks backward in time from that event, selecting (for processing) the preceding 12 (however, it is only ten and a fraction of these i.e., 4096 points that will ultimately be processed). successive records, provided all are free of flaws. If one (or more) records in this string is flawed, TPSCAN shifts successively further back in time, searching for a contiguous string of 12 good records. This search is pursued only until there is risk of the earliest of the records in the string overlapping the phase-locking interval of the preceding frequency update process.

If the search fails to yield valid data, TPSCAN/TAPE19 directs that no processing be applied to the corresponding 168 second block of data. On the other hand, if a valid string of 12 records is

187

available, TAPE19 is provided appropriate timing information to ensure subsequent processing of those, and only those, 12 records. Appended to that timing information are the appropriate I&Q corrections to suppress coherent leakage throughout the 11 record block of data to be processed [Bass et al., 1984].

7.1.2 Spaced Receiver Analysis

The scintillation of radio signals is caused by the ionospheric irregularities. Hence, the scintillation of radio signals is related to the structure of the ionospheric irregularities. In order to study these irregularities in the ionosphere, correlation analysis methods have been applied to signals detected on the ground by spaced receivers after an interaction with the ionosphere. The correlation function analysis methods assume that surfaces of constant correlation are ellipsoidal yielding elliptical contours in any plane. Two methods based on two different algorithms were used in the analysis of spaced-receiver data: one called Modified Fedor (MF) algorithm, originally devised by Fedor, and another suggested by Rino and Livingston called the Rino-Livingston algorithm. These algorithms are described in detail by Costa and his colleagues [1988]. Both algorithms are based on the autocorrelation and cross-correlation functions of the received signals. These correlation functions can be modeled by a decreasing function of two spatial variables, which represent the distance between the receivers, and the time delay.

These methods provide solutions of the anisotropy and the true drift velocity of the ground diffraction pattern. The anisotropy and the true velocity of the in situ irregularities are related to those of the ground diffraction pattern under certain assumptions [Rino and Livingston, 1982, Costa et al, 1988]. The drift velocity of the ground diffraction pattern is simply related to the drift velocity of the in situ irregularities and the satellite velocity (which is negligible for quasi-geostationary satellites). The ellipses, which characterize the anisotropy of the diffraction pattern, are the geometrical projections along the ray path onto the ground of the anisotropy ellipsoids of the in situ irregularities.

The results from the MF and RL algorithms are compared, using signals transmitted by a quasi-geostationary polar beacon and received at Thule, Greenland (76.5°N, 68.7°W). Similar comparative studies were done by Costa and his colleagues [1988] in the correlation analysis of signals collected by three spaced receivers at Goose Bay, Labrador (53.3°N, 60.3°W), and at Tromso, Norway (69.7°N, 18.9°E). The received signals are sampled at 50 Hz. From a 168-second data block, only 72 seconds are used in the analysis. The reduction of the data window is due to the fact that data records at the beginning and end of a data block are not useful. The loss of the signal phase lock after each frequency updating and pre-processing requirements make it necessary to reduce the data window to 72 seconds for each 168 second data block. This corresponds to 3600 samples of the signal intensity per channel. The results from these two algorithms are, in general, in good agreement.

The anisotropies of the diffraction pattern on December 3 from both the MF and RL algorithms are illustrated in Figure 7.1. The circles cover the corrected geomagnetic latitudes (CGL) from 80° to 90° and corrected geomagnetic local times (CGLT) for a full day. The results cover a time span from 1600 to 1800 CGLT. The CGL of their 350 km penetration point P remained at about 84.5°N. The magnitude of the axial ratios are given by a line segment centered at the vertical projection on the ground of the point P along the ray path. The direction of a line segment is the orientation of the major axis of the ellipse. This orientation is measured by the angle between the radial direction through a penetration point P and the major axis of the ellipse. Figure 7.1 shows good agreement between the two algorithms for estimated axial ratios and their orientations.
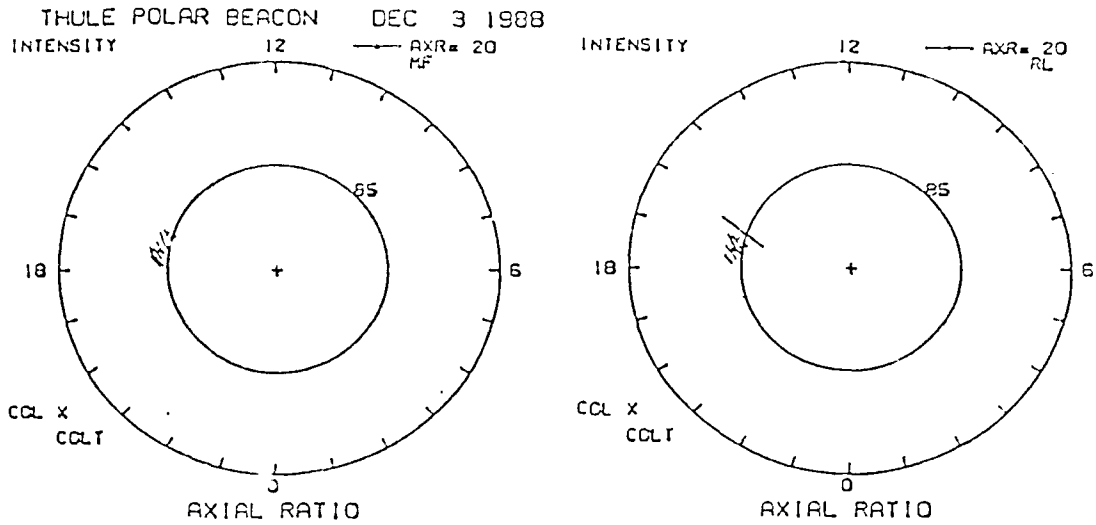
Figure 7.1. Polar plot of axial ratios and o.ientations of the major axes of anisotropy ellipses of the diffraction pattern, using the modified Fedor (MF) and the Rino-Livingston (RL) algorithms.
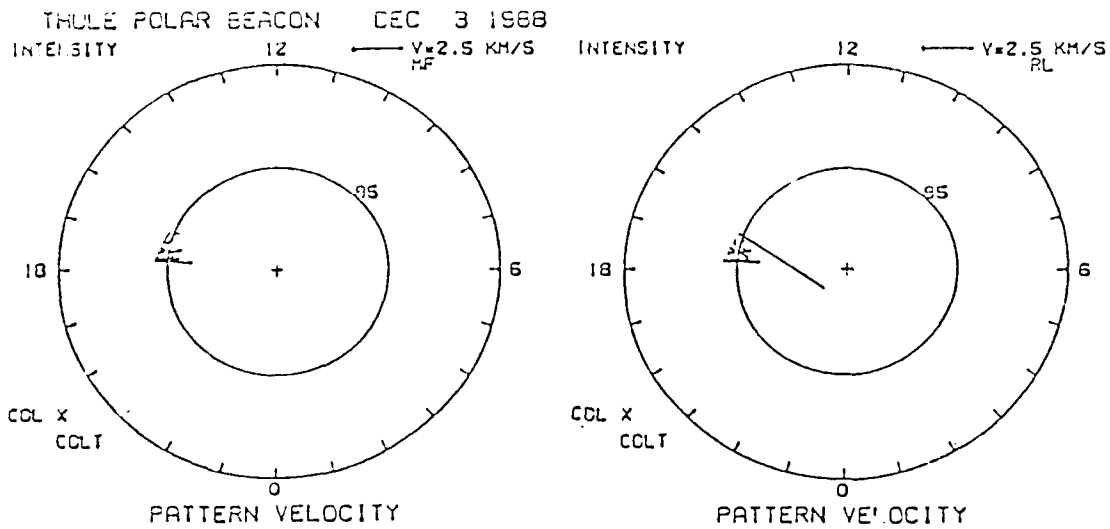
Figure 7.2. Polar plot of magnitudes and orientations of the true drift velocity of the diffraction pattern, using the modified Fedor (MF) and the Rino-Livingston (RL) algorithms.

The drift velocity of the diffraction pattern are displayed in Figure 7.2 in the polar CGL versus CGLT coordinate system. The magnitude of the velocity vector is represented by the length of the line segment starting at the length of the vertical projection on the ground of the penetration point P. The velocity direction is measured exactly as for the axial orientation. Again, the results are in good agreement, except that the RL method, being more sensitive than the MF method, gave fewer solutions [Costa et al, 1988]. In general, the drift velocity of the diffraction pattern tends to increase from about 0.5 km/s at 16.65 CGLT to about 2.0 km/s at 17.75 CGLT.

Rectangular plots of the anisotropies and the drift velocity of the diffraction pattern are also shown in Figure 7.3 and Figure 7.4, respectively. These plots display the solutions in a different reference frame. The solutions from the MF method are represented by triangles and those from the RL method by plus signs. The orientations of the major axes in Figure 7.3 are measured in the CGLxCGLT reference frame. As discussed above, in general, a good agreement between the results are obtained by the two algorithms.

7.1.3 Processing of New Data Format

The processing of scintillation induced by the ionosphere in the high latitude region is performed by the SDS software system. The SDS scintillation processing system was originally developed by Stanford Research Institute (SRI) International. Data reduction and analysis takes place at GL and involves unpacking the raw data, and processing the scintillation signal. Roberts [1983] discussed the different stages of the software processing system. The reference by Bryant and Robinson [1985] covers the NOS procedures involved in the processing and the display of the intensity and phase scintillations in both the time and frequency domains at different processing stages.

7.1.3.1 New Data Format

Recently, the data tape format has been changed. The processing software system must be changed accordingly. The unpacking of the raw data has been accomplished. The data used for testing was recorded at a ground station in Sondrestrom, Greenland. Table 7.2 shows the tape data format.

The complex data pairs are the in-phase and quadrature components. A sample is stored in a 16-bit word. The data are stored in the first 6000 words for every record. The last 20 words contain pertinent information for this record. The data pairs are sampled at 100 Hz. Currently, the sampling frequency used is 50 Hz. There are two possible data modes. In mode 1 operation, a single receiver was used to collect the complex data pairs. In mode 3 operation, three receivers were used to collect data in three separate channels. In mode 1, a record contains 30 seconds of complex data pairs, and in mode 3, every record contains 10 seconds of complex data pairs. In mode 3, the complex data pairs from the channels are interleaved.

The data are unpacked and stored in the format given in Table 7.3.

In mode 1, the intensity and phase pairs in words 1 through 3000 represent a single channel. In mode 3, however, the 3000 words contain the intensity and phase pairs from three separate channels. Words 1 through 1000 represent 10 seconds of data from channel 1; words 1001 through 2000 represent data in channel 2; and words 2001 through 3000 represent data in channel 3.

190

Table 7.2 Field Tape Data Format for a Single Record.

Word	Description
1-6000	Complex data pairs sampled at 100 Hz
6001	Year
6002	Millisecond
6003	Second
6004	Minute
6005	Hour
6006	Day
6007	Station identification
6008	Unassigned
6009	Mode
6010	Unassigned
6011-6012	RF frequency
6013-6020	Unassigned

Table 7.3 Unpacked Data Format

Word	Description
1-3000	Intensity and phase pairs
3001	Year
3002	Day
3003	Hour
3004	Minute
3005	Second
3006	Millisecond
3007	Time in seconds
3008	Sampling frequency
3009	Mode
3010	Station identification
3011	RF frequency
3012-3020	Unassigned
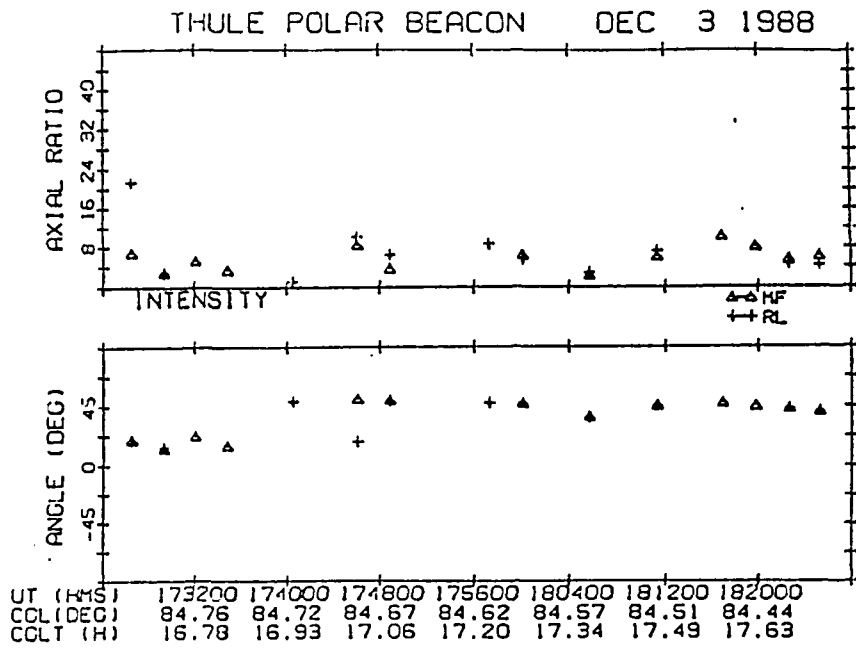
Figure 7.3. Rectangular plot of axial ratios and orientations of the major axes of anisotropy ellipses of the diffraction pattern, using the modified Fedor (MF) and the Rino-Livingston (RL) algorithms.
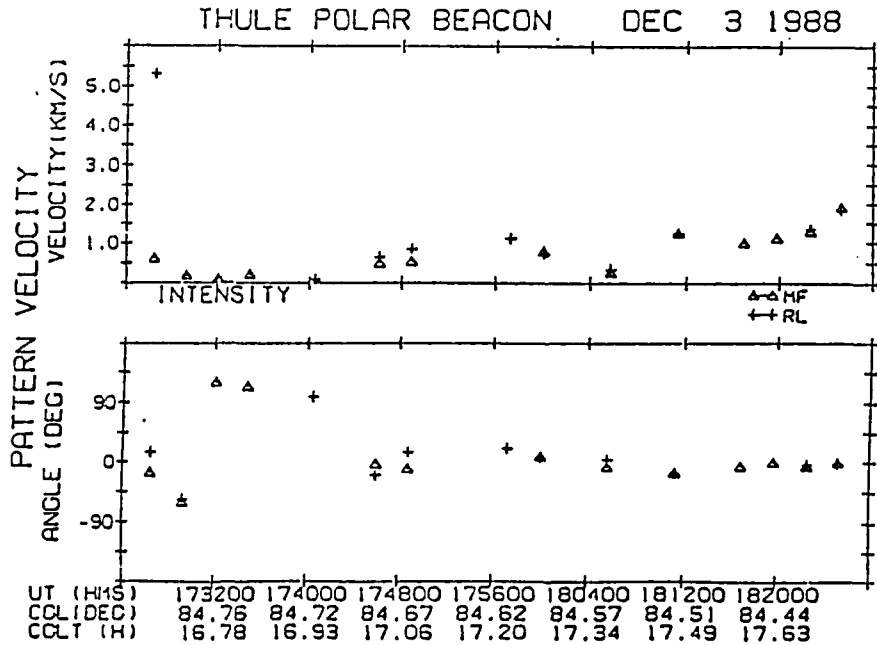
Figure 7.4. Rectangular plot of magnitudes and orientations of the true drift velocity of the diffraction pattern, using the modified Fedor (MF) and the Rino-Livingston (RL) algorithms.

7.1.3.2 Data Processing

The data on the physical tape are recorded digitally as quadrature components. A typical sample of the in-phase and quadrature signals are shown in Figure 7.5. The data in Figure 7.5 was collected at Sondrestrom, Greenland, on 6 December 1988. The first stage of the processing is to obtain the time intervals with useful data. Then, the intensity and phase of these complex data pairs are computed. The phase is the total phase which includes the scintillation phase. The intensity and phase are shown in Figure 7.6 for data collected at three different receivers, and recorded in three separate channels. The signal sampling frequency is 50 Hz. The intensity level is between 60 and 70 dB for a time span of 15 minutes. In these plots, the sample decimation is 20. The satellite updates its frequency at fixed intervals of time (every 168 seconds). The frequency updates are clearly seen in the phase plots in Figure 7.6. The frequency updating occurs where the phase slope changes abruptly. The second stage of the processing is to extract the scintillation phase. This is done by detrending the total phase data by removing the phase due to the Doppler shift and the low frequency propagation effects to obtain the scintillation phase. The third stage of processing is to spectrum analyze the scintillation data and to compute statistical parameters such as the S_4 index, the intensity zero crossing, the intensity phase depth, and the decorrelation time.
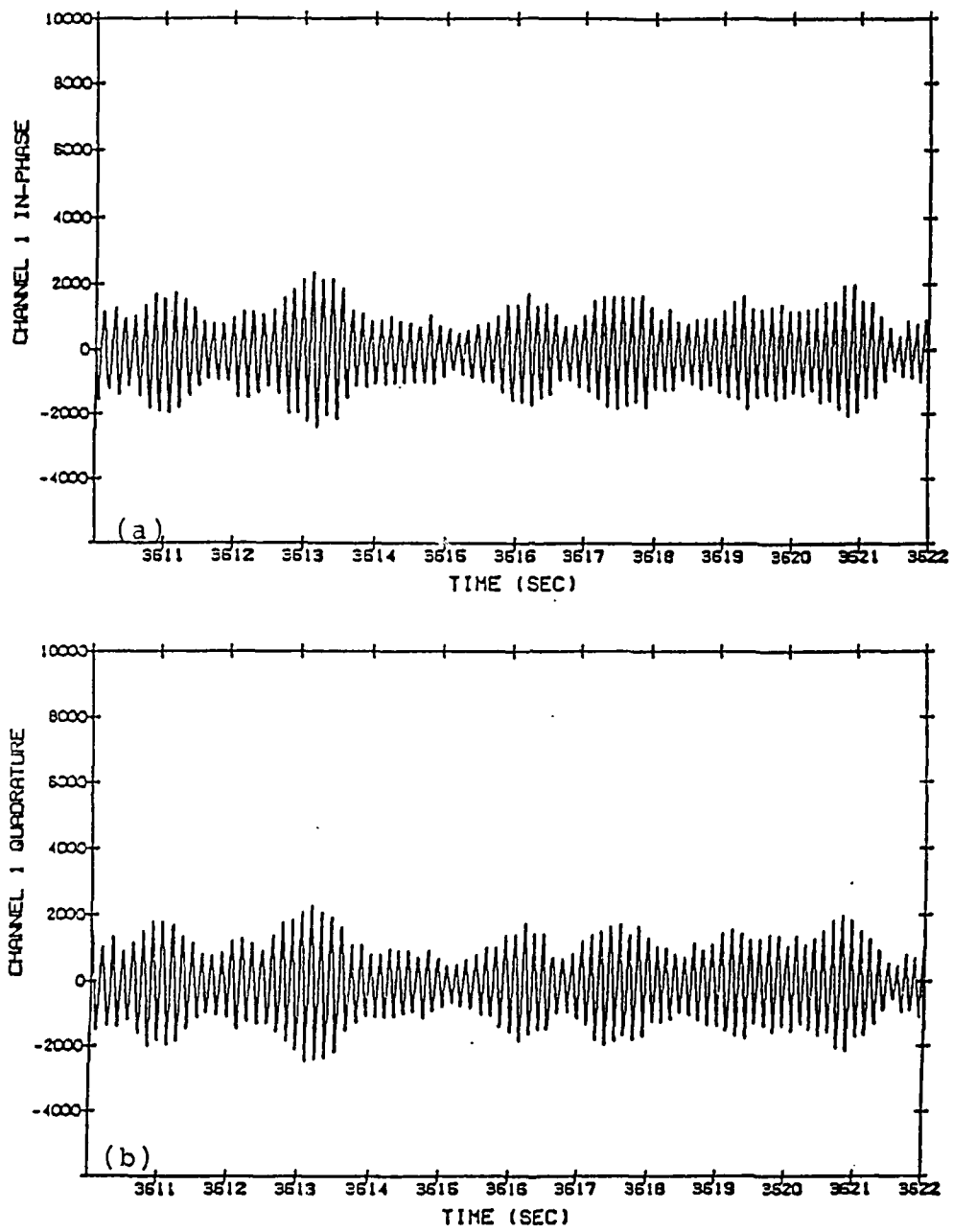
Figure 7.5. A sample plot (12 second window) of quadrature components of data collected from one of three receivers at Sondrestrom, Greenland, on 7 December 1988: In-phase (a) and Quadrature (b) components.

194
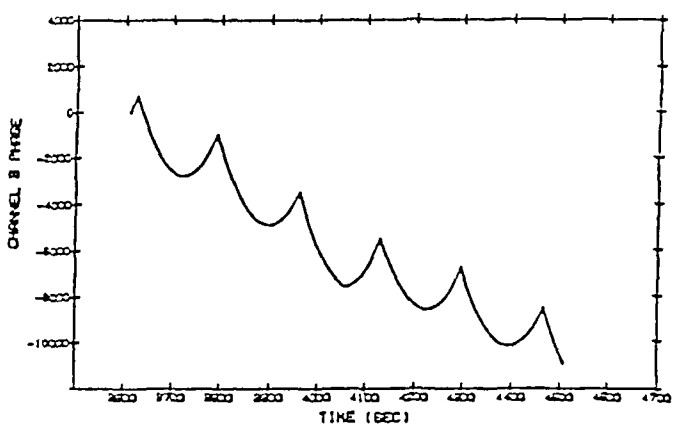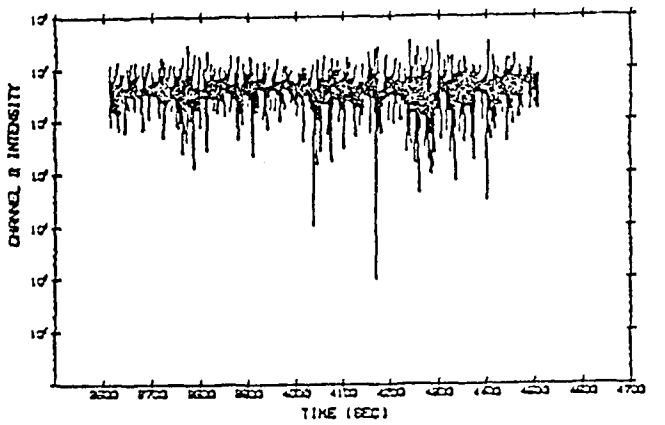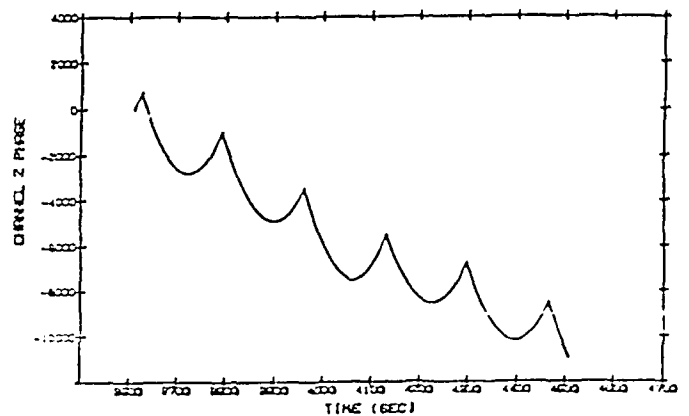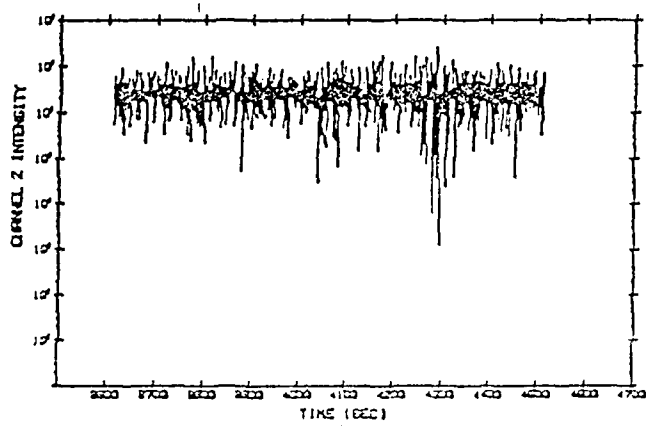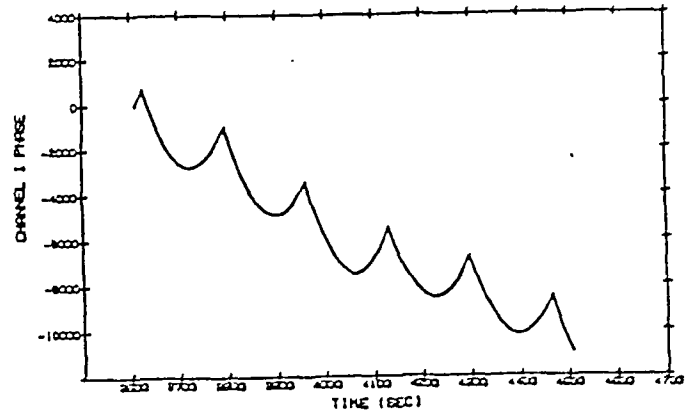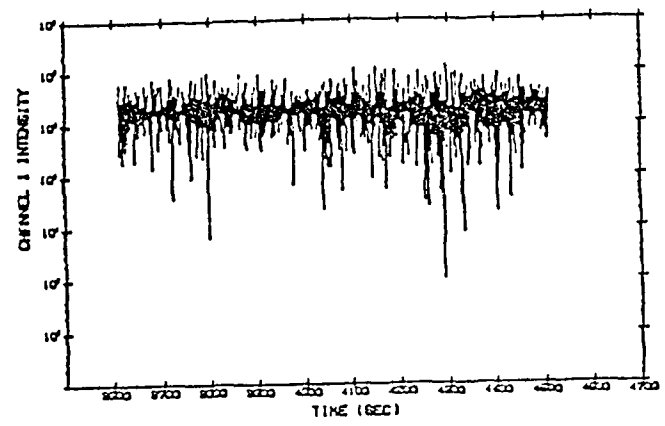
Figure 7.6. Sample intensity (left panel) and phase (right panel) plots (15 minute data segment) obtained at Sondrestrom, Greenland, on 7 December 1988. In mode 3 opertion, data samples are recorded in three channels, shown above with a decimation of 20.

195

7.2 GENERAL ELECTRIC OVER THE HORIZON BACKSCATTER RADAR

The Over The Horizon Backscatter (OTHB) is a radar system designed for long range air surveillance. The General Electric (GE) system extends the coverage area of a radar system by bouncing the signal off the ionosphere to see around the earth's curvature. This makes possible radar surveillance of otherwise inaccessible sectors.

The ionosphere is dynamic and is affected by various solar conditions. The OTHB system requires an accurate ionospheric model program to determine the proper radar signal frequency to view a sector. Certain inconsistancies in the ionospheric model data were detected during the model's use at GE. The most current version of the software was requested from GE. The code was used to produce a working version of the OTHB ionospheric model at GL. The model is used to produce data for specific test cases. When a discrepancy is found, it is possible to trace the error through the software to the source.

7.2.1 Delivery Of The FORTRAN Code

The delivery of the ionospheric modeling program included all necessary data bases and most of the software. The delivered software consisted of two programs. The first program, MU2DP, is responsible for modeling the ionosphere. The second program, SMUDG, allows the entry of parameters into the model. SMUDG also displays result values from the model.

The model could not be made to execute upon its arrival at GL. Several parameters were not defined in the software, causing compilation errors. Any software routines written in assembly language were not sent with the FORTRAN code. These missing portions blocked an immediate attempt to generate the working test case model.

Each variable must be defined as either integer or real type. The software is written to fail during compilation when a variable is not defined. The software uses a medium called an INCLUDE file. The INCLUDE files contain the definitions of variables and are inserted into the software during compilation. Some INCLUDE files were missing from the software delivery. It was necessary to determine which variables were contained in each INCLUDE file. The variable types were determined from their use in the software.

The software uses routines written in assembly language. None of these routines were included in the delivery of the software. The software was examined to determine the function of the assembly routines. When the function was ascertained, routines were written to perform the tasks. The two programs must be able to pass parameters and data sets to each other. A majority of the missing assembly routines dealt with this interprocess communication. The first type of interprocess communication routines were designed to have one program write a data file for the other to read. A second type of interprocess communication is a shared memory location. This area is overlapping local storage area accessed by both programs.

7.2.2 Overview of the Ionospheric Model

The GE Ionospheric Model uses a grid system in determining the values of the ionosphere. The grid, shown in Figure 7.7, is twenty-one points along twenty-six beams from the radar site. There are three layers in the ionosphere, the E, F1, and F2. The result from the model are the heights of these layers and their frequency. The values for the ionosphere are calculated at these grid points.

IONOSPHERIC MODEL OUTPUT
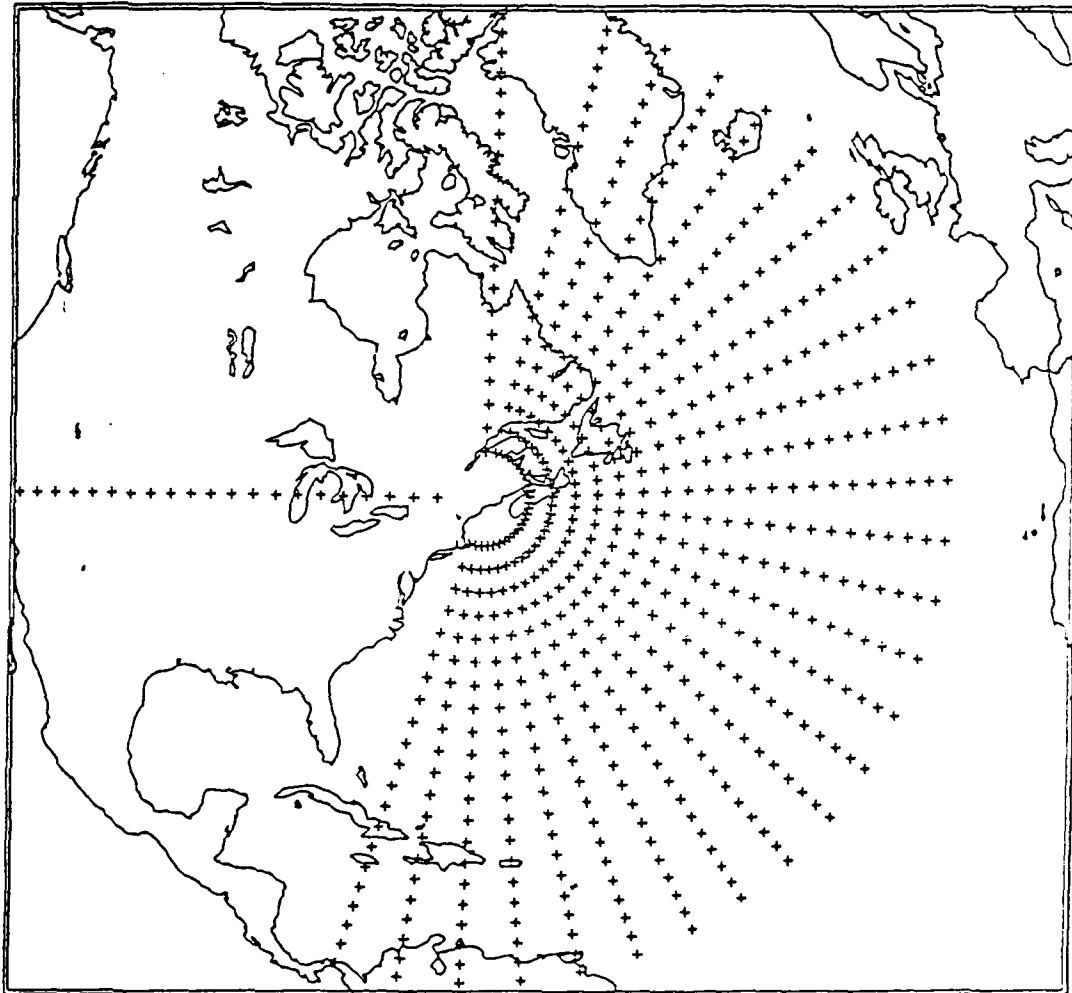
Figure 7.7. Grid system used by OTHB Ionospheric Model

The program generates an initial base model of the ionosphere known as IONCAP. The program compensates for auroral activity and updates the IONCAP to produce the auroral model. The program modifies the auroral model using actual ionosphere data received from Vertical Incidence (VI) radar sites. The auroral model grid point values are enhanced depending upon the proximity of the point to the radar sites. This update produces the final model results.

7.2.3 Generation and Analysis of Data

7.2.3.1 Data Bases

Selected input data was used and the program was run for certain dates and times to locate problems in MU2DP. The model is run using a variety of conditions to isolate its use of parameters for sun spot number, auroral index, and the Kp index. Sample data from the VI radar sites is used to ascertain if the MU2DP program processes it correctly.

A routine was added to the MU2DP code to produce data bases for analysis. The routine was placed at points in MU2DP to generate data bases containing the IONCAP model, the auroral model, and the completed model. These data bases are used in a program that displays and generates listings of the model data.

A portion of the SMUDG program was extracted and modified for use in a program to produce listings of data from the model. The program, PLANET, also uses graphics in displaying the output from the model (Figure 7.8). PLANET reads the data bases generated from MU2DP and displays the model values over a continental outline. The program supplies a representation of the auroral oval and the day/night terminator.

The PLANET displays and listings proved to be invaluable in the determination of any inconsistency. The graphic displays allowed a quick estimation of the data being generated. The displays show the program's modification to the model at each step in the processing. It was found from the displays and listings where problems existed in the process of the MU2DP ionospheric model.

7.2.3.2 Modifications to the Model

Once a problem in the ionospheric model FORTRAN was identified, a solution or correction was devised. Several modifications were made to the model. Each one of these changes underwent a series of test conditions to insure their accuracy. Plots and listings are made to compare the unchanged model results to the results from the modified model data. The changes made were documented after the case was shown that the modification was correct.

7.2.4 Generation of Maps

Several maps were generated displaying the radar's scanning range to gain a better understanding of the OTHB radar system. The maps were done in a variety of formats to provide a display of the entire coverage area of a radar system. A set of maps with an overlay of the auroral contour were made. The collection also included the ground track of an ionospheric research aircraft.
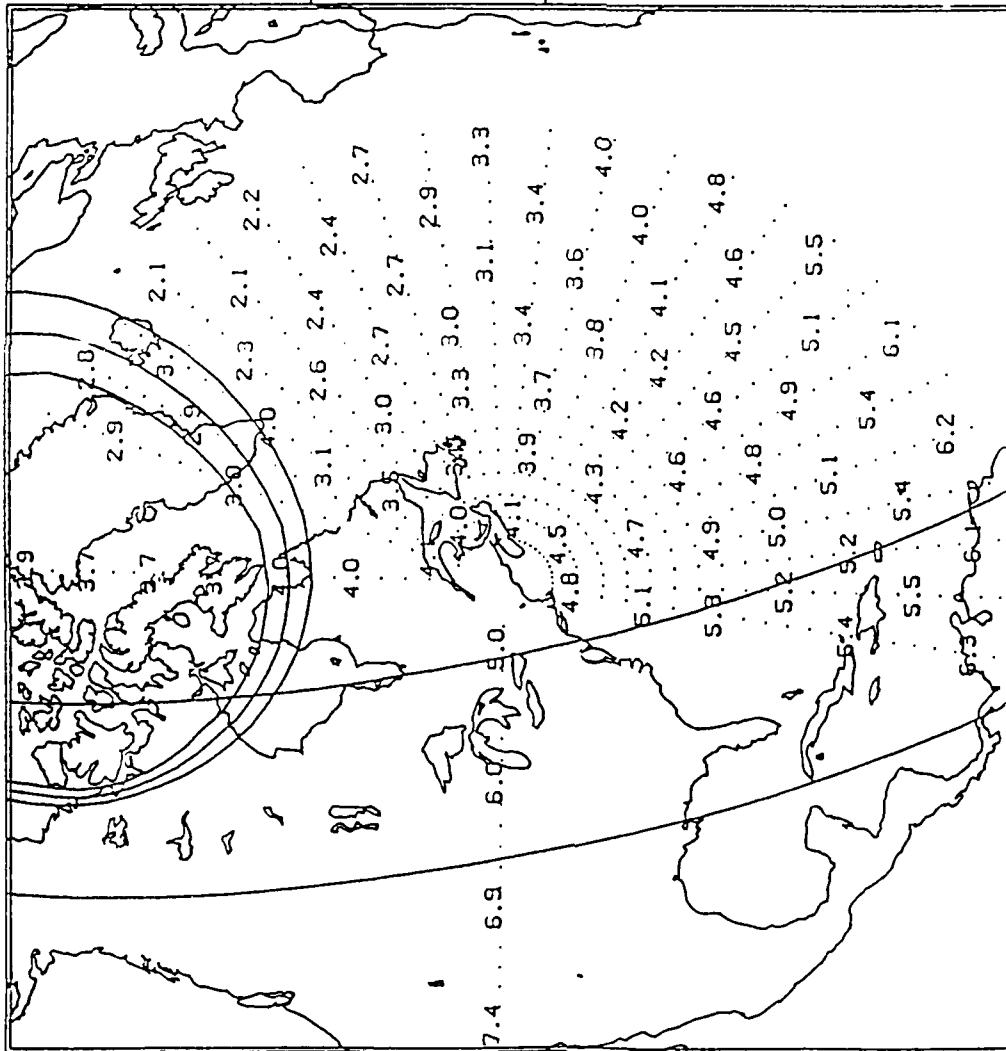
Figure 7.8. Ionospheric model output displayed by PLANET

The first series of maps were an Aitoff projection of the OTHB radar (Figure 7.9). It is necessary to center the plot on the radar site to display the entire range of the system. The edge of each sector is drawn with a mark every one thousand nautical miles. A mercator projection (Figure 7.10) is used also to display the OTHB coverage area.

The second series of maps were a spherical projection of the northern hemisphere. The geographic coordinates were plotted in corrected geomagnetic coordinates (Figure 7.11A). The latitude and longitude of several radar stations were given with their area of coverage. These maps were produced with auroral oval contours (Figure 7.11B). The oval contours and the maps are used as an auroral oval plotter. The plotter is used show the radar coverage areas affected by auroral activity.

The PLANET program was used to generate the ground track maps of the ionospheric research aircraft (Figure 7.12). This program reads data from a radar track and displays the flight into predefined segments. Each flight track has the OTHB grid system and the continental outline of the northern east coast. A mark has been placed on the ground track path to annotate a half hour index.

7.2.5 Conclusion

The efforts being made to confirm the results of the GE Ionospheric model are vital. The OTHB radar system is dependent upon this software. It is necessary that the model delivers consistently accurate results for the confident use of the OTHB radar system. The study and modifications being made to the model will improve the entire system.

GROUND-TRACK RANGE VERSUS AZIMUTH

PLOT CENTERED ON :: 44.80   291.17
RANGE IN NAUTICAL MILES
+ = 1000 NAUTICAL MILE RANGE
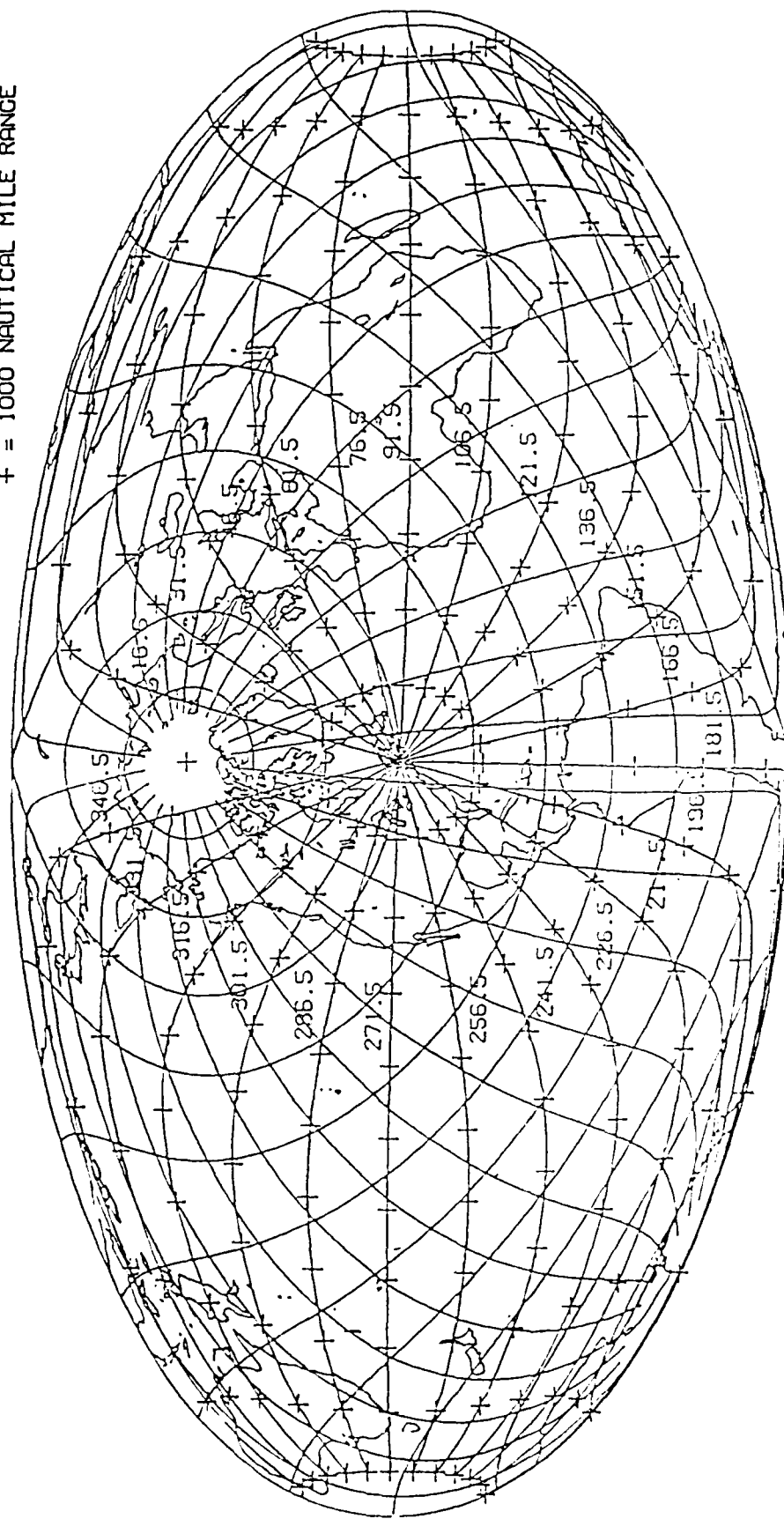
Figure 7.9. Aitoff projection of OTHB radar scanning range
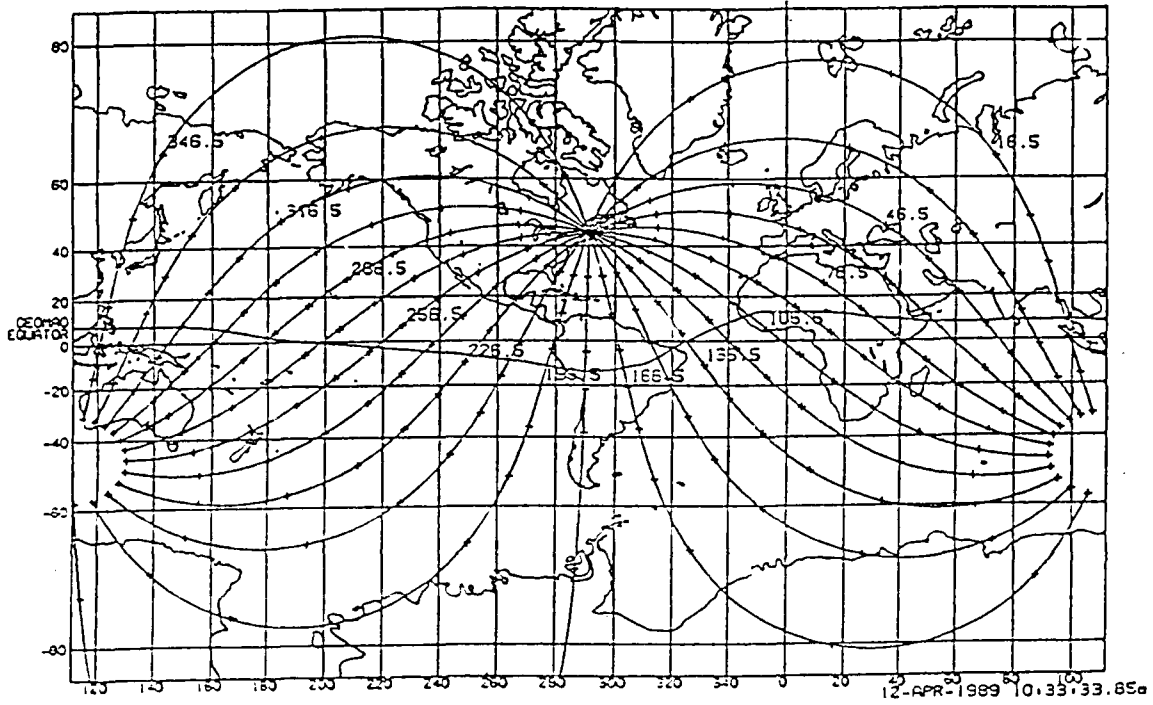
Figure 7.10. Mercator projection of OTHB scanning range

202

CONUS OVER-THE-HORIZON BACKSCATTER RADAR SYSTEM
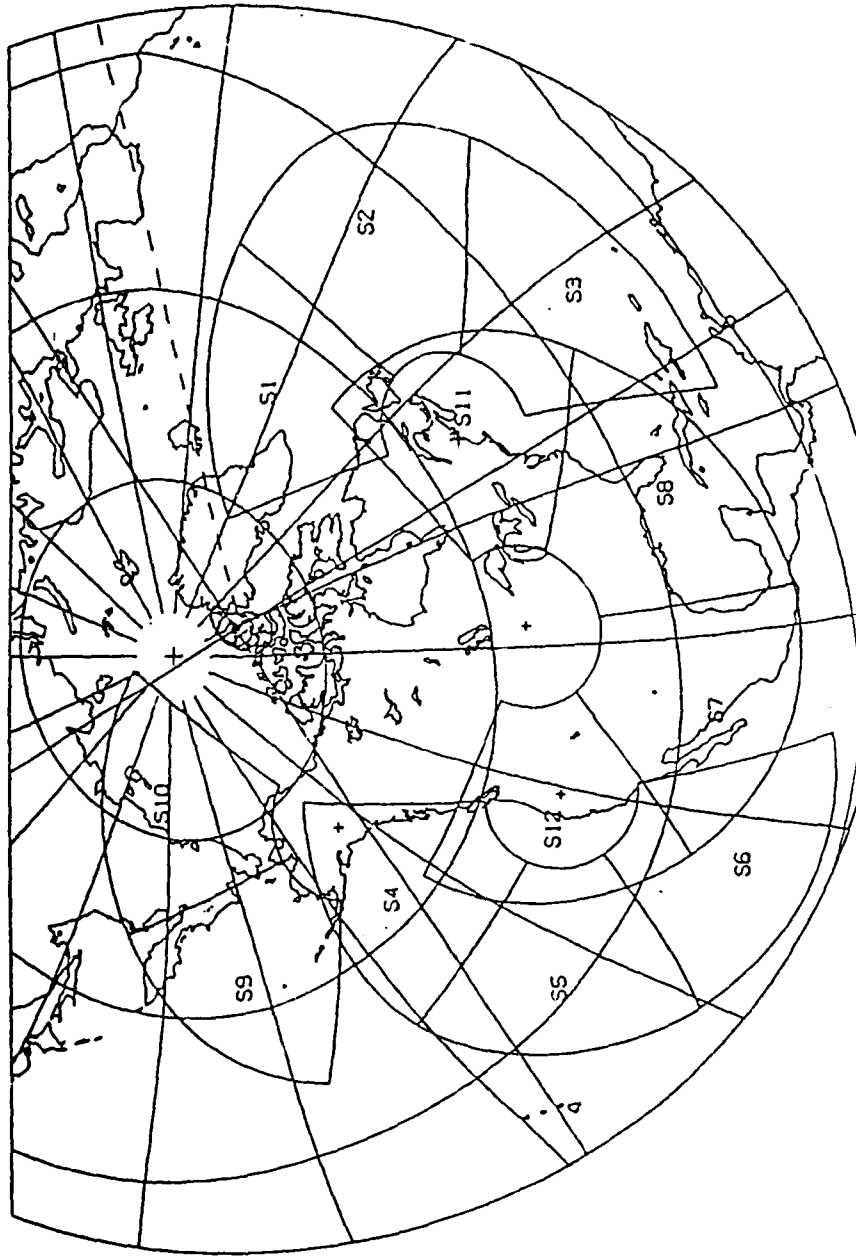
Figure 7.11a. Radar coverage sectors and continental outlines for use as auroral oval plotter

CONUS OVER-THE-HORIZON BACKSCATTER RADAR SYSTEM
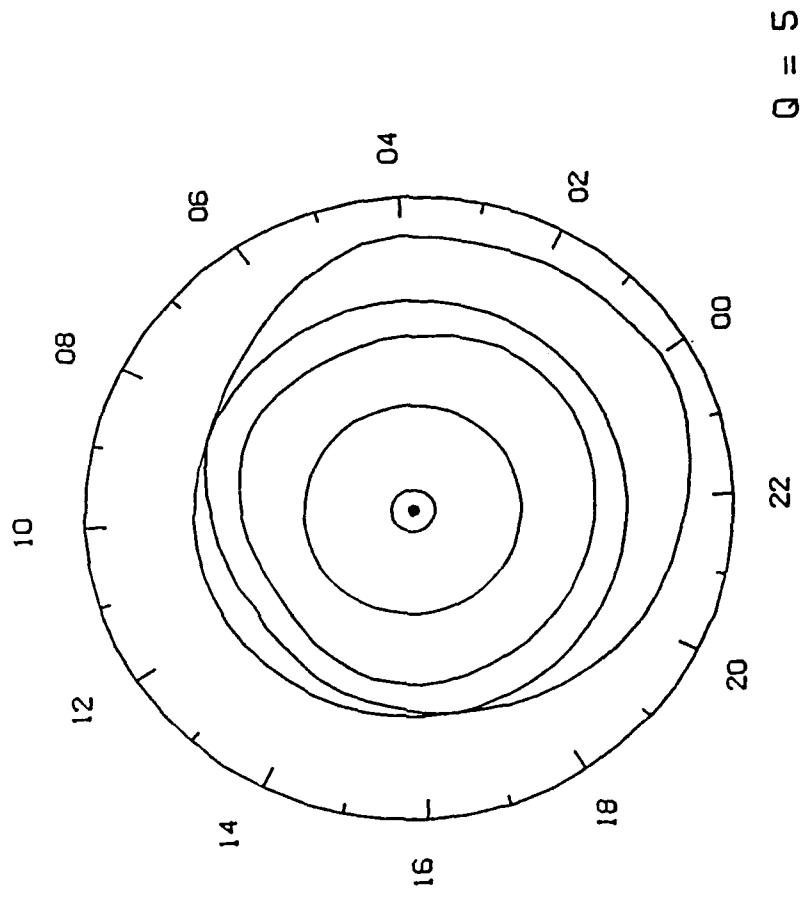
Figure 7.11b. Auroral contour for use on auroral oval plotter

IONOSPHERIC MODEL FLIGHT

START YEAR: 1989
MONTH: 3
DAY: 2

START TIME: 01:38
END TIME: 04:57

01 39

04
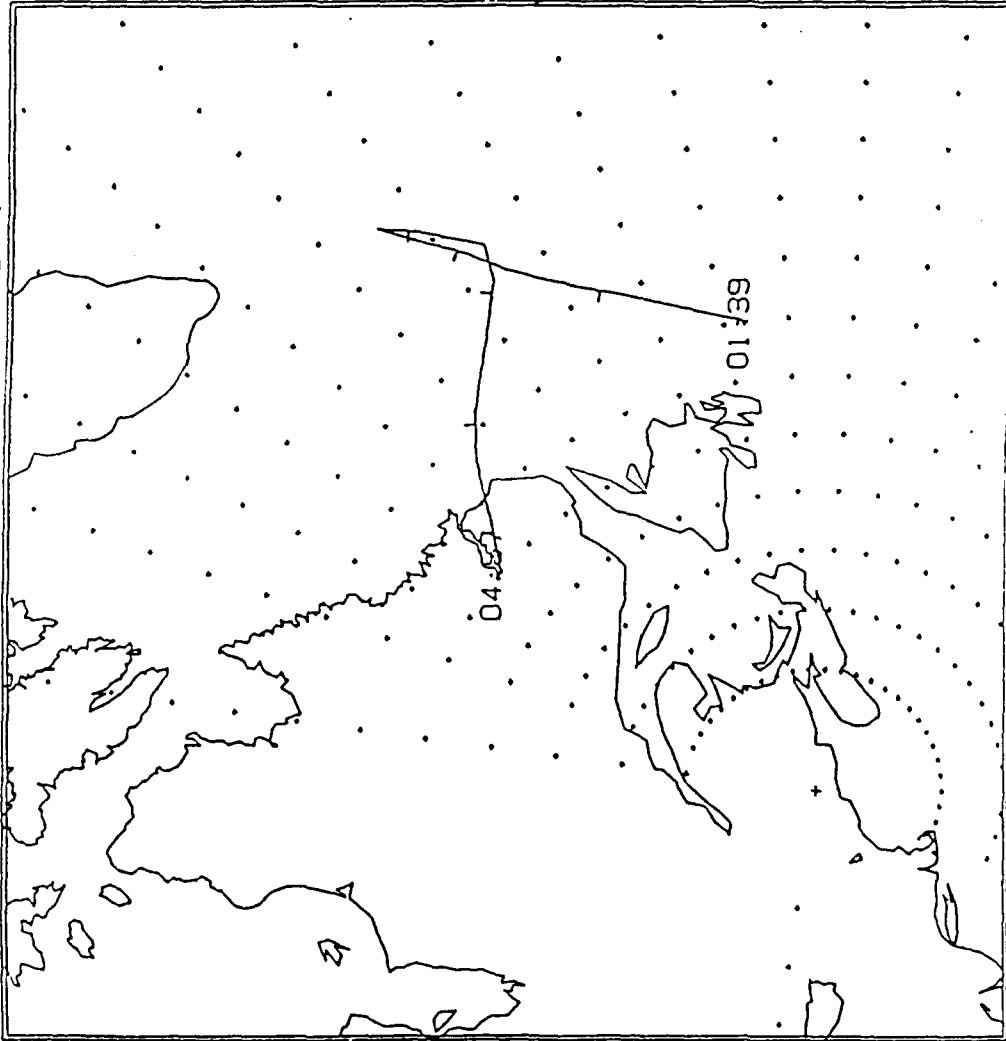
Figure 7.12. Sample output from ground track display

References

Bass, J.N., and Roberts, F.R., "Analysis and Programming for Research in the Physics of the Upper Atmosphere", AFGL-TR-84-0066, February 1984, ADA144203.

Bryant, C.M., and Robinson, E.C., Private Communication, August 1985.

Costa, E., Basu, S., and Fougere, P., "Cross-Correlation Analysis and Interpretation of Spaced-Receiver Measurements," Radio Science, Vol., 23, No. 2, pp 141-162, March-April 1988.

Rino, C.L., and Livingston, R.C., "On the Analysis and Interpretation of Spaced-receiver Measurements of Transionospheric Radio Waves", Radio Science, Vol. 17, No. 4, pp 845-854, July-August 1982.

Roberts, F.R., Private Communication, April 1983.

8. METEOROLOGY

8.1 Description of Lightning Detection Network

A lightning detection network has been developed by the State University of New York at Albany (SUNY/Albany). This network consists of about forty lightning detectors scattered around the United States, linked to a central computer system at SUNY/Albany. The researcher at the Geophysics Laboratory, Dr. H.A. Brown, receives near real-time lightning data via a satellite link, using a PC-based software package called THUNDER supplied by SUNY/Albany. This software graphically displays the location of all lightning strikes, and also stores information for each lightning strike in a "flash buffer". This flash buffer, which stores information for up to approximately 45,000 lightning strikes, can be saved to a floppy disk.

The objective of performing this analysis is to determine the accuracy of the lightning detection network developed by SUNY/Albany. Using the THUNDER software package, lightning data for July and August of 1987 has been saved on sixty-four floppy disks. The lightning data will be compared to data from forty-two Air Force Air Weather Service Observation stations, most of which lie within the area covered by the lightning detection network and are listed in Table 8.1.

8.1.1 Analysis of Lightning Detection Network for 1987 Data

8.1.1.1 Processing of Lightning Data

A PC-based program, ZAPPC, was written to process the archived lightning data by determining the azimuth and range from each of the forty-two stations to the lightning strikes. This program was designed to use a single bin range where any lightning strike within a specified range of a station would be recorded.

For each floppy disk containing lightning data, the ZAPPC program is run to produce an output listing all strikes within thirty nautical miles of each of the forty-two stations. Approximately one hundred to two hundred pages of output are produced for each disk. Each page of output contains lightning strike data for one of the forty-two stations, which is identified by a three-letter station code and the station's latitude and longitude. The initial format of the output was the Single Range format, an example of which is shown in Figures 8.1 and 8.2. The Single Range listing contains the lightning strikes's time, latitude and longitude extracted directly from the archived lightning data and the calculated range and azimuth. Also on the listing is a bar graph representing strike ranges which fall within thirty nautical miles of the station, and an approximation of the compass points to aid in the comparison with observer notes. Since the data on the disk is processed chronologically, the pages of output are then sorted by station. Initially, the time required to process a single disk of lightning data was about three hours, but minor improvements to the ZAPPC program decreased the time required to about thirty minutes. A total of approximately 10,000 pages of output was generated for the two month time period for the forty-two stations.

Table 8.1. Forty-two Air Force Weather Service Observation Stations from which Lightning Data was Acquired

AIR FORCE
AIR WEATHER SERVICE
OBSERVATIONS

JULY-AUGUST 1987

		LATITUDE Deg/Min	Deg	LONGITUDE Deg/Min	Deg	DF
ADW	Andrews AFB, MD	N 38 49	38.817	W 76 52	76.867	6
AGR*	Avon Park AFR, FL	N 27 39	27.650	W 81 20	81.333	5
AYE*	Fort Devens, MA	N 42 34	42.567	W 71 36	71.600	4
BIX	Keesler AFB, MS	N 30 25	30.417	W 88 55	88.917	2
BLV	Scott AFB, IL	N 38 33	38.550	W 89 51	89.850	0
BYH	Blytheville AFB, AR	N 35 58	35.967	W 89 57	89.950	3
CBM	Columbus AFB, MS	N 33 39	33.650	W 88 27	88.450	6
CEF*	Westover AFB, MA	N 42 12	42.200	W 72 32	72.533	4
COF*	Patrick AFB, FL	N 28 14	28.233	W 80 36	80.600	5
DAA	Davison AAF, VA	N 38 43	38.717	W 77 11	77.183	6
DOV	Dover AFB, DE	N 39 08	39.133	W 75 28	75.467	5
FAF*	Felker AAF, VA	N 37 08	37.133	W 76 37	76.617	7
FBG	Simmons AAF, NC	N 35 08	35.133	W 78 56	78.933	5
FFO	Wright-Patterson AFB, OH	N 39 50	39.833	W 84 03	84.050	0
FME*	Tipton AAF, MD	N 39 05	39.083	W 76 46	76.767	5
FMH	Otis ANGB, MA	N 41 39	41.650	W 70 31	70.517	2
FTK	Fort Knox AIN, KY	N 37 54	37.900	W 85 58	85.967	2
GSB	Seymour Johnson AFB, NC	N 35 20	35.333	W 77 58	77.967	6
GTB*	Fort Drum, NY	N 44 03	44.050	W 75 43	75.717	4
GUS	Grissom AFB, IN	N 40 39	40.650	W 86 09	86.150	0
HRT	Hurlburt FLD, FL	N 30 26	30.433	W 86 41	86.683	3
HST	Homestead AFB, FL	N 25 29	25.483	W 80 23	80.383	3
LCK	Rickenbacker ANGB, OH	N 39 49	39.817	W 82 56	82.933	0
LFI	Langley AFB, VA	N 37 05	37.083	W 76 22	76.367	6
LIZ	Loring AFB, ME	N 46 57	46.950	W 67 53	67.883	0
MCF	MacDill AFB, FL	N 27 51	27.850	W 82 31	82.517	5
MGE*	Dobbins AFB, GA	N 33 55	33.917	W 84 31	84.517	6
MTC	Selfridge ANGB, MI	N 42 37	42.617	W 82 50	82.833	1
MUI*	Muir AAF, PA	N 40 26	40.433	W 76 34	76.567	6
MXF	Maxwell AFB, AL	N 32 22	32.367	W 86 23	86.383	5
MYR	Myrtle Beach, SC	N 33 41	33.683	W 78 56	78.933	2
OSC	Wurtsmith AFB, MI	N 44 27	44.450	W 83 24	83.400	0
PAM	Tyndall AFB, FL	N 30 04	30.067	W 85 35	85.583	3
PBG	Plattsburgh, NY	N 44 39	44.650	W 73.28	73.467	4
POB	Pope AFB, NC	N 35 10	35.166	W 79 01	79.017	6
PSM	Pease AFB, NH	N 43 05	43.083	W 70 49	70.817	3
SAW	K.I.Sawyer AFB, MI	N 46 21	46.350	W 87 24	87.400	0
SSC	Shaw AFB, SC	N 33 58	33.967	W 80 28	80.467	4
VAD	Moody AFB, GA	N 30 58	30.966	W 83 12	83.200	5
VPS	Eglin AFB, FL	N 30 29	30.483	W 86 32	86.533	3
WRB	Robins AFB, GA	N 32 38	32.633	W 83 36	83.600	5
WRI	McGuire AFB, NJ	N 40 10	40.167	W 74 36	74.600	5

* THESE STATIONS ARE CLOSED ON WEEKENDS

TIME	LATITUDE	LONGITUDE	RANGE	AZIMUTH	0----|----|----30	
00:36:23	30.510	-87.062	20.1	283.4		WNW
00:53:01	30.509	-87.201	27.2	279.8		W
05:33:27	30.138	-86.893	20.8	211.6		SSW
05:40:00	30.040	-86.834	24.9	198.4		SSW
06:11:26	30.376	-87.212	27.6	263.1		W
06:13:55	30.463	-87.259	29.9	273.6		W
06:15:32	30.387	-87.240	29.0	264.6		W
06:17:54	30.428	-87.232	28.4	269.5		W
06:21:13	30.375	-87.223	28.2	263.0		W
06:23:31	30.311	-87.128	25.7	252.5		WSW
06:27:01	30.135	-86.983	23.7	221.0		SW
06:28:40	30.160	-87.020	23.9	227.0		SW
06:28:44	30.367	-87.231	28.6	262.2		W
06:30:27	30.157	-87.021	24.9	228.2		SW
06:31:23	30.185	-87.062	23.1	229.7		SW
06:31:28	30.392	-87.258	29.3	238.4		WSW
06:32:55	30.127	-87.012	25.1	265.4		W
06:34:56	30.232	-87.014	21.0	222.9		SW
06:35:01	30.032	-86.410	27.9	234.6		SW
06:36:27	30.189	-87.033	23.3	149.5		SSE
06:38:53	30.345	-87.247	29.7	231.1		SW
06:41:05	30.100	-86.417	24.1	255.9		SE
06:41:06	30.254	-86.779	11.8	145.1		SSW
06:42:32	30.266	-87.004	19.4	204.8		SSW
06:44:37	30.102	-86.451	23.2	238.9		SSE
06:43:11	30.169	-86.529	17.8	148.7		SSE
06:43:29	30.242	-87.035	21.6	153.2		VSW
06:46:41	30.073	-86.448	24.8	237.9		SSE
06:48:07	30.063	-86.454	25.2	150.5		SSE
06:48:08	30.115	-86.416	23.6	143.9		SE
06:49:21	30.253	-87.163	13.0	259.2		W
06:50:25	30.118	-86.823	22.9	213.8		SE
06:51:45	30.326	-86.436	26.9	145.9		SE
06:52:18	30.381	-87.118	22.8	236.4		VSW
06:52:59	30.155	-86.419	21.6	262.2		SE
06:54:22	30.347	-87.145	24.5	140.5		VSW
06:54:31	30.378	-87.171	25.5	257.9		W
06:55:16	30.171	-86.425	20.7	262.6		SE
06:56:19	30.351	-87.163	25.3	135.6		V
06:57:26	30.354	-87.149	24.6	259.0		SE
06:57:42	30.338	-87.374	23.4	136.8		VSW
06:58:41	30.148	-87.146	25.7	248.9		SE
06:59:18	30.278	-86.405	29.6	150.7		SE
06:59:26	30.003	-86.384	22.5	136.7		V
07:00:58	30.162	-86.429	17.1	129.7		SE
07:01:01	30.251	-87.187	26.3	263.3		
07:03:44	30.190	-86.466	18.4	142.3		

TIME	LATITUDE	LONGITUDE	RANGE	AZIMUTH	0----|----|----30	
07:05:47	30.087	-86.513	22.6	156.9		SSE
07:10:08	30.020	-86.480	26.9	156.9		SSE
07:12:07	30.053	-86.348	28.7	142.7		SE
07:12:31	30.061	-86.362	27.9	143.2		SE
07:13:35	30.050	-86.359	28.5	143.7		SE
07:16:20	30.018	-86.378	29.5	147.5		SSE
07:16:20	30.255	-86.584	11.8	154.4		SSE
07:16:28	30.096	-86.324	27.5	137.2		SE
07:17:34	30.059	-86.378	27.5	144.8		SE
07:18:49	30.064	-86.343	28.3	141.4		SE
07:19:18	30.087	-86.444	24.2	149.2		SSE
07:19:41	30.082	-86.366	26.7	142.0		SE
07:19:59	30.097	-86.355	26.4	139.8		SE
07:20:22	30.338	-86.459	12.9	116.2		ESE
07:20:50	30.094	-86.385	25.6	142.7		SE
07:22:27	30.072	-86.412	25.8	147.0		SSE
07:22:54	30.053	-86.364	28.2	144.0		SE
07:23:20	30.120	-86.439	22.7	146.0		SSE
07:23:49	30.088	-86.342	27.2	139.4		SE
07:24:12	30.087	-86.365	26.5	141.5		SE
07:24:12	30.106	-86.395	24.7	142.7		SE
07:24:49	30.170	-86.651	15.9	173.9		SSE
07:25:15	30.066	-86.428	25.7	149.0		SSE
07:25:42	30.146	-86.317	25.6	132.2		SE
07:26:03	30.177	-86.454	23.9	150.2		SSE
07:26:03	30.084	-86.664	15.4	176.4		S
07:26:21	30.129	-86.443	24.4	149.2		SSE
07:26:59	30.093	-86.483	21.0	150.3		SSE
07:27:18	30.108	-86.413	24.8	145.6		SSE
07:28:03	30.030	-86.355	25.9	138.8		SE
07:28:03	30.140	-86.355	29.6	144.7		SSE
07:28:42	30.029	-86.445	21.5	144.9		SSE
07:28:43	30.023	-86.369	29.2	146.0		SE
07:29:22	30.134	-86.847	26.1	199.1		SSW
07:29:54	30.131	-86.453	21.6	146.4		SSE
07:30:27	30.111	-86.389	23.7	139.9		SE
07:31:06	30.112	-86.432	23.3	145.9		SSE
07:31:30	30.152	-86.412	23.8	143.8		SSE
07:32:12	30.130	-86.380	23.0	137.0		SE
07:32:44	30.143	-86.439	22.1	145.1		SSE
07:33:04	30.148	-86.475	22.2	141.7		SSE
07:33:04	30.289	-86.527	20.2	136.9		SE
07:33:27	30.123	-86.423	23.0	144.0		SSE
07:34:10	30.064	-86.447	25.3	150.9		SSE
07:34:10	30.134	-86.559	19.1	160.2		SSE
07:34:35	30.148	-86.381	23.2	137.5		SE
07:34:59	30.184	-87.211	27.6	277.6		W
07:35:33	30.155	-86.441	20.9	143.0		SE

Figure 8.1. Single range format

TIME	LATITUDE	LONGITUDE	RANGE	AZIMUTH	0----|----|---30

TIME	LATITUDE	LONGITUDE	RANGE	AZIMUTH	0----|----|---30

Figure 8.2. Single range format

8.2 Compilation of Lightning Data and Observer Data

To compare the observer data with the lightning detection network data, both sets of data are put on a large timeline. This timeline consists of four lines, the first for the observer data and the other three for the network data. See Table 8.2 and Figures 8.3 and 8.4. Data for the observer line comes from the daily Surface Weather Observation sheets for each station. (See Figure 8.5) In addition to marking the start and stop times of thunderstorms as recorded by the observer, any comments concerning the frequency and type of lightning observed are noted on the timeline. The lightning detection network data is broken up into three ranges, 0-10 nautical miles, 10-20 and 20-30, each of which has its own timeline. This separation of data allows selective comparison of the observer data with the network data. The approximate frequency of the lightning strikes and the start and stop times of the lightning storms (the stop time of the storm defined as 15 minutes after the last lightning strike) are annotated for each of the three range timelines. This process of transferring the data for the observer and the three ranges of the network to the timelines is performed for each of the forty-two stations for the two month time period. Because each of the approximately 10,000 pages of output for the lightning detection network data are scanned for start and stop times of the lightning storms and frequency of the lightning strikes, this portion required a significant percentage of the total time to complete the study.

8.2.1 Correlation of Lightning Data and Observer Data

When the timelines are completed, they are analyzed by comparing the timeline of the observer with those of the network. A small analysis table is created for each day for both months for each of the forty-two stations. These analysis tables relate the correlation between the two sets of data and the lead or lag times of the network start times and observer start times for each of the three network ranges. See Table 8.3. and Figures 8.6 and 8.7. The analysis tables are completed by comparing the observer timeline with those of the network and counting the number of daily agreement and/or disagreement of the observer data and the network data.

This comparison process consists of scanning the timeline sheets for storms. When a storm is encountered, the presence of both network data and observer reported thunderstorms is checked. If the observer reports no storms, but the network indicates lightning in the R1 range, the tally is increased in the box for the network "R1" column and the observer "NO" row. If the observer reports a storm, and the network does not detect any strikes, the tally is increased in the box for the network "NO" column and the observer row corresponding to the type of lightning reported by the observer. A distinction is made between the single ("Rare") lightning strikes and lightning storms of several ("Occasional") or many ("Frequent") lightning strikes on the analysis tables. If both observer and network report a storm, the lead/lag time for each of the three ranges are measured and annotated, and the appropriate boxes relating the observer comments and network ranges have their tallies increased.

In order to prevent ambiguous and/or duplicate correlation data from being generated, several rules are needed. These rules include: placing a storm which straddles two days in the day which contains the majority of the storm; throwing out data for storms where either the network or observer data contained large gaps; defining a series of lightning storms detected by the network which frequently start and stop during a single observer-reported thunderstorm as a single lightning storm; defining a lightning storm detected by the network which is reported to be two thunderstorms by the observer is considered as two lightning storms. These last two rules prevent "assigning" storms on a one-to-one basis, which could have created many "orphan storms", which in turn, could have artificially degraded the network's accuracy ratings.

211

Table 8.2. Timetable Notations and Definitions

Observer and network timelines:

↑	-	start time of storm
↓	-	stop time of storm

Observer timeline comments:

(blank)	-	no comments
O	-	occasional lightning observed
F	-	frequent lightning observed
>	-	cloud to ground lightning observed
V	-	cloud to cloud lightning observed
*	-	both cloud to ground and cloud to cloud observed

Network timeline comments:

R	-	single lightning strike detected in a 15 minute period (Rare)
O	-	two to five lightning strikes detected in a 15 minute period (Occasional)
F	-	more than five lightning strikes detected in a 15 minute period (Frequent)

General:

Horizontal bars - denote times for which there is no observer data (station closed or data not available) or when the satellite link to the network was down and the data was lost.

Figure 8.3. Sample of data timeline, page 1

213
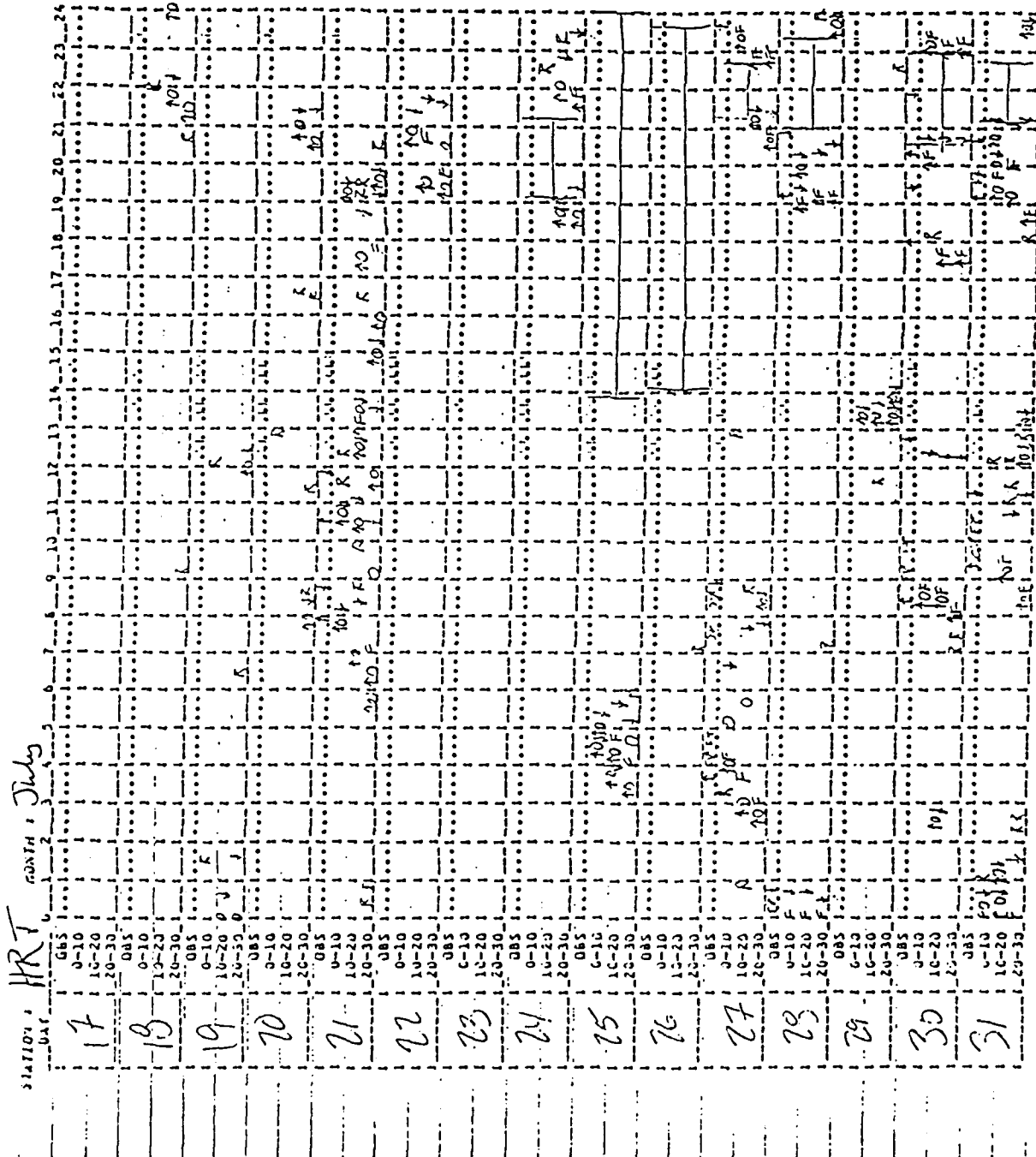
Figure 8.4. Sample of data timeline, page 2

214

Figure 8.5. Samples of surface weather observation sheets

Table 8.3. Lightning Network Analysis Chart Description

Set identification →

NETWORK

S	R1	R2	R3	NO
*				
⋗				
V				
T				
NO		T2	T3	

OBSERVER

T1

Lead (+) or Lag (-) times (in minutes) of start time of lightning storm detected by network to start time of thunderstorm reported by observer

N
M

N = number of lightning storms detected by network during observer reported thunderstorm
M = number of "Rare" lightning strikes detected by network during observer-reported thunderstorms

Lightning detected by network:
R1 - in 0-10 nautical mile range
R2 - in 10-20 nautical mile range
R3 - in 20-30 nautical mile range
NO - no lightning detected in any range

Observer reported thunderstorm with:
* - both cloud to ground and cloud to cloud
⋗ - cloud to ground
V - cloud to cloud
T - no comments
NO - no thunderstorm reported

Definitions:

Lightning storm - storm detected by network
Thunder storm - observer-reported storm

Time lead/lags are rounded to the nearest 5 minutes
* positive time = network reported storm before observer
* negative time = observer reported storm before network
* "NA" = time not able to be determined or gaps in data
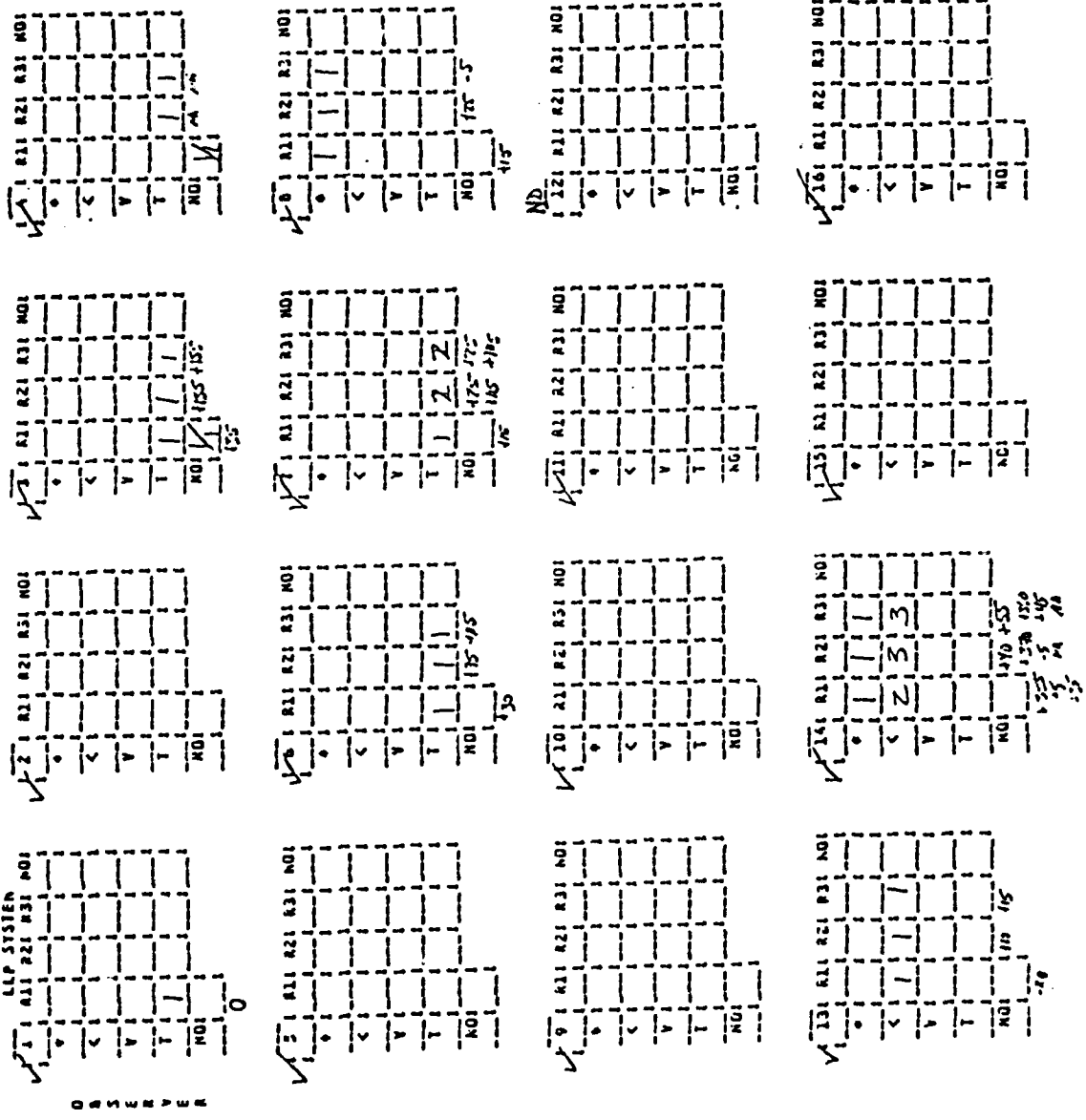
Figure 8.6. Sample of station daily analysis charts

217

Figure 8.7. Sample of station daily analysis charts, cont'd

After each month of data is analyzed for each station, a monthly analysis table is created by summing each of the boxes of the daily analysis tables and averaging the lead/lag times. After some initial results were examined, the researcher decided to limit the lightning detection network analysis to the first range (0-10 nautical miles). To accommodate this, a new column was created in the analysis table, to count the number of times when the observer reported a thunderstorm and the network did not detect any lightning storms within the 0-10 nautical mile range. Rather than re-analyzing the entire data set of forty-two stations for the two month time period, the data for this new column is calculated by summing the lightning storms and the rare strikes for both the 0-10 and 10-20 nautical mile ranges, and subtracting the second range total from the first range total for each thunderstorm type. Although the calculated number did not match the actual number in all test cases examined, this method was a fairly good approximation.

8.2.2 Formulas Used and Results

When all analysis was complete, the stations were divided into eight groups, based on the number of lightning detectors covering them. The monthly analysis tables for each station in each group are summed, in order to show the variation of the accuracy of the lightning detection network by the amount of coverage.

Four formulas are applied to the results in order to produce meaningful numbers from the tallies for all data. For each set of analysis data, the focus was upon the data showing agreement between the lightning detection system and weather observer in the 0 to 10 nautical mile range, and the data showing disagreement, where the observer reported a thunderstorm and the lightning detection system did not, and vice versa, in the 0 to 10 nautical mile range. For this particular study, the different types of lightning reported by the observer was ignored, and their tallies summed. This created a much simpler table:

NETWORK

		Yes	No
OBSERVER	Yes	N1	N3
	No	N2	

where:

N1 = sum of observer/network agreement box tallies

N2 = network/observer

N3 = sum of observer/network disagreement box tallies

By using these three datapoints, the four statistical formulas are applied to measure the accuracy of the lightning detection system against the weather observer. These four formulas are as follows:

219

- Probability Of Detection

  Probability of the lightning being detected
  by the network and reported by the observer.

$$POD = \frac{N1}{(N1 + N3)}$$

- False Alarm Rate

  Rate of network falsely detecting lightning
  storm when the observer did not report storm.

$$FAR = \frac{N2}{(N1 + N2)}$$

- Missed Threat Rate

  Rate of network not detecting lightning when the
  observer reported a thunderstorm.

$$MTR = \frac{N3}{(N1 + N3)}$$

- Critical Success Index

  A general success rating of the lightning detection
  network.

$$CSI = \frac{N1}{(N1 + N2 + N3)}$$

The three numbers for each station are tabulated, and the results for the four formulas are calculated. In addition to rating the lightning detection network at the individual stations, it is also rated for the coverage-dependant groups of stations. This is done for the data for the two months separately and together. See Tables 8.4, 8.5 and 8.6.

8.2.3 Summary of 1987 Lightning Data Analysis Process

The method used for analyzing the 1987 lightning data was far more efficient than the method used for the 1986 data, which was analyzed visually on the terminal screen. Still, the human processing portion is very time-consuming and tedious. The scanning of the numerous pages of output for the start and stop times of the lightning storms was inefficient and prone to error. The timelines were very useful, as they placed the lightning detection network data and observer data together in an easy-to-read time-oriented format. The analysis chart provides more information than is needed, but is flexibile, as it allows other parameters to be examined without having to re-analyze the entire data set. Although it does have its limitations, approximations can be employed in certain situations (such as the addition of the "NO R1" column in the analysis table). If other parameters were to be examined, such as lightning detected in the 0-5 nautical mile range, a new set of timelines would have to be created and analyzed. Because scanning the output pages to create the timelines of the network is the most time-consuming task of the network analysis study, improvements have been made to the lightning data processing software. These software upgrades not only remove much of the human effort required for the study and decrease the chance of errors, but also allow greater flexiblity in reprocessing the data.

MONTH : JULY

STATION	N1	N2	N3	POD	FAR	MTR	CSI
BLV	6	5	0	100.0	45.5	.0	.545
FFO	1	1	0	100.0	50.0	.0	.500
GUS	0	1	3		100.0	100.0	.000
LCK	1	0	2	33.3	.0	66.7	.333
LIZ	0	0	2	.0	999.9	100.0	.000
OSC	0	1	3	.0	999.9	100.0	.000
SAM	0	0	0	999.9	999.9	999.9	9.999
GR 0	8	7	10	44.4	46.7	55.6	.320
MTC	2	0	5	20.6	.0	71.4	.206
GR 1	2	0	5	20.6	.0	71.4	.206
BIX	17	3	2	89.5	15.0	10.5	.773
PMH	0	2	0	.0	100.0	100.0	.000
FTK	3	0	4	42.9	.0	57.1	.429
MYR	11	0	1	91.7	.0	0.3	.917
GR 2	31	5	8	79.5	13.9	20.5	.705
BYH	0	2	0	100.0	20.0	.0	.000
HRT	17	6	3	85.0	26.1	15.0	.654
HST	14	12	1	82.4	46.2	17.6	.403
PAM	11	8	0	100.0	42.1	.0	.579
PSM	0	0	1	.0	999.9	100.0	.000
VPS	21	4	5	80.8	16.0	19.2	.700
GR 3	71	32	12	85.5	31.1	14.5	.617

STATION	N1	N2	N3	POD	FAR	MTR	CSI
AYE*	0	0	1	.0	999.9	100.0	.000
CEF*	2	3	1	100.0	60.0	.0	.400
GTD*	2	0	0	100.0	.0	.0	1.000
PBG	10	1	1	90.9	9.1	9.1	.833
SSC	9	1	2	81.0	10.0	10.2	.750
GR 4	23	5	4	85.2	17.9	14.8	.719
AGR*	15	1	2	100.0	6.3	.0	.938
COF*	11	0	1	84.6		15.4	.846
DOV	0	4	3	72.7	33.3	27.3	.533
PBG	12	4	1	92.3	25.0	7.7	.706
FME*	1	0	1	75.0		25.0	.750
MCP	21	10	3	87.5	32.3	12.5	.613
MXF	9	1	2	81.8	25.0	10.2	.643
VAD	14	2	1	93.3	12.5	6.7	.824
WRB	7	9	1	87.5	56.3	12.5	.412
WRI	11	4	2	84.6	26.7	15.4	.647
GR 5	111	37	16	87.4	25.0	12.6	.677
ADW	8	3	2	80.0	27.3	20.0	.615
CDH	7	3	3	70.0	30.0	30.0	.530
DAA	6	5	2	75.0	45.5	25.0	.462
GSB	14	12	0	93.3	46.2	6.7	.519
LFI	6	5	1	100.0	25.0	.0	.750
MGE*	4	2	0	80.9	30.5	21.1	.571
NUI*	0	9	1	100.0	33.3	.0	.667
POB	0	1	1	88.9	52.9	11.1	.444
GR 6	61	41	10	85.9	40.2	14.1	.545
FAP*	3	0	0	100.0	.0	.0	1.000
GR 7	3	0	0	100.0	.0	.0	1.000

STATION	N1	N2	N3	POD	FAR	MTR	CSI
GR 0	8	7	10	44.4	46.7	55.6	.320
GR 1	2	0	5	20.6	.0	71.4	.206
GR 2	31	31	8	79.5	13.9	20.5	.705
GR 3	71	32	12	85.5	31.1	14.5	.617
GR 4	23	5	4	85.2	17.9	14.0	.719
GR 5	111	37	16	87.4	25.0	12.6	.677
GR 6	61	41	10	85.9	40.2	14.1	.545
GR 7	3	0	0	100.0	.0	.0	1.000
0+1	10	7	15	40.0	41.2	60.0	.313
2+3	1102	37	20	83.6	26.6	16.4	.642
4+5	1134	42	20	87.0	23.9	13.0	.604
6+7	64	41	10	86.5	39.0	13.5	.557
ALL	1310	1127	65	82.7	29.1	17.3	.610

Table 8.4. Results Table for July 1987 Data

221

MONTH : AUGUST

STATION	N1	N2	N3	POD	FAR	HTR	CSI
BLV	7	2	0	100.0	22.2	.0	.770
FPO	0	4	0	999.9	100.0	999.9	.000
GUS	0	0	1	.0	999.9	100.0	.000
LCK	0	0	1	.0	100.0	100.0	.000
LIZ	0	1	0	999.9	999.9	999.9	9.999
OSC	1	0	0	100.0	.0	.0	1.000
SAM	0	0	0	999.9	999.9	999.9	9.999
GR 0	0	7	2	80.0	46.7	20.0	.471
NTC	1	1	0	100.0	50.0	.0	.500
GR 1	1	1	0	100.0	50.0	.0	.500
BIX	12	0	2	85.7	.0	14.3	.057
FMH	0	1	0	999.9	999.9	999.9	9.999
FTK	5	1	0	100.0	16.7	.0	.033
MYR	9	2	0	100.0	10.2	.0	.010
GR 2	26	3	2	92.9	10.3	7.1	.039
BYH	2	0	0	100.0	.0	.0	1.000
HRT	8	4	1	00.9	33.3	11.1	.615
HST	6	4	0	100.0	40.0	.0	.600
PAM	5	4	2	71.4	44.4	28.6	.455
PSM	0	0	0	999.9	999.9	999.9	9.999
VPS	6	1	3	66.7	14.3	33.3	.600
GR 3	27	13	6	81.8	32.5	10.2	.507

STATION	N1	N2	N3	POD	FAR	HTR	CSI
AXE*	0	0	0	999.9	999.9	999.9	9.999
CEP*	0	0	0	999.9	999.9	999.9	9.999
GTD*	1	1	0	100.0	.0	100.0	1.000
FBG	0	1	1	.0	999.9	100.0	.000
SSC	6	2	1	05.7	25.0	14.3	.667
GR 4	7	2	2	77.0	22.2	22.2	.636
AGR*	0	0	0	999.9	999.9	999.9	9.999
COF*	2	0	2	50.0	.0	50.0	.500
DOV	3	1	0	100.0	25.0	.0	.750
FBG	9	1	0	100.0	18.2	.0	.818
FME*	1	0	1	100.0	27.0	.0	1.000
HCZ	13	5	1	92.9	27.0	7.1	.604
HXP	10	1	1	100.0	9.1	.0	.909
VAD	9	2	1	75.0	10.2	25.0	.643
WRB	7	6	1	87.5	46.2	12.5	.500
HRI	3	0	1	75.0	.0	25.0	.750
GR 5	57	17	8	07.7	23.0	12.3	.695
ADW	3	1	2	60.0	25.0	40.0	.500
CBM	11	2	1	91.7	15.4	0.3	.786
DAA	0	2	1	999.9	100.0	999.9	.000
GSB	5	2	0	100.0	28.6	.0	.714
LFI	6	5	0	100.0	45.5	.0	.545
MGE*	9	4	1	90.0	30.8	10.0	.643
HOI*	3	0	0	100.0	25.0	.0	.750
POB	9	2	1	90.0	10.2	10.0	.750
GR 6	46	19	5	90.2	29.2	9.0	.657
FAP*	6	1	1	85.7	14.3	9.0	.657
GR 7	6	1	1	85.7	14.3	14.3	.750

STATION	N1	N2	N3	POD	FAR	HTR	CSI
GR 0	8	7	2	80.0	46.7	20.0	.471
GR 1	1	1	0	100.0	50.0	.0	.500
GR 2	26	3	2	92.9	10.3	7.1	.839
GR 3	27	13	6	81.0	32.5	10.2	.507
GR 4	7	1	2	77.0	22.2	22.2	.636
GR 5	57	17	8	87.7	23.0	12.3	.695
GR 6	46	19	5	90.2	29.2	9.8	.657
GR 7	6	1	1	05.7	14.3	14.3	.750
0+1	9	0	2	81.0	47.1	10.2	.474
2+3	53	16	8	86.9	23.2	13.1	.608
4+5	64	19	10	86.5	22.9	11.5	.600
6+7	52	20	6	89.7	27.8	10.3	.667
ALL	1178	63	26	87.3	26.1	12.7	.667

Table 8.5. Results Table for August 1987 Data

MONTH : JULY & AUGUST

STATION	N1	N2	N3	POD	FAR	MTR	CSI
BLV	13	7	0	100.0	35.0	.0	.650
FFO	1	5	0	100.0	83.3	.0	.167
GUS	0	1	4	.0	100.0	100.0	.000
LCK	1	1	3	25.0	50.0	75.0	.200
LIZ	0	0	2	.0	999.9	100.0	.000
OSC	1	0	3	25.0	.0	75.0	.250
SAM	3	0	0	999.9	999.9	999.9	9.999
GR 0	16	14	12	57.1	46.7	42.9	.301
MTC	3	1	5	37.5	25.0	62.5	.333
GR 1	3	1	5	37.5	25.0	62.5	.333
BIX	29	3	4	87.9	9.4	12.1	.006
FMH	0	2	1	100.0	100.0	100.0	.000
FTK	8	1	4	66.7	11.1	33.3	.615
MYR	20	2	1	95.2	9.1	4.8	.070
GR 2	57	0	10	85.1	12.3	14.9	.760
BYH	10	2	0	100.0	16.7	.0	.833
HRT	25	10	4	86.2	28.6	13.0	.641
HST	20	16	3	87.0	44.4	13.0	.513
PAM	16	12	2	88.9	42.9	11.1	.533
PSM	0	0	1	.0	999.9	100.0	.000
VPS	27	5	8	77.1	15.6	22.9	.675
GR 3	98	45	10	84.5	31.5	15.5	.609

STATION	N1	N2	N3	POD	FAR	MTR	CSI
AXE*	0	0	1	.0	999.9	100.0	.000
CEPA	2	3	1	100.0	60.0	.0	.400
GTD*	3	1	0	100.0	.0	.0	1.000
PDG	10	1	2	83.3	9.1	16.7	.769
SSC	15	3	3	83.3	16.7	16.7	.714
GR 4	30	7	6	83.3	10.9	16.7	.690
AGR*	15	1	0	100.0	6.3	.0	.938
COF*	13	0	4	76.5		23.5	.765
DOV	11	5	3	78.6	31.3	21.4	.579
FDG	21	6	1	95.5	22.2	4.5	.750
FME*	4	15	1	80.0	.0	20.0	.000
MCF	34	4	4	89.5	30.6	10.5	.642
MXF	19	4	2	90.5	17.4	9.5	.760
VAD	23	4	4	85.2	14.8	14.8	.742
WRB	14	15	2	87.5	51.7	12.5	.452
WRI	14	4	3	82.4	22.2	17.6	.667
GR 5	1160	54	24	87.5	24.3	12.5	.603
ADW	11	4	4	73.3	26.7	26.7	.579
CBM	18	5	4	81.8	21.7	18.2	.667
DAA	6	7	2	75.0	53.0	25.0	.400
GSD	19	14	1	95.0	42.4	5.0	.559
LFI	12	7	0	100.0	36.8	.0	.632
NGF*	17	9	2	89.5	34.6	10.5	.632
HUT*	7	3	0	100.0	30.0	10.0	.607
POB	17	11	2	89.5	39.3	10.5	.567
GR 6	1107	60	15	87.7	35.9	12.3	.580
FAF*	9	1	1	90.0	10.0	10.0	.010
GR 7	9	1	1	90.0	10.0	10.0	.010

STATION	N1	N2	N3	POD	FAR	MTR	CSI
GR 0	16	14	12	57.1	46.7	42.9	.301
GR 1	3	1	5	37.5	25.0	62.5	.333
GR 2	57	8	10	05.1	12.3	14.9	.760
GR 3	98	45	18	84.5	31.5	15.5	.609
GR 4	30	7	6	83.3	10.9	16.7	.690
GR 5	1160	54	24	87.5	24.3	12.5	.603
GR 6	1107	60	15	87.7	35.9	15.3	.588
GR 7	9	1	1	90.0	10.0	10.0	.010
0+1	19	15	17	52.0	44.1	47.2	.373
2+3	155	53	28	84.7	25.5	15.3	.657
4+5	1198	61	30	86.0	23.6	13.2	.685
6+7	1116	61	16	87.9	34.5	12.1	.601
ALL	1408	1190	91	84.3	20.0	15.7	.635

Table 8.6. Results Table for July and August 1987 Data

223

8.3 Software Improvement for Subsequent Lightning Data Processing

8.3.1 Improved Processing Technique

The processing technique used for the Single Range output format, listing all lightning strikes within a specified range of the stations, proved to be overwhelming for large scale analysis, considering the amount of output produced for the forty-two stations over a two month period. For subsequent lighting data processing, a new technique was developed to reduce the amount of output.

The new technique groups the network data using six concentric range zones centered about the observer stations. Each range zone group has a time limitation which defines an end of data for that zone. The new process produces the Proximity listing, shown in Figure 8.8. The data is formated by columns, each column corresponding to one of the six range zones. The lightning data is placed in a block format containing the start time, the end time, the number of strikes, and the length of time the range area was active. The number of strikes counted is annotated with an "H". The delta time appears as total minutes and is annotated with an "m". The list is broken with a series of "=" after the largest range area is closed. This information is reformatted to be compatible with the LOTUS spread sheet package.

The Proximity correlation process reduces the output considerably by creating groups of data rather than listing every data point. The updated ZAPPC routine uses the time of the first lighting strike in a range area as a storm start time. Any strike within a particular range will increment that range area counter. The range zone is closed when no lighting strikes are detected for a fifteen minute period. When this occurs, the time of the first and last strike are written to the output listing.

8.3.2 Optimization of PC Processing

The range and azimuth to each strike is determined for every station. Due to the amount of lightning data on one floppy disk and the number of stations, these calculations are done over two million times. The ZAPPC program was designed to minimize processing time by restricting the local data storage and by limiting the number of mathematical operations. The program was written to perform only those mathematical calculations necessary for the requested output format. ZAPPC is designed to flush output data to the system printer as individual pieces are completed. The freed local storage space is reallocated to avoid a disk overflow.

8.3.3 Program Capabilities and Options

The ZAPPC program reports the total number of strikes processed and the number of strikes which fall within the ranges zones. It also reports the start and end times of the lightning data contained on the floppy disk currently being processed. These times are useful when selecting portions of the lightning data to be processed, particularly in a case of overlapping lightning data disks.

Other options enable the operator to select subsets of observer stations for processing. This allows a quick analysis of the lightning data for a specific area. In addition, there is an option which allows the user to enter new station data into the ZAPPC system. The user may enter a new station name and a corresponding latitude and longitude.

224

```
STATION :: NYC  LATITUDE  ::  40.75  LONGITUDE ::  -73.98  DATE ::  07/01/89
RANGE<30.0      RANGE<25.0      RANGE<20.0      RANGE<15.0      RANGE<10.0      RANGE< 5.0

04:22           04:25           04:25           04:25           04:25           04:25
07:00           07:00           07:00           04:38           04:38           04:38
36H  158m       33H  155m       30H  155m       4H   12m        2H   12m        2H   12m
===========                                     04:59           04:59           05:07
07:19                                           06:50           06:13           05:53
07:19                                           22H  111m       17H  74m        10H  45m
1H   1m                                                         06:33           06:33
===========                                                     06:50           06:44
15:22           15:22           15:22                           3H   17m        2H   11m
15:22           15:22           15:22
1H   1m         1H   1m         1H   1m
============
17:10
17:10
1H   1m
============
17:56
17:56
1H   1m
============
18:25
18:25
1H   1m
============
```

Figure 8.8. Proximity format

225

9. SOFTWARE SYSTEMS

9.1 CRRES EPHEMERIS SYSTEM

This section provides extracts from the Final Product Specifications for the Ephemeris Parameter Processing System for the two primary phases, Low Earth Orbit (LEO) and Geosynchronous Transfer Orbit (GTO), of the CRRES (Combined Release and Radiation Effects Satellite) mission. Specifications for the Ephemeris File conform with the CRRES Data Management Plan, Data Processing Task document. Note that in actuality the LEO phase may be dispensed with.

The CRRES Ephemeris File system generates standard satellite ephemeris, solar/lunar ephemeris, model magnetic field parameters, and coordinate conversion data at uniform intervals, on an orbit-by-orbit basis. These standard data are provided at an accuracy and frequency that will support the CRRES research investigations.

The specification describes in detail the parameters and files that are generated, and defines the software used in order to obtain the parameter values efficiently. The only initial input data needed to generate these values are SCF position and velocity vectors, coefficients for generating solar/lunar astronomical ephemerides and model magnetic fields, and the processing information data file. Satellite orbit, solar-lunar ephemerides, model magnetic field components, field line tracing, and coordinate transformation routines are analytically derived using model programs which provide the requisite parameters at uniform intervals.

For reference, considerations that have guided the design of this ephemeris file processing system, background information about related analyses, the coordinate systems and conversion relations, as well as the system testing that was performed are summarized later in this document. A glossary as well as a User's Guide follow.

9.1.1. Generation of Ephemeris File Parameters

SCF position/velocity vectors provided regularly to GL are evaluated and edited to generate Ephemeris File parameters at uniform intervals. The parameters primarily describe the spacecraft geographic, solar/lunar, and geomagnetic model environments, and as such consist of satellite position and velocity, location in geographic and geomagnetic coordinates, solar and lunar ephemeris information, model magnetic field and related quantities derived by field line tracing. Additionally, a header record on each ephemeris file provides special information applicable to the orbits, including file identification, time span, and solar eclipsing.

Table 9.1 defines the Ephemeris File Header record, and each of the identical records that follow is defined in Table 9.2. The word locations in the record, and the coordinate system and units for each parameter are indicated in these tables.

The parameters are determined exclusively by model program and coordinate conversion calculations. The basic models are:

- satellite ephemeris generator
- solar/lunar ephemeris and eclipsing
- magnetic field model & field line trace parameters
  (IGRF85 internal & Olson-Pfitzer external field)

Table 9.1. CRRES Ephemeris File Header Record

WORD NO.	PARAMETER DESCRIPTION	UNITS
1	Vehicle ID	Alphanum
2	Orbit No. (start of data file)	
3	Modified Julian Date (start of data file)	
4	Year (start of data file)	
5	Day of Year (start of data file)	
6	UT at Start of Data	msec
7	UT at End of Data	msec
8	UT at time of first Ascending Node	msec
9	UT at time of first Perigee	msec
10	Eclipse (1) Max. Obscuration	
11	Penumbra (1) Start Time (UT)	msec
12	Penumbra (1) End Time (UT)	msec
13	Umbra (1) Start Time (UT)	msec
14	Umbra (1) End Time (UT)	msec
15	Eclipse (2) Max. Obscuration	
16	Penumbra (2) Start Time (UT)	msec
17	Penumbra (2) End Time (UT)	msec
18	Umbra (2) Start Time (UT)	msec
19	Umbra (2) End Time (UT)	msec
20	Date of Tape Generation	Alphanum
21	Local Time of Tape Generation	Alphanum
22	Data Status Flags	
23-60	VACANT (0 filled)	

Note 1: All values except alphanumeric are floating point; alphanumeric values are in CDC 6-bit display code.

Note 2: -999999999. indicates a dummy fill value, such as for eclipse times not available.

Note 3: All times in the header are with respect to start time of data. Total milliseconds may be negative or greater than 86,400,000. Negative implies the previous day, with 86,400,000 milliseconds added.

Table 9.2. CRRES Ephemeris File Parameters

WORD NO.	PARAMETER DESCRIPTION	COORDINATE SYSTEM	UNITS
1	Modified Julian date	---	days
2	Universal time	---	msec
3	X, satellite position	ECI	m
4	Y, satellite position	ECI	km
5	Z, satellite position	ECI	km
6	VX, satellite velocity	ECI	km/s
7	VY, satellite velocity	ECI	km/s
8	VZ, satellite velocity	ECI	km/s
9	Radius, from earth center	GEOCEN	km
10	Altitude	GEODETIC	km
11	Latitude	GEOCEN	deg
12	Longitude	GEOCEN	deg
13	Satellite Velocity	ECI	km/s
14	Local time	GEOCEN	hr
15	Radius	MAG	EMR
16	Latitude	MAG	deg
17	Longitude	MAG	deg
18	Radius	SM	EMR
19	Latitude	SM	deg
20	Local time	SM	hr
21	Radius	GSM	EMR
22	Latitude	GSM	deg
23	Local time	GSM	hr
24	B (Model)	---	nT
25	BX (Model)	ECI	nT
26	BY (Model)	ECI	nT
27	BZ (Model)	ECI	nT
28	Magnetic Local time	MAG	hr
29	Solar Zenith Angle	GEOCEN	deg
30	Invariant latitude	B,L	deg
31	B100N latitude	GEOCEN	deg
32	B100N longitude	GEOCEN	deg
33	B100S latitude	GEOCEN	deg
34	B100S longitude	GEOCEN	deg
35	L-Shell	B,L	EMR
36	BMin	---	nT
37	BMin latitude	GEOCEN	deg
38	BMin longitude	GEOCEN	deg
39	BMin altitude	GEODETIC	km
40	BConJ latitude	GEOCEN	deg
41	BConJ longitude	GEOCEN	deg
42	BConJ altitude	GEODETIC	km
43	Sun position, X-coord.	ECI	km
44	Sun position, Y-coord.	ECI	km
45	Sun position, Z-coord.	ECI	km
46	Moon position, X-coord.	ECI	km
47	Moon position, Y-coord.	ECI	km
48	Moon position, Z-coord.	ECI	km
49	Right Ascen. of Greenwich	ECI	deg
50	B100N mag. field	---	nT
51	B100S mag. field	---	nT
52	Mx, dipole moment	ECI	nT
53	My, dipole moment	ECI	nT
54	Mz, dipole moment	ECI	nT
55	Dx, dipole offset	ECI	km
56	Dy, dipole offset	ECI	km
57	Dz, dipole offset	ECI	km
58-60	VACANT (0 filled)		

Constants required for astronomical calculations such as Greenwich Hour Angle (GHA) conform to definitions in the Nautical Almanac [1985] and will not be changed for the duration of the CRRES mission. Figure of Earth is given by equatorial radius a_e=6378.135 km, and flattening f=1/298.26. Distances are given either in kilometers or in Earth mean radii (EMR = 6371.2 km). All latitudes are geocentric for consistency, but altitudes are geodetic, i.e. the vertical distance above the reference ellipsoid. Some geophysical parameters such as magnetic dipole moment and offset change very slowly with time, and fixed "average" values of these quantities are used as the basis for deriving satellite coordinates in the geomagnetic systems.

Certain parameters that are based on external magnetic field calculations or magnetospheric coordinates are not needed in the LEO phase. However, since the LEO phase constitutes a small fraction of the overall CRRES experiment, identical header and data file formats are employed for files created in either the LEO or the GTO phase. This commonality will also prove beneficial while operating this processing system.

The data are provided at integral minutes, with one file per orbit in both the LEO and GTO phases, but the following differences apply in recording the data:

- The LEO phase contains data once per minute throughout. File/orbit segmentation is by revolution number i.e. by South-to-North nodal crossing.
- The GTO phase contains data once per minute for satellite geocentric distances less than 3 Earth radii, R_E, and once every 5 min. for greater distances. File/orbit segmentation is on a perigee-to-perigee basis.

The ephemeris file is designed to facilitate investigations on an orbit-by-orbit basis. A short time extension at the start and end of the file for each orbit allows the use of interpolation techniques near orbit start and end without requiring access to additional ephemeris files. Continuity and overlap of parameter values is thus always maintained between successive files.

9.1.2 Ephemeris Processing System

The system is designed for operation on the CYBER 860 system at GL. The processing system is integrated and designed to produce Ephemeris Files orbit-by-orbit with a minimum of operator intervention. The process generates integral orbit files in a single computer run using the following auxiliary, non-concurrently created, on-line files:

- An SCF vector library file must be created, quality checked, and accumulated by the orbital analyst.
- A high accuracy daily solar/lunar ephemeris file spanning the days to be processed must be previously created.
- A process management data base which is updated after each run, and may be queried and revised.

Data from these files are used for initiation and input to new processing runs.

Section 9.1.4 gives a description of the Ephemeris Processing System. The same processing software is applicable for both the LEO and GTO phases of the mission. The design allows straightforward adaptation of the system for many other satellite missions, however field line

229

tracing in polar orbits has not been investigated. Ephemeris File generation at arbitrary recording frequencies, and the option to switch between these frequencies based on Earth radial distance are inherently available in this system.

9.1.3 Developmental Approach

Software packages and techniques in current use at GL were the basis for this Ephemeris processing system. The orbital, magnetic field line tracing, and astronomical ephemeris programs were selected so as to give model accuracies suited to the requirements of the CRRES mission.

The satellite orbit generation system was evaluated by comparison with benchmark runs from highly accurate orbit determination programs. Solar/lunar ephemeris accuracy was evaluated, and high speed routines were developed to take advantage of the fact that limited time spans are processed during each CRRES ephemeris file generating run. An accurate solar eclipse calculation program was also developed to run concurrently, during ephemeris file header record generation.

Magnetic field model and parameter generation algorithms were investigated for accuracy and computation speed. The predominant subject for these studies was magnetic field line tracing, since this requires numerous magnetic field model calls at each ephemeris time to determine parameters for 100 km N intercept, 100 km S intercept, Magnetic Equator (Bmin), Conjugate point, and L-shell.

9.1.3.1 Considerations in Design

This section summarizes the results of analyses which have guided the development of this product specification. Items that were investigated and are covered below include:

- orbital ephemeris accuracy
- astronomical ephemeris
- solar eclipse parameters
- magnetic field model
- field line tracing
- magnetic field parameters
- parameter frequency/switching
- system performance

In addition, coordinate systems are an ever important consideration for carrying out the scientific studies. Geocentric, Earth Centered Inertial (ECI), Magnetic, Solar Magnetic (SM), Geocentric Solar Magnetospheric (GSM), and Vertical-Dipole-Horizon (VDH) coordinates are among the reference coordinate systems that are useful for the investigators.

9.1.3.2 Orbital Ephemeris and Element Frequency

Orbit generation is performed using a reduced version of program LOKANGL, which is regularly used at GL. This program accounts for the first two zonal perturbations J_2 and J_3 of the Earth's geopotential. The program converts Satellite Control Facility (SCF) position-velocity vectors to mean elements based on this geopotential model, interpolates to obtain the mean elements for any desired epoch, and reconverts to osculating elements and position-velocity using

the same geopotential model in reverse. This program will reproduce orbits with 3-4 seconds in-track accuracy, using vectors one or two days apart.

9.1.3.3 Solar/Lunar Ephemeris

The astronomical ephemeris program selected, SLEPHEM, gives accuracy to about 0.5 seconds of arc in right ascension and declination, when compared with the Astronomical Almanac. This accuracy is more than adequate for the CRRES mission, even when considering the stringent requirements for calculating solar eclipsing at the satellite.

High accuracy is retained using interpolation techniques that start from "pre-generated" results obtained by SLEPHEM at 0 hr. UT for each day. By application of simple interpolation techniques, using a cubic fit to four pre-calculated values, each 1 day apart, the solar ephemeris deviates from Almanac values by less than 1 sec. of arc.

9.1.3.4 Calculation of Solar Eclipsing Circumstances

The separation of the solar disk and the Earth limb is, like the solar/lunar ephemerides, smooth as a function of time. Thus, solar eclipse conditions may be determined by solving for the times of intercept, if any, of the solar disk and the Earth limb as viewed from the satellite. Exacting requirements for prediction of solar eclipses are met by using eclipsing geometry calculations which account for Earth oblateness as well as for true satellite-Earth and satellite-Sun vector directions.

9.1.3.5 Magnetic Field Models

This section provides back-up material for derivation of the Dipole Model from the full internal field model, based on the first order terms of the IGFR85 Schmidt normalized spherical harmonic coefficients. The dipole moment, axis orientation, and eccentric offset are defined according to [Geomagnetism, Chapman and Bartels, Oxford Press, 1940]:

$$V_1 = g_{10}\cos\theta + (g_{11}\cos\phi + h_{11}\sin\phi).\sin\theta$$

This is transformed by the relationship

$$V_1 = H_0 \cos W$$

where

$$\cos W = \cos\theta\cos\theta_0 + \sin\theta\sin\theta_0\cos(\phi-\phi_0)$$

$$H_0^2 = g_{10}^2 + g_{11}^2 + h_{11}^2, \quad \cos\theta_0 = g_{10}/H_0, \quad \tan\phi_0 = h_{11}/g_{11}$$

This field has the same magnetic potential as a dipole field, and the dipole moment, which is the same as the magnetic force at $W=90°$, is given by H_0.

The axis of the dipole corresponding to V_1 above is along (θ_0,ϕ_0), and the Cartesian coordinates of this axis are:

$$(-g_{11}, -h_{11}, -g_{10})$$

231

The location of the <u>dipole magnetic center</u> is chosen so that the spherical harmonic expansion

$$f_n(\theta,\phi)/r^{n+1}$$

of the field at the location contains no $n=2$ term. If we define

$$L_0 = 2g_{10}g_{20} + (g_{11}g_{21}+h_{11}h_{21})\sqrt{3}$$

$$L_1 = -g_{11}g_{20} + (g_{10}g_{21}+g_{11}g_{22}+h_{11}h_{22})\sqrt{3}$$

$$L_2 = -h_{11}g_{20} + (g_{10}h_{21}-h_{11}g_{22}+g_{11}h_{22})\sqrt{3}$$

$$E = (L_0g_{10}+L_1g_{11}+L_2h_{11})/4H_0^2$$

the center of the eccentric dipole is given by

$$x_0=a(L_1-g_{11}E)/3H_0^2, \quad y_0=a(L_2-h_{11}E)/3H_0^2, \quad z_0=a(L_0-g_{10}E)/3H_0^2$$

9.1.3.6 Field Line Tracing

The predominant subject for these studies was magnetic field line tracing, since it requires numerous magnetic field model calls at each ephemeris time. Products of the field line tracing are:

1) 100 km N intercept coordinates
2) 100 km S intercept coordinates
3) Magnetic Equator (Bmin) coordinates
4) Conjugate point coordinates
5) L-Shell (involves calculation of a weighted integral along the field line to the conjugate point)

A detailed study of existing field line tracing algorithms was undertaken to determine how to maximize computational speed (minimize steps) for a specified accuracy using the analytically known dipole field solution as the test field. The tracing algorithms and the associated software packages investigated were:

Subroutine	Package/Source	Originator
LINES	INVAR/MFP	McIlwain-GSFC 1965
LINTRA	MGFLD2/MFP	Stassinopoulas-Mead-GSFC 1971
LINER	FLDTRC or GTUBLN	Pfitzer-McDonnell AC 1972
TRACK	BFLD/SCATHA	Hilton-Aerospace 1979

Techniques used in these studies included comparison of results with exactly known values for magnetic dipole fields, calculations at typical points under various orbital conditions, and control of line integral step size to give comparable miss distances. The evaluation emphasized performance at lower latitudes and locations above $2R_E$, and therefore for the CRRES orbit which does not extend much beyond L-shells equal to 8. The studies established an optimum set of routines which would determine magnetic field parameters that are dependent on field line tracing. Other improvements were included in the existing routines when these were reasonably evident. The approaches implemented are as follows:

232

1)	Field Line Integrator	-	4th order Open Adams in Cartesian coordinates.
2)	100 km Interceptor	-	4th order Runge-Kutta
3)	Invariant Integral	-	Simpson's Rule
4)	L-shell Evaluator	-	Routine CARMEL/INVAR

A step size that results in a minimum of about 100 steps for fixed line lengths of $2R_E$, increasing linearly to around 200 steps at the shortest ($\approx 0.5R_E$) and the longest ($\approx 20R_E$) field line lengths, was found to give uniform and adequate accuracy throughout, with no rapid improvement in accuracy of magnetic parameter calculations as the minimum number of integrations exceeded 100. The field line length is estimated to be proportional to the dipole equatorial radius r_{eq}, which is given by $r_{eq} = r/\cos^2 W$ where r is the satellite radial distance, and W is the geomagnetic latitude. For r_{eq} less than 2 and for $|W|$ less than 30°, more accuracy is desired in estimating field line lengths, and this is achieved by a model quadratic in r and linear in geographic latitude and longitude, using coefficients at 10° latitude and 15° longitude intervals.

9.1.3.7 Magnetic Field Parameters

Model magnetic field calculations, field line tracing and determination of the associated magnetic field parameters is implemented in routine OPTRACE. Magnetic field related parameters useful for CRRES investigations are calculated from the results of line tracing, using the IGRF 85/Olson-Pfitzer fixed field model. The accuracy in determining quantities for 100 km intercept, magnetic equator, conjugate point, L-shell, and other parameters were studied for the Olson-Pfitzer and the Dipole models.

The magnetic field parameters that are provided are listed in Table 9.2. This complement is designed to satisfy most researcher needs, but if additional parameters or greater resolution of parameters is required, these must be determined independently.

9.1.3.8 Parameter File Frequency/Switching

The approach taken provides for the user to employ linear interpolation to obtain parameter values at intermediate ephemeris times. Higher frequency occurrence of these parameters is therefore desirable when their second derivatives become larger. Investigations have shown that at a distance of $3R_E$ the second derivative of the parameters decreases to about 5% of the maximums that are encountered (usually near perigee). Furthermore, the CRRES orbit spends about 5 times as much time outside $3R_E$ as it does inside. Therefore two recording frequencies, once every minute and once every 5 minutes, are employed, with the transition between these recording frequencies taking place near $3R_E$.

9.1.4 Description of Ephemeris File Processing System

The only data input needed to generate the Ephemeris File parameters are SCF position and velocity vectors, solar/lunar ephemeris, and the processing information data file. All the parameters in Table 9.1 are obtained using well-tested satellite generation, solar-lunar astronomical ephemeris, magnetic field model, and magnetic field line tracing routines. These parameters are calculated at the level of accuracy required to create the Time History and Product Associated Data Bases for subsequent CRRES investigations. For satellite geocentric distances greater than $3R_E$, the parameters change more slowly, and the parameter file generation rate is once every 5 minutes. Figure 9.1 gives a flow chart of the overall processing system.

233
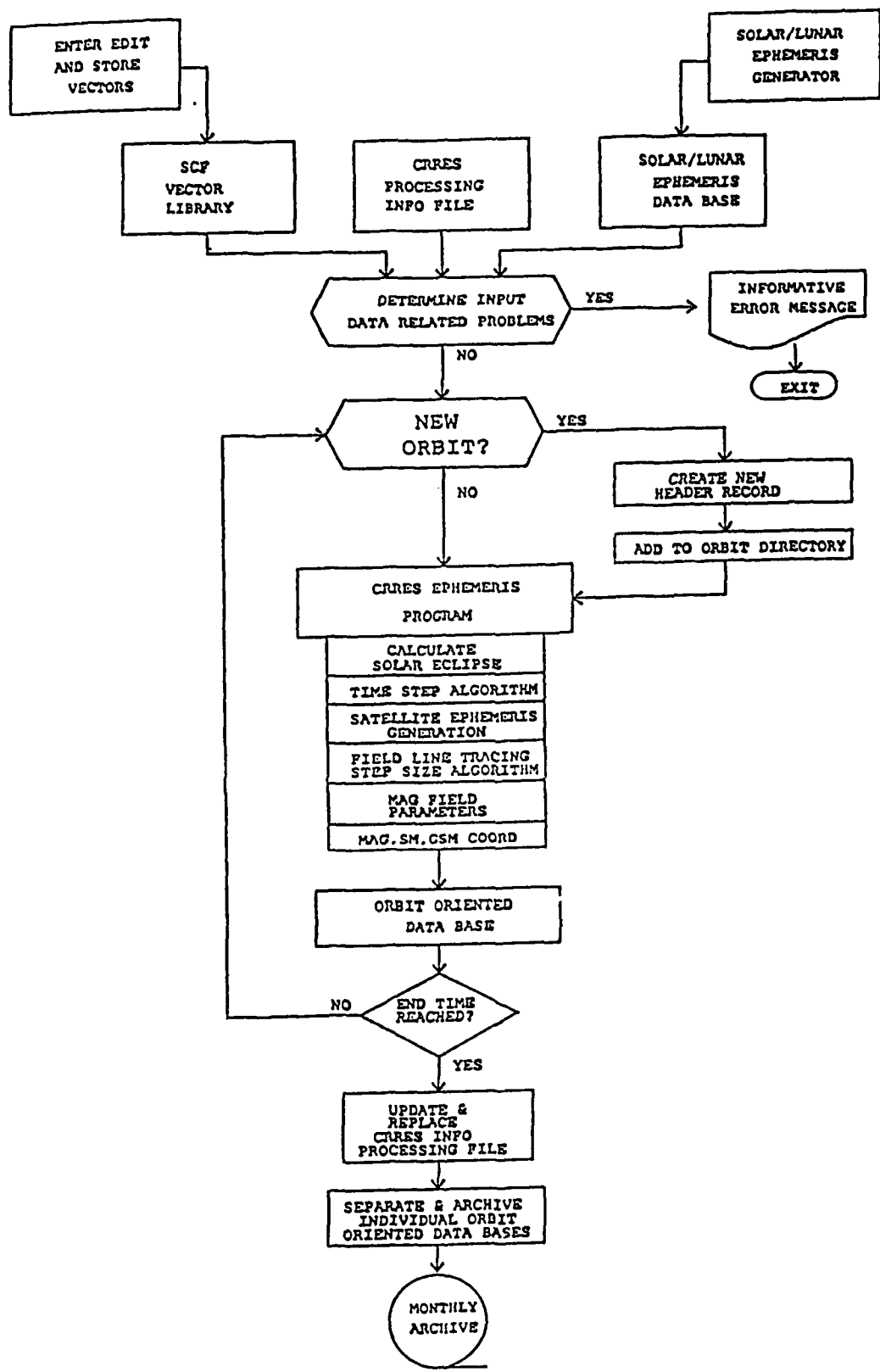
Figure 9.1. CRRES Ephemeris File Processing System

9.1.4.1 Satellite Ephemeris Routine & SCF Vectors

Orbit generation is performed using a reduced but compatible version of program LOKANGL, which is regularly used at GL. SCF vector sets will comprise the satellite element inputs. These vectors are usually provided for 00:00 hr UT, and are therefore randomly located around the orbit. Transmittal errors as well as inconsistencies that show up during trend analyses must be screened by the orbital analyst.

Trajectory generation is performed exclusively by interpolating between element sets, i.e. no extrapolated predictions are made. The orbital ephemeris program includes the first two zonal perturbations J_2 and J_3 of the Earth's geopotential. The program converts SCF position-velocity elements to mean elements based on this geopotential model, interpolates to obtain the mean elements for any desired epoch, and reconverts to osculating elements and position-velocity using the same geopotential model in reverse.

9.1.4.2 Operational Procedures for Handling SCF Vectors

SCF vectors will be entered, edited, and evaluated by the contractor responsible for orbit analysis, prior to being saved in the vector library. The orbital analyst will maintain plots of the Keplerian values to allow quick verification of reliability of the approved vector sets. Approval of vector sets must nevertheless include screening for duplicates and to ascertain that sets spaced a few hours or less apart are not allowed. The complete database will be maintained on the computer system permanent storage at all times. The ephemeris generating system will utilize all valid SCF state vectors in the library to calculate the CRRES orbit over the time period covered by the vectors.

The SCF vector library should exclusively contain the vectors employed for the actual ephemeris files generated or approved for generation. Therefore if the orbital analyst finds that previously approved vector sets should be revised, but that ephemeris files have been generated and released over the affected time span, a decision to update the SCF vector library and regenerate the ephemeris should be implemented only after joint approval by the orbital analyst and the contractor generating the ephemeris files.

9.1.4.3 Solar/Lunar Ephemeris

The astronomical ephemeris program employed gives extremely high accuracy for requirements of the CRRES mission, and astronomical ephemeris calculations are performed consistent with equations and procedures defined in the Astronomical Almanac for 1985.

Pre-generated results are obtained by an accurate ephemeris program, SLEPHEM, at 0 hr. UT for each day. Interpolation using cubic polynomials then provides a high speed, high accuracy solar-lunar ephemeris for any arbitrary time, so that the maximum solar ephemeris error is less than 1 sec. of arc. This cubic is fit to four pre-calculated values, each 1 day apart, and thus spans 3 days. The value being determined always lies in the central day of this span. The CRRES ephemeris file production procedure issues a warning if the requisite file covering the days of interest, and 60 days beyond, has not been pre-generated.

9.1.4.4 Calculation of Solar Eclipsing Circumstances

The separation of the solar disk and the Earth limb is, like the solar/lunar ephemerides, smooth as a function of time. Exacting requirements for prediction of solar eclipses are met by using refined eclipsing geometrical calculations which take into account Earth oblateness and true

satellite-Sun and satellite-Earth vector directions. Solar eclipse conditions are then determined by solving for the times of intercept, if any, of the solar disk and the Earth limb as viewed from the satellite. Eclipse magnitude M is defined as the fraction of the solar diameter obscured by the Earth. The degree of obscuration is the fraction of the solar disk area that is obscured by the Earth.

If a solar eclipse occurs near the start of an orbit, and repeats at the end, two solar eclipses are possible in one orbit, and are entered in the ephemeris file header. This information consists of the maximum obscuration during each eclipse, and the times of first through fourth contacts in each case. These times may extend beyond the ephemeris data time spans actually recorded on that file, and may therefore be duplicated on successive files.

9.1.4.5 Magnetic Field Models

The main magnetic field model consists of the IGRF 85 internal field model with temporally varying coefficients, coupled with the Olson-Pfitzer quiet external field model. The major part of the computation time is required for evaluation of the internal field which, in the case of the IGRF 85 model, involves calculation of an 11x11 spherical harmonic field. For orbital locations within $2R_E$, external field contributions are negligible, and those calculations are bypassed.

A dipole field model, based on the first order coefficients of the IGRF 85 model, is employed to determine many of the ephemeris parameters, particularly Magnetic, Solar Magnetic, and Geocentric Solar Magnetospheric coordinates, as well as Magnetic Local Time. The geographic coordinates of the magnetic poles are determined from the fundamental components of the IGRF 85 internal field propagated to the appropriate epoch, and the direction of the dipole axis is obtained as described in Section 9.1.3.5..

9.1.4.6 Field Line Tracing

The main magnetic field model is employed at each location in the CRRES orbit in order to carry out complete field line traces. One such trace could require over 200 integration steps, and consequently the computational speed of evaluation of the B field vector at any point was extremely important in the development of OPTRACE, which calculates CRRES Ephemeris package magnetic field parameters.

Products of the field line tracing at each location are:

1) 100 km N intercept coordinates
2) 100 km S intercept coordinates
3) Magnetic Equator (Bmin) coordinates
4) Conjugate point coordinates
5) L-Shell (involves calculation of a weighted integral along the field line to the conjugate point)

236

9.1.5 Organization and Operation of Processing System

The ephemeris and model magnetic field computational system allows for ease of operation by the user. Figure 9.1 shows the software system's functional flow and the data bases required to calculate the necessary parameters. The software utilizes a processing data base to determine the proper time period to be generated. This data base eliminates the need for user entry of information and protects against possible data entry errors.

The system determines, prior to performing any calculations, if the solar/lunar data base residing on computer disk contains sufficient information to cover the time period to be processed. When periods being processed are within the last 60 days of the solar/lunar data base, an informative warning is provided that the data base should be updated.

The time period processed is determined by the SCF vectors that are available in the vector library. The END period is the epoch for the last accepted SCF vector set. Information about the processed data bases is updated at completion of the file generation.

The software system uses permanent disk storage to temporarily archive the orbit oriented ephemeris and model field data bases. Each permanent disk file name contains, as part of the naming convention, the orbit number on which the data base commences. This allows the user to examine data bases on a single orbit basis and to directly determine available orbits from the permanent file directory. Note that, due to progression of the argument of perigee, the file annotation will indicate a missing orbit approximately every 500 days.

All orbit oriented data bases may be periodically archived to magnetic tape using standard disk archiving techniques. Archiving should not be performed until the agency ephemeris file product has been verified for release by the orbital analyst.

9.1.5.1 Data Bases

Orbit oriented ephemeris data files are stored as permanent disk files for access by other software packages that require these files for creating agency tapes, and may be archived as required onto magnetic tape. Other on-line files are used during execution of the processing system.

9.1.5.1.1 SCF State Vector Library

This is a sequential data base of acceptable values of X, Y, Z, X-dot, Y-dot, and Z-dot. These vector sets must be within prescribed tolerance and trends based on evaluation of the equivalent Keplerian elements. The SCF vector format is compact enough that the elements can be maintained on-line with a minimal amount of storage. Accepted elements may be periodically added to the vector library, and may also be archived as required.

9.1.5.1.2 Solar/Lunar Ephemeris

This data base is generated periodically as additional time spans are required. The data base structure is such that each logical record contains year, day, solar position, and lunar positions for 0 hours UT. The position of the Sun and Moon are stored as right ascension, declination. and distance from center of Earth. This daily eight word record format allows for more than one year of data without presenting a computer storage problem.

237

9.1.5.1.3 Processing Information Data Base

This data base contains the start time for processing, low/ high data rates, the R_E value at which to change data rates, and an indicator for file segmentation. This file will initially be created by the orbital analyst. The file will be updated with a new start time only upon successful completion of processing. Time interval and orbit segmentation are user controllable options.

9.1.6 Implementation and Performance

Software for the CRRES Ephemeris File Generation System is written in Fortran V, and is designed to operate on mainframe computers such as the CYBER 860 at GL. CP memory and mass storage requirements are modest:

- The program is composed of the basic Orbit Generator, the Solar/Lunar Ephemeris and Eclipse package, Magnetic Field Model, Line Tracer, L-shell Calculator, associated coordinate conversion routines, and the File Directory Management process. Since these routines are called sequentially at each time step, a segmented organization is possible, but was not considered necessary.
- The program requires on-line availability of relatively small solar/lunar ephemeris, SCF vector, and Management Directory files during execution. The major mass storage requirement should be to keep completed ephemeris files resident while the Agency Tapes are in preparation.

One 9-track 6250 bpi group-encoded (GE) or 1600 bpi phase-encoded (PE) tape drive is required for archiving groups of completed ephemeris files on a weekly or longer basis. Data for each orbit consists of the header record and about 240 data records, 60 words each. Records are written blocked, the header record followed by 10 data records per block, so that one month of data, about 67 orbits, presents no problem.

During a 635 minute orbit, the CRRES satellite will spend about 20% of its time below $3R_E$. On the CYBER 860, the ephemeris parameter calculations take about 0.5 seconds per point, most of which is for field line tracing. Therefore, transitioning the frequency of these calculations from once per minute below $3R_E$ to once per 5 minutes at greater radial distances where the parameters change slowly, total ephemeris computation time per orbit is about 120 CP secs.

9.1.7 Test Results

Preliminary testing of the complete system consisted of duplicating the known results from previous studies made during development of this specification. In particular, comparisons were made with present implemented laboratory versions of LOKANGL and BFLD. More complete testing was performed through analyses of prototype LEO and GTO files. These tests verified the program's capability to function with the Directory Management File while processing by perigee or node, and also checked generated file formats.

238

9.1.7.1 Accuracy Tests for Orbital Ephemerides

Vehicle orbital ephemerides were created and position and velocity vector values were compared with LOKANGL results for the same cases. First differences of X, Y, Z as well as X', Y', Z' were listed and plotted, to ensure that the operational system at GL had been incorporated accurately.

9.1.7.2 Accuracy Tests for Astronomical Ephemerides

The solar ephemeris portion of the package was compared against the output from SLEPHEM, the high accuracy astronomical ephemeris generator used at GL. Listings and plots of differences in right ascension and declination were made at 12 hour intervals to ascertain that there was no unusual behavior or irregularities. The lunar ephemeris was checked similarly, consistent with the lower accuracy requirements. The algorithm for the Right Ascension of Greenwich has been obtained from and was verified against the Astronomical Almanac [1985].

Extensive testing was conducted for performance and accuracy of solar eclipsing calculations. Eclipsing conditions were tested while progressing a) from no eclipse to eclipse, and b) from eclipse to no eclipse. Eclipsing scenarios were considered for four orbital conditions:

i)	Eclipse near perigee
ii)	Eclipse near apogee
iii)	Eclipse 90° from perigee
iv)	Eclipse 270° from perigee

9.1.7.3 Accuracy Tests for Field Line Tracing

Three tests were carried out for verifying calculations of field line related properties in the CRRES Ephemeris File. All used a prototype ephemeris file in comparison to values generated by either OPTRACE or the original SCATHA package BFLD. The input needed consisted of Julian Day, UT, Sun position and satellite position. For consistency, these were taken from the Ephemeris file. Both the coordinate transformations and the field line related properties were compared.

9.1.7.3.1 Test 1. Transmittal

In this test, an ephemeris file generated with IGRF85 was compared to the output from the program OPTRACE using the same model field. Selected points at various altitudes were examined in detail. Agreement was determined to be exact to machine precision level, with residual errors traceable to the conversion between Gauss and nT done on the coefficients. Assuming that this discrepancy is due to rounding Table 9.3 gives the approximate errors arising from truncation.

9.1.7.3.2 Test 2. The Model Field

In this test, the magnitude of the field in the Ephemeris file was compared to that generated by the SCATHA ephemeris package BFLD. BFLD was chosen instead of OPTRACE to cover possible errors made in using the field coefficients as well as in coding them. Table 9.4 gives the magnetic field difference between the Ephemeris file and Barraclough75 evaluated at 1980.5 in the second column and the difference between the Ephemeris file and IGRF80 which, appropriately, compares more favorably for the range of L-shells.

Table 9.3 Truncation Errors for Selected Properties

B $< 10^{-9}$ nT
B_{100}int $< 10^{-8}$ nT
B_{100}lat $< 10^{-11}$ deg
B_{100}lon $< 10^{-11}$ deg
L_{shl} $< 10^{-12}$ R_E

Table 9.4 Magnetic Field Values

L-shell	ΔB(BARR75)	ΔB(IGRF80)
1.05	95.00	-.30
1.09	112.00	8.90
1.45	40.00	5.00
1.93	14.00	2.60
2.43	6.00	1.30
2.91	3.00	.70
3.36	1.70	.40
5.25	.26	.08
6.64	.09	.04
7.60	.04	.03
8.16	.03	.03

Table 9.5 Errors in North Intercept Field

L-shell R_E	Δ(.05) nT	Δ(.02) nT
1.5	190.0	23
1.7	153.0	-8
1.9	114.0	-8
2.2	9.0	3
2.4	-.2	3
5.2	53.0	-2
5.4	-2.0	-8
5.6	80.0	-4
5.7	-3.0	-2
6.6	110.0	8
7.6	130.0	11

240

Comparisons were made for all field line related properties. The maximum difference for Barraclough is rather larger than the difference in dipole moment (about 20 nT). Differences in third moment terms $(1/r^4)$ are as high as 50 nT, however, so the larger discrepancy is probably not troublesome. As expected, IGRF agrees much better because of closer epoch dates and probable similarities in data bases and techniques for calculating the coefficients. Also of note is the small residual error, at large r. The difference between dipole moments for Barraclough and for IGRF80 compared to IGRF85 is about 20 nT for both. Since the dipole term alone would lead to a difference of about 0.03 nT at 8 R_E, this supports the conclusion that the model field is correctly implemented.

9.1.7.3.3 Test 3. General Integrity of the Tracer

In this test, the original version of BFLD was used to perform the same field line traces as were generated in the ephemeris file. BFLD does not perform well at all for L-shells less than about 1.5, since for these shorter field line lengths BFLD takes too few steps to achieve a reasonable level of accuracy. Therefore comparisons were restricted to L-shells greater than 1.5 R_E. Runs were carried out with the original value of step size proportionality constant of .05 and a more accurate .02. For proportionality constant of 0.05 (.02), the largest errors were in 100 km intercepts where the field was in error by about 100 (20) nT, and the latitudes in error by about .05 (.003). Table 9.5 lists several north intercept errors in field magnitude.

Errors in all ephemeris field related properties were evaluated, and it was found that the differences between BFLD and the ephemeris system were quite small, lower than the error bounds on the quantities themselves for the .02 case. Also, since the error was substantially smaller for the .02 case than for the .05, it is evident that the ephemeris system is more accurate than BFLD. The errors do not show systematic tendencies, which is also a favorable indication.

9.1.7.4 Operational Tests and Data Management Files

System operation was tested for normal behavior as well as for many of the functional capabilities implicit for proper processing or termination under abnormal conditions. Orbit segmentation procedures were exercised for perigee times (GTO), and for ascending node times (LEO). Processing and handling of the Data Management File was verified for updating and abnormal termination cases. System procedure file generation for data base control and archiving after aborted or normal runs was also verified.

9.1.8 CRRES Ephemeris System -- USER'S GUIDE

This User's Guide describes the configuration and use of the CRRES Ephemeris System (CRESEPH) on the NOS/VE operating system of the AFGL Cyber 860 computer. Even though a single orbit may be generated if necessary, the system is designed for routine batch processing, typically on a weekly basis. Usually this should amount to no more than the submission of a batch job and examination of the job output file to verify successful operation. Special attention should be required only in the initial run of the system or when selected files need to be regenerated. Instructions for these special cases are included this guide.

9.1.8.1 Files

Three input data files are required for generation of the orbital data file. The system also creates and updates a library file providing a record of orbits that have been processed and cataloged and an output log file of the run. For convenience, a command file to control the overall

operation of the system has been provided. This file could be modified or replaced at the convenience of the operator. The formats and contents of these files are described below.

9.1.8.1.1 The STATE_VECTOR_LIBRARY file

This file contains position and velocity vector type orbital element sets at a frequency of approximately one-per-day.

9.1.8.1.2 The PROCESSING_INFORMATION file

This file communicates to the system the start time of the first orbit to process and controls various options of the system.

9.1.8.1.3 The SOLAR_LUNAR_EPHEMERIS File

This file contains daily ephemeris information for the sun and moon.

9.1.8.1.4 The Orbital Data File

Each orbital data file contains a sixty word header record, described in Table 1. Following this is a series of 600 word records, each containing ten sequential sets of ephemeris file parameters as described in Table 2. If the final record contains less than ten sets, the remaining words are 0 filled.

9.1.8.1.5 The ORBITAL_DATA_FILE_LIBRARY

This file contains a list of all orbits which have been processed.

9.1.8.1.6 The OUTPUT_LOG file

This is a permanent file which is updated each time the system is run. It contains a list of the elements used in the calculation and the orbits generated. It also contains any error messages printed during processing.

9.1.8.1.7 The CRESEPH_COM command file

The command file CRESEPH_COM performs a number of system commands controlling operation of the software.

9.1.8.2 System Operation

The usual run will consist of the following steps, (supposing that the ephemeris system is assigned to a subcatalog called creseph).

1) Locate the updated state vector library and copy it to the working catalog of the ephemeris system under the name STATE_VECTOR_LIBRARY.

2) Submit a batch job with the following three lines.

   set_working_catalog $user.creseph create_command_list_entry $catalog creseph_com

242

Output from this job will inform the user whether the ephemeris system terminated normally and will tell you if new orbital data files have been created. If so, the files will appear in the working catalog and the orbital data file library and processing information files will have been updated.

If the job informs you of errors during processing, you should consult the output log file for the error message and refer to section B.3 for the appropriate response.

9.2 IBSS EPHEMERIS

9.2.1 Introduction

The IBSS Ephemeris File system generates standard satellite ephemeris, solar ephemeris, model magnetic field parameters, and coordinate conversion data at uniform intervals, throughout each segment of the shuttle's flight. These standard data are provided at an accuracy and frequency that will support the requirements of the research investigations. Two types of ephemeris file are supplied: one which provides data relative to the Orbiter; and a second, which provides data relative to the IBSS (i.e., relative to the SPAS platform).

Position/velocity vectors provided by NASA are extracted from the PATH tape and used to generate Ephemeris File parameters at uniform intervals. The parameters primarily describe the spacecraft geographic, solar, and geomagnetic coordinates, solar ephemeris information, solar illumination conditions at the vehicle, and modeled values of the geomagnetic field together with quantities such as L-shell and the associated invariant latitude. In addition, a header record on each ephemeris file provides special information applicable to the individual data collection period, including ephemeris file identification and time span, and identification of the individual PATH and RELBET tapes used as data sources. Table 9.6 defines the Ephemeris File Header record. The format of the Ephemeris Parameter files for the orbiter and the SPAS are similar, and Table 9.7 shows the latter.

The parameters are determined exclusively by model program and coordinate conversion calculations. The basic models are:

- satellite ephemeris generator
- solar ephemeris
- magnetic field models
  (IGRF 85 internal and Cain's model [Cain] used for L-shell interpolation)
  (IGRF 80 internal for corrected geomagnetic computations)

An Orbiter file is provided for each PATH Tape on a one-for-one basis. Throughout each ephemeris file, complete sets of data are provided at each of the sampling times, which are at uniformly spaced intervals. The value of the time increment is a selectable parameter to be specified for each run. Thus the option is available to provide rapid sampling rates to cover special circumstances.

Orbiter ephemeris files span the entire Shuttle flight. SPAS ephemeris files, unlike those for the Orbiter, are limited to coverage of those periods during which the SPAS platform is free-flying. Their computation is based on Orbiter-SPAS relative position data from the RELBET Tapes.

243

Table 9.6. <u>IBSS Ephemeris File Header Record</u>

WORD NUMBER	PARAMETER
1 - 4	Start Time for File Day, Month, Year, UT (SEC)
5 - 8	End Time for File Day, Month, Year, UT (SEC)
9	Duration
10	Data Rate
11	Number of History Phrases (N)
12	40 Character Header Blocks from Tapes • PATH Tape for Orbiter Ephemeris • Both PATH and RELBET Tapes for SPAS Ephemeris
12 + N	20 Character Date and Time of File Generation

Table 9.7. SPAS Ephemeris File Parameters

WORD NO.	PARAMETER	COORD. SYSTEM	UNITS
1	Day of year		days
2	Calendar month		months
3	Calendar day		days
4	Calendar year		years
5	Hour of day		hour
6	Minute of hour		min
7	Second of minute		sec
8	GMT seconds		sec
9	MET		sec
10	Orbit Number		
11	X coordinate of position vector	ECI	km
12	Y coordinate of position vector	ECI	km
13	Z coordinate of position vector	ECI	km
14	X coordinate of velocity vector	ECI	km/sec
15	Y coordinate of velocity vector	ECI	km/sec
16	Z coordinate of velocity vector	ECI	km/sec
17	SPAS altitude	GEODETIC	km
18	SPAS distance from center of earth	km	
19	SPAS velocity	ECI	km/sec
20	Geocentric latitude	GEOCEN	deg
21	Geodetic latitude	GEODETIC	deg
22	Longitude (+E)	GEOCEN	deg
23	Right Ascension of Greenwich	ECI	deg
24	SPAS Local time	GEOCEN	hours
25	Geomagnetic local time	GEOM	hours
26	X coordinate of magnetic field	ECI	gammas
27	Y coordinate of magnetic field	ECI	gammas
28	Z coordinate of magnetic field	ECI	gammas
29	Geomagnetic coordinate - B	B, L	gammas
30	Geomagnetic coordinate - L	B, L	EMR
31	Geomagnetic latitude	GEOM	deg
32	Geomagnetic longitude	GEOM	deg
33	Magnetic inclination	IBSS LVLH	deg
34	Magnetic declination	SPAS VEN	deg
35	Invariant latitude	B, L	deg
36	Corrected geomagnetic latitude	CGM	deg
37	Corrected geomagnetic longitude	CGM	deg
38	Corrected geomagnetic local time	CGM	hours
39	Solar declination	ECI	deg
40	Solar right ascension	ECI	deg
41	Solar disk semi-diameter		deg
42	Solar zenith angle	SPAS VEN	deg
43	Solar azimuth angle	SPAS VEN	deg
44	Sun/shade indicator		deg
45	X coord. SPAS relative to Orbiter	ECI	km
46	Y coord. SPAS relative to Orbiter	ECI	km
47	Z coord. SPAS relative to Orbiter	ECI	km
48	X coord. SPAS in Orbiter LVLH	LVLH	km
49	Y coord. SPAS in Orbiter LVLH	LVLH	km
50	Z coord. SPAS in Orbiter LVLH	LVLH	km
51	Range of SPAS from Orbiter		km
52-64	Vacant for future parameter storage (TBD)		

245

9.2.1.1 Ephemeris Processing System

The system is designed for operation on the VAX 8650 mainframe system at GL. The processing software system is integrated and designed to produce ephemeris files with a minimum of operator intervention. The process generates files in a single computer run using the following auxiliary, non-concurrently created, on-line files:

- A file of time-sequenced sets of position/velocity vectors.
- A high accuracy daily solar ephemeris file spanning the days to be processed must be previously created.

Data from these files are used for initiation and input to new processing runs.

9.2.2 Developmental Approach

The CRRES ephemeris program and other software packages and techniques in current use at GL form the basis for the IBSS ephemeris processing system. The orbital, magnetic field, L-shell routine, and astronomical ephemeris programs have accuracies suited to the requirements of the IBSS mission as specified in the IBSS Data Management Plan [McInerney, 1987].

The satellite orbit generation system was evaluated by comparison with benchmark runs from highly accurate orbit determination programs. The solar ephemeris accuracy was evaluated, and high speed routines were developed to take advantage of the fact that limited time spans are processed during each IBSS ephemeris file generating run.

Magnetic field model and parameter generation algorithms were investigated for accuracy and computation speed. The process of field line tracing and integration associated with the traditional computation of the L-shell parameter [McIlwain, 1961] is computationally burdensome. An efficient alternative is the method L-shell interpolation tables provided by Cain [Cain]. It was of particular interest to evaluate the accuracy of this attractive alternative.

Subjects investigated during the development of this processing system were:

- orbital ephemeris accuracy
- astronomical ephemeris
- magnetic field model
- magnetic field related parameters
- time interval between successive computations
- system performance

Special attention was given to the determination of the magnetic shell L parameter, due to the availability of a new rapid interpolation scheme for calculating this parameter. The classical method for computing L is that presented by McIlwain [1961]. Unfortunately this method is computationally burdensome. To alleviate that problem, Kluge [1972] and Kluge and Lenhart [1972] developed an interpolation scheme for rapid computation of L.

The rapid interpolation scheme proved useful during the epoch through which the geomagnetic model from which the tables were computed remained valid. Thereafter, the method lost validity and fell into disuse. Recently Cain [Cain] has revived the method by recalculating the interpolation tables using current geomagnetic models. This scheme was validated and was incorporated to obtain L-shell for IBSS ephemerides.

246

9.2.3 Description of Ephemeris File Processing System

The only data input needed to generate the Ephemeris File parameters are position and velocity vectors, solar ephemeris, and the input data file. All the parameters in Table 9.7 are obtained using well-tested satellite generation, solar astronomical ephemeris, and magnetic field model. These parameters are calculated at the level of accuracy required to create the Engineering Unit and Product Associated Data Bases for subsequent IBSS investigations. The parameter generation rate is specified on the input data file by the user. The criterion for this selection is that linear interpolation between successive ephemeris file data values should yield adequate precision at intermediate points. Figure 9.2 gives a flow chart of the overall processing system.

9.2.3.1 Satellite Ephemeris Routine & Use of Vector Sets

Generation of quick-look orbit is performed using a reduced but compatible version of program LOKANGL, which is regularly used at GL. Position/velocity vector sets will comprise the satellite element inputs. Upon its release, the PATH tape will constitute the source of high precision vector sets. Alternative sources of position/velocity data, which may be used prior to release of the PATH tape, include individually furnished vector sets, the NASA Quick Look Ancillary Data Tape (content and format TBD) and possibly raw tracking data. For these quick look types of data, transmittal errors as well as inconsistencies that show up during trend analyses must be screened and resolved by the orbital analyst.

Trajectory generation using LOKANGL is performed exclusively by interpolating between element sets, i.e. no extrapolated predictions are made. The orbital ephemeris program includes the first two zonal perturbations J_2 and J_3 of the Earth's geopotential. The program converts position-velocity elements to mean elements based on this geopotential model, interpolates to obtain the mean elements for any desired epoch, and reconverts to osculating elements and position-velocity using the same geopotential model in reverse.

9.2.3.2 Operational Procedures for Handling "Quick-look" Vectors

Quick-look Vector sets will be entered, edited, and evaluated by the analyst responsible for orbit analysis, prior to being saved in the vector library. The orbital analyst will maintain plots of the Keplerian values to allow quick verification of reliability of the approved vector sets. The quick-look vector set data base will be maintained on the computer system permanent storage until these data are superseded by the PATH Tapes. The ephemeris generating system will utilize all valid quick-look state vectors in the library to calculate the orbits over the time period covered by these vectors.

The vector library should exclusively contain the vectors employed for the actual ephemeris files generated or approved for generation. Therefore, if the orbital analyst finds that previously approved vector sets should be revised, but that ephemeris files have been generated and released over the affected time span, a decision to update the vector library and regenerate the ephemeris should be implemented only after joint approval by the orbital analyst and the contractor generating the ephemeris files.

9.2.3.3 Solar Ephemeris

Astronomical ephemeris calculations are performed consistent with equations and procedures defined in the Astronomical Almanac [1985]. They yield extremely accurate results.
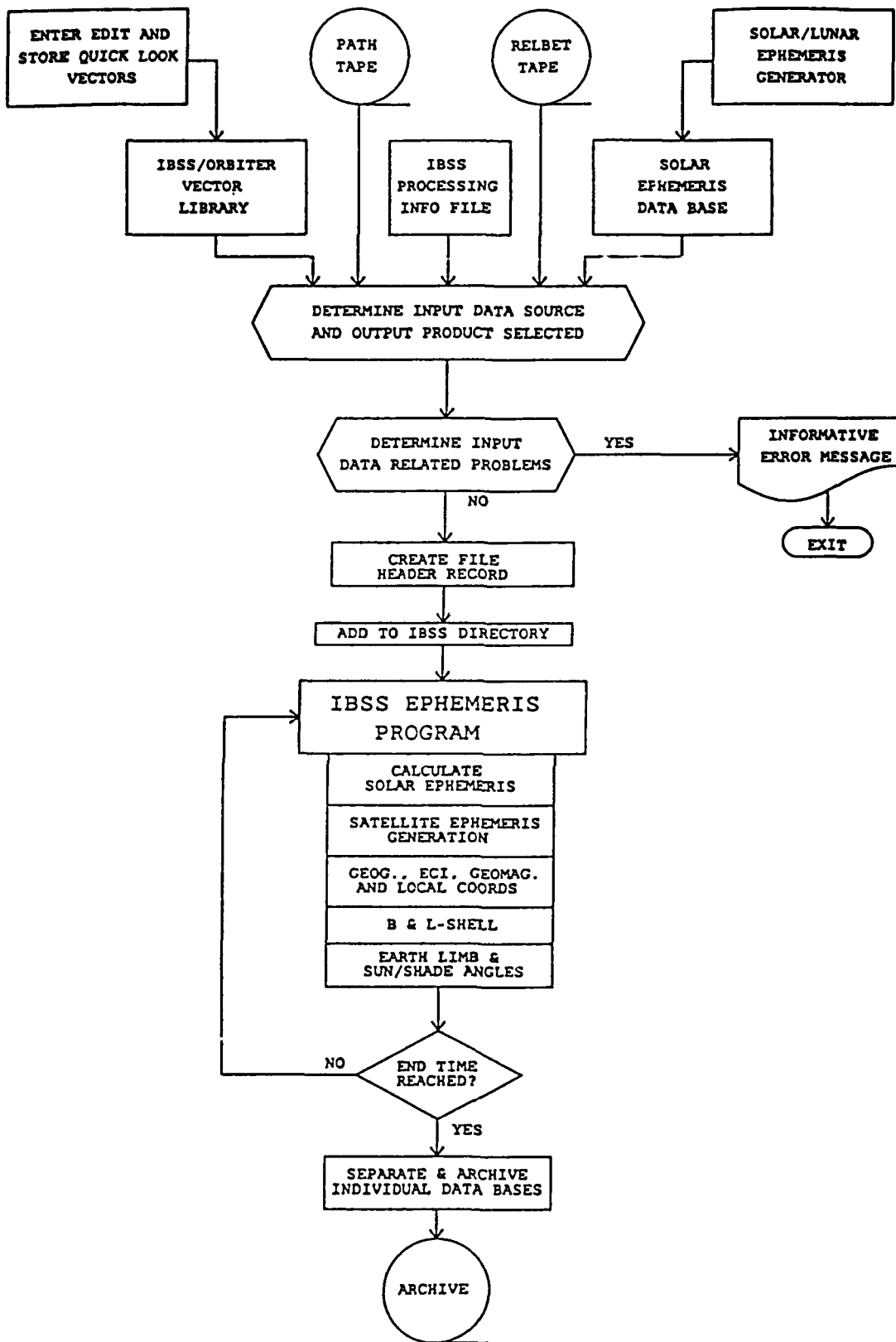
Figure 9.2   IBSS Ephemeris File Processing System

248

Pre-generated results are obtained by an accurate ephemeris program, SLEPHEM, at 0 hr. UT for each day. Interpolation using cubic polynomials then provides a high speed, high accuracy solar ephemeris for any arbitrary time, so that the maximum solar ephemeris error is less than 1 sec. of arc.

9.2.3.4 Calculation of Solar Eclipsing (Sun/shade indicator)

As an indicator of Sun/shade conditions at the vehicle, the angle is calculated between the line to the center of the solar disk and the vehicle's earth horizon. The calculation takes the Earth's oblateness into account, as described in Section 9.1 of this report. For positive values of this angle, the center of the disk is above the horizon (i.e., sunlight); for negative values, below (i.e., shade). The solar elevation angle is computed relative to an oblate earth by using a spherical Earth solution to initialize a Newton iteration scheme. The idea is to find the point H on the surface such that the observer-H line is tangent to the surface and such that the surface normal at H lies in the observer-H-Sun plane. The elevation angle is then the angle between the observer-H line and the observer-Sun line. Let H have coordinates x,y,z the observer x_o,y_o,z_o and let $u=(u_x,u_y,u_z)$ be the components of a unit vector in the observer-Sun direction. If $N = (n_x, n_y, n_z)$ is the surface normal at H then the equations are,

1. $(1-e^2) x^2+(1-e^2)y^2 + z^2 = b^2$ (H lies on surface)
2. $(x-x_o)n_x+(y-y_o) n_y + (z-z_o) n_z = 0$ (H-0 tangent to surface)
3. $(u \times N) \bullet (H - 0) = 0$ (H-0 in plane of u,N)

In this equation b is the Earth's semi-minor axis and e is the eccentricity. If H is transformed to polar coordinates and (1) is used to eliminate u then the system becomes

$$(1-e^2) (x_o\cos\theta + y_o \sin\theta) \cos\phi + z_o \sin\phi - b(-e^2\cos^2\phi)^P = 0$$

$$(A\cos\phi \cos\theta + B\cos\phi \sin\theta + C\sin\phi)(1-e^2\cos^2\phi)^P + (b/2)\sin(2\phi)(D\cos\theta+E\sin\theta) = 0$$

where,

$A = (1-e^2) (u_z y_o - u_y Z_o)$
$B = (1-e^2) (u_x z_o - u_z x_o)$
$C = u_y x_o - u_x y_o$
$D = -e^2 u_y$
$E = e^2 u_x$

These equations are solved for θ, ϕ using Newton iteration.

9.2.3.5 Magnetic Field Models

The main magnetic field model consists of the IGRF 85 internal field model with temporally varying coefficients. (For orbital locations within $2R_E$, external field contributions are negligible, and those calculations are not included.) Computation of the internal field, in the case of the IGRF 85 model, involves calculation of an 11x11 spherical harmonic field.

249

A dipole field model, based on the first order coefficients of the IGRF 85 model, is employed to determine Magnetic coordinates and Magnetic Local Time. The geographic coordinates of the magnetic poles are determined from the fundamental components of the IGRF 85 internal field propagated to the appropriate epoch, and the direction of the dipole axis is obtained as described in Section 9.2.3.3 of the IBSS Data Processing Product Specification.

9.2.3.6 Choice of IBSS Ephemeris Time Step Size

The choice of time interval for IBSS ephemeris computations is based on the criterion that the interval should be the maximum value which guarantees the requisite inter-interval accuracies when linear interpolation is employed. The evaluation proceeds as follows:

Assuming linear interpolation is used on IBSS ephemeris data gives,

$$\hat{y} = y_i + \frac{y_{i+1} - y_i}{t_{i+1} - t_i} (t - t_i) \quad \text{for } t_i \le t \le t_{i+1}$$

for any component y of the data base. The error is then,

$$e = |y(t) - \hat{y}(t)|$$

If $y(t)$ and y_{i+1} are expanded about t_i, e becomes,

$$e = |(1/2) y_i''.(t - t_i)^2 - (1/2) y_i''(t - t_i)(t_{i+1} - t_i) + O(y_i''')|$$

Assuming the third derivative term are small and assuming, without loss of generality, that

$$y_i'' \ge 0,$$

gives

$$e \le (1/8) y_i'' (t_{i+1} - t_i)^2$$

An absolute error limit of e can be assured provided

$$t_{i+1} - t_i \le (8 e/y_i'')^{1/2}$$

In Table 9.8 values for max $| y_i'' |$ are given for each of the data base parameters. These were determined by computing second derivatives at one-minute intervals for a 90 minute orbit and taking maximum values.

9.2.3.7 Numerical Validation of L-Shell Interpolator

A two-step procedure was employed to validate Cain's L-shell interpolation procedure [Cain]. In the first step, the interpolator scheme and an accurate routine based on the McIlwain field line tracing approach were applied separately, to a common model of the field: Cain's 1990 model [Cain]. A second test substituted IGRF 85 (updated to 1990) for Cain 1990. The close agreement of the results in both cases (less than 1% error), verified the interpolation scheme.

250

Table 9.8 Time Step Size Error Analysis

Parameter	second derivative	30 sec. error	60 sec. error
x-coord.	$.79 \times 10^{-2}$ km/s^2	.89km	$.36 \times 10^{1}$km
y-coord.	$.70 \times 10^{-2}$ km/s^2	.79km	$.32 \times 10^{1}$km
z-coord.	$.68 \times 10^{-2}$ km/s^2	.77km	$.31 \times 10^{1}$km
x-vel.	$.91 \times 10^{-5}$ km/s^3	$.10 \times 10^{-2}$ km/s	$.40 \times 10^{-2}$km/s
y-vel.	$.81 \times 10^{-5}$ km/s^3	$.91 \times 10^{-3}$ km/s	$.36 \times 10^{-2}$km/s
z-vel.	$.78 \times 10^{-5}$ km/s^3	$.88 \times 10^{-3}$ km/s	$.35 \times 10^{-2}$km/s
alt.	$.29 \times 10^{-4}$ km/s^2	$.33 \times 10^{-2}$ km	$.13 \times 10^{-1}$km
radius	$.63 \times 10^{-5}$ km/s^2	$.71 \times 10^{-3}$ km	$.28 \times 10^{-2}$km
velocity	$.13 \times 10^{-7}$ km/s^3	$.15 \times 10^{-5}$ km/s	$.60 \times 10^{-5}$km/s
geoc. lat.	$.89 \times 10^{-4}$ deg/s^2	$.10 \times 10^{-1}$ deg	$.40 \times 10^{-1}$deg
geod. lat.	$.89 \times 10^{-4}$ deg/s^2	$.10 \times 10^{-1}$ deg	$.40 \times 10^{-1}$deg
east lon.	$.79 \times 10^{-4}$ deg/s^2	$.88 \times 10^{-2}$ deg	$.35 \times 10^{-1}$deg
lt. geomag.	$.11 \times 10^{-4}$ /s	$.12 \times 10^{-2}$ s	$.48 \times 10^{-2}$s
local time	$.53 \times 10^{-5}$ /s	$.60 \times 10^{-3}$ s	$.24 \times 10^{-2}$s
Bx	.23nT /s^2	26nT	$.10 \times 10^{3}$nT
By	.24nT /s^2	27nT	$.11 \times 10^{3}$nT
Bz	.23nT /s^2	26nT	$.10 \times 10^{3}$nT
B	.11nT /s^2	12nT	$.48 \times 10^{2}$nT
L	$.49 \times 10^{-4}$ er/s^2	$.55 \times 10^{-2}$ er	$.22 \times 10^{-1}$er
geomag. lat.	$.13 \times 10^{-3}$ deg/s^2	$.15 \times 10^{-1}$ deg	$.60 \times 10^{-1}$deg
geomag. lon.	$.16 \times 10^{-3}$ deg/s^2	$.18 \times 10^{-1}$ deg	$.72 \times 10^{-1}$deg
mag. inc.	$.22 \times 10^{-3}$ deg/s^2	$.25 \times 10^{-1}$ deg	.10deg
mag. dec.	$.66 \times 10^{-3}$ deg/s^2	$.74 \times 10^{-1}$ deg	.30deg
inv. lat.	$.36 \times 10^{-3}$ deg/s^2	$.41 \times 10^{-1}$ deg	.16deg
cor. geom.lat.	$.11 \times 10^{-3}$ deg/s^2	$.12 \times 10^{-1}$ deg	$.48 \times 10^{-1}$deg
cor. geom.lon.	$.21 \times 10^{-3}$ deg/s^2	$.24 \times 10^{-1}$ deg	$.96 \times 10^{-1}$deg
cor. geom.lt.	$.14 \times 10^{-4}$ /s	$.16 \times 10^{-2}$ sec	$.64 \times 10^{-2}$sec
sol. zen. ang.	$.19 \times 10^{-3}$ deg/s^2	$.21 \times 10^{-1}$ deg	$.84 \times 10^{-1}$deg
sol. lon.	$.82 \times 10^{-12}$deg/s^2	$.92 \times 10^{-10}$deg	$.37 \times 10^{-9}$deg
sol. rt. asc.	$.37 \times 10^{-12}$deg/s^2	$.42 \times 10^{-10}$deg	$.17 \times 10^{-9}$deg
sol. incl. ang	$.19 \times 10^{-3}$ deg/s^2	$.21 \times 10^{-1}$ deg	$.84 \times 10^{-1}$deg
sol. az. ang.	$.36 \times 10^{-3}$ deg/s^2	$.41 \times 10^{-1}$ deg	.16deg
sol. declin.	$.67 \times 10^{-12}$deg/s^2	$.75 \times 10^{-10}$deg	$.30 \times 10^{-9}$deg

9.2.3.8 Organization and Operation of Processing System

The ephemeris and model magnetic field computational system allows for ease of operation by the user. Figure 9.2 shows the software system's functional flow and the data bases required to calculate the necessary parameters.

The software system uses permanent disk storage to temporarily archive the ephemeris and model field data bases. All data bases will be periodically archived to magnetic tape using standard disk archiving techniques. Archiving should not be performed until the ephemeris file product has been verified for release by the orbital analyst.

9.2.3.9 Data Bases

Ephemeris data files are stored as permanent disk files for access by other software packages that require these files for creating product associated data bases, and may be archived as required onto magnetic tape. Other on-line files are used during execution of the processing system.

9.2.3.9.1 Quick look State Vector Library

This is a sequential data base of acceptable values of X, Y, Z, X-dot, Y-dot, and Z-dot. To qualify for release by the orbital analyst, these vector sets must be within prescribed tolerance and trends based on evaluation of the equivalent Keplerian elements. The vector format is compact enough so that the elements can be maintained on-line with a minimal amount of storage. Accepted elements may be periodically added to the vector library, and may also be archived as required.

9.2.3.9.2 Solar Ephemeris

This data base is generated periodically as additional time spans are required. Each logical record of the data base contains values for the year, the day number, and the corresponding solar position for 0 hours UT. The position of the Sun is stored as right ascension, declination, and distance from center of Earth. This daily record format can accommodate all the data without presenting a computer storage problem.

9.2.3.9.3 Input Information Data Base

This data base contains the start and end times for processing and data rate. This file will initially be created by the orbital analyst. Time interval is a user controllable option. For quick-look runs, launch date and time will be included to facilitate computation of mission elapsed time.

9.2.4 Implementation and Performance

Software for the IBSS Ephemeris File Generation System is written in Fortran V, and is designed to operate on the VAX 8650 mainframe computer at GL. CPU memory and mass storage requirements are modest:

- The program is composed of the basic Orbit Generator, the Solar Ephemeris, Magnetic Field Model, L-shell Calculator, and the associated coordinate conversion routines.
- The program requires on-line availability of relatively small solar ephemeris and vector set files during execution. The major mass storage requirement should be to keep completed ephemeris files resident, for convenient access by analysts.

Data for each file consists of a header record followed by an arbitrary number of data records, each containing 512 bytes. Records are written blocked, with the header record followed by 64 (8-byte) real data words per block. Each record contains all ephemeris data computed for a particular sample time.

The total computation time per record (i.e., per time sample) is less than 0.1 CPU seconds on a VAX 8650.

9.3 SIMULATION OF CRRES ATTITUDE DATA

In the course of development and testing of large software systems which manipulate and analyze data in complicated ways, it is essential that suitable test data is available. This is especially true in the case of attitude determination software because these algorithms involve sometimes delicate analysis of instrument readings of Sun and Earth positions and magnetic field values. To aid in the development of this system by Space Applications Corp., and to supplement the testing program of the completed software, we have performed detailed simulations of the CRRES attitude data for several orbit scenarios. In this section, we briefly describe the test orbits and the simulation scheme. Details of the simulation are given elsewhere [McNeil and McInerney, 1988].

9.3.1 Test Orbits

The object of the simulation of attitude test files was to provide, as much as possible, a thorough test of the operation of the Attitude Determination System, Figure 9.3, over a wide range of conditions. For this, seven orbits were chosen for simulation. Two of these orbits were from the Low Earth Orbit (LEO) phase. The first was for a nominal case with no special maneuvers and the second added a simulated canister release, modeled by an instantaneous change in the spin rate. The next four orbits were Geosynchronous Transfer Orbit (GTO) types. The first two of these are nominal orbits with an eclipse at apogee and perigee respectively. The third includes a simulated attitude adjustment which is modeled by a linear change in the declination of the spin axis by 15° followed by a simulated nutation with decay time of about ten hours. The sixth orbit included a change in the horizon sensor to other than its nominal spin plane position. The seventh orbit was a simulated LASSII type, which included only data for altitudes less than 5000 km.

253
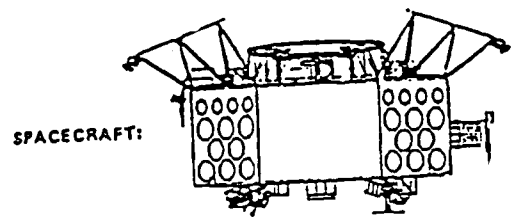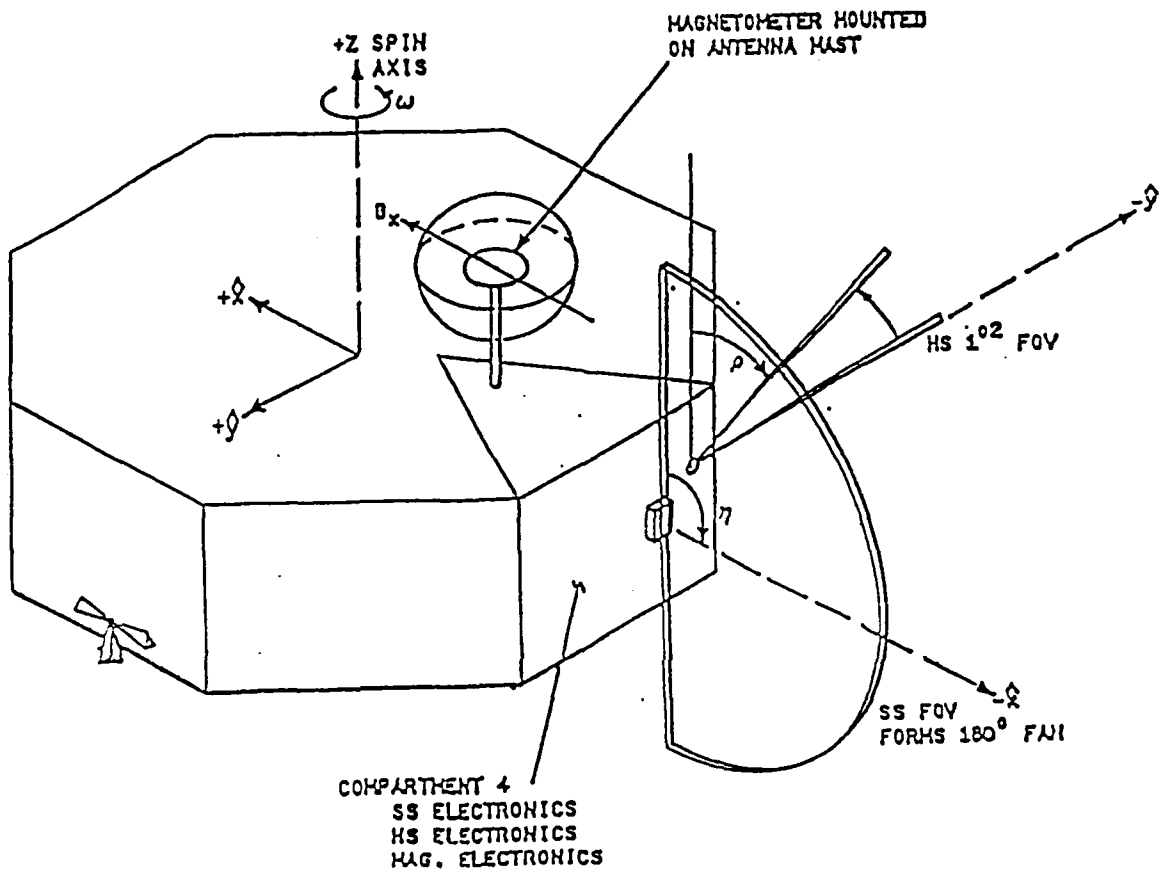
Figure 9.3. CRRES Attitude Determination System

254

9.3.2 Simulation Methods

The first step in the simulation was to model the positions of the CRRES Spacecraft axes as a function of time in ECI coordinates. Routines were constructed that would give these three vectors at arbitrary times to facilitate the calculation of instrument data. Secondly, the position of the satellite, Earth and Sun had to be available at arbitrary times. For this, these data were interpolated from the CRRES Ephemeris File by fifth-degree polynomials. The instruments simulated were three in number, the Sun sensor, the Earth horizon sensor and the engineering magnetometer. To simulate the response of the Sun sensor to the Sun, the Sun was considered to be a single point in the sky. At each time step in the simulation, it was determined whether the Sun passed through the field of view of the sensor and, if so, the precise time of crossing was calculated by bi-section and the declination angle was determined. The same method was used to calculate the leading and trailing edge of passage of the Earth through the horizon sensor field of view. The Earth's CO_2 layer, to which the horizon sensor responds, was modeled by a constant altitude of 40 km and the Earth itself was modeled as the standard ellipsoid. The magnetometer was included, giving not only the magnitude of the external field at the required times but also the time of crossing of the x-axis sensor through the magnetic equator. This time was found by bi-section as were the other times above. Eclipses were modeled by turning off the Sun crossing time calculation.

9.3.3 Construction of the Raw Attitude Data File

The final task in the simulation involved calculation and presentation of the data items described above in as close a manner as possible to what they actually would be in the data file to be read by the Attitude Determination System. This involved an accurate modeling of the telemetry stream from each instrument. For each major frame of data (4.096 sec.) the readout times of each of the crossing times had to be considered and the time intervals examined for crossings were adjusted appropriately to correspond to what would have been sensed by the instruments between the previous readout and the present. The magnetometer values were also adjusted to correspond to the field at actual time of readout. Several other bit flags were also appropriately set. Times and other values were transformed to their appropriate binary representations by calibration factors or encoding algorithms.

9.3.4 Conclusion

Overall, the effort to produce mock attitude data files was quite successful in catching several errors during the development of the Attitude Determination System. The effort also helped to insure the integrity of the system once delivered and the simulation tools developed in the process continue to prove valuable in the generation of simulated data sets for other CRRES instruments.

9.4 COMMON DATA FORMAT STUDY

In connection with the large data set which will come from CRRES, generalized data formats were assessed to see which one, if any, will be suitable to contain this data base. An evaluation of two such data formats has been done. The National Space Science Data Center has developed a data format system called the Common Data Format (CDF) which is designed to be useful to many different disciplines and flexible enough to accomodate many different types of data sets. The currently available VAX/VMS Fortran Version 1.0 was compared to the Flat Data Base Management System (FlatDBMS) from Stanford University. Both of these systems were compared with Fortran direct access files with various record structures.

The storage space required by the two packages is comparable to that of the Fortran direct access files and not greatly in excess of that required by the data itself (Table 9.9). Of the two packages, CDF is found to be more flexible and is adaptable to a broader range of data sets (multi-dimensional as well as flat files -- see Table 9.10). However, FlatDBMS is faster to process the data (Table 9.11). If CPU time is truly critical, one should probably use a highly specific Fortran direct access structure and forego a generalized data structure altogether. The speed of the CDF will be improved following the implementation of the C version of the code which will allow random aggregate access of the data. This version will retain Fortran bindings so that the routine may still be called within Fortran source code.

In this evaluation, an unbiased comparison based on storage and CPU requirements was done. However, one should keep in mind that there are several attributes of a common data structure which are not so readily measured, for example: a self-documenting data structure, a capability for handling diverse multi-dimensional data, and facilitating data exchange and software development. These too need to be considered when making a decision as to whether or not a common data structure should be used to organize the data.

9.5 SUATEK INTERACTIVE GRAPHICS

SUATEK is an interactive graphics program written to satisfy requirements for flexible data presentation and evaluation by researchers. The data must be in a specified standard format, with no basic length limit, and can be flexibly plotted and edited without further programming. SUATEK originated in the late 70's as a result of the recognized need for this type of data manipulation and plotting system. Specifications were formulated by LCY in order to support GL researchers, and enhancements continued to evolve over the years while accommodating numerous applications in GL research [Ziemba et al., 1979]. The more universal requirements became incorporated as standard features or options. The package remains available on the CYBER under NOS [Bhavnani et al., April 1989] and NOS/VE, on the VAX and compatible computers, and on the RIDGE mini-computer.

Recently, the increasing availability of new technology in the form of powerful personal computers with good graphics capability, coupled with convenient local availability of high resolution dot matrix and laser printers provided the impetus for hosting the SUATEK package onto PCs. A major obstacle was the system problem of supporting an assortment of graphics boards and printers, and this was resolved by using a graphics utility package *GraphiC* (written in C), from Scientific Endeavors Corp. of Kingston, TN [1989]. This package includes many features tailored for the microcomputer, and developments were possible which compared favorably with the Tektronix 4014/main frame environment.

Table 9.9. Storage Comparisons for files with a Flat Structure

File Type	Storage Blocks	Overhead
Data alone	372	-
Fortran file	388	16
FlatDBMS file	372	0
CDF 22 variables	390	18
CDF 4 variables	569	197
CDF 4 optimized	375	3
CDF 2 optimized	373	1

Table 9.10 Storage Comparisons for files with a Multi-dimensional Structure

File Type	Storage Blocks	Overhead
Data alone	2407	-
CDF 26 variables	24174	21767
CDF 26 optimized	2415	8
Fortran File 1	2407	0
Fortran File 2	3789	1382
Fortran File 3	2891	484
Fortran File 4	2881	474

Table 9.11 Timing Comparisons for files with a Flat Structure

	CPU(sec)	BUFIO	DIRIO	FAULTS
Flatfile:	17.66	37	79	764
	17.32	37	79	758
	17.16	37	79	760
CDF 4 optimized:	43.69	52	246	1041
	43.70	52	242	892
	43.69	52	243	884
Fortran Direct Access	18.72	35	75	726
(1 record/time sample):	18.63	35	75	718
	18.56	35	75	730
Fortran Direct Access	34.24	45	1511	721
(22 records/time sample):	34.11	45	1512	718
	33.52	45	1511	725

A site license was obtained for use of *GraphiC* at GL, and work was directed to develop an interface to an equivalent of the CYBER graphics library TEKSIM. The SUATEK Fortran code could then be installed directly, without the need for recoding in C. Some special features that were unavailable heretofore were developed, including ASCII, binary or TKF metacode file input, improved cross-hairs and interaction, an annotation capability with note saving and Un-Do option, generation of SUSPEC files, stacking of printer plot files, and some operating system convenience facilities.

Problems remain, including the slow learning curve of would-be users, and the need to continue developments in the face of unpredictable behavior of some hardware/software combinations. Part of this effort has been the development of a User Guide [Bhavnani et al., June 1989] and Distribution Disk with some tutorial material. Utilization of SUATEK on some extensive data bases was not achieved during this period, and this objective remains to be emphasized. Feature improvements, such as annotation, proved attractive, and the development of similar features on the main-frames and the RIDGE were initiated, however this section describes mainly the PC version of SUATEK.

9.5.1 Generating a Typical SUATEK File

SUATEK requires that your input data file conform to the simple but rigid specifications below. The SUATEK format is essentially "flat file" in nature, i.e. except for a few control and labelling records, all subsequent records are uniform in length, and consist of one value for each of "NOV" variables. Binary or ASCII files are allowed:

SUATEK File Format

SUATEK format files consist of one to three header
records describing the data, followed by uniform data
records, each consisting of one real number per variable.

Generally these files result from varied analysis or
processing procedures, and are readily manipulated and
plotted using SUATEK and associated programs.

A binary SUATEK file (TAPE1) may be accessed as follows:

```
READ(1) NOV,MN,LAE,MMA,((LBL(I,J),I=1,32),J=1,NOV)
IF(LAE.NE.0) READ(1) ((MLBL(I,J),I=1,52),J=1,LAE)
IF(MMA.NE.0) READ(1) ((DMNX(I,J),I=1,2),J=1,NOV)
READ(1) (D(J),J=1,NOV)    ..... all subsequent records
```

Where

NOV	-	Number of variables
MN	-	Flag (Presently unassigned)
LAE	-	1 to 3 if 'MLBL' header labels follow
MMA	-	1 if plot Min-Max ranges follow
LBL	-	32 character alpha-numeric label per variable
MLBL	-	up to three 52 character labels (if LAE≠0)
DMNX	-	Min and Max plot range per variable (if MMA=1)
D	-	Array of real numbers
		NOTE ... special reserved values
	-	9.0E35 denotes a deliberately deleted value, for possible subsequent replacement.
	-	9.9E35 denotes an ignored value, eg. sample not present, transparent to SUATEK

9.5.2 Description of the SUATEK Software Package for the PC

Files provided on the distribution disk include:

1) SUATEK.EXE	-	the SUATEK executable module
2) CONFIG.GPC	-	copy of appropriate CONFIG.___ file for your installed graphics card
3) PRINTER1.PRN	-	copy of appropriate ____.PRN file for active printer of your choice
4) CONFIG.PEN	-	for vector mode plotter or laser
5) ******.FNT	-	graphics text font files
6) HDR.POS	-	PostScript file header
7) SAMPLE.DAT	-	sample data in SUATEK/ASCII format
8) TAPE1.BIN	-	binary equivalent of SAMPLE.DAT (created initially by SUATEK)
9) SUSPEC.DAT	-	sample auxiliary SUATEK data entry
10) METAFILE.TKF	-	sample created for a typical plot
11) SUNOTE.DAT	-	sample annotation data file

SYSTEM REQUIREMENTS

SUATEK is designed for use on IBM compatible personal computers running under the MS-DOS operating system. A hard disk and at least 512K of memory are required. An 8087 or 80287 coprocessor is used, if installed, resulting in a substantial increase in speed.

9.5.3 SUATEK Plot Control Facilities

The plotting options fall into one of three categories:

1) Plot Presentation Control
This relates to presentation of the data, including number of variables to be plotted, linear or log axes, lengths of axes, etc.

2) Data Handling Options
Sorting, editing, curve fitting, smoothing, and some computational features may be activated by setting the appropriate flags to non-zero.

3) Convenience Utilities
Allow automated entry instead of repeated keying, and an option to terminate plotting in midstream.

9.5.3.1 SUATEK Plot Control Parameters

The following parameters control the presentation of the data, including number of variables to be plotted, axes lengths, etc.

NXV	-	Number of the X-variable
NY1...NY4	-	Number of the Y-variable (up to 4 per plot)
XL	-	Length of X-axis in inches
Y1L...Y4L	-	Length of Y1...Y4 axis
XMIN,XMAX	-	Leftmost,rightmost ends of X-axis
		(power of 10 when using log scale)
Y1MN...Y4MN	-	Bottom end values of Y1...Y4 variables
		(power of 10 when using log scale)
Y1MX...Y4MX	-	Top end values of Y1...Y4 variables
		(power of 10 when using log scale)
XOFF	-	Left(-ve) or right(+ve) X-axis offset in inches
Y1OF...Y4OF	-	Down(-ve) or up(+ve) Y1...Y4-axis offset
IPLX	-	X-axis scale linear(0) or log(1)
		2 starts linear scale from XMIN marked as "0"
IPL1...IPL4	-	Y1...Y4 scale and plot option
		linear(0,2,4) or log(1,3,5) or bi-polar (-1,-3,-5)
		0,1 produces symbols at data points
		2,3 produces a line through data points (default)
		4,5 produces connected symbols through data points
IMORX	-	Overlay plots for original independent Y-variable
		and additional X-variables with existing X-Y axes
		(up to 3 allowed, selected as NX1, NX2, NX3)
NX1...NX4	-	Number of extra X-axis variable
		it IMORX=0, draw extra X-axes only
		if IMORX=1, overlay using existing X-axis
NTAG	-	Marks plot at specified modulo of variable NTAG
		Prompting for modulo and tolerance occurs
ILBL	-	Revise plot axes and header labels
		Prompting for revision occurs
IRANGE	-	Revise X and Y plot min-max ranges
		Default is the plot frame ranges
INOTE	-	Enable interactive annotation upon
		completion of the plot

9.5.3.2 SUATEK Data Handling Options

"N" options are those that generally take on numeric values,
  and plotting proceeds without interactive prompting.
"I" options are flags: off when 0, on when 1 in most cases,
  so that interactive prompting occurs before plotting.
NOTE: Options continue in development; some may be obsolete.

IST	-	Start reading from this record number (def=1)
ISP	-	Stop reading data after this record (def=1)
IREP	-	Repeat factor, read every "IREP"th record only (default=all=1)
NDPN	-	Number of dependency parameters (up to 5 allowed) IDP1,P1MN,P1MX..... for each must be specified
IDP1...IDP4	-	Number of the dependency variable
P1MN...P4MN	-	Min acceptance range for variable IDP1...IDP4 for corresponding data to be plotted
P1MX...P4MX	-	Max acceptance range for variable IDP1...IDP4 for corresponding data to be plotted
ICOMB	-	(1)= linear combination of up to 4 variables (D(NV)*FACTOR + ...)
ICOMB	-	(2)= exponential product of up to 4 variables (D(NV)**FACTOR * ....) NV=0 defines additive or multiplicative constant. Prompting for NV,FACTOR occurs
IPARM	-	Overlay plots for specified ranges of parametric variable. Use "NDPN" or prompting to fix other significant variables. Includes option to:
ISORT	-	Sort up to 512 data points on X(=1) or Y(=2)
IRAV	-	Running average for window of 'N' data points
IPOLF	-	Fit N'th order polynomial to data in plot range
ICURF	-	Running cubic fit for window of 'N' data points
IEDIT	-	Delete, replace, interpolate, or smooth data (value of "delete variable" is set to -9.E35) Prior to editing, prompting guide is displayed
IMERG	-	Replace edited and curve fit Y-variable results Option to merge is offered after plotting
ICORR	-	Find correlation coefficient between Y variable and the variable number specified per request
IDER	-	Find first or second derivative of 'NY1' curve using results of polynomial or curve fit, with inverted and/or normalized(0-100) scale options

262

9.5.3.3 SUATEK Convenience Utilities

NSPEC	Update Plot Spec from 'NSPEC'th record on pre-prepared auxiliary file. The name of this ASCII file is requested once only. Records on this file are as if entered from the keyboard, separated by "/" in column 1. (eg. SUSPEC.DAT on the distribution disk) After updating NSPEC is reset to "0"
SAVE	Allows the creation of a "SUSPEC" file from the current plot specification.
NCHK	Option to abort after plotting 'NCHK' points Prompting to continue or abort occurs
IVARD	Allows parameter control ("NDPN" option) information to be read from auxiliary file "SUVARD" while plotting, thus avoiding the need to respond to prompts.
ISING	Single plot (1-4) from multiple Plot Spec
SHELL	Allows the user to return to DOS temporarily without terminating the program. Type "EXIT" to return to SUATEK.

9.5.3.4 Cross Hair Operation

The cross hair functions are used during editing and annotation to provide the user with a means of specifying coordinate positions. Cross hair motion may be controlled either with the cursor keys or with a mouse. Several additional operations are available:

ALT-I	Display cross hair coordinates in inches.
ALT-U	Display cross hair coordinates relative to the user-defined axes. During the annotation process this option indicates the cross hair position in Tektronix 4096 x 3120 coordinates.
ALT-Y	Change the cross hair motion step size. Four sizes are available; the default value is the second largest size. The other sizes are 5, 1/5 and 1/25 times the default value.

9.5.3.5 Description of Annotation (INOTE Option) Operations

Interactive annotation allows the user to place text and symbols at any location on the screen. The cross-hairs are used to indicate the position of the lower left corner of the first letter of the string or symbol. The operations available are the following:

1 ENTER TEXT	Allows the entry of a text string (given in response to a prompt) at the current cross-hair location.
2 ENTER SYMBOL	Allows a TEKSIM symbol to be plotted at the current crosshair location. Symbols are specified by number - see the table in Appendix D.
3 CHANGE SIZE	Provides the user with control over the height of the characters. The default size is .15". The new size should be given in 1/100's of an inch (i.e., enter "15" for .15").
4 CHANGE ROTATION	Allows text to be written at an angle. The default value is 0 degrees.
5 RESTORE DEFAULTS	Restores the size and rotation parameters to their default values.
6 SAVE NOTES	Allows the notes currently displayed to be saved in a file for future use. A prompt for the file name occurs.
7 RESTORE NOTES	Allows notes saved with option 6 to be merged onto the current plot.
8 UNDO	Allows the most recent annotation to be removed from the plot.
9 DONE	Ends the annotation session.

Figures 9.4(a) and (b) show plots that were produced (excluding the cross-hairs) with the PC SUATEK package. In 9.4(a) editing of spikes has commenced after the plot is displayed. In 9.4(b) parametric plots of the raw data have been made versus one of the other parameters, and the curves have been appropriately annotated using the INOTE option.

264

Figure 9.4b. Parametric plot with annotation in process

Figure 9.4a. SUATEK plot with editing in process

9.5.4 <u>Obtaining Hard Copy (and/or reviewing the plot)</u>

Each plot is saved in a Tektronix Metacode file "METAFILE.TKF" and is available for re-plotting. Entering <u><ESC></u> after a plot is made, introduces a menu which allows selection of hard copy options.

Enter <u>M</u> or <u>m</u> for portrait orientation output and <u>L</u> or <u>l</u> for landscape orientation output. <u>L</u> and <u>M</u> give high resolution copies, while <u>l</u> and <u>m</u> give plots with a lower resolution if available.

METAFILE.TKF is translated specifically for your printer into a file PRTRFILE.BIN which may be saved or routed at your convenience.

Selecting <u>c</u> or <u>C</u> allows conversion of METAFILE.TKF to a different format. Lotus.PIC, Ventura .GEM, HPGL, and Encapsulated PostScript files may be created in this manner.

Note: If you saved METAFILE.TKF, you may re-display your plot by entering <u>SUATEKMETAFILE.TKF</u> Hard copy may be obtained again as before.

9.5.5 <u>Supported Hardware</u>

Through use of the *GraphiC* package, SUATEK supports more than twenty graphics cards, and over thirty types of printers, and this list is summarized in Table 9.12. Drivers for the most important ones at GL are provided on the distribution disks.

Table 9.12. Graphics Boards and Printers supported by SUATEK

Graphics Boards

Drivers are provided on the distribution
disks for the following:

IBM color graphics (CGA)
IBM Enhanced Graphics Adapter (EGA)
VGA 640x480 color
Hercules monochrome board
Genoa SuperEGA HighRes 800x600 color

Drivers are also available for a number of
other graphics cards, including products
of the following manufacturers:

AT&T
Corona (Cordata)
Video Seven V-RAM
Tatung VGAs
HP Vectra
Texas Instruments
Toshiba
Ahead Systems EGA Wizard/Deluxe
Sigma LaserView PLUS
Everex EVGA
STB VGA Extra/EM
Paradise VGA Professional
AST VGA Plus
Hewlett-Packard D1180A
VEGA Deluxe EGA
Graphics Boards

Printers

Drivers are supplied on the distribution
disks for several common printers; other
printer drivers are also available.

Laser Printers

Hewlett Packard LaserJet+
Corona Laser printer
Canon LBP-8II Laser printer
Digital LN03+ Laser printer
Quandum QuadLaser
PostScript(TM) printers

Dot Matrix/Inkjet Printers

IBM Graphic or Professional
Epson FX, RX, MX, LQ1500, LQ2550
C. Itoh Prowriter, 24LQ
NEC 8023, 8025, Pinwriter P series
Smith Corona D100
Okidata 92, 93, 192+, ML 393
Toshiba P321 and P351, P351C, 1340
Micro Peripherals 150, 180
CALCOMP ColorMaster
Tektronix 4695, 4696
Hewlett Packard ThinkJet, PaintJet

Plotters

Hewlett Packard HP-GL plotters
Epson, Houston, Roland, Watanabe

9.6 GLOSSARY FOR CRRES AND IBSS EPHEMERIS SYSTEMS

Acronym Description

Acronym		Description
a	-	Semi-major axis (orbital element)
a_e	-	Equatorial Radius of Earth (6378.135 km)
B	-	Magnetic Field magnitude
Bmin	-	Minimum field strength obtained by line tracing
Bconj	-	Field strength at conjugate or mirror point (=B)
CRRES	-	Combined Release and Radiation Effects Satellite
e	-	Eccentricity (orbital element)
E	-	Eccentric anomaly (orbital quantity)
ECI	-	Earth Centered Inertial coordinates
EMR	-	Earth Magnetic Dipole Radius (6371.2 km)
ET	-	Ephemeris or Dynamical Time
f	-	Flattening of Earth (1/298.26)
GE	-	Group-encoded (6250 cpi) magnetic tape
GEO	-	Earth-centered Geographic Coordinate System
GHA	-	Greenwich Hour Angle (same as RAG)
GL	-	Geophysics Laboratory
GMST	-	Greenwich Mean Sidereal Time (same as RAG)
GTO	-	Geosynchronous Transfer Orbit
GSM	-	Geocentric Solar Magnetospheric coordinates
i	-	Inclination (orbital element)
I	-	Longitudinal adiabatic invariant integral
IBSS	-	Infrared Background Survey System
IGRF	-	International Geomagnetic Reference Field
ILAT	-	Invariant Latitude (function of L-shell)
L-shell	-	Equatorial Radius of Equivalent Dipole which gives adiabatic invariant I and Field B
LASSII	-	Low Altitude Satellite Studies of Ionospheric Irregularities
LEO	-	Low Earth Orbit
LVLH	-	Local Vertical-Local Horizontal coordinates
M	-	Mean anomaly (orbital element)
MAG	-	Magnetic Earth-centered Dipole coordinates
MET	-	Mission Elapsed Time
MLT	-	Magnetic Local Time
n	-	Mean motion (orbital quantity)
PATH	-	NASA Postflight Attitude and Trajectory History Tape
PE	-	Phase-encoded (1600 cpi) magnetic tape
RAG	-	Right Ascension of Greenwich
R_E	-	Equatorial Radius of Earth (6378.135 km)
RELBET	-	NASA Relative Best Estimate Trajectory Tape
SM	-	Solar Magnetic coordinates
SCF	-	Satellite Control Facility
SPAS	-	Shuttle Pallet Satellite
SZA	-	Solar Zenith Angle
UT	-	Universal Time
VDH	-	Vertical-Dipole-Horizon coordinates (local)
VEN	-	Vertical-East-North Coordinate System
v	-	True anomaly (orbital quantity)
ω	-	Argument of perigee (orbital element)
Ω	-	Right ascension of ascending node (orbital element)

References

The Astronomical Almanac, (1985), U.S. Government Printing Office, Washington, D.C.

Bhavnani, K.H. and McInerney, R.E., "SUATEK Interactive User's Guide (for the CYBER)", Version April 1989.

Bhavnani, K.H., Raistrick, R.J. and Reynolds, D.S., "SUATEK Interactive User's Guide (for the PC)", Radex, Inc., Bedford, MA., Version June 1989.

Cain J.C., Gussenhoven, M.S., Private Communication.

Cottrell, K.G. and McInerney, R.E., Private Communication, December 1985.

Escobal, P.R., Methods of Orbit Determination, John Wiley & Sons, Inc., New York-London-Sydney, 1965.

"International Geomagnetic Reference Field (1985)", EOS, June 17, 1986.

Kluge, G., "Calculation of Field Lines and the Shell Parameter L from Multipole Expansions of the Geomagnetic Field, "ESOC Int. Note 66, October 1970.

Kluge, G., "Geomagnetic Field Models; Scalar and Vector Potential. Induction Vector and its Gradient Tensor Computed by a Common Algorithm", Comp. Phys. Comm. Vol 4, p347-360, 1972.

Kluge, G., and Lenhart, K.G., "Numerical Fits for the Geomagnetic Shell Parameter", Comp. Phys. Comm. Vol 3, p36-41 1972.

McIlwain, C.E., "Coordinates for Mapping the Distribution of Magnetically Trapped Particles", JGR 66 3681-3691, 1961.

McInerney, R.E. and Abelowitz, A., "MFP (Magnetic Field Package): A Flexible System of Computer Programs for Theoretical Magnetic Field Calculations", Special Report No. 161, AFCRL-TR-73-0356, 1973, AD766208.

McInerney, R.E., Raistrick, R., Robinson, E., Griffin, A., Private Communication, June 1986.

McInerney, R.E., Private Communication, August 1987.

McNeil, W.J. and McInerney, R.E., Private Communication, May 1988.

NASA Mission Operations Directorate, "OPS On-Orbit Postflight Attitude and Trajectory History (PATH) Product Description", August 1985. Radex, Inc. Report RXR87041, "CRRES Data Processing Ephemeris File Generating System Product Specification, 15 Apr 1987.

Rockwell International, "Internal ICD RELBET Product", ICD-1-TOP-001 January 15, 1988.

Scientific Endeavors Corp., GraphiC™ 5.0 Publication Quality Scientific Graphics, March 1989, Kingston, TN.

References (cont'd)

Williams, W. Jr., "Prediction and Analysis of Solar Eclipse Circumstances", A.D.Little, Inc., AFCRL 71-0049, March 1971, AD726626.

Ziemba, E.J. and McInerney, R.E., Private Communication, August 1979.